Models of the Transition Regions and Coronae of Late-Type Stars

Despina A. Philippides

Wolfson College

Department of Physics · Theoretical Physics
University of Oxford

A thesis submitted for the degree of Doctor of Philosophy at the University of Oxford

Hilary Term, 1996

To my parents

Since he was travelling east, he was going away from the sun at a speed of 17,500 miles an hour. But because he was riding backward he could see the sun out the window ...The edge of the sun began to touch the edge of the horizon ...The brilliant light over the earth began to dim. It was like turning down a rheostat. It took five or six minutes ...Then he couldn't see the sun at all but there a tremendous band of orange light that stretched from one side of the horizon to the other, as if the sun were a molten liquid that had emptied into a tube along the horizon. Where there had been a bright-blue band surface, there was now the orange band; and above it a wider, dimmer band of oranges and red shading off into the blackness of the sky. Then all the reds and oranges disappeared and he was on the night side of the earth. The bright-blue band reappeared at the horizon. Above it, stretching about eight degrees, was what looked like a band of haze created by the earth's atmosphere. And above that ...for the first time he could see the stars.

Tom Wolfe, *The Right Stuff*
(Bantam Books, 1983)

Models of the Transition Regions and Coronae of Late-Type Stars

Despina A. Philippides
Wolfson College
Department of Physics · Theoretical Physics
University of Oxford

A thesis submitted for the degree of Doctor of Philosophy at the University of Oxford

Hilary Term, 1996

Abstract

This thesis examines the structure and heating requirements of the outer atmospheres (the lower transition region, upper transition region and corona) of the five dwarfs χ^1 Ori (G0V), ϵ Eri (K2V), ξ Boo A (G8V), α Cen A (G2V) and α Cen B (K0V), and the sub-giant Procyon (F5 IV-V).

Alternative fits to X-ray spectra of ten late-type dwarfs from ROSAT are made using the latest available versions of the radiative power loss codes of Raymond and Smith, Landini and Monsignori Fossi, and Mewe *et al.*. Differences between these codes are found to arise from the choice of atomic physics and the number of transitions included. The resulting coronal temperatures and emission measures are found to follow correlations proposed by Montesinos & Jordan (1993).

The lower transition region is modelled using observations made with the *International Ultraviolet Explorer* and up-to-date atomic data. Models of the upper transition region and corona are derived assuming a balance between the radiative and conductive losses. Wave pressure is included in these models for the first time. Recent observations with the *Extreme Ultraviolet Explorer* aid the choice of starting parameters. The calculations are carried out in plane parallel and spherically symmetric geometries. The models of the lower and upper transition region are then combined; the spherically symmetric models of the upper transition region fit more smoothly on to those of the lower transition region than do the plane parallel models. The new model of Procyon and new measurements of N_e resolve a previous discrepancy which led to suggestions that emission in the transition region is restricted in area.

The heating requirements are examined. In the five dwarfs, but not in Procyon, the conductive fluxes at the base of the upper transition region are found to exceed the radiative energy losses for the layers immediately below. In Procyon, it is shown that acoustic wave heating is a viable mechanism for heating the lower transition region and corona, while the correlation of coronal properties with the dynamo Rossby number suggest that magnetic heating models are more likely for the five dwarfs.

Acknowledgements

First and foremost, I am grateful to my supervisor Professor Carole Jordan for her invaluable guidance and advice while I was a research student.

I would like to thank Drs Graham Harper, Benjamin Montesinos and Hong Chao Pan for useful discussions related to this thesis, and for helping me find my way with computing. A special mention goes to my office mates: Stephen John Magorrian, Neil William Griffiths, Andrew McMurry, Jenny Read, and Andy Rowe, for making Rm 2.9 a truly extraordinary and fun place to work in!

A big thanks to Ann, Gavin, Joy, Andreas, Yoko, Vicky, and Mamas, for being terrific friends!

I dedicate this thesis to my parents, $A\nu\delta\rho\epsilon\alpha\varsigma$ and $B\alpha\sigma\iota\lambda\iota\kappa\eta$, not only for their constant encouragement and support, but for everything they have done for me!

This research was partially funded by PPARC.

Contents

Chapter 1

Introduction

§*1.1* *Overview*

The overall objectives of my research have been to model the structure of the transition regions and coronae of late type stars in order to investigate the heating requirements of these regions. Such detailed studies of a few stars will help to understand how the coronal parameters and heating depend on the stellar parameters, including rotation rates and convection zone structure.

Observations of emission line spectra with the International Ultraviolet Explorer (IUE) have shown that all main-sequence stars between spectral types F5 V to M5 V have ultraviolet spectra similar to that of the Sun (Jordan & Linsky, 1987). I set out to examine five such stars, (namely, χ^1 Ori (G0V), ϵ Eri (K2V), ξ Boo A (G8V), α Cen A (G2V) and α Cen B (K0V)), for which it is possible to obtain high quality IUE and X-ray spectra. These stars are important in understanding a range of correlations observed from a larger sample of stars for which only more limited observations are possible. Three of these stars (χ^1 Ori, ξ Boo A and ϵ Eri) have measured surface magnetic fields and filling factors (Saar, 1987; Marcy & Basri, 1989). Earlier models were made by Jordan *et al.* (1987), but since then new observations of coronae in the X-ray and extreme ultraviolet wavebands have been made with the **RÖ***entgen* **SAT***ellit* (ROSAT) and the Extreme Ultraviolet Explorer (EUVE). My aim has been to compute improved models of the lower transition regions and new models of the upper transition regions and coronae of these stars. A well-observed slightly evolved star, Procyon (α CMi, F5 IV - V) was also examined, for comparison with the five dwarfs.

In order to put the work of this thesis into a more general context, the remainder of this chapter presents a brief overview of the development of studies of stellar transition regions and coronae, starting with the Sun.

§1.2 The Sun

The Sun (G2V) is the most thoroughly studied star merely because of its proximity to the earth, which allows observations to be made with high spectral and spatial resolution, and hence detailed investigations of its atmosphere. Studies of the Sun provide results that can be applied to the interpretation of the properties of other main-sequence stars.

1.2.1 The Structure of the Solar Atmosphere

The overall structure of the Sun is illustrated in Figure 1.1.

The Photosphere

This is a dense and opaque layer of plasma which is only $\sim$ 550 km thick but is the source of the bulk of the emitted radiation. Its spectrum consists of a continuum with superimposed dark absorption lines. High resolution photographs show a granulation network, which is due to the outflow of plasma from the tops of small convection cells ($\sim$ 700 km) that are overshooting from the upper convection zone.

Owing to the presence of a magnetic field (Beckers, 1976; Howard, 1977), the photosphere contains rapidly evolving, small magnetic elements which distribute themselves in large scale patterns in the form of:

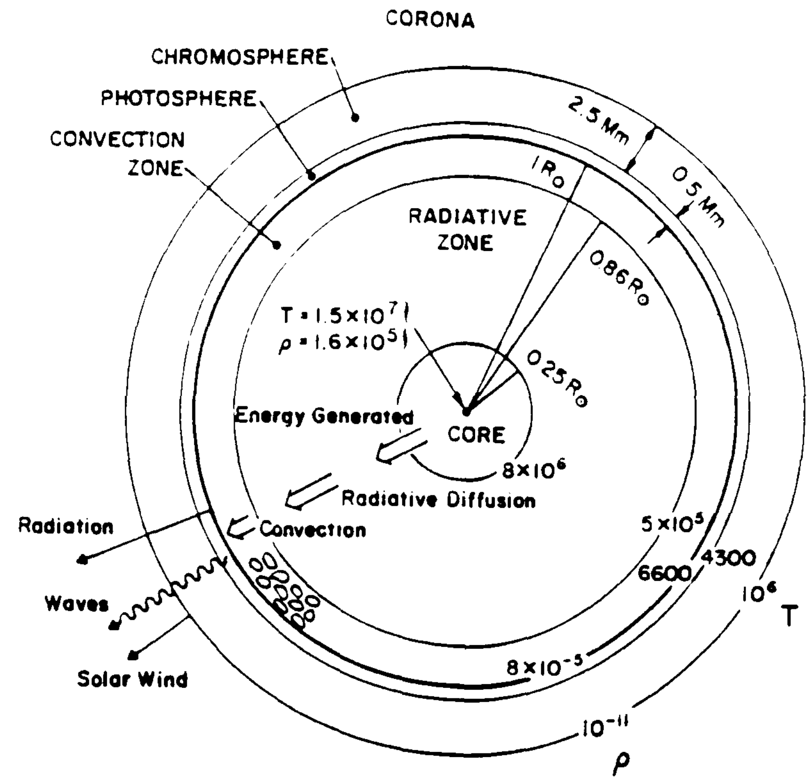

Figure 1.1: The solar structure, indicating the sizes of the various regions. The temperatures are expressed in units of degrees K, and the densities in kg m^{-3}. The thickness of the chromosphere and photosphere are not to scale and recent models place the base of the convection zone at $\sim$ 0.70 $R_\odot$ rather than 0.86 $R_\odot$. The average thickness of the chromopshere is also an over-estimate and a more realistic value would be $\sim$ 2.0 Mm. (From Priest, 1982).

1. *Sunspots*: these form from large concentrations of magnetic flux.

2. *Plage regions*: These are regions of high magnetic flux surrounding sunspots.

3. *Large-scale unipolar areas*: These contain elements of predominantly one polarity; they are exceptionally long-lived and can extend over several 10^5 km in latitude and longitude.

4. *Supergranulation fields*: these are concentrations of magnetic flux found in supergranule boundaries (see below). They are made up of small flux (< 700 km) tubes of field strength 1-2 kG.

5. *Ephemeral regions*: they are small ($\sim$ 700 km) bipolar magnetic regions which correlate in position with coronal bright points.

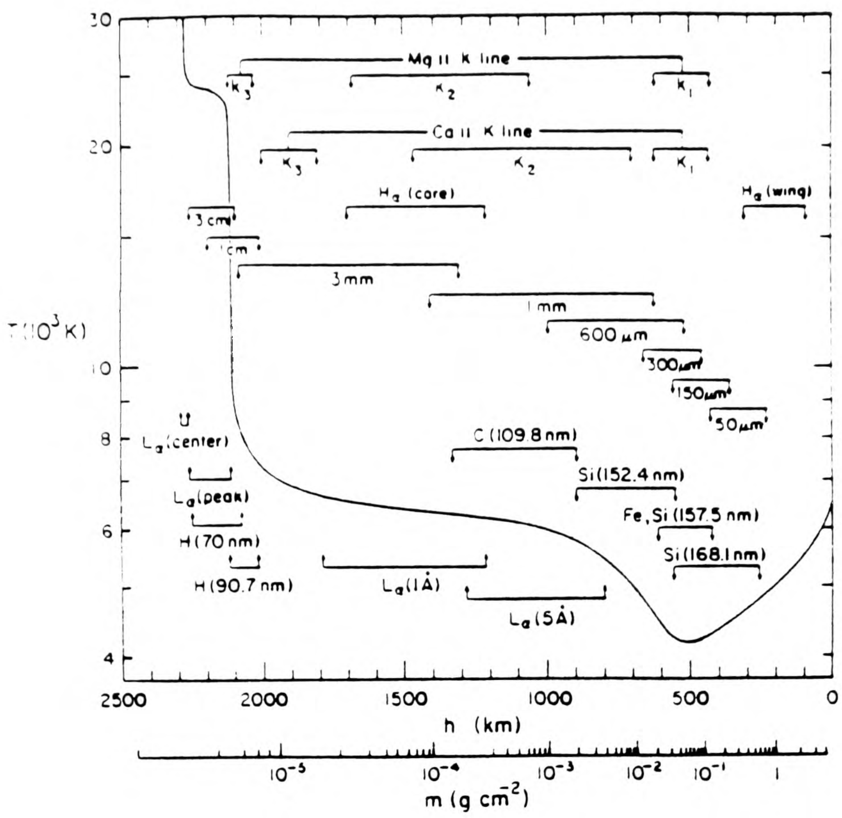

Figure 1.2: A schematic diagram indicating the regions of formation of the most important chromospheric lines w.r.t. height and mass column density. From Vernazza, Avrett & Loeser (1981).

The Chromosphere

This region is more transparent than the photosphere, and has a temperature between $\sim$ 4000 K and $\sim$ 10^4 K. The boundary between the photosphere and the chromosphere is usually defined as the region of temperature minimum, beyond which a non-radiative energy deposition mechanism causes an increase in temperature.

The Mg II h (2808 Å) and k (2796 Å) lines, and the Ca II H (3968 Å) and K (3934 Å) lines are the two most readily observed indicators of the presence of chromospheres in late-type stars (spectral type F to M). Figure 1.2 illustrates the regions of formation of the most important chromospheric lines from a model by Vernazza. Avrett & Loeser (1981). High spatial resolution observations of the Sun of strong lines provide important information about the structure of the chromosphere. In particular, the Ca II K line has revealed the existence of an irregular network pattern known as supergranulation. Also, the Hα line shows evidence of small scale structures at the supergranulation boundaries. They in turn consist of horizontal structures known as fibrils. and an inhomogeneous distribution of vertical jet-like structures (known as spicules) which appear above a height of $\sim$ 2000 km (Withbroe, 1983). The upward mass flux carried by the spicules (averaged over the solar surface) lies in the range 4 to 8×10^{-9} g cm^{-2} s^{-1}. Since the mass loss due to solar wind is 3×10^{-11} g cm^{-2} s^{-1}, most of the spicular material falls back to the chromosphere (Beckers, 1972; Athay, 1976).

The Transition Region

This region is a relatively narrow layer that separates the chromosphere from the corona, and is characterised by its very steep temperature gradient where the temperature increases from $\sim 2\times10^4$ K to $\sim 10^6$ K in only a few thousand kilometers. Typically, transition region models show that the temperature jumps from 3×10^4 K to 3×10^5 K in only 30 km, while the increase from 3×10^5 K to 10^6 K occurs over 2500 km. The average height of the transition region at $\sim 10^5$ K in the quiet sun was found to be 1700 $\pm$ 800 km (Burton *et al.*, 1971).

Resonance lines such as those of C IV ($\sim$ 1548 Å) and Si IV (1400 Å), which are formed at temperatures $\sim 10^5$ K, are typical indicators of a transition region. Observations of the solar transition region in EUV and soft X-ray wavelengths also show evidence of spatial structures; the supergranulation network pattern appears in lines formed up to $\sim 5\times10^5$ K (*e.g.* Ne VII), but disappears in the Mg X line which is formed at $\sim 10^6$ K. This pattern consists of bright network elements and darker cell interiors, whose contrast varies with temperature, which implies that the relative contribution of the network to the spatially averaged emission in each line must also change with temperature. Reeves (1976) found that the quiet solar network contributes $\sim$ 60% of the total intensity of lines formed at temperatures $\sim 10^4$ K, $\sim$ 75% for those formed at $\sim 2\times10^5$ K and $\sim$ 50% for lines formed above 10^6 K.

The Corona

Grotrian (1939) suggested that the red emission lines at 6374 Å and 7892 Å, which were observed in coronal spectra, were due to forbidden transitions in Fe X and Fe XI respectively and this was later confirmed by Edlén (1942). These findings showed that a high temperature existed in the corona. Since the thermal radiation of the photosphere cannot lead to an electron temperature of $\sim 10^6$ K in the corona, this implied that some non-thermal mechanism must heat the corona.

Early calculations of the coronal temperature were made assuming that for each stage of ionisation the collisional ionisation rate equals the radiative recombination rate. This gave lower values than those implied from radio observations. This discrepancy was resolved by Burgess (1965) who showed that di-electronic recombination must be included in the total recombination rate. This increased by a factor of 2 the temperature at which for coronal ions the collisional ionisation rate balanced the recombination rate, leading to an average coronal temperature of $\sim 1.5 \times 10^6$ K, which was in agreement with other observations.

Above a height of $\sim 3 \times 10^4$ km the corona becomes almost isothermal and a maximum temperature (2×10^6 K) is reached by $\sim 1R_\odot$ (Mariska, 1992). Because the magnetic field diverges in the high transition region, it is difficult to relate coronal features to the underlying structure of the transition region. At EUV and X-ray wavelengths loop-like structures appear embedded in the diffuse coronal emission. These coronal loops show the presence of relatively low-lying closed magnetic field lines which are rooted in active regions. The magnetic field in the average corona may be associated with the fields in the supergranulation boundaries and the remnants of the closed fields that have expanded above active regions. In coronal holes, which are regions of lower than average density and temperature, the magnetic field lines are open and diverging. The latter regions are not in a state of hydrostatic equilibrium and there is an outward flow of plasma known as the solar wind (Hundhausen, 1972). X-ray bright points distributed across the solar disk, also show the presence of magnetic fields in the low corona, and are associated with small ephemeral regions of magnetic flux in the photosphere (see earlier discussion).

1.2.2 The Role of Magnetic Fields

Magnetic fields are observable at photospheric levels and emission in the overlying atmosphere tends to be enhanced where the fields are strong. Wave and energy can be transported along the magnetic field lines which hence play an important role in heating the stellar atmosphere (Kopp, 1972; Gabriel, 1976a). The generation of magnetic fields is thought to occur at the base of the sub-photospheric convection zone by the interaction of convection and differential rotation, through dynamo action. At the photosphere of the quiet Sun, $\sim 90\%$ of these fields clump into discrete elements within supergranule boundaries in the network (Stenflo, 1989). These fields can only be confined in the photosphere where the pressure is $\sim 10^5$ dyn cm^{-2} (Vernazza *et al.*, 1981). However, the density and the pressure decrease with increasing height and this causes an imbalance between the magnetic and gas pressures; as a result a confined flux tube in the photosphere will expand in layers above.

For a unipolar magnetic field, Gabriel (1976a) developed a model where the field expands with height until the elements fill up the available volume as shown in Figure 1.3. If the neighbouring filaments are of opposite polarity, loop-like structures are likely to develop but expansion will still occur as they arch up into regions of lower density.

§1.3 The Outer Atmospheres of Stars

The presence of coronae in stars other than the Sun became apparent from rocket observations which detected low-luminosity X-ray sources associated with nearby stellar objects. One of the first stars to be identified as having a corona was Capella (Catura, Acton & Johnson, 1975), but later observations have shown that all types of main-sequence stars with spectral type classification later than F0, possess hot coronae whose temperatures exceed 10^6 K. Figure 1.4 shows the distribution of stars on a Hertzprung-Russell (H-R)

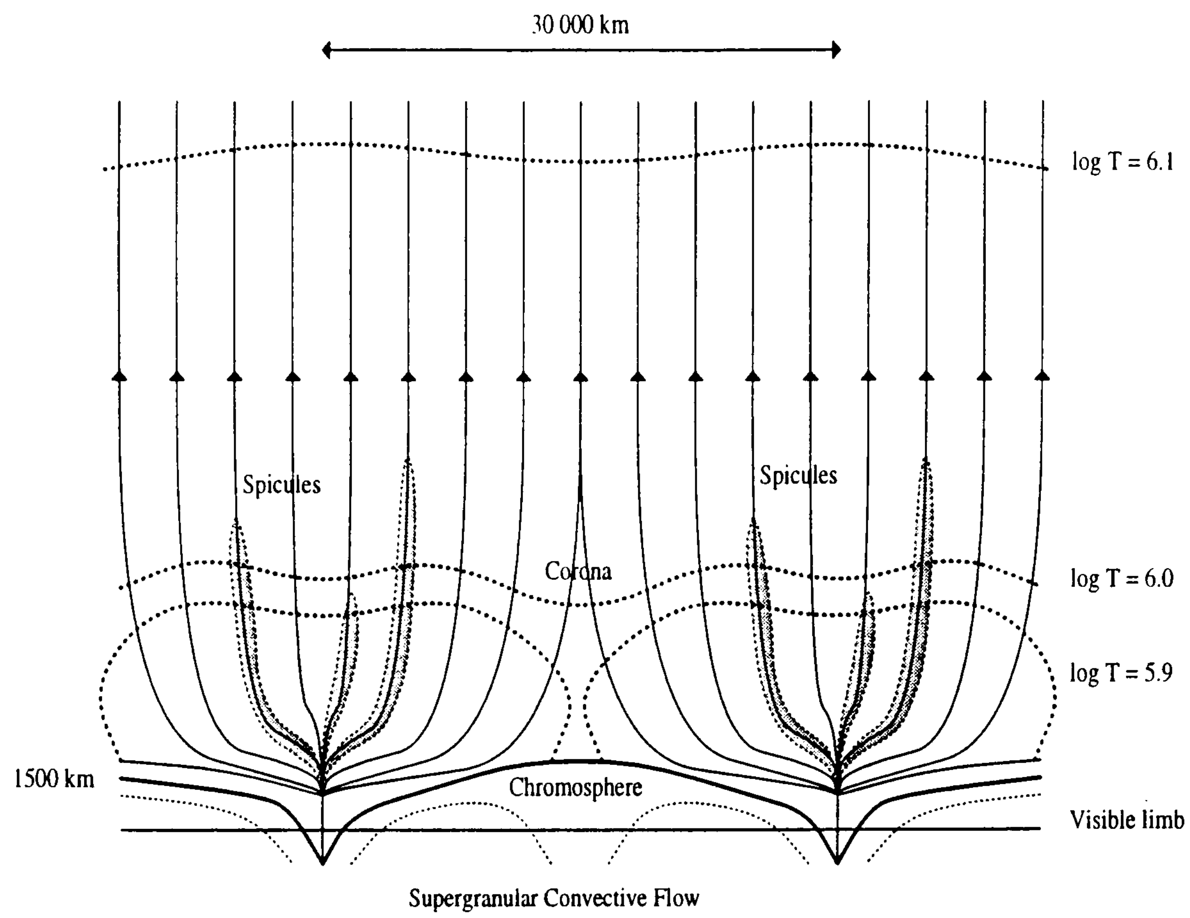

Figure 1.3: The magnetic field geometry (from Gabriel, 1976a).

diagram that have *(i)* transition regions and hence coronae, and *(ii)* those that only have chromospheres. Although more recent observations have changed the details of this diagram, it shows that coronae in evolved stars are mostly restricted to spectral type F and G.

An outer convection zone (*i.e.* a region of convective turbulence which for the sun lies above a radius of 0.70 $R_{\odot}$) in stars of spectral type F, G, K and M, was found to be an indicator of the existence of a chromosphere by Böhm-Vitense & Dettman (1980). They also found that a dividing line exists between stars with and without an efficient hydrogen convection zone, which corresponds to the red boundary of the Cepheid instability strip in the H-R diagram. This is supported by the fact that the characteristic chromospheric Ca II and Mg II k emission occurs beyond the red side of this boundary (Böhm-Vitense & Canterna, 1974).

The spectral type of main-sequence stars is related to their convection zones properties:

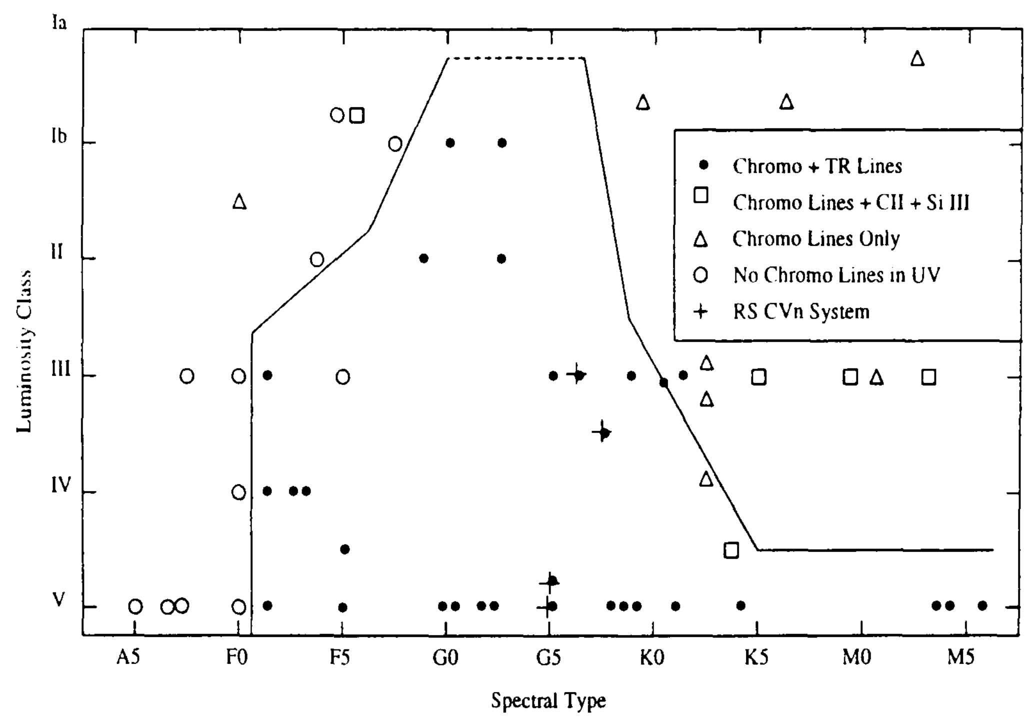

Figure 1.4: H-R diagram indicating the position of stars that show spectroscopic evidence of chromospheres and/or transition regions (Linsky, 1980). Stars with transition regions are found in the region which is outlined by solid lines.

the later types have deeper convection zones relative to their radii. According to dynamo theory, magnetic fields are generated through the stellar rotation, differential rotation and convection (Gilman, 1983). For a given rotation period, stars of a later spectral type should have stronger dynamo action and magnetic fields, and larger magnetic surface fluxes, reflected through higher chromospheric, transition region and coronal emission. However, for a *given* spectral type, faster rotators should have the stronger emission, as observed.

The increase of the depth of the convection zone relative to the stellar radius causes an increase in dB/dt. Rutten (1986) found that dwarfs with $B - V \geq 0.4$ and giants with $B - V > 0.5$ to 0.6 have a convection zone that is thick enough to sustain dynamo action.

§1.4 *Observations of Chromospheres, Transition Regions and Coronae*

Many technological developments have been made in the context of instruments for observations of the Sun in the UV, EUV and X-ray regions. Here, I summarize the principal results from satellites and instruments that have been used for stellar observations, up to those made with ROSAT, which are discussed in Chapter 2.

Although various rocket flights (*e.g.* Skylark) and satellites (*e.g.* HEAO-1, the *Astronomical Netherlands Satellite* (ANS)) were used to detect X-ray emission from some stars, the first extensive observations were made with the *Einstein Observatory* (Giacconi *et al.*, 1979). The Imaging Proportional Counter obtained low spectral resolution observations (essentially broad-band), for which it was possible to estimate coronal temperatures as well as total average coronal fluxes. Vaiana *et al.* (1981) carried out an extensive stellar survey using observations made with *Einstein*, and found that X-ray emission appeared to be characteristic of some main-sequence stars, pre-main sequence and late-type giants and supergiants of type $\sim$ G, and of stars in close binary systems. Throughout the main-sequence (later than F0), the data showed a range of X-ray luminosities covering $\sim$ 3 orders of magnitude. A comparison of these data with theories of coronal heating by acoustic waves, showed that this mechanism is inadequate. The observed correlations between coronal properties determined from X-rays and stellar rotation rates and convection zone properties, suggest that magnetic fields are the cause of coronal activity. Observations of the coronae of late-type stars were also made with EXOSAT in the wavelength range of 20 - 200 Å.

Observations of stars in the ultraviolet were made with some rocket flights which observed the Mg II h & k lines, and with the *Copernicus* and *TD-1* satellites, which observed the H Ly-α line. The first evidence of material at transition region temperatures came from observations of Procyon with *(i) Copernicus*, which detected the O VI (1032 Å) line at $\sim 3 \times 10^5$ K (Evans, Jordan & Wilson, 1975), and *(ii) TD-1* which detected C IV (1550 Å) emission formed at 2×10^5 K (Jamar Macau-Hercot & Praderie, 1976).

The *International Ultraviolet Explorer* (IUE) satellite, which was launched in 1978 and is still operating, has been used to observe an extensive number of stars at low resolution

(6 Å) in the wavelength range between 1200 - 3000 Å. These observations have enabled the properties of chromospheres and transition regions of late-type stars to be studied as a function of spectral type and luminosity class. The brighter late-type stars can be observed with the high resolution capability of IUE (~ 0.2 Å), including all the stars that are examined in this thesis (see Brown & Jordan, 1981; Ayres *et al.*, 1983; Jordan *et al.*, 1986; Jordan *et al.*, 1987). Observations at high resolution allow the profiles and/or widths to be measured for the stronger lines, as well as the line fluxes. Properties of stellar chromospheres and transition regions derived from early observations with IUE are discussed in the review by Jordan and Linsky (1987).

Observations with the *Goddard High Resolution Spectrograph* (GHRS) on the *Hubble Space Telescope* (HST) should improve measurements of line widths. In the last few years, ROSAT and the *Extreme Ultraviolet Explorer* (EUVE), have completed the first ever all-sky surveys in the EUV waveband. Observations made of the five dwarfs and Procyon are discussed in Chapters 3 and 4, respectively.

§1.5 Flux Correlations

Correlations have been made between stellar rotation rates and chromospheric emission (Ca II H and K lines) for stars with convection zones (Kraft, 1967), which are in turn linked to the magnetic activity found on the surface of these stars (Parker, 1978). Pallavicini *et al.* (1981), extended these relations to coronal activity. Chromospheric, transition region line fluxes from IUE and X-ray fluxes from *Einstein*, have allowed further correlations to be made between these fluxes (known as *flux - flux* correlations), that are independent of spectral type or luminosity class (see Ayres, Marstad & Linsky, 1981; Oranje, Zwaan & Middlekoop, 1982; Oranje, 1986; Schrijver & Rutten, 1987). Correlations between the stellar rotation period Π_{rot} and line fluxes (known as *flux - period* correlations), do show a colour dependence for dwarf stars, as was found by Mangeney & Praderie (1984), Noyes *et al.*, (1984), Vilhu (1984), Simon, Herbig & Boesgaard, (1985), Simon & Fekel, (1987), Maggio *et al.*, (1987), and Dobson & Radick, (1989).

Jordan & Montesinos (1991) and Montesinos & Jordan (1993) extended the correlations to coronal parameters and the observed surface magnetic fields and filling factors. They found that for stars of the same spectral type, the fast rotators exhibit larger surface magnetic fluxes, filling factors and implied coronal magnetic fields; however, in the fast rotators a smaller fraction of the surface magnetic flux extends to the corona.

While studies of correlations are valuable in showing the general trends in coronal properies, to *understand* these in terms of the structure and energy balance in the atmosphere requires detailed modelling of individual stars, as well as measurements of B-fields and filling factors for a larger sample of stars. Improving the models of a few well-studied stars (see Chapter 3) has been the main motivation of the present work. In Chapter 2, some of the correlations found by Montesinos & Jordan (1993) are investigated in relation to the sample of stars whose ROSAT observations are analysed in this work.

§1.6 Heating Mechanisms

The ultimate aim of modelling the outer atmospheres of cool stars, is to answer the most important question concerning the heating of chromospheres and coronae: *what mechanism/s transport the energy from the convection zone and dissipate it in the outer atmosphere?* Initially, it was thought that sound waves were responsible for coronal heating (Biermann, 1946; Schwarzchild, 1948), but it was later shown that such a mechanism was incapable of sustaining an energy that was high enough to heat the solar corona (Athay & White, 1978, 1979). Attention then focused on Alfvén wave heating (Hollweg, 1982) and heating by the energy released by the reconnection of magnetic fields (Parker, 1983). It is thought that Alfvén waves originate at the supergranulation boundaries and the strong concentration of magnetic fields allows them to penetrate into the photosphere; they then propagate to the corona where they arrive totally undamped and unreflected. However, Anderson & Athay (1989) propose that the chromosphere exhibits characteristics which are compatible with heating by sound waves while magnetic fields are more likely to be responsible for heating the corona. Narain & Ulmschneider (1990) have recently reviewed the types of heating mechanisms proposed. Since the chromospheric emission is concentrated to the supergranulation network, it is possible that both acoustic and MHD waves are playing a role.

The mechanisms that are responsible for *energy loss* are:

1. *Radiation*: is the principal *overall* energy loss mechanism.
2. *Thermal conduction*: This is most important mechanism for removing energy from the corona. The energy is transported downwards to the photosphere where it is lost by radiation, and a smaller fraction is transported in the solar wind.
3. *Mass flow*: This idea was proposed by Parker (1958) and is based on the theory of conversion of the random thermal energy of the stellar atmosphere by a stellar wind in isothermal equilibrium, into potential energy as well as an outwardly directed kinetic energy of the plasma. Beyond a critical point, the plasma has enough energy to escape from the corona. A comprehensive introduction is given in Brandt (1970).

While radiation is the main mechanism for energy loss for the chromosphere, all three mechanisms are responsible for the energy lost from the solar corona. In the quiet Sun, the coronal radiative losses are typically 10^5 erg cm^{-2} s^{-1} (Withbroe, 1976) while solar wind losses are an order of magnitude lower. The energy that is conducted *down* from the corona to the lower atmospheric layers is $\sim 4.4 \times 10^5$ erg cm^{-2} s^{-1} (Gabriel, 1976b), hence it is clear that conduction is the dominant energy loss mechanism from the average corona.

Possible *energy input* mechanisms are:

1. *Dissipation of magnetohydrodynamic (MHD) waves*: Hollweg, Jackson & Galloway (1982), showed that waves (which originate in the sub-photospheric convection zone), with periods smaller than a few minutes steepen into fast (longitudinal) and slow (acoustic, guided along the field) MHD shock waves in the chromosphere. They proposed that the fast waves dissipate and heat the coronal plasma as they propagate outward. It is believed that slow MHD waves (Bierman, 1948; Ulmschneider, 1971), are responsible for chromospheric heating. Alfvén (1947) first suggested that the corona may be heated by Alfvén waves and Withbroe (1988) found evidence of their presence in the solar wind. However, the extent to which they can heat the corona is not yet certain as there are insufficient observations of non-thermal line widths above 2×10^5 K to derive the non-thermal fluxes as a function of temperature.

2. *Dissipation of energy stored in magnetic fields*: Coronal heating is thought to be a consequence of this process through magnetic reconnection. Convection in the layers below the photosphere continually twist and displace the footpoints of the magnetic fields which results in the random twisting of magnetic field lines around each other, and this transfers the work done at the footpoints into energy dissipated in the corona (Parker, 1983). At the interface between two magnetic fields of opposite polarity, a current sheet is formed whose pressure at the centre greatly exceeds that outside and this forces an outflow of plasma from the sides of the sheet at the Alfvén speed. As a result, the magnetic field lines of the two flux tubes connect and a large amount of energy is released as a consequence of the energy of the system being reduced and converted to kinetic energy of the plasma. This is known as magnetic reconnection.

3. *Thermal conduction*: heating of the low transition region and perhaps the upper chromospheric layers can occur via thermal conduction of coronal energy which is conducted downwards. (In solar flares conduction certainly penetrates down to the chromosphere.)

4. *Mass flow*: It is possible to heat the chromosphere by the energy released from down-

falling coronal material. Athay & Holzer (1982) suggested that the quasi-steady downflow of spicular material may be a possible secondary source of heating of the upper chromosphere, by converting the gravitational potential energy that was gained during the upflow into thermal energy. At the base of the spicules, this energy was calculated to be $\sim 10^6$ erg cm^{-2} s^{-1}, which is comparable to the amount radiated at the base of spicules in the upper chromosphere. In order to release this energy, the spicules must be heated to heights $\geq$15 000 km. It has also been suggested that if sufficient heat is added, the spicules may be responsible for maintaining the high temperature of the corona. The heating rate must be slow enough so as to allow the spicular material to expand in pressure equilibrium with the corona. However, there is no observational evidence that significant amounts of spicules are heated to coronal temperatures. It is therefore unlikely that mass flow acts as a major heating mechanism.

§1.7 *This Thesis*

The starting point in the analysis of low resolution X-ray spectra is to compare them with the predictions of plasma emissivity codes that attempt to take into account the dominant atomic processes in solar-like stellar coronae. Several such codes have been developed. I carried out a detailed investigation of three in common use (those of Raymond & Smith, 1992 (private communication), Landini & Monsignori-Fossi, 1993 (private communication), and Mewe, Gronenschild & van den Oord, 1985). Often, these codes are used as a 'black box' in spectral analysis packages, with little consideration of the atomic physics contained in this thesis. This analysis has allowed me to understand the differences between the results of spectral fitting and the limitations of the codes. Some systematic differences are noted and discussed. The reduced X-ray data from ROSAT observations of ten stars are then fitted to radiative power loss codes using one and two temperature fits and continuous emission measure distribution fits, so as to obtain coronal emission measures and temperatures.

These are then compared with the correlations proposed by Jordan & Montesinos (1991) and Montesinos & Jordan (1993). The above work is covered in Chapter 2.

Adopting the line fluxes from previous IUE observations (Brown & Jordan, 1981; Ayres *et al.*, 1983; Jordan *et al.*, 1986; Jordan *et al.*, 1987), and using updated atomic data and abundances, I have derived emission measure distributions for the transition regions of five dwarf stars and written a new code to give an optimum fit to the observed fluxes. The coronal emission measure distribution is derived using the ROSAT data, and EUVE data where available. The coronal temperatures and emission measures provide boundary conditions for the subsequent modelling. Immediately below the corona, I assume a balance between the energy deposited by thermal conduction and that lost by radiation. Models are computed for plane parallel and spherically symmetric geometries, and are then compared to the observations. The models are made in hydrostatic equilibrium, and unlike earlier ones, take account of wave pressure. The models of the transition regions and coronae are then combined using an iterative procedure to give the full distribution between the corona and base of the transition region. These models are discussed in Chapter 3.

X-ray and UV observations of the subgiant Procyon (α CMi F5 IV-V) have been used to model its outer atmosphere following the same procedure adopted for the five dwarfs, and this work is presented in Chapter 4. There are differences between Procyon and the five dwarfs which probably relate to its lower surface gravity and shallower convection zone.

Chapter 5 discusses the implications of the results, draws some final conclusions and makes suggestions for future work.

Chapter 2

X-Ray Data Analysis

§2.1 *Introduction*

Observations at X-ray wavelengths are required in order to determine the physical conditions in the corona and upper transition region. Ten late-type dwarfs and a subgiant have been observed with the Position Sensitive Proportional Counter (PSPC) instrument on ROSAT (see Section 2.2.2), as part of Jordan's guest investigator programme. The PSPC observations of the dwarfs χ^1 Ori (G0V), ϵ Eri (K2V) and ξ Boo A (G8V) and the subgiant Procyon (F5 IV-V), (which are modelled in Chapters 3 and 4), have been complemented with the EUV all-sky survey observations (Pounds *et al.*, 1993), made with the Wide Field Camera (WFC) on ROSAT, and are discussed in Section 2.2.3. Since there are no PSPC pointed observations of α Cen A & B (G2V and K0V), the WFC observations have been used to deduce their coronal parameters and these stars are modelled in Chapter 3.

The above observational data have been reduced and several types of fits have been made to the spectra using radiative power loss codes. Quite often, these codes are used as 'black boxes' in spectral analysis packages with little consideration of the atomic physics contained in them. In order to understand the potential uncertainties and limitations of these fits, I have examined three of the most widely used codes, which are discussed further in Section 2.4.

Section 2.3 gives a brief account of how the raw data were reduced and analysed, while the spectral fitting is described in Section 2.5. The results obtained from the analyses are presented in Section 2.6, some conclusions are drawn, and comparisons are made between the present results and the correlation functions of Jordan & Montesinos (1991) and Montesinos & Jordan (1993).

§2.2 *The ROSAT Observations*

2.2.1 The Stars Observed

The stellar parameters of the stars that were observed with the PSPC and WFC are given in Table 2.1, while a log of the PSPC observations is given in Table 2.2. The stars χ^1 Ori, ϵ Eri, ξ Boo A, α Cen A and B are referred to as *the five dwarfs*, since they were the subject of earlier studies by Ayres *et al.* (1983) and Jordan *et al.* (1987).

2.2.2 The Position Sensitive Proportional Counter (PSPC)

The PSPC detector operates in the energy range 0.1-2.4 keV and has a moderate energy resolution of 43% at 0.93 keV and an on-axis spatial resolution of $\sim$ 25 arcsec (FWHM). A Boron filter could be optionally inserted in the optical path of the PSPC instrument during the observations. (The filter has little transmission between 0.188 keV and 0.280 keV and so excludes the low energy channels.) For a detailed description of ROSAT and the PSPC instrument see the document titled *'ROSAT AO-2 Technical Description'*, (1991). (A brief description of this instrument is given in Appendix A).

Several problems have been associated with the detector which have consequently affected the observations and these and the spectral fitting of the data are described below:

- A synchronization problem in the timing of individual PSPC events affected all data after 25th January, 1991, which was due to a tumbling incident of the satellite.

Table 2.1: Stellar Parameters.

HD	Star	*Sp.Type*	d (pc)	B − V	R_* ($R_\odot$)	$log\, g_*$ (cgs)	R_o
22049	$\epsilon\, Eri$	$K2V^a$	3.30^a	$+0.88^a$	$0.82^{k,l}$	4.75^b	0.52^m
165341	$70\, Oph A$	$K0V^a$	5.00^a	$+0.86^a$	0.85^f	4.50^h	0.93^m
201091	$61\, Cyg A$	$K5V^a$	3.40^a	$+1.18^a$	0.74^f	4.62^h	1.55^m
39587	$\chi^1\, Ori$	$G0V^a$	9.90^a	$+0.59^a$	1.20^k	4.39^h	0.61^m
45088	$OU\, Gem$	$K3V^g$	12.00^a	$+0.96^g$	0.33^g	4.53^h	0.33^m
20630	$\kappa\, Cet$	$G5V^a$	9.30^a	$+0.68^a$	0.93^e	4.43^h	0.69^m
61421	$Procyon$	$F5\, IV - V^a$	3.40^a	$+0.76^a$	2.05^c	4.00^c	–
131156	$\xi\, Boo A$	$G8V^a$	6.90^a	$+0.42^a$	0.76^d	4.58^d	0.35^m
115404	–	$K2V^e$	12.00^a	$+0.94^e$	0.84^e	4.53^h	0.84^m
152391	–	$G8V^e$	16.00^a	$+0.76^e$	0.62^e	4.46^h	0.62^m
155886	$36\, Oph$	$K0V^a$	5.40^a	$+0.86^a$	0.85^f	4.50^h	0.96^m
128620†	$\alpha\, Cen\, A$	$G2V^a$	1.34^a	$+0.71^a$	$1.10^{i,j}$	4.40^d	1.99^m
128621†	$\alpha\, Cen\, B$	$K0V^a$	1.34^a	$+0.88^a$	$0.75^{i,j}$	4.65^d	1.23^m

[a] Hoffleit (1982).
[b] Drake & Smith (1993).
[c] Steffen (1985).
[d] Smith, Edvardsson & Frisk (1986).
[e] Saar (1987).
[f] Basri (1987).
[g] Saar & Linsky (1986).
[h] Gray (1976): $\log g_* = 4.17 + 0.38(B - V)$
[i] Flannery & Ayres (1978), for mass.
[j] Kamper & Wesselink (1978), for mass.
[k] Ayres *et al.* (1983).
[l] Kelch (1978).
[m] Montesinos & Jordan (1993).

† ROSAT observations of these stars have been made only with the Wide Field Camera and thus do not form part of the main PSPC analysis in this chapter. Their parameters have been shown as they are modelled using the WFC data in Chapter 3.

Table 2.2: Dates of observation and net exposure times for the PSPC observations used in this analysis.

Star	Proposal ID	First Date of Observation	Last Date of Observation	Net Exposure Time (s)	B – Filter Status
$\epsilon\,Eri$	$UK200446FP$	23/01/1992	24/01/1992	3088	on
$70\,Oph\,A_1$	$UK200792$	05/03/1992	05/03/1992	748	on
$70\,Oph\,A_2$	$UK200792-1$	17/03/1993	17/03/1993	1967	on
$61\,Cyg\,A$	$UK200793FP$	02/05/1992	02/05/1992	4982	on
$\chi^1\,Ori$	$UK200794FP$	04/03/1992	04/03/1992	5274	on
$OU\,Gem$	$UK200795FP$	27/03/1992	28/03/1992	3464	on
$\kappa\,Cet$	$UK200796FP$	24/01/1992	24/01/1992	2166	on
$\xi\,Boo\,A$	$CA150090F$	22/07/1990	23/07/1990	4388	on
$\xi\,Boo\,A$	$CA150090$	22/07/1990	23/07/1990	533	off
$HD\,115404$	$UK201372FP$	11/07/1992	11/07/1992	3649	on
$HD\,115404$	$UK201372P$	11/07/1992	11/07/1992	1710	off
$HD\,152391$	$UK201371FP$	08/09/1992	09/09/1992	2968	on
$HD\,152391$	$UK201371P$	08/09/1992	08/09/1992	2022	off
$HD\,155886$	$UK201373FP$	22/09/1992	22/09/1992	1450	on
$HD\,155886$	$UK201373P$	21/09/1992	22/09/1992	1824	off

- In October 1991, the PSPC developed a slightly higher background rate which extended over the whole sensitive area of the detector, but was restricted to the lower pulse height channels. A hot spot was also observed near the edge of its field of view, and this resulted in a count rate increase from 10^{-3} to 10^{-2} counts/sec over the preceding six month period. This effect was reduced (by a factor of 2) by switching to another gas supply tank on the detector. As a result, an unwanted 30% drop in the gain of the PSPC occured, which raised the lower cut-off energy of the detector from 70 to $\sim$ 100 eV. Owing to this, the X-ray spectra below Pulse Height Amplitude (PHA) channel 18 (of a total of 256) have an increased background.

- Owing to the 'wobble' in the movement of the satellite which compensates for the permanent point source occultation due to the wire mesh window support system on the PSPC, wing-like structures appear at the edges of soft X-ray point source images. These consequently led to a degradation in the PSPC images (Nousek & Lesser, 1993) and are known as 'electronic ghost images'. It is thought that they are partially responsible for the widespread spectral fitting problems associated with the first three channels of the PSPC data.

- Further, the spectral response of the PSPC changed non-linearly with time (see *ROSAT Status Report #64*), and this variation caused a shift of the pulse-height distribution to lower channels (Hasinger *et al.*, 1994).

In order to minimise the errors that have been introduced in the data, the data analysis was restricted to the energy range 0.2-2.0 keV. These instrumental problems can in principle affect interpretation of the results, and this should be borne in mind.

2.2.3 Observations with the Wide Field Camera

The University of Leicester proposed a Wide Field Camera (WFC), to fly with the X-ray telescope on ROSAT, which would enable observations to be carried at lower energies (EUV,

Table 2.3: Properties of the S1 and S2 filters on-board the WFC. (From Pounds *et al.*, 1993).

Filter	Composition	Energy (eV)	Wavelength ($\AA$)
$S1$	$C/Lexan/B$	$90 - 206$	$60 - 140$
$S2$	$Be/Lexan$	$62 - 110$	$110 - 200$

40-200 eV). Although the WFC was an independent instrument, it relied on ROSAT for power, data storage and telemetry. The optics of the instrument were made of a three-fold nested Wolter-Schwarzchild telescope with an aperture of 58 cm and focal length 52.5 cm. In order to define the wavebands in which the instrument was to operate more accurately, two filters (S1 and S2) were used whose properties are described in Table 2.3. A comprehensive description of the WFC has been published by Wells *et al.* (1990), which covers the in-orbit performance of the instrument as well as calibration data. The WFC successfully completed its survey from 30th July 1990 - 25th January 1991, and covered 96% of the sky, while observations of the remaining 4% were made in August 1992. A reduction of the all-sky survey data is presented in the WFC Bright Source Catalogue (Pounds *et al.*, 1993) and this includes detections of the five dwarfs and Procyon all of which will be modelled in Chapters 3 and 4 respectively. The count rates for these stars and their respective 1σ errors are listed in Table 2.4, and these are the values I used to analyse the WFC observations. Pye *et al.* (1995), have reprocessed the results of the initial all-sky survey and these are also listed in Table 2.4, and with the exception of ϵ Eri and ξ Boo A, are to within $\pm$ 20% of the results of Pounds *et al.* (1993). The data were analysed using XSPEC and the Raymond-Smith and the Landini-Monsignori Fossi spectral emission codes for one temperature (hereafter 1T) fits. (Two temperature (2T) fits cannot be carried out statistically for WFC data as there are an insufficient number of free parameters; *i.e.* there are two energy bins corresponding to each of the two filters).

The results are discussed in Section 2.6.

Table 2.4: Count rates and 1σ errors for each of the WFC filters in counts per kilosecond as quoted in The WFC Bright Source Catalogue (Pounds *et al.*, 1993), as used in the analyses in Chapters 3 and 4. The numbers in brackets are the reprocessed count rates and their errors from Pye *et al.*, 1995 (see text).

Star	S1a $(counts/ks)$	error	S2a $(counts/ks)$	error
χ^1 *Ori*	47 (47)	6 (6)	36 (36)	9 (7)
ϵ *Eri*	110 (84)	18 (13)	254 (83)	74 (25)
ξ *Boo A*	28 (45)	5 (7)	60 (70)	8 (9)
α *Cen A & B*†	123 (125)	10 (10)	248 (287)	14 (15)
Procyon	101 (115)	8 (9)	210 (191)	14 (14)

† The α Cen binary system was not resolved by the WFC and the observed number of counts is the total number of counts from the system. The two stars are separated by 2 arcsec and the observed total emission measure is a linear combination of the two components. The ratio of the surface fluxes A : B $\simeq$ 0.22 (Golub *et al.* (1982); see Section 3.5.5 of Chapter 3).

§2.3 Reduction and Analysis of the PSPC Data

The raw data from ROSAT were reduced and analysed using ASTERIX, which is an instrument independent data analysis system and is available on STARLINK.

2.3.1 Data Reduction

The raw data from the PSPC instrument were converted from their original FITS to SASS (Standard Analysis and Software System) format which allows the data to be used as input into standard science analysis software. However, problems such as bugs in the processing software or the need to incorporate new information in the system (*e.g.* the non-linear time dependent change of the spectral response matrix of the PSPC) led to successive data reprocessing which manifested themselves as multiple releases of SASS. The final reprocessing of the PSPC data began on 1st April, 1994 (Pisarsky *et al.*, 1994) and has not been completed at the time of writing this thesis. The results which are presented have taken into account the latest available SASS output (January, 1993).

Using the ASTERIX spectral analysis package, an image of the target star was created from the SASS output by sorting each of the 256 energy channels. The net count rate from the star under investigation was found by subtracting the background radiation from an area of the image far removed from the source. This was achieved with the aid of the routine XRTBCKBOX, which is installed in ASTERIX.

The real stellar counts were rebinned into a total of 34 PHA channels and were then folded with the instrument response matrix so that the intensity of the sum of events in each channel could be determined. Rebinning the energy channels was necessary in order to produce a uniform distribution of counts and signal-to-noise along the energy channels.

2.3.2 Analysis

The data analysis was carried out using the instrument independent software packages ASTERIX and XANADU/XSPEC (Version 8.4) (Shafer *et al.*, 1990). The data were fitted with the following two spectral codes, which will be discussed more extensively in Section 2.4:

1. **The Raymond-Smith (RS) Code:** The 1990 version of the code (Raymond, 1990) which is the most up-to-date generally available version (Raymond, 1992, private communication), is also installed in XSPEC (another instrument independent data analysis package), while ASTERIX contains the 1986 version of the code (see Raymond & Smith, 1977, and Raymond, 1988).

2. **The Landini-Monsignori Fossi (LMF) code:** This was installed in ASTERIX (March 1993) by Dr. H. C. Pan, using the results I obtained from the 1992 version of the code for the specified temperature range log T_e = 5.66 - 7.76 K, (see Landini & Monsignori Fossi (1970, 1990) and Landini, Monsignori Fossi & Stern, 1985).

The spectral fitting codes in their original form (*i.e.* before being installed in the spectral fitting packages), will henceforth be referred to as *stand-alone* codes.

The method for fitting the various models in both ASTERIX and XSPEC is based on the CURFIT code of Bevington (1969) which performs a least squares fit to a function which does not have to be linear in its parameters. It uses the algorithm of Marquardt which combines a gradient search with an analytical solution developed from linearising the fitting function. In this case, the least squares fit is a χ^2 minimisation, carried out by a combined gradient/quadratic fitting minimisation. Parameters are pegged on bounds and are excluded from the fitting process until they are returned by the χ^2 gradient.

If each of a total of N data points (where i = 1, 2,..., N), do not have equal uncertainties σ_i^2, (*i.e.* $\sigma \neq \sigma_i$), then the individual standard deviations are included as *weighting factors.* The weighting factor for each data point is the inverse of its uncertainty (or variance), and is normalised to the average of all the weighting factors, w_i:

$$w_i = \frac{1/\sigma^2}{(1/N)\Sigma(1/\sigma_i^2)} \tag{2.1}$$

In the case of astronomical data obtained with satellites, the weighting factor which is incorporated in the fitting procedure is due solely to instrumental errors (*i.e.* the response of the instrument at a particular energy).

However, this factor yields biased results as it makes a greater effort to fit those points with smaller uncertainties (*i.e.* those at higher energies) than those with larger ones, which tend to be at low energies. This is clearly seen in Figures 2.17 to 2.22 where I show one and two-temperature fits using the RS code and XSPEC, to spectra of ξ Boo A, χ^1 Ori and ϵ Eri. (The spectra for the LMF code are similar and thus have not been shown). The same behaviour occurs in the remaining sample of stars. Overall, the effect of the adopted weighting factor on the fits is to overestimate the coronal temperature as most of the weight is placed at the higher energies. As this is the only fitting method in the spectral fitting packages, the above discussion must be borne in mind when interpreting the results of the analysis that follows.

§2.4 Spectral Models

In the absence of resolved line spectra, the modelling of low resolution X-ray spectra is carried out using radiative power-loss codes to predict the radiation as a function of temperature. The theoretical prediction is then compared with the observations to determine the plasma parameters.

A substantial amount of detailed atomic physics is required for the modelling of low resolution X-ray emission spectra from hot, optically thin plasmas. Nevertheless, several such models have been developed over a number of years, for example by Tucker & Koren (1971), Landini & Monsignori Fossi (1972), Mewe (1972), Mewe *et al.* (1975), Kato (1976), Raymond & Smith (1977) and Kaastra (1992). The differences between these calculations arise from the different wavelength ranges covered, the number of emission lines included, the collisional excitation rates adopted, and the ionisation and recombination rates used.

For the purposes of analysing X-ray data from ROSAT, the current calculations by Raymond (1990) and by Landini & Monsignori Fossi (1992, private communication) are the most comprehensive. The following sections give a discussion of these two codes and the differences between them.

2.4.1 The Raymond-Smith Code

This code calculates the emission spectrum of a hot, optically thin plasma whose electron temperature T_e, is in the range 1.6×10^5 to 1.0×10^8 K. The calculations were originally intended to apply to high temperature regions of the interstellar medium (Raymond & Smith, 1977). A simplified flowchart of the code is shown in Appendix B.

2.4.2 The Landini-Monsignori Fossi Code

The first version of this code (Landini & Monsignori Fossi, 1970) calculated the expected emission from the solar corona in the spectral region of 1-100 Å and for temperatures ranging from $10^6 - 10^7$ K. Since then, it has been developed to compute the radiative losses of optically thin plasmas in the X-ray and EUV wavelength range (0.1-2000 Å) and for temperatures ranging from $10^4 - 10^8$ K. A simplified flow diagram of this code is also shown in Appendix B. The code has recently been updated (Monsignori Fossi & Landini, 1994) to improve the treatment of the strong lines of highly ionised iron, in preparation for the analysis of spectra which should be observed from the SOHO mission.

2.4.3 Abundances

Both the 1990 version of the RS code, as well as the 1986 version which has been installed in ASTERIX, make use of the elemental abundances as given in Allen (1973), while the stand-alone LMF code makes use of those of Anders & Grevesse (1989). The most up-to-date recommended abundances for the solar photosphere are those of Grevesse *et al.* (1992) and Anders & Grevesse (1989), which are listed in Table 2.5. It is assumed that most main-sequence stars considered here have solar abundances, although α Cen A & B are known to have have a higher metallicity: Flannery & Ayres (1978) and Smith, Edvardsson & Frisk (1986) found that the metals are a factor 1.58 times greater than solar. More recently, Furenlid and Meylan (1990) estimated the average metal abundance of the system to exceed that of the Sun by a factor of 1.3, while according to Lydon *et al.* (1993) the Fe abundance of α Cen A & B is 1.7 times higher than the solar value. For the models of α Cen A & B in Chapter 3, I have adopted the value found by Flannery & Ayres (1978) and Smith, Edvardsson & Frisk (1986), which is in good agreement with the result of Lydon *et al.* (1993).

It is possible to replace the abundances in both stand-alone codes with the most up-to-date

Table 2.5: Elemental abundances log n_E, on scale where log n_H=12.00. The values adopted in the analysis are given in bold type. (These apply to all stars examined here, except for α Cen A & B; see text).

Element	(i)	(ii)	(iii)
H	12.00	**12.00**	–
He	10.93	**10.99**	–
C	8.52	8.56	**8.55**
N	7.96	8.05	**7.95**
O	8.82	8.93	**8.87**
Ne	7.92	**8.09**	–
Mg	7.42	**7.58**	–
Si	7.52	**7.55**	–
S	7.20	**7.21**	–
Ar	6.90	**6.56**	–
Ca	6.30	**6.36**	–
Fe	7.60	7.67	**7.51**
Ni	6.30	**6.25**	–

i) Allen (1973), **ii)** Anders & Grevesse (1989), **iii)** Grevesse *et al.* (1992) .

values. Unlike ASTERIX, XSPEC does not make use of default abundance values, and this allows the user to choose values for the abundances. Thus, I used the abundances from Grevesse *et al.* (1992) and Anders & Grevesse (1989) and the XSPEC code for fitting the RS model to the data. There have been a number of recent claims that the coronal abundances are not the same as the photospheric abundances. These are based on EUVE spectra (Drake *et al.*, 1995) but for elements other than iron the analyses rely on weak, blended lines. Similarly, anomalous abundances derived from ASCA spectra may arise from inadequacies in the number of lines included in the codes (see Jordan, 1995a). Until this matter is resolved by obtaining improved spectra, we adopt the photospheric abundances. Further, the measurements of Veck & Parkinson (1981) as well as those of Meyer (1985), showed that heavy elements with a high first ionisation potential (FIP) ($\geq$ 10 eV) *e.g.* C, N, O, and S appeared to be *underabundant* in the upper solar atmosphere by factors of up to 10 compared with the photosphere. Alternatively, low FIP elements *e.g.* Ca, Mg, Fe and Si, are *enhanced* with respect to their photospheric values. This is referred to as the FIP effect. No solar atmospheric structure has been discovered in which the abundances of low FIP ions are *lower* than their photospheric values.

2.4.4 Treatment of lines in the stand-alone codes

One of the most important differences between the two codes is the number of lines included. I have also made a comparison of the emissivities of the strongest lines (*i.e.* those lines whose peak emissivity exceeded 10^{-25} erg cm^{-2} s^{-1}), which depend on the ion fractions and collision strengths adopted. Owing to the large number of lines that are involved in these calculations, I do not give detailed comparisons, but some overall conclusions. I only considered emission lines in the energy band 0.1 - 2.4 keV, since the PSPC is insensitive to longer wavelengths.

1. Each of the codes contains an input file with wavelegths and atomic data for emission lines that have been previously identified in the spectra of the quiet and active sun and solar flares. Unlike the RS code, the LMF code is more systematic in this respect since references to every identification are included in the code. Lines which are common to both codes, but which were quoted from different sources, sometimes differ by a few angstroms in wavelength. This complicates the comparison of the emissivities from the two stand-alone codes, but is not important when the codes are applied to low resolution spectra.

2. The RS code includes more individual lines (as opposed to multiplets) than the LMF code. However, the latter includes lines from Na and Al which are ignored by RS. This is not too important for the present application, since the majority of the strongest lines that appear in coronal spectra are those of Si, Fe, and Ni, and those of the H-like and He-like ions of elements more abundant than Na and Al.

3. The treatment of multiplets is inconsistent in both models (as well as within each model), in that in some cases a multiplet is described only through the strongest line

of a multiplet, while in others, the lines are grouped together in various ways.

4. Some transitions in Fe IX-XIV of the type $3d - 4p$ and $3d - 4f$ which are found between 170 Å and 70 Å, have been excluded from both models and those included are treated only schematically with crude approximations for the excitation rates. These lines are formed by spontaneous radiative decay following collisional transitions from $3p^n$ to $3p^{n-1}4p$ and $3p^{n-1}4f$ (see Figure 2.1). Jordan (1968), suggested that such transitions could account for some unidentified lines in the solar spectrum, provided that the $3p^n - 3p^{n-1}4p$ and $3p^n - 3p^{n-1}4f$ transitions have cross-sections comparable with those of $3p^n - 3p^{n-1}4s$ and $3p^n - 3p^{n-1}4d$. Fawcett *et al.* (1972) subsequently identified many of these transitions (which now appear in the tabulation of Kelly, 1987). Although the $3d - 4l$ transitions do not add more than 10% to the strong $3p - 3d$ transition array (Jordan, 1968) they will result in a number of weak lines in the range 70 - 170 Å, contributing to the background. There are similar omissions for higher stages of ionisation of iron. (See discussion in Jordan, 1995a,b).

5. The output of the LMF code gives the emissivities in wavelength bins and so it is difficult to obtain the absolute emissivity of each line which was given in the input file, since the lines do not occur at equal wavelength intervals. The RS code however, outputs emissivities that correspond to each line of its input file, as well as providing a binned format.

From the above points one can see that neither model considers emission lines in an ideal way and from this point alone one cannot say *a priori* which of the codes is better.

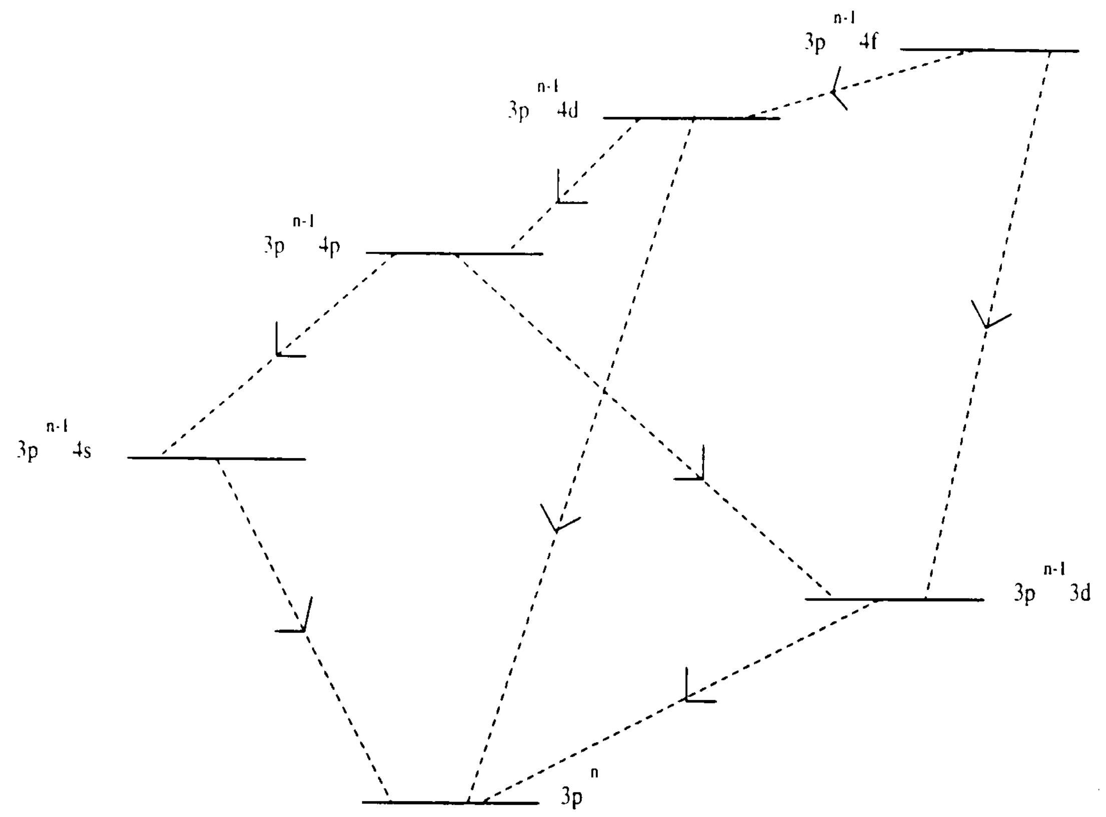

Figure 2.1: Configuration diagram for the $3d-4p$ and $3d-4f$ transitions in $Fe\,IX-XIV$ (Jordan, 1968). The decay routes after excitations in the $3p-4f$ and $3p-4p$ transitions are shown (not to scale).

2.4.5 The Ionisation Balance

Consider a low-density plasma, where all the ions are in their ground state, then the rate of change of the population of ion i, is

$$\frac{dn_i}{dt} = n_e(q_{i-1}n_{i-1} + n_{i+1}a_{i+1}) - n_e n_i(q_i + a_i) \tag{2.2}$$

where, q_i and a_i are the ionisation and recombination rates of ion i, and n_e is the electron density. The first term on the R.H.S of equation (2.2) expresses the rate at which the ion i is created from electron impact ionisations from ion *i-1* and by recombinations from ion *i+1* while the second term is the rate at which ion i is destroyed by ionisations to *i+1* and recombinations to *i-1*. The sum of the ion number densities n_i, must equal the elemental number density n_E, such that

$$n_E = \sum_{i=0}^{Z} n_i \tag{2.3}$$

where Z is the nuclear charge of the element. Assuming the plasma is in statistical equilibrium so that $dn_i/dt=0$ and all ions can be taken to be in their ground term, equation (2.2

) can be rewriten for each ion as:

$$n_i q_i = n_{i+1} a_{i+1} \tag{2.4}$$

At sufficiently low densities the above expression is independent of the electron density and the ionisation balance n_i/n_E is solely temperature dependent and can thus be calculated for each ion. As n_e increases, the di-electronic recombination rate is reduced (Summers 1974a), but this is not taken into account in the versions of the codes used. Examination of Summers' results shows that at coronal temperatures the density dependence is small.

In the 1977 version of RS code (Raymond & Smith, 1977), the ionisation rates were evaluated using the *Exchange Classical Impact Parameter* (ECIP) of Summers (1974a,b)

$$q_i = 2.65 \times 10^8 (\frac{I_H}{kT_e})^{\frac{1}{2}} \sum_i \zeta(i) \int_{\chi_i}^{\infty} Q(\epsilon)\, e^{-\frac{\epsilon}{kT_e}}\, d\epsilon \tag{2.5}$$

where, I_H is the ionisation potential of hydrogen, T_e is the electron temperature, $\zeta(i)$ is the number of electrons in the shell, χ_i is the ionisation potential of the i^{th} shell, ϵ is the electron energy, and $Q(\epsilon)$ is the ionisation cross-section in units of $\pi\alpha_o^2 = 8.79 \times 10^{-17}$ cm^2. The above expression has been normalised to experimental data (Burgess *et al.*, 1977, and Burgess & Chidichimo, 1983). On the basis of comparisons with a wider set of experimental data, these rates are now considered to be about a factor of 2 too small compared with those computed using the Lotz (1967) formula which is defined as follows:

$$q_i = A\, \zeta(i)\, F\, T_E^{\frac{1}{2}}\, (\frac{I_H}{kT_e})^2\, e^{\frac{\chi_i}{kT_e}} / (1 + \frac{a_i k T_e}{\chi_i}) \tag{2.6}$$

where, $A = 4 \times 10^{-14}$, F is the focusing factor of order unity (Cox, 1970), for most instances $a_i \sim 0.1$, and χ_i is the ionisation potential from sub-shell i. The empirical formula of Seaton (1964) (near the ion population peak) or the Lotz formula (which was aimed to account for the decrease in ionisation cross sections at high energies where $kT_e > I_H$) give better approximations for the ionisation rates than the ECIP approximation of Summers. Figure 2.2 is a comparison of the results found using the formulae of Lotz and Summers using results from Si XII as an example (Raymond, 1988). The ionisation rates of Younger (1981) are also shown and these have replaced the ECIP rates in the RS code. The ionisation rates of

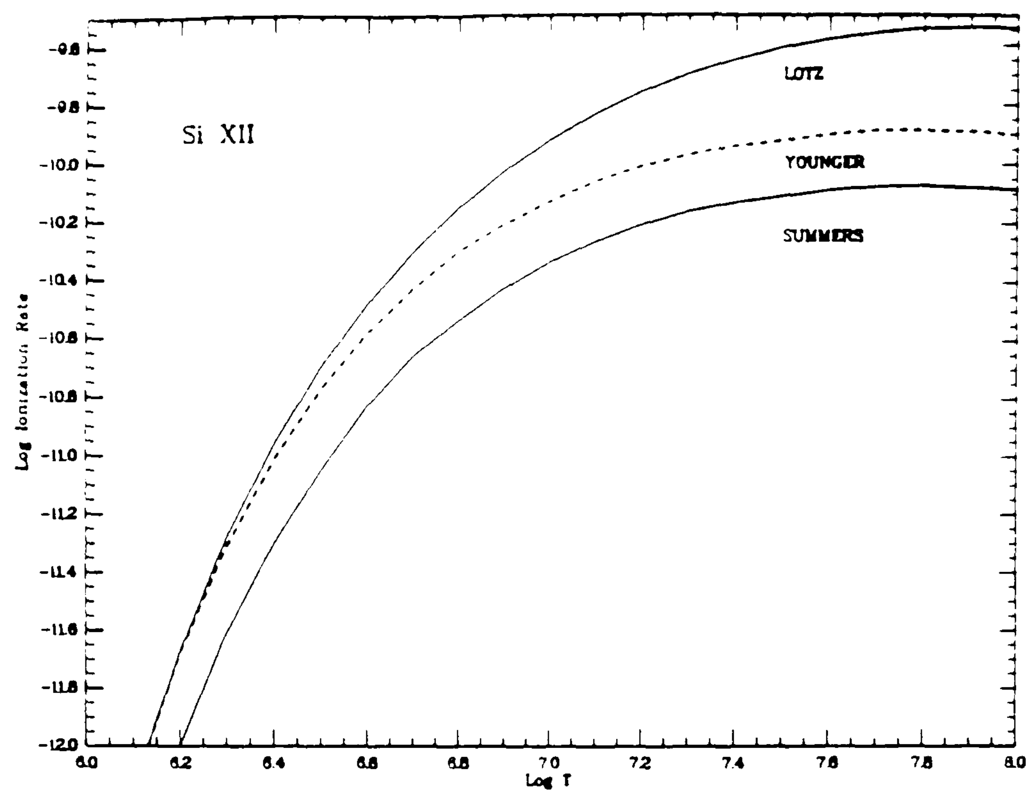

Figure 2.2: Comparison of ionisation rates for Si XII as computed using formulae of Lotz (1967), Younger (1981) and Summers (1974a,b), from Raymond (1988).

Younger (1981, 1982 and 1983) use the Distorted Wave (DW) approximation which includes a four parameter fit to the computed cross section of each ion. This deals with the details of the atomic structure of each ion more effectively than most simpler formulae. In the cases where DW results have not been published, Coulomb Born calculations and interpolations have been employed as required.

For *non* H-like ions, the LMF code adopts the ionisation rates in Shull & van Steenberg (1982) which are based on the Lotz formula, while the classical ionisation rates of Mewe *et al.* (1980) are used for H-like ions. Direct comparison of the ion populations for iron computed in the LMF code with those published by Shull and van Steenberg (1982) show considerable differences which appear to be due to a number of errors in the latter programme.

The rates for excitation followed by autoionisation are excluded from the calculations of RS who claim that they do not have any effect on X-ray emission. On the other hand, LMF compute such rates from

$$C_{au} = A_{au}T^{-\frac{1}{2}}exp(-T_{au}/T_e)f(y) \tag{2.7}$$

where T_{au} and A_{au} are fitting coefficients. $A_{au} = (8.63 \times 10^6\, cm^{-3} s^{-1})(\Omega B/\omega)$ and Ω is the collision strength of the inner shell excitation of the ionising level, ω is the statistical weight of the lower level and B is the branching ratio for autoionisation following excitation. The function *f(y)* is taken from Arnaud & Rothenflug (1985).

The recombination processes that balance ionisation are described below:

1. **Radiative Recombination:** This is the inverse process of photoionisation. LMF compute this as in Shull & van Steenberg (1982), adopting

$$\alpha_r = A_{rad}(T_e/10^4)^{X_{rad}} \tag{2.8}$$

where A_{rad} and X_{rad} are radiative fitting coefficients. The RS code takes a different approach to this calculation; hydrogenic recombination is assumed for shells above the valence shell, while for sub-shells of the valence shell other than the lowest, the hydrogenic recombination is modified so that it corresponds to the energy of the state. For recombinations to the ground level, photoionisation cross-sections are used to calculate the recombination rate from detailed balance.

2. **Di-electronic Recombination:** RS use the General Formula (GF) of Burgess (1965)

$$\alpha_{di} = 0.03\, A\, B\, f\, T_e^{-\frac{3}{2}}\, e^{-\frac{\overline{E}}{kT}} \tag{2.9}$$

where f is the absorption oscillator strength for the optical electron transition, A and B are functions of ionic charge, and the energy of the electron transition and $\overline{E}$ is the average energy of the doubly excited levels into which an electron is captured. This formula was intended for electron transitions that involve no change in their principal quantum number ($\Delta n = 0$). The correction factor of Burgess & Tworkowski (1976) is included in the GF for He-like ions where there is accidental degeneracy of the orbital angular momentum states of the ion before it recombines. The addition of this factor to the GF gives better agreement with more detailed calculations. LMF compute α_{di}

according to Shull and van Steenberg (1982) as shown below,

$$\alpha_{di} = A_{di} T^{-\frac{3}{2}} exp(-T_o/T_e)[1 + B_{di} exp(-T_i/T_e)] + \alpha_{ns} \tag{2.10}$$

where, A_{di}, B_{di}, T_0 and T_i are fitting coefficients. In addition, the LMF calculation has incorporated the correction of Nussbaumer & Storey (1983, 1986, 1987), α_{ns}, to include dielectronic recombination at low temperatures ($3.0 \leq \log T_e \leq 4.8K$) where $kT_e \leq E_R$, E_R being the excitation energy of the first resonance transition of the recombining ion. However, this effect is only important at temperatures much lower than those of stellar coronae and can be ignored here; it becomes relevant in the analysis of IUE spectra. The calculations of Shull & van Steenberg (1982) also make use of the Burgess & Tworkowski (1976) correction factor for He-like ions. However, they are unsystematic in the rates that they adopt. In some cases they have used the GF while in others they have used the rates of Jacobs *et al.* (1977, 1980) and extrapolated along isoelectronic sequences as required. The latter authors found that radiative transitions are the most important stabilization processes for ions that recombine mainly via di-electronic recombination (DER) and calculated total DER rates for Ca and Ni ions by taking into account the autoionisation to excited states of the recombining ion as well as the stabilizing radiative transitions of the recombining electron. This causes a shift in the coronal ionisation equilibrium abundance curves to higher temperatures and as a result it substantially alters the relative intensities of spectral lines as well as the total radiative emission rates at a given temperature. Jacobs *et al.* (1980) point out that the Burgess formula overestimates α_{di} for certain ions because it neglects autoionisation for transitions where $\Delta n \neq 0$.

In Figures 2.3 and 2.4, I show a comparison of the resulting ion balance for Fe calculated by Jordan (1969, 1970) and those computed in the RS and LMF codes. Since emission from Fe ions dominates in the temperature range $10^6 - 10^7$ K which is representative of coronal temperatures, I have chosen a set of Fe ions which are predominantly formed in this range. The ion balance has been cut off where $n_{ion}/n_E < 10^{-2}$ owing to the larger uncertainties

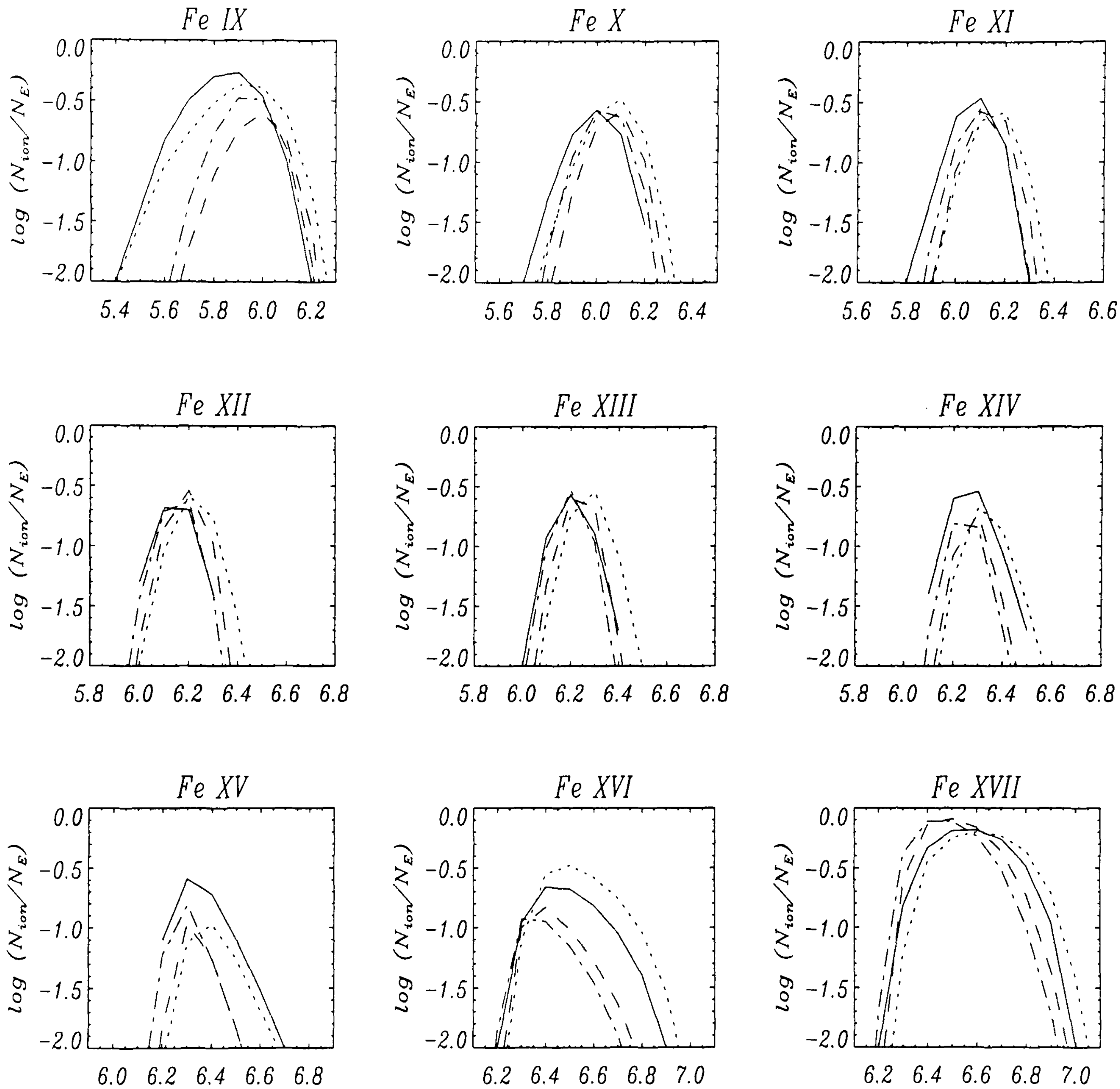

Figure 2.3: Comparison of the ion balance ($\log \frac{n_{ion}}{n_E}$) for Fe IX-XIV computed in the RS (——) and LMF (- - -) codes as well as from the calculations of Jordan (1969, 1970) (. . .) and Arnaud & Rothenflug (1985) (– · –).

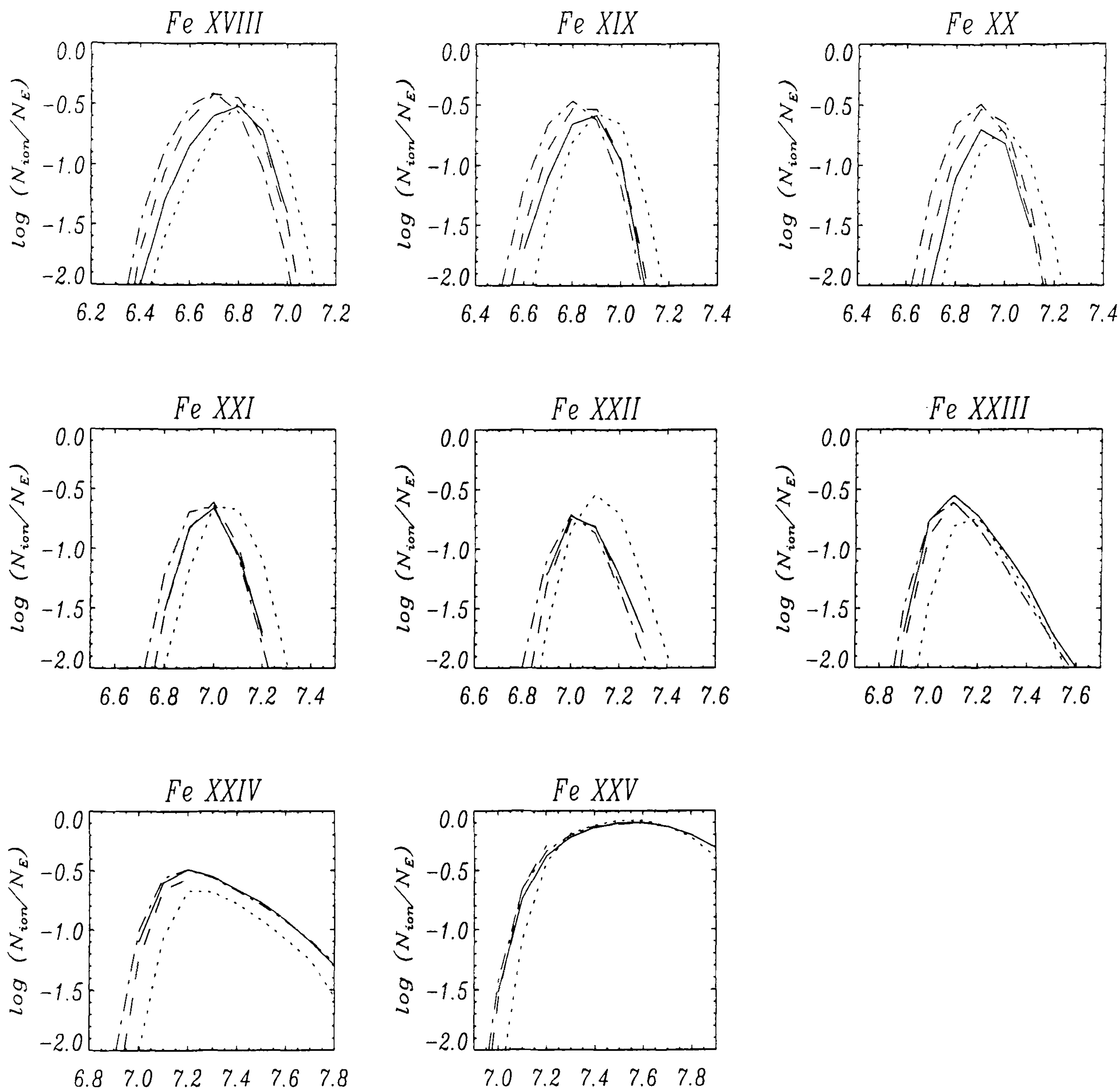

Figure 2.4: Comparison of the ion balance (log $\frac{n_{ion}}{n_E}$) for Fe XV-XXI computed in the RS (——) and LMF (- - -) codes as well as from the calculations of Jordan (1969, 1970) (. . .) and Arnaud & Rothenflug (1985) (— · —).

that are involved outside this range and also because of their minimal contribution to the emissivities. The ion balance calculations of Arnaud & Rothenflug (1985) are also shown since these values are used in the spectral emission code of Mewe *et al.* (1985) (see Section 2.4.8), and they appear to be in excellent agreement with those computed by RS especially for the higher stages of ionisation.

For Fe IX to Fe XI, the temperatures of maximum formation of the ions computed by RS tend to be in better agreement with those of LMF than with those of Jordan (1969,1970), where the latter exceed those of RS on average by ~ 0.1 dex. The differences can be traced the different recombination rates used in the calculations and a detailed discussion can be found in Jordan (1995b).

A recent version of the LMF code (Monsignori Fossi & Landini, 1994) has adopted the ion balance of Arnaud & Raymond (1992) for Fe ions. In Fe XVII and above, these new ion populations are very similar to those of Jordan (1970).

The treatment of di-electronic recombination remains the main uncertainty in all the calculations, and is the main factor in the different results for Fe IX. In Fe XV and XVI, ionisation by excitation followed by autoionisation should be included, and the treatment of this is the main cause of the differences between the different calculations. For most ions there are no substantial differences between the peak ion abundances calculated by the different authors. For Fe XVIII - XXI, the calculations in the RS code are to be preferred, owing to the reduction in the di-electronic rates made by Arnaud & Rothenflug (1985), which is probably overestimated.

2.4.6 Continuum Radiation

In both models, the continuum emission calculations include contributions from brehmsstrahlung (free-free), recombination (free-bound) and two-photon decay.

1. **Brehmsstrahlung Radiation:** This emission is caused when an electron approaches an ion close enough for it to be decelerated by the electric field of the ion, and this is expressed as

$$\frac{1}{n_e n_H}\frac{d\mathbf{\Lambda}}{d\lambda} = 2.04 \times 10^{-22}\lambda^{-2}T_e^{-\frac{1}{2}}10^{-\frac{62.53}{kT}} < g > \sum[Z^2\frac{n_z}{n_H}] \tag{2.11}$$

in units of erg cm^3 s^{-1}, where the emitted power is given by $\mathbf{\Lambda}$, λ is the photon wavelength, Z is the nuclear charge and $< g >$ is the mean Gaunt factor which in both models is evaluated following the method of Karzas & Latter (1961).

2. **Two-photon Decay:** This process is due to the decay of the $2s^2S$ and $1s2s^1S$ states of H and He-like ions, whereby photon pairs are emitted whose total energy equals the excitation energy of the level. This emission accounts for 10-20% of the total emission in H and He-like ions provided collisional excitation to higher levels is negligible, this process is the most important one for depopulating the $2s$ level. The LMF calculations consider emission from H-like ions only according to Tucker & Koren (1971), while RS include emission from both H and He-like ions making use of the more widely used Gaunt factors of Mewe (1972). The two-photon spectrum is given by

$$\frac{1}{n_e n_H}\frac{d\mathbf{\Lambda}}{d\lambda} = 4\frac{\mathbf{\Lambda}_\alpha}{\lambda}(\frac{\lambda_o}{\lambda})^3(1-\frac{\lambda_o}{\lambda}) \tag{2.12}$$

in units of erg cm^3 s^{-1} $\AA^{-1}$, where $\mathbf{\Lambda}_\alpha$ is the power emitted by the Ly-α transition of the emitting ion, and λ_o is the wavelength associated with the Ly-α transition.

2.4.7 Line Emission:

Both models assume that for a low density plasma, the X-ray spectrum is dominated by lines excited by ion-electron collisions. LMF considers only direct collisional excitation from the ground term. For a transition $i \rightarrow j$, the power in the line emission $\mathbf{\Lambda}_{ij}$, is given by

$$\mathbf{\Lambda}_{ij} = \frac{n_i}{n_E}\frac{n_E}{n_H}(n_H n_e)C_{ij}E_{ij}B_{ji} \tag{2.13}$$

where, n_i/n_E is the ionisation balance, n_E/n_H is the element abundance, E_{ij} is the energy of the transition and B_{ji} is the branching ratio when other decays from level j are possible. The collisional excitation rate C_{ij} is given by

$$C_{ij} = 8.63 \times 10^{-6}\frac{\Omega_{ij}}{\omega_j}T_e^{-\frac{1}{2}}exp(-E_{ij}/kT_e) \tag{2.14}$$

where ω_i is the statistical weight of the lower level and Ω_{ij} is the average collision strength (Seaton, 1964). Ideally, the calculation of Ω_{ij} using modern techniques should be used and the effective value of Ω_{ij} averaged over the Maxwellian velocity distribution should be found as a function of temperature. However, where these are not available it has been traditional to use the van Regemorter (1962) approximation,

$$\Omega_{ij} = \frac{8\pi}{\sqrt{3}}(\frac{\omega_j}{E_{ij}(Ry)})f_{ij} < g > \tag{2.15}$$

where f_{ij} is the absorption oscillator strength and $< g >$ is the mean Gaunt factor, which has been computed according to Mewe (1972), and Mewe *et al.* (1985), in both RS and LMF codes. Van Regemorter's approximation (VRA) was intended to provide values of Ω_{ij} which could not be computed in 1962. This approximation is still used today in many calculations, sometimes unnecessarily. However, advances in computer technology have enabled rigorous atomic calculations to be done much faster and with much greater accuracy than was possible in 1962. These more recent calculations have shown, as was pointed out by Sampson & Zhang (1992), that the accuracy of the VRA is limited because:

1. For transitions where $\Delta n \geq 1$, the formula omits the dominant forbidden transitions, while it does not treat the allowed transitions with sufficient accuracy, and

2. Van Regemorter chose a value $< g >$ at low energies which was merely in agreement with the theoretical and experimental results for the cross sections, that were available at the time; for higher energies (*i.e.* the scattered electron energy $x^2 = E_j/\Delta E \leq$ 2 in threshold units) he used $< g >= 0.2$. However, in cases where the allowed transitions dominate (*i.e.* $\Delta n = 0$), one can achieve 30-40% greater accuracy by

using a larger value for $< g >$ than van Regemorter's choice, since at these high energies $< g >$ is accurately represented by the expression $< g >= \frac{\sqrt{3}}{2\pi} \ln x^2$, where x^2 is the scattered electron energy in threshold units. Hence, choosing $< g > \simeq 0.8$ at or near threshold, and larger values at higher energies that agree with the above expression for $< g >$, increases the accuracy of the VRA. Higher values of $< g >$ are also derived from the impact approximation of Burgess (1965), as found by Jordan (private communication).

For all inner shell transitions, RS use effective oscillator strengths such that $< g >= 0.2$ yields collision strengths that are in agreement with those used by Tucker & Koren (1971). Di-electronic satellite lines (*i.e.* found near the He I-like ion resonance lines) are included in the RS code but not in the LMF code.

Figures 2.5 - 2.16 show the spectra that are predicted by the stand alone RS and LMF codes at temperatures that are typical of stellar coronae (the energy is in units of keV). It is evident that both codes yield very similar results for the continuum. The main differences lie in the line spectra. The number of lines included is greater in the RS code and the intensity of the lines is systematically higher, but the LMF code gives spectra at higher resolution at low energies. There is clearly room for improvement in both codes, to take account of the more recent and more accurate atomic data, and the major groups are still working to achieve this.

2.4.8 The Mewe Code

Another spectral emission code is that of Mewe & Gronenschild (1981) who calculated line and continuum X-ray fluxes for an optically thin plasma in the wavelength region 1 - 250 Å. Mewe *et al.* (1985) reinvestigated the X-ray spectrum in the region 1-300 Å and computed emissivities for 2131 spectral lines in the temperature range 3×10^4 - 1×10^9 K.

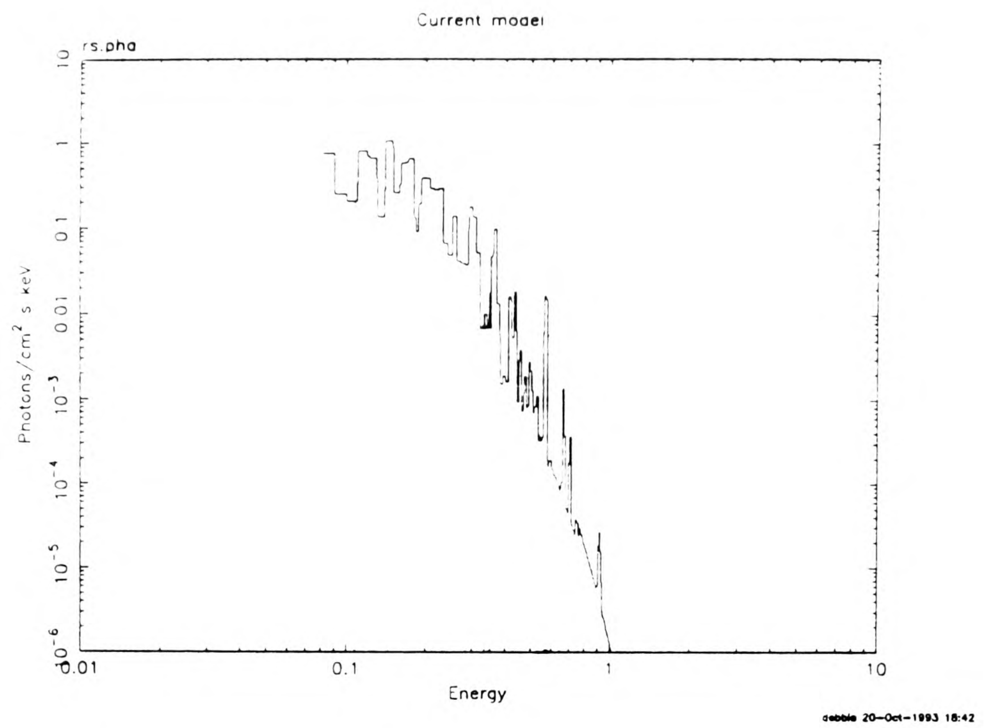

Figure 2.5: Spectrum from RS model at log T = 6.0 K and normalisation = 0.01 cm^{-5}. The energy is in units of keV.

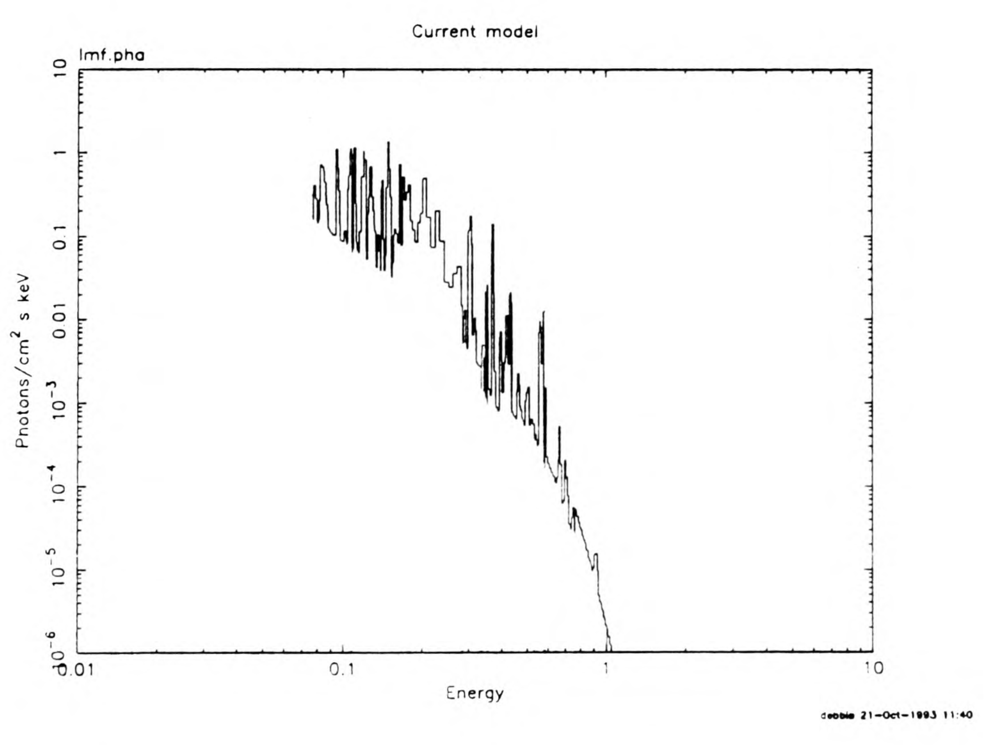

Figure 2.6: Spectrum from LMF model at log T = 6.0 K and normalisation = 0.01 cm^{-5}. The energy is in units of keV.

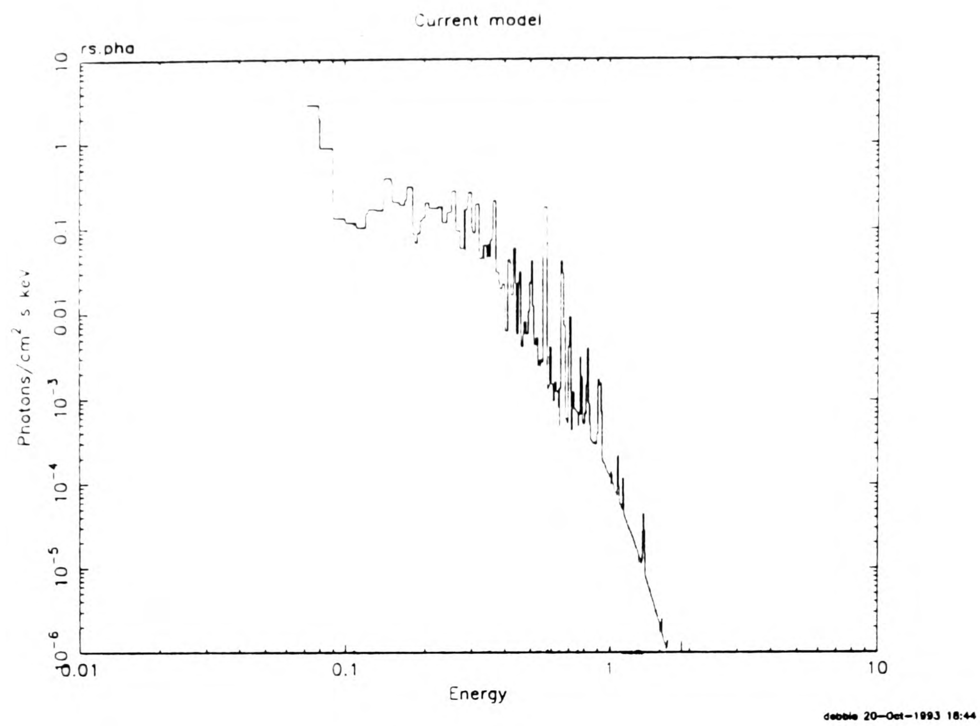

Figure 2.7: Spectrum from RS model at log T = 6.2 K and normalisation = 0.01 cm^{-5}. The energy is in units of keV.

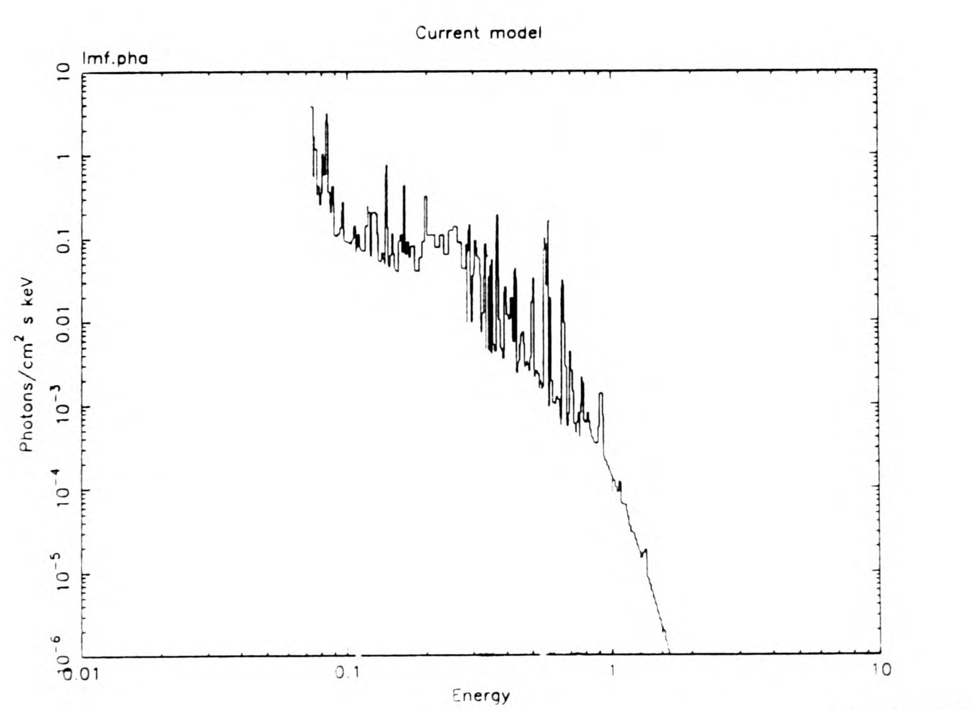

Figure 2.8: Spectrum from LMF model at log T = 6.2 and normalisation = 0.01 cm^{-5}. The energy is in units of keV.

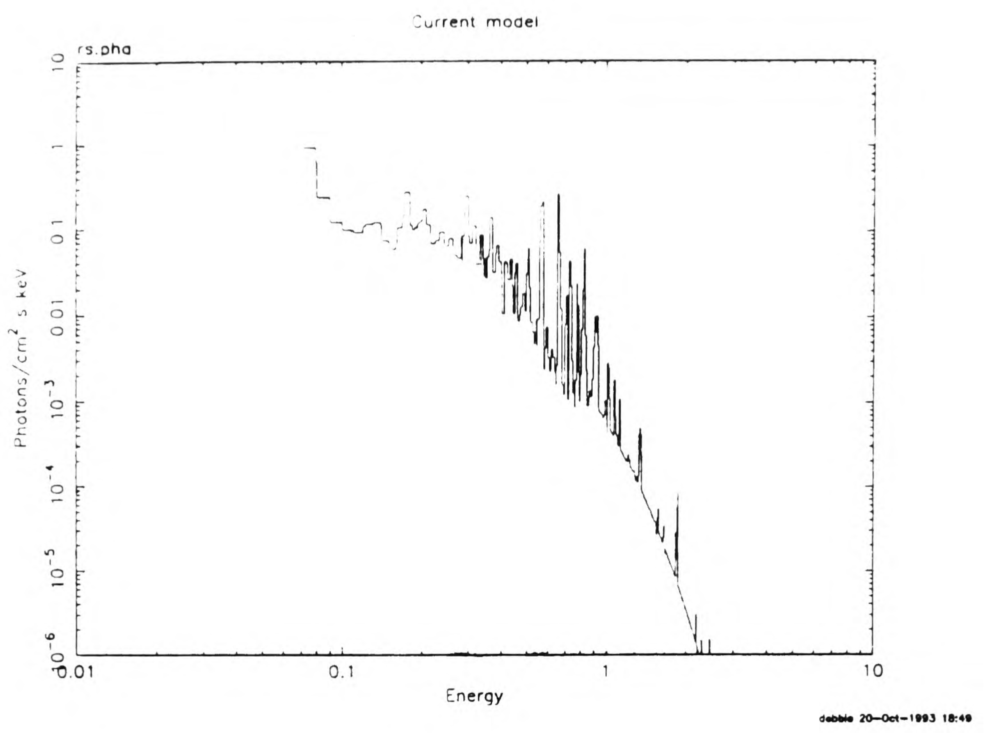

Figure 2.9: Spectrum from RS model at log T = 6.4 K and normalisation = 0.01 cm^{-5}. The energy is in units of keV.

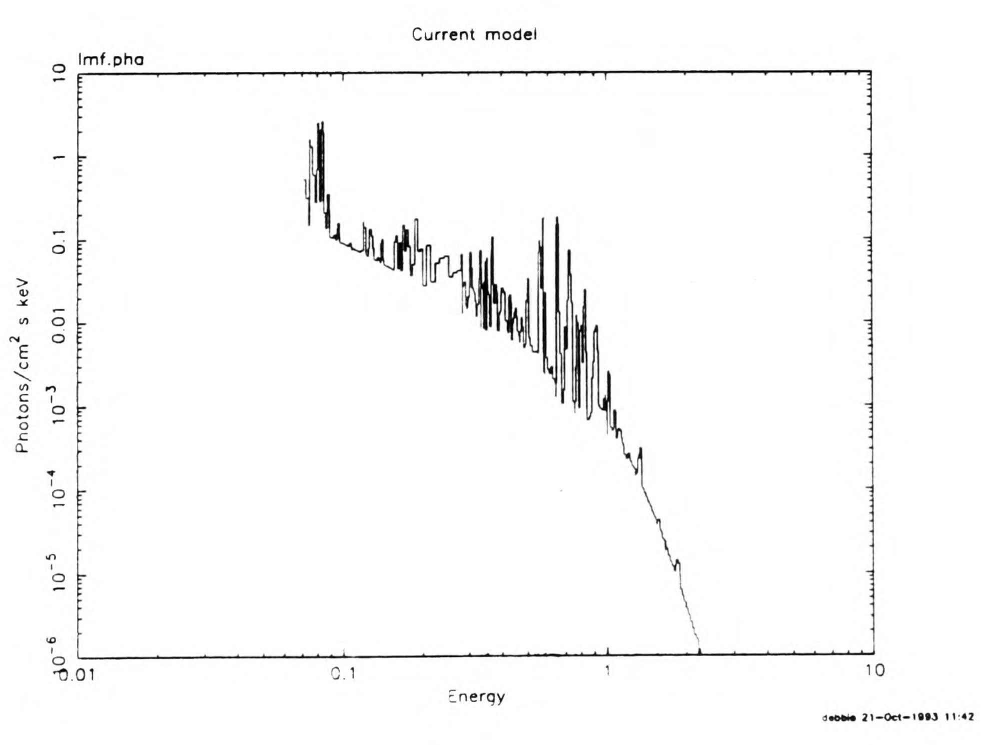

Figure 2.10: Spectrum from LMF model at log T = 6.4 K and normalisation = 0.01 cm^{-5}. The energy is in units of keV.

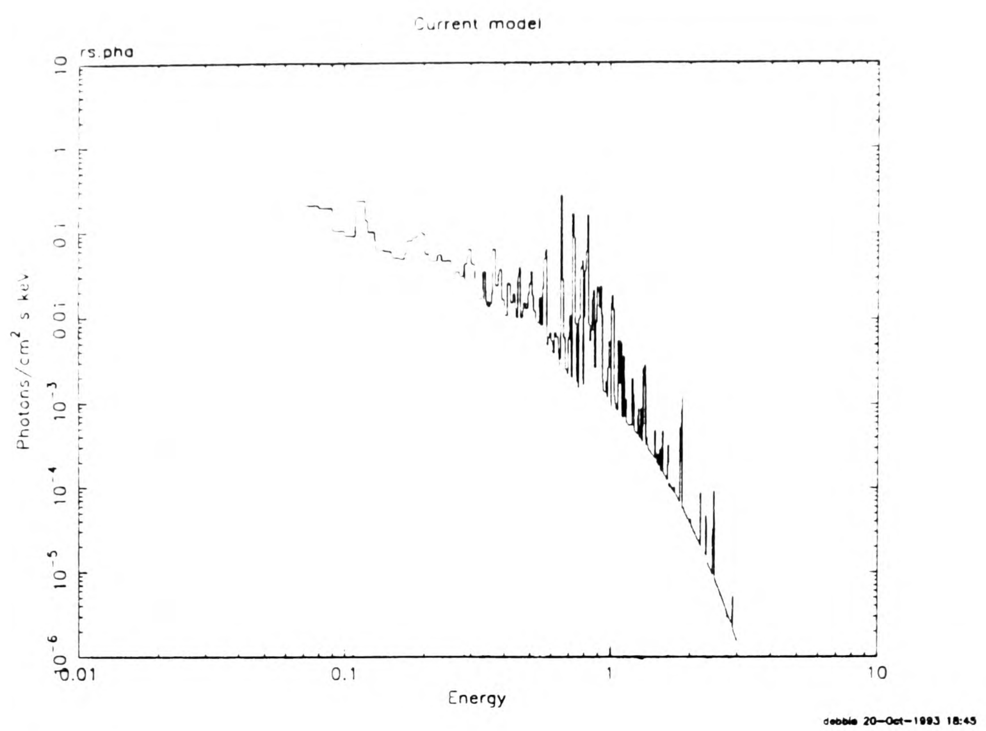

Figure 2.11: Spectrum from RS model at log T = 6.6 K and normalisation = 0.01 cm^{-5}. The energy is in units of keV.

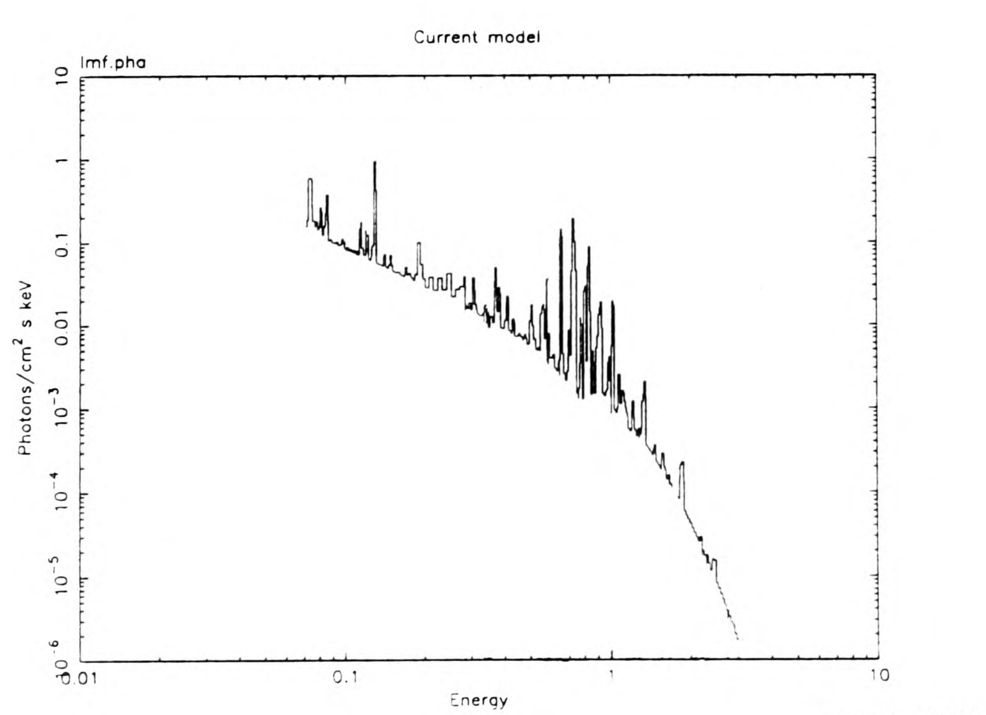

Figure 2.12: Spectrum from LMF model at log T = 6.6 K and normalisation = 0.01 cm^{-5}. The energy is in units of keV.

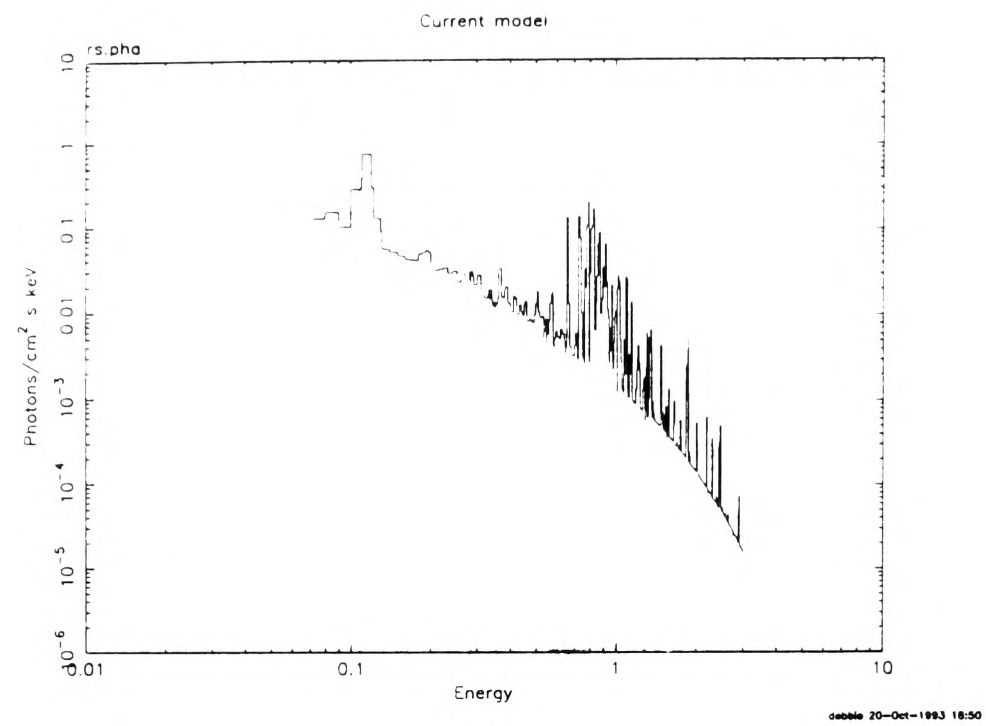

Figure 2.13: Spectrum from RS model at log T = 6.8 K and normalisation = 0.01 cm^{-5}. The energy is in units of keV.

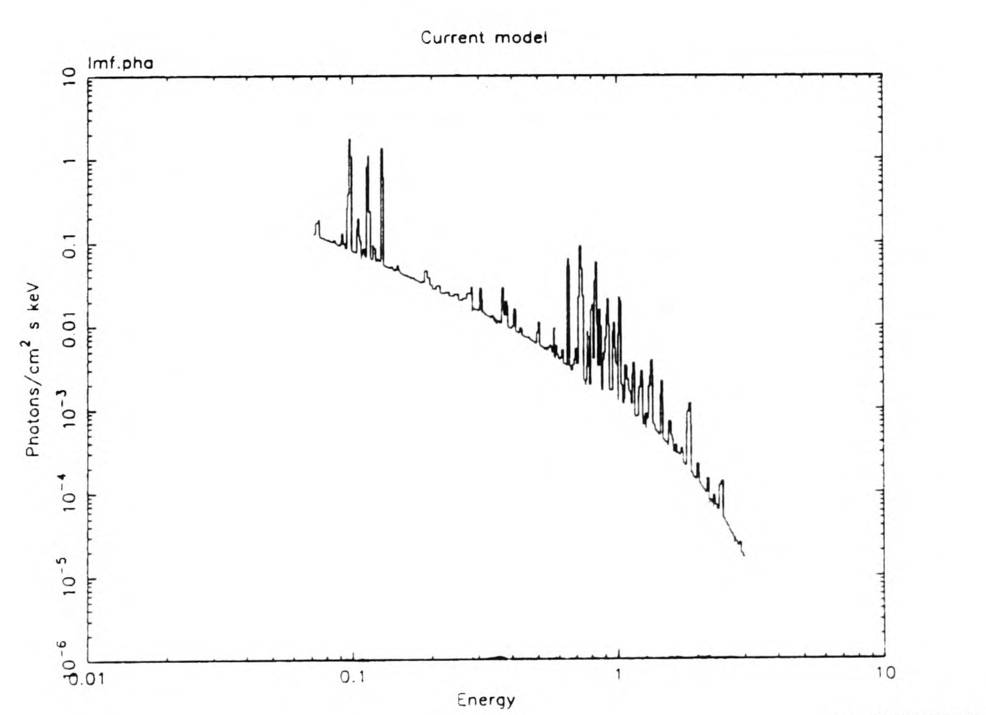

Figure 2.14: Spectrum from LMF model at log T = 6.8 K and normalisation = 0.01 cm^{-5}. The energy is in units of keV.

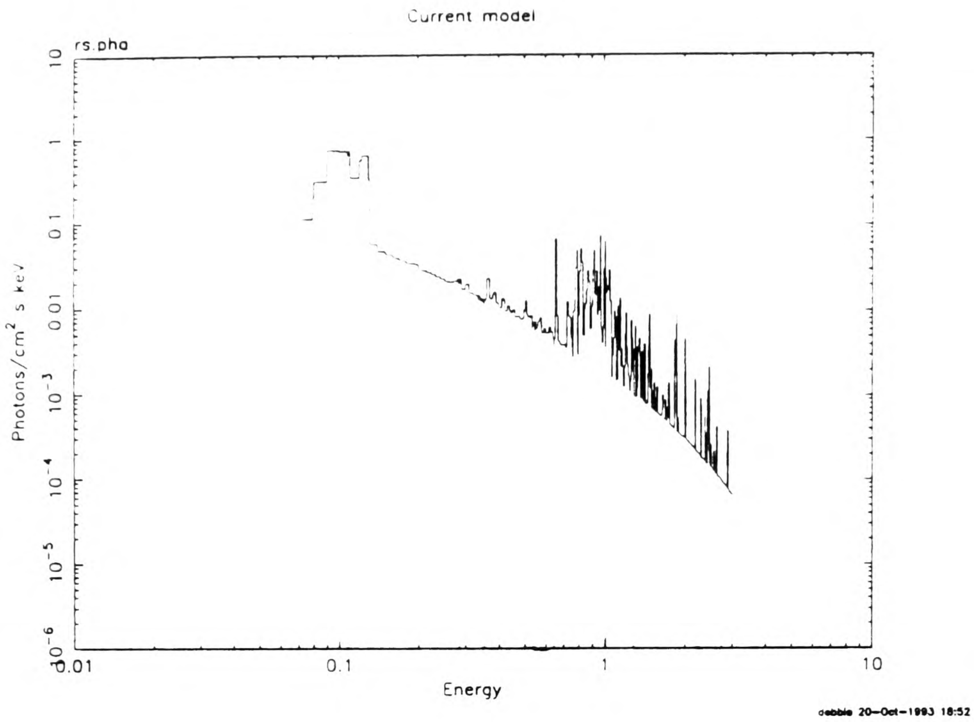

Figure 2.15: Spectrum from RS model at log T = 7.0 K and normalisation = 0.01 cm^{-5}. The energy is in units of keV.

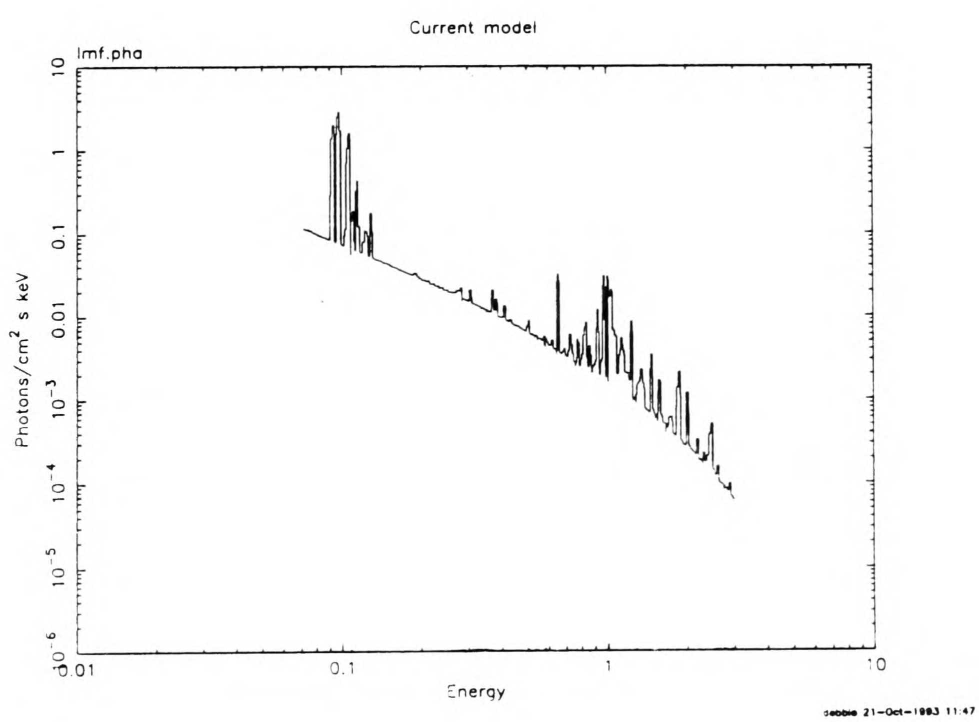

Figure 2.16: Spectrum from LMF model at log T = 7.0 K and normalisation = 0.01 cm^{-5} The energy is in units of keV.

I have used their emission code to fit the ROSAT observations for the five dwarfs and Procyon although I have not examined the code in as much detail as RS and LMF. A brief explanation of the treatment of the atomic data and spectral lines is presented below.

Treatment of Lines:

They have included H- and He-like lines together with their satellites for C to Ni ions which dominate the short wavelength region of the X-ray spectrum (below 40 Å), while for the 170-300 Å region they focused on a large number of highly stripped Fe ions. For the lighter elements they adopted the intensities from a detailed line list published by Doschek & Cowan (1984) for the wavelength region 10 - 200 Å. For lines with wavelengths > 200 Å the line list of Fawcett (1974) has been used in conjunction with the tables of Wiese *et al.* (1966, 1969) for oscillator strengths and wavelengths, and Kelly and Palumbo (1973) for wavelengths only.

Continuum Radiation:

This has been computed by taking emission from brehmsstrahlung and two-photon decay into account. The calculations for the former process have used the method of Karzas & Latter (1961) for computing Gaunt factors, as did LMF and RS. The approach of Mewe *et al.* (1985) for the latter process, is similar to that of RS where emission from H- and He-like ions is considered.

In the stand-alone code they have used the ionisation balance of Arnaud & Rothenflug (1985) the abundances of Allen (1973) which in XSPEC were substituted with those of Anders & Grevesse (1989) and Grevesse *et al.* (1992).

In order to compare the results of the Mewe code w.r.t. those of RS and LMF (1T and 2T fits) the respective differences in logs of the coronal temperatures and emission measures for these models are given in Table 2.6. There is very good agreement between Mewe and RS (generally within ± 0.1 dex which is within error margins). One reason for this is the agreement in the ion balance populations used by the two codes, as was discussed earlier

Table 2.6: Logs of coronal temperature and emission measures as derived from the Mewe spectral emission code for 1T and 2T fits. The superscripts correspond to either log T^{Mewe} – log T^{RS} or log Em^{Mewe} – log Em^{RS}, as indicated, while the subscripts similarly correspond to the differences between the Mewe and LMF results. (The RS and LMF 1T and 2T results are given in Tables 2.9 - 2.12).

Star	T^{1T}	Em^{1T}	$\mathrm{T1}^{2T}$	$\mathrm{Em1}^{2T}$	$\mathrm{T2}^{2T}$	$\mathrm{Em2}^{2T}$
χ^1 *Ori*	$6.75^{+0.14}_{+0.02}$	$28.40^{-0.25}_{-0.45}$	$6.06^{-0.02}_{+0.18}$	$28.54^{+0.08}_{+0.09}$	$6.76^{-0.04}_{+0.04}$	$28.39^{-0.04}_{-0.44}$
ϵ *Eri*	$6.32^{-0.08}_{-0.08}$	$28.34^{-0.03}_{-0.24}$	$6.21^{-0.02}_{+0.09}$	$28.31^{+0.02}_{-0.24}$	$6.80^{-0.08}_{+0.07}$	$27.78^{+0.01}_{-0.45}$
ξ *BooA*†	$6.79^{+0.13}_{+0.03}$	$28.48^{-0.19}_{-0.48}$	$6.13^{+0.19}_{+0.32}$	$28.69^{-0.11}_{-0.15}$	$6.80^{-0.07}_{+0.04}$	$28.46^{-0.03}_{-0.47}$
Procyon	$6.11^{-0.01}_{+0.01}$	$27.57^{+0.07}_{-0.13}$	$6.07^{-0.01}_{+0.03}$	$27.56^{+0.09}_{-0.12}$	$6.55^{-0.08}_{+0.16}$	$26.02^{-0.12}_{-0.66}$

† B-filter status *on*.

in Section 2.4.5. However, when comparing Mewe with LMF, it is evident that although the temperatures derived by the two models agree well for 1T and 2T fits to within ± 0.1 dex (although the Mewe results are systematically higher), there is less good agreement between the emission measures. The LMF values tend to be roughly 0.50 dex *higher* than the Mewe values, indicating that overall *lower* emissivities have been made by LMF.

§2.5 *Spectral Fitting:*

The observed X-ray data were modelled with the RS and LMF codes, using several types of fits for the temperatures. The resulting coronal temperatures and emission measures, together with their respective reduced χ^2, are listed in Tables 2.6, 2.7 and 2.9 - 2.12. The emission measures which form the output from both the RS and LMF stand-alone codes are defined as

$$Em(r) = \int n_e n_H \, dr. \tag{2.16}$$

However, XSPEC operates in terms of

$$Em(V) = \int n_e^2 \, dV \tag{2.17}$$

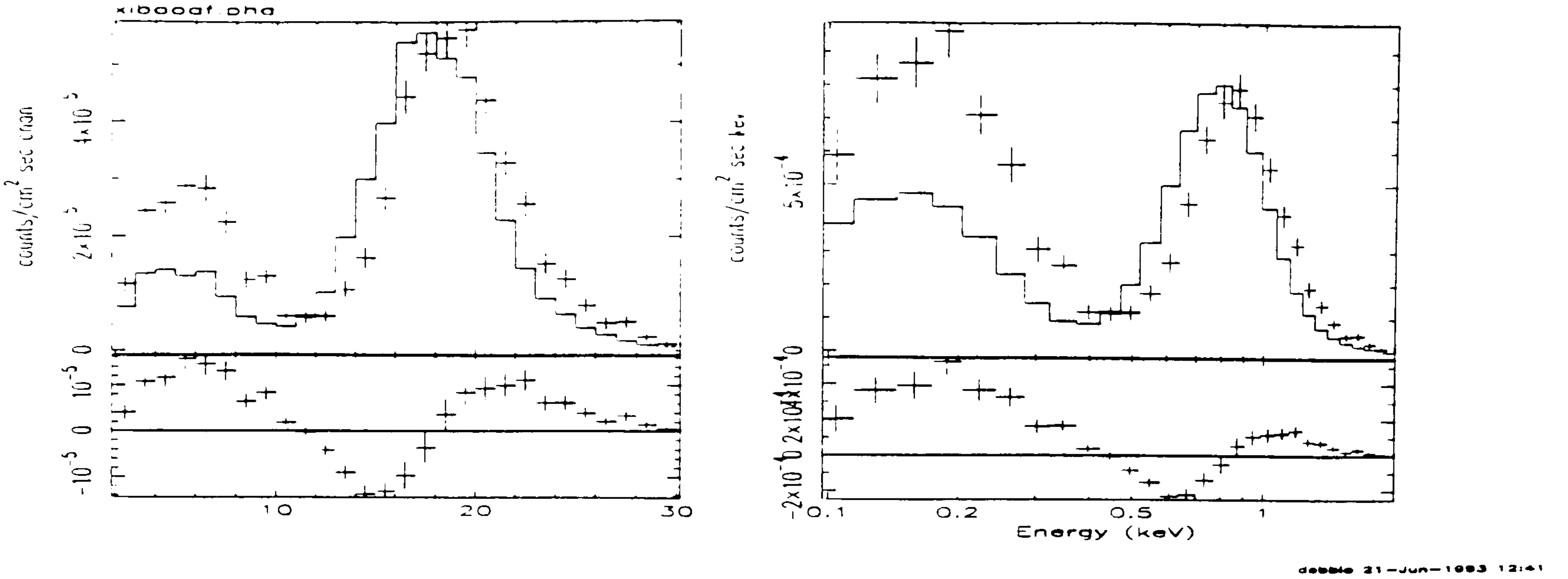

Figure 2.17: The upper graphs are the 1T fits to the PSPC spectrum of ξ Boo A (B-filter on) using the RS code and XSPEC while the lower graph shows the difference between the spectrum and the predicted model. The LHS fit is shown as a function of channel number, while the RHS fit is shown as function of energy. The crosses are the data points, and the histograms are the model results.

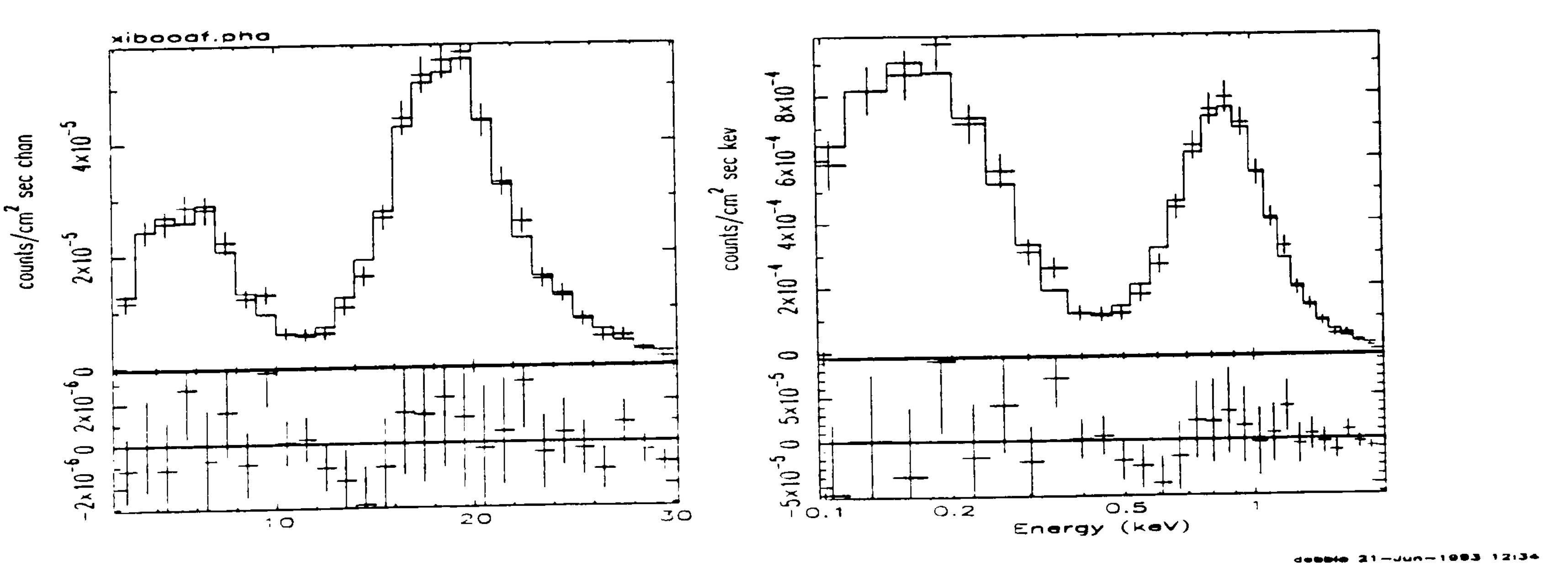

Figure 2.18: The upper graphs are the 2T fits to the PSPC spectrum of ξ Boo A (B-filter on) using the RS code and XSPEC while the lower graph shows the difference between the spectrum and the predicted model. The LHS fit is shown as a function of channel number, while the RHS fit is shown as function of energy. The crosses are the data points, and the histograms are the model results.

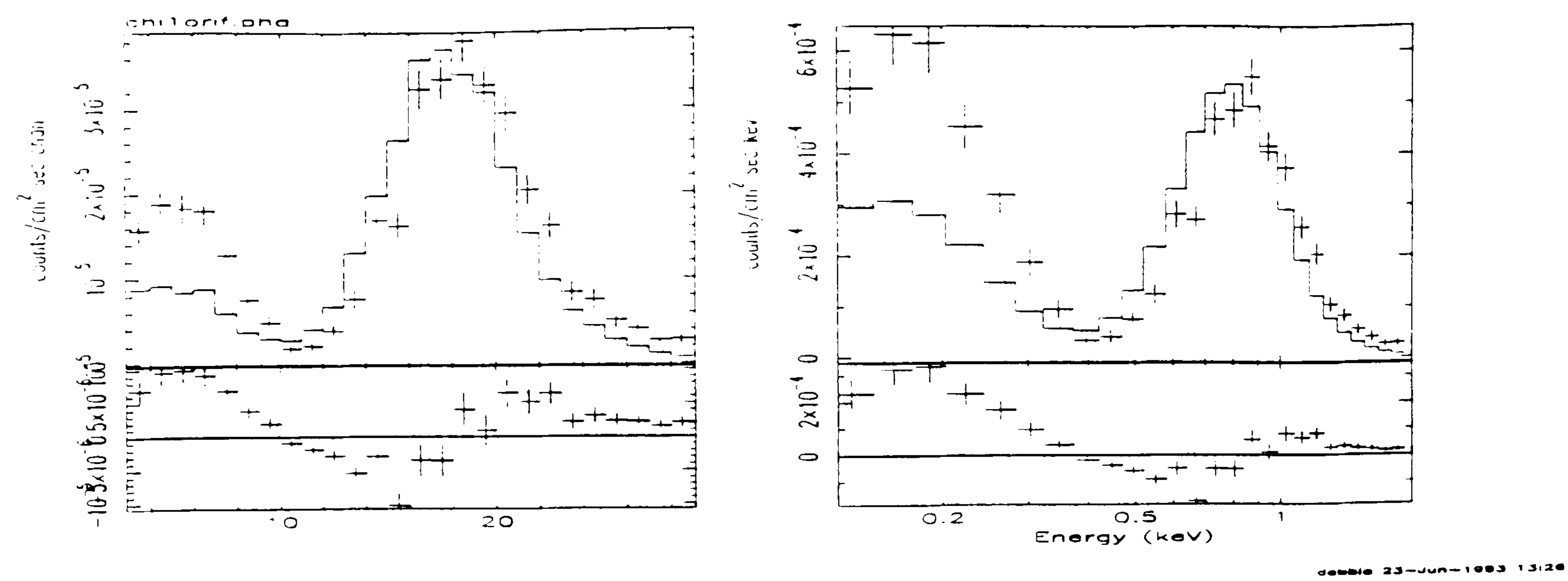

Figure 2.19: The upper graphs are the 1T fits to the PSPC spectrum of χ^1 Ori using the RS code and XSPEC while the lower graph shows the difference between the spectrum and the predicted model. The LHS fit is shown as a function of channel number, while the RHS fit is shown as function of energy. The crosses are the data points, and the histograms are the model results.

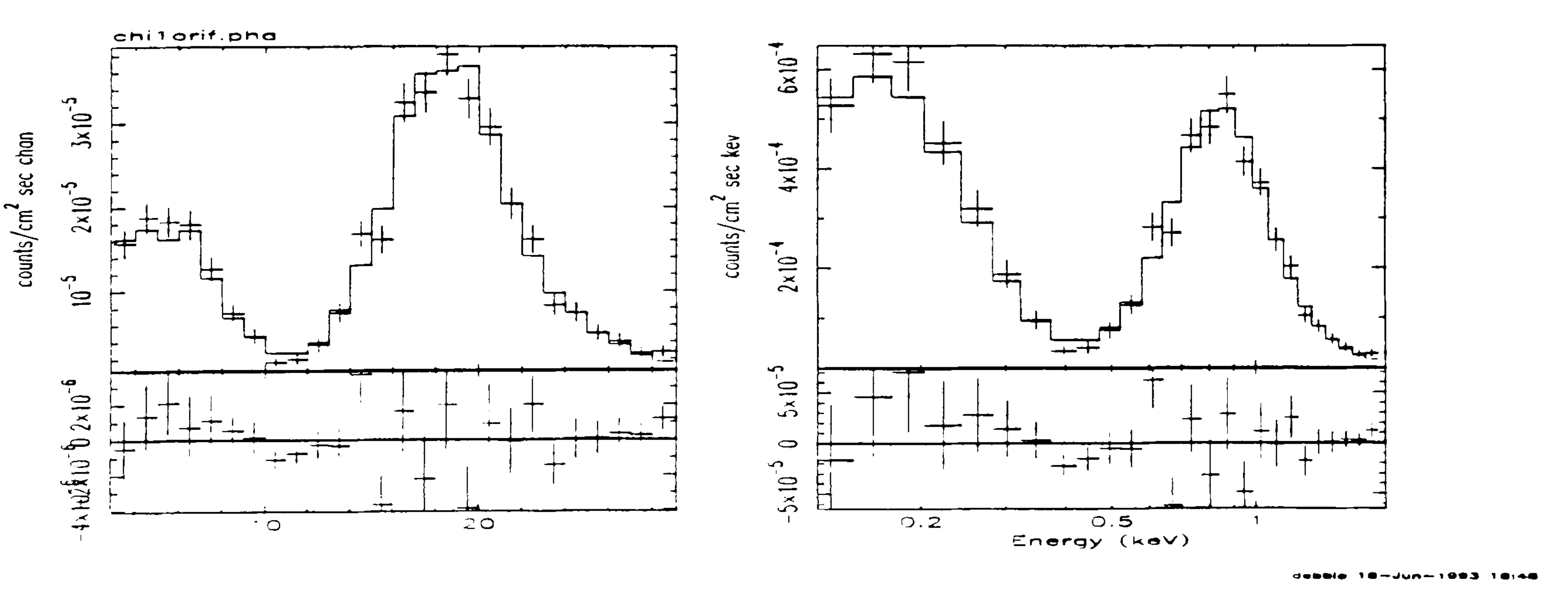

Figure 2.20: The upper graphs are the 2T fits to the PSPC spectrum of χ^1 Ori using the RS code and XSPEC while the lower graph shows the difference between the spectrum and the predicted model. The LHS fit is shown as a function of channel number, while the RHS fit is shown as function of energy. The crosses are the data points, and the histograms are the model results.

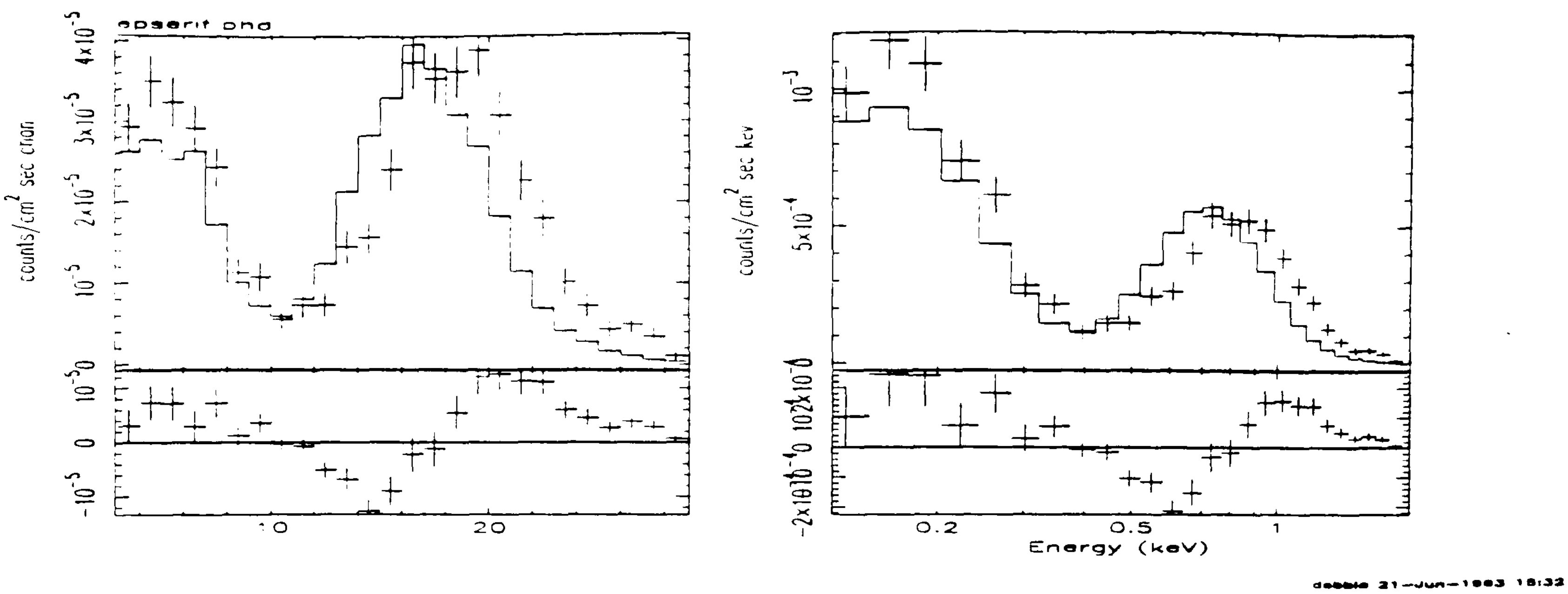

Figure 2.21: The upper graphs are the 1T fits to the PSPC spectrum of ϵ Eri using the RS code and XSPEC while the lower graph shows the difference between the spectrum and the predicted model. The LHS fit is shown as a function of channel number, while the RHS fit is shown as function of energy. The crosses are the data points, and the histograms are the model results.

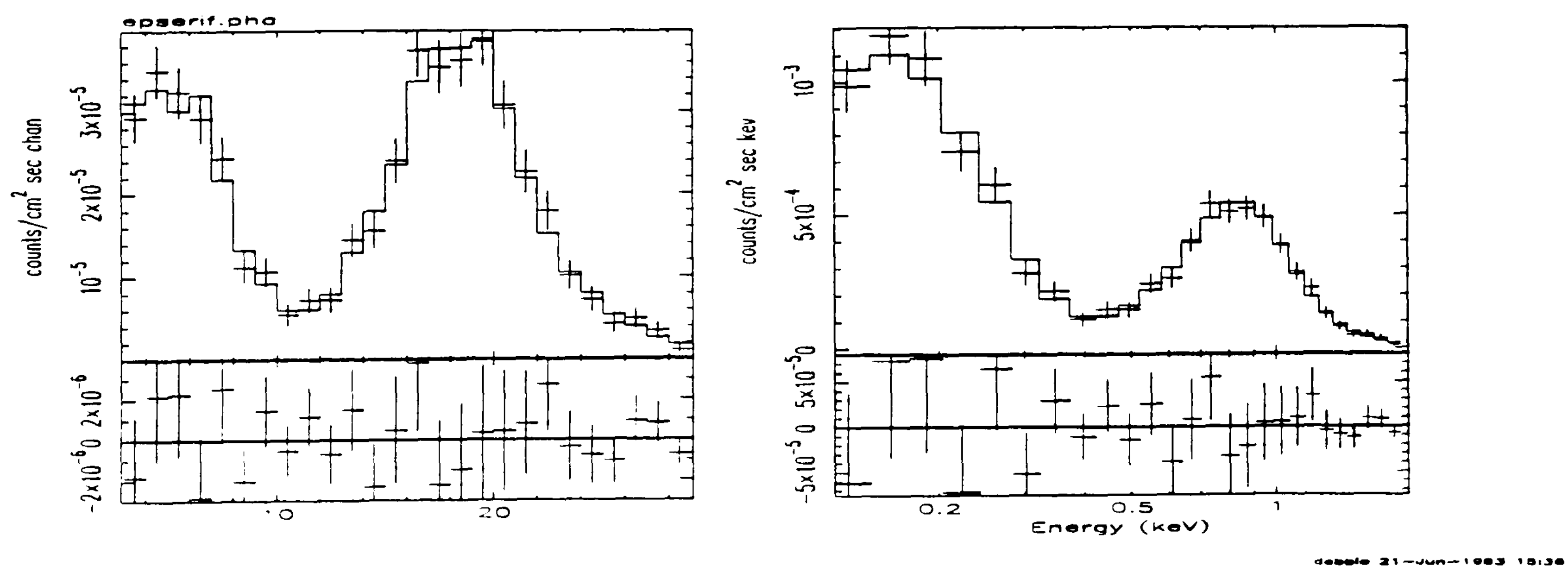

Figure 2.22: The upper graphs are the 2T fits to the PSPC spectrum of ϵ Eri using the RS code and XSPEC while the lower graph shows the difference between the spectrum and the predicted model. The LHS fit is shown as a function of channel number, while the RHS fit is shown as function of energy. The crosses are the data points, and the histograms are the model results.

where $Em(V)\Lambda_{rad} = 4\pi d^2 F_{\oplus}$, and Λ_{rad} is the radiative power loss (see Section 3.5.3 of Chapter 3) and $F_{\oplus}$ is the flux at the earth corrected for the interstellar absorption and the instrument sensitivity.

The emission measures in Tables 2.6, 2.7 and 2.9 - 2.12 are defined as

$$Em(r) = \int n_e^2 \, dr = \frac{\int n_e^2 \, dV}{4\pi R_*^2} \tag{2.18}$$

whereas in the analyses in Chapters 3 and 4, the forms

$$Em(r) = \int n_e n_H \, dr = \frac{\int n_e n_H \, dV}{4\pi R_*^2} \tag{2.19}$$

have been used (see Section 3.2 of Chapter 3).

1. **One-Temperature Model:** This is the simplest model considered as it defines a *dominant* single coronal temperature T_c together with its corresponding emission measure, Em. However, the values of χ^2 are unacceptably high and these fits do not adequately fit the observed spectra as is illustrated in Figures 2.17, 2.19, and 2.21.

2. **Two-Temperature Model:** This model assigns two coronal temperature components ($T1$ and $T2$), together with their corresponding emission measures ($Em1$ and $Em2$ respectively). Even though this model generally yields better fits to the observed data than does the one-temperature fit (which is evident from Tables 2.9 - 2.12), this is because there are more free parameters, and the agreement may not be any more physically significant. The temperatures should be interpreted as *effective temperatures* which reflect the instrumental response to a complex distribution of fluxes. Jordan *et al.* (1996, in preparation) have shown that observations of ξ *Boo A* with EUVE do not confirm the presence of the low temperature component found from the PSPC data (see also Jordan 1995a). This is apparent in the XSPEC fits (see Figures 2.18, 2.20 and 2.22), where unlike the higher temperature component, the lower temperature component does not fit the observed counts of the unfolded spec-

trum. A further illustration is given in Chapter 3, where these results are compared with the emission measure distribution that is obtained from energy balance models.

3. **Continuous Emission Measure Model (CEM):** The flux F obtained from the spectrum was fitted using the RS code to the following expression which is the general definition of a CEM model:

$$F(T^{CEM}, E) = \frac{\alpha Em(V)^{CEM}}{4\pi d^2} \frac{1}{T^{CEM^{\alpha}}} \int_{T_{min}}^{T^{CEM}} T_e^{\alpha-1} \epsilon(T_e, E)\, dT_e \; erg\, cm^{-2} s^{-1} keV \tag{2.20}$$

where α is the gradient of the emission measure with temperature, T^{CEM} corresponds to the coronal temperature T_c, d is the earth-star distance in cm, and $\epsilon(T_e, E)$ is the plasma emissivity as given by the RS code at a temperature T_e (in units of K) and energy E (in units of keV). The CEM fit yields a coronal temperature (T^{CEM}) and its respective emission measure (Em^{CEM}). These values correspond to an emission measure distribution in the temperature range $T_{min} < T_e < T^{CEM}$ with gradient α. In this instance the choice of α was determined by the constraints imposed by energy balance (see Section 3.5 of Chapter 3) which require that $\alpha \simeq 3/2$. A comparison between the (Em^{CEM}) and (T^{CEM}) found with respect to the 1T fits is given in Table 2.7. It can be seen that both Em^{CEM} and T^{CEM} are roughly a factor of 0.1 dex *higher* than those found by the corresponding 1T fits, the exception being ϵ Eri, for which the temperatures are also significantly different.

Table 2.7: Logs of coronal temperature and emission measures derived for the CEM model using the RS code, with $\alpha = 3/2$ (see text). The numbers in brackets correspond to either $\log T^{CEM} - \log T^{1T(RS)}$ or $\log Em^{CEM} - \log Em^{1T(RS)}$, as indicated. The results for the 1T (RS) fits are given in Table 2.9.

Star	log $\mathbf{T}^{CEM}$	log $\mathbf{Em}^{CEM}$
χ^1 *Ori*	6.75(+0.14)	28.72(+0.07)
ϵ *Eri*	6.62(+0.22)	28.36(−0.01)
ξ *BooA*†	6.75(+0.09)	28.76(+0.10)
Procyon	6.26(+0.14)	27.64(+0.14)

† B-filter status *on*.

Absorption by the Interstellar Medium

The interstellar medium (ISM) primarily consists of clouds of ionised and neutral hydrogen, together with a smaller proportion of molecular clouds as well as dust grains composed of carbon, silicates and iron. Although the dust grains make up $\sim$ 1% of the ISM mass, they can cause considerable absorption of starlight. In particular, UV spectra of distant sources show a strong broad absorption feature at 2200Å known as the UV extinction bump, which can be observed in IUE spectra. The reddening of the stars studied here is very small and interstellar absorption has no significant effect on IUE spectra. Below the H Lyman limit (911Å), absorption by H is important even for stars as close as α Cen A & B. For completeness, the interstellar absorption by both H and He has been taken into account in all calculations. For each star, the interstellar absorption was computed as follows:

$$N_x^* = n_H^{ISM} \times d \qquad (2.21)$$

where n_H^{ISM} is the hydrogen column density of the interstellar medium which is taken as an average value of 0.07 cm^{-3} in the local bubble (Paresce, 1984), while d is the stellar distance from the earth in centimeters. The values of N_x (which are frozen during spectral fitting) are given in Table 2.8, and the resulting transmission of the ISM as used in this analysis is shown in Figure 2.23, for $N_x = 7.0 \times 10^{17}$, 1.0×10^{18} and 3.5×10^{18} cm^{-2}.

Table 2.8: The interstellar absorption N_x^* that is adopted for each star, as computed using equation (2.21).

Star	$N_x(cm^{-2})$
$\epsilon\, Eri$	7.1×10^{17}
$70\, Oph A$	1.1×10^{18}
$61\, Cyg A$	7.3×10^{17}
$\chi^1\, Ori$	2.1×10^{18}
$OU\, Gem$	2.6×10^{18}
$\kappa\, Cet$	2.0×10^{18}
$Procyon$	7.3×10^{17}
$\xi\, Boo A$	1.5×10^{18}
$HD\, 115404$	2.6×10^{18}
$HD\, 152391$	3.5×10^{18}
$HD\, 155886$	1.2×10^{18}
$\alpha\, Cen\, A\&B$	2.9×10^{17}

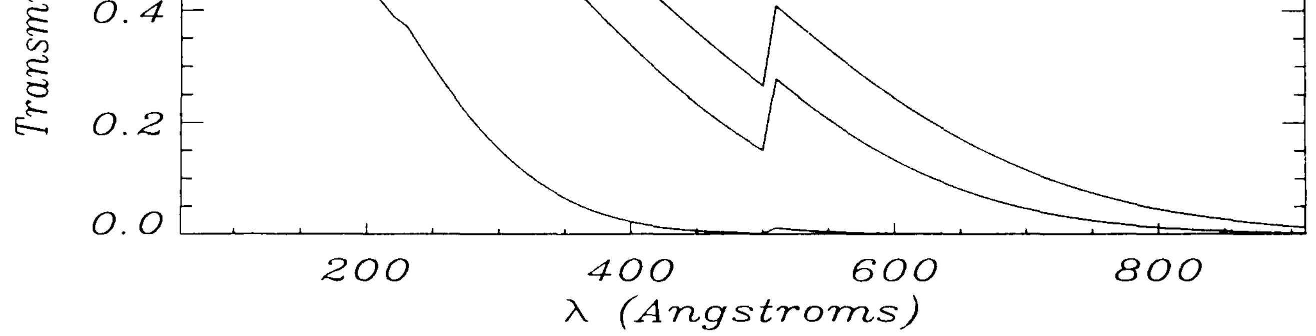

Figure 2.23: The transmission of the ISM for $N_x = 7.0 \times 10^{17}$, 1.0×10^{18} and 3.5×10^{18} cm^{-2}, using the description of ISM absorption of Rumph, Bowyer & Vennes (1994). This model accounts for H, He as well as metals, which are treated as in Morrison & MacCammon (1983).

§2.6 *Results and Conclusions*

The resulting coronal emission measures and temperatures from the PSPC observations are given in Tables 2.6, 2.7 and 2.9 - 2.12. A comparison between the parameters that were obtained from the two codes is shown in Figures 2.24 and 2.25 from which the following general trends emerge (bearing in mind that deviations from such trends are possible owing to the varying quality of the spectra):

1. Both $T1$(LMF) and $T2$(LMF), are systematically *lower* than the corresponding $T1$(RS) and $T2$(RS)values (see Figure 2.25). The lower component of the 2T fit for 61 Cyg A shows a striking deviation to this pattern. This is because the RS code could not fit a lower temperature component to the spectrum within the bounds permitted by XSPEC; thus, the value given (log $T1 \leq 5.97$; see Table 2.11) is an upper limit which is unrealistically low for a coronal temperature. This result is an extreme case; however, the 2T LMF fit yields identical values for both the upper and lower components of the emission measure and temperature (log $Em1\,\&\,2 = 27.03$, $\log T1\,\&\,2$ = 6.76 (see Table 2.12). A similar behaviour is shown in the results for 70 Oph A_2 (log $T1(RS) \leq 5.97$ and log $T2$(RS) = 6.79, log $T1$(LMF) = 6.72 and log $T2$(LMF) = 6.74) (For an explanation of the two spectra for 70 Oph A, see note to Table 2.9).

2. The emission measures computed from the LMF code for both 1T (Figure 2.24) and 2T fits (see Figure 2.25), are systematically *higher* than the corresponding values found using the RS code. Pan & Jordan (1994) analysed PSPC spectra of CC Eri and also found a systematic decrease in the ratio $Em2(LMF)/Em2(RS)$ as $T2$(LMF) or $T2$(RS) increase. These differences are consistent with the higher emissivities found from the RS code (a higher emissivity leads to a lower emission measure, and vice-versa).

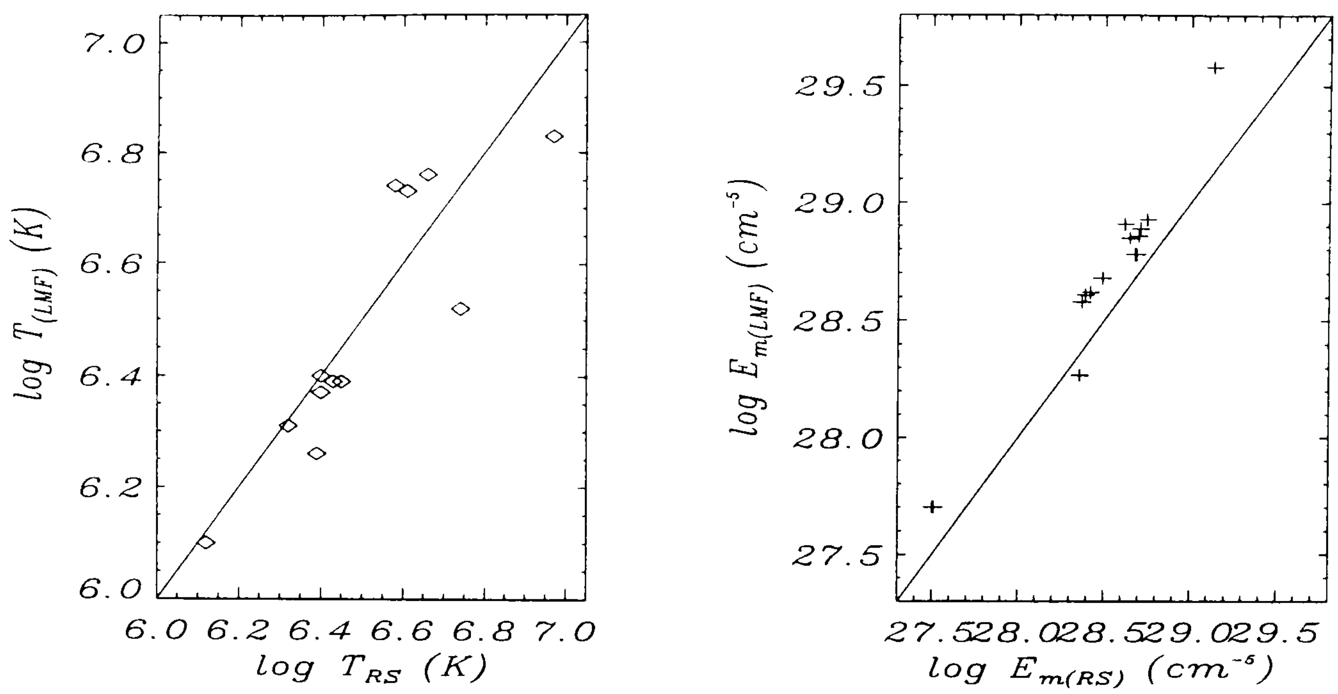

Figure 2.24: Plots of the of T(RS) vs T(LMF) and Em(RS) vs Em(LMF) for 1T fits. The solid lines indicate where log Em(RS) = log Em(LMF) and log T(RS) = log T(LMF). Owing to the varying quality of the spectra, some stars exhibit deviations from the general trends (see text).

A fit is considered to be good if $\chi^2 \leq 1.0$; however, the fits from the RS and LMF codes for most cases, tend to have uncomfortably high χ^2.

Four stars have been observed with the B-filter both *(i)* on, and *(ii)* off. As expected, the temperatures deduced with the B-filter on, are systematically higher, since the filter excludes the low energy channels. However, the general behaviour of the fits with acceptable χ^2, is that the emission measures and temperatures for each stellar observation in cases *(i)* and *(ii)* tend to agree to within 0.1 dex with the tendency for the former to give slightly higher results than the latter.

From the discussion above, it is difficult to decide which code is best, as each has some shortcomings. In Chapter 3, comparisons are made between the 1T, 2T and CEM fits (for the RS, LMF and Mewe codes) and some results from the EUVE obserations; the question of which code and which type of fit is best will be discussed there.

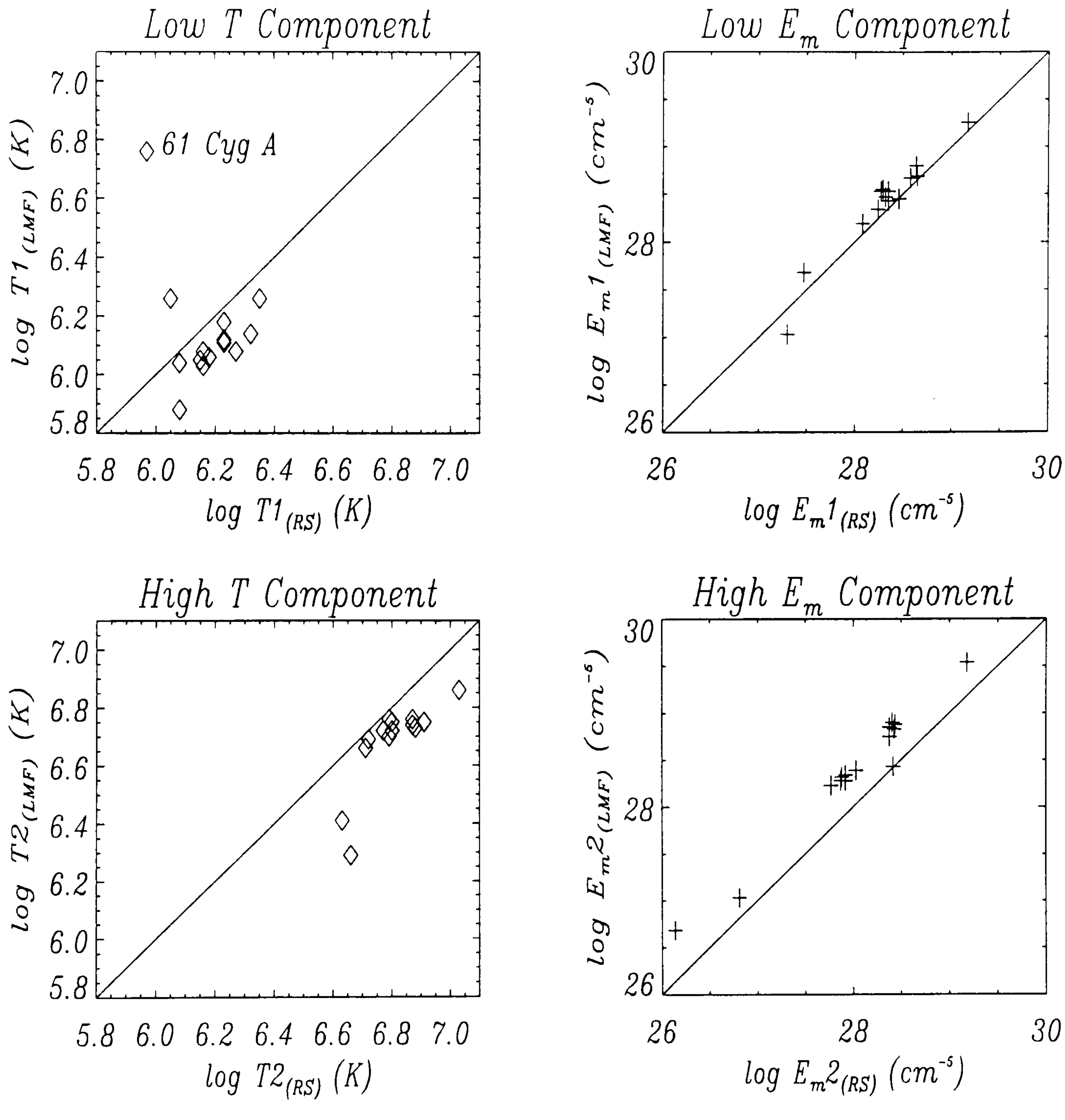

Figure 2.25: Plots of the low and high temperature components of T(RS) vs T(LMF) and Em(RS) vs Em(LMF) for 2T fits. The solid lines indicate where log Em(RS) = log Em(LMF) and log T(RS) = log T(LMF). Owing to the varying quality of the spectra, some stars exhibit deviations from the general trends (see text).

Table 2.9: One-Temperature Fits from the RS code (1990), using XSPEC.

Star	log **Em(RS)** (cm^{-5})	log **T(RS)** (K)	χ^2	**B – filter status**
$\epsilon\,Eri$	28.37	6.40	8.21	*on*
$70\,OphA_1$ †	28.42	6.40	1.94	*on*
$70\,OphA_2$ †	28.24	6.39	7.86	*on*
$61\,CygA$	27.51	6.32	3.77	*on*
$\chi^1\,Ori$	28.65	6.61	9.58	*on*
OU Gem	29.13	6.97	5.77	*on*
$\kappa\,Cet$	28.70	6.58	2.79	*on*
Procyon	27.50	6.12	3.93	*on*
$\xi\,Boo\,A$	28.62	6.66	15.08	*on*
$\xi\,Boo\,A$	28.71	6.45	4.81	*off*
HD 115404	28.39	6.43	1.65	*on*
HD 115404	28.49	6.40	1.09	*off*
HD 152391	28.75	6.58	1.22	*on*
HD 152391	28.69	6.39	2.25	*off*
HD 155886	28.36	6.74	2.81	*on*
HD 155886	28.68	6.39	7.99	*off*

† The data for $70\,Oph\,A_1$ are from a 747 sec exposure made in March 1992, while the data for $70\,Oph\,A_2$ are from a 1798 sec exposure made in March 1993, so as to complete the requested observation time for the target. The two sets could not be combined as the response matrix of the PSPC changed non-linearly with time as was mentioned in Section 2.2.2. Owing to the high χ^2 for 1T and 2T RS and LMF fits of $70\,Oph\,A_2$(also see Tables 2.9 - 2.12), only the results of $70\,Oph\,A_1$ have been considered.

Table 2.10: One-Temperature Fits from the LMF code (1991), using XSPEC.

Star	log **Em(LMF)** ($\mathbf{cm^{-5}}$)	log **T(LMF)** (**K**)	χ^2	**B – filter status**
$\epsilon\,Eri$	28.58	6.40	9.93	*on*
$70\,OphA_1$	28.62	6.37	2.25	*on*
$70\,OphA_2$	28.23	6.73	7.36	*on*
$61\,CygA$	27.70	6.31	4.05	*on*
$\chi^1\,Ori$	28.85	6.73	8.68	*on*
$OU\,Gem$	29.58	6.83	2.61	*on*
$\kappa\,Cet$	28.86	6.74	2.52	*on*
$Procyon$	27.70	6.10	5.38	*on*
$\xi\,Boo\,A$	28.91	6.76	12.30	*on*
$\xi\,Boo\,A$	28.89	6.39	5.30	*off*
$HD\,115404$	28.61	6.39	1.79	*on*
$HD\,115404$	28.68	6.37	1.13	*off*
$HD\,152391$	28.93	6.74	1.10	*on*
$HD\,152391$	28.78	6.26	5.84	*off*
$HD\,155886$	28.27	6.52	2.95	*on*
$HD\,155886$	28.78	6.26	8.12	*off*

Table 2.11: Two-Temperature Fits from the RS code (1990), using XSPEC.

Star	log **Em1(RS)** (cm^{-5})	**T1(RS)** (**K**)	log **Em2(RS)** (cm^{-5})	$\mathbf{T2_{(RS)}}$ (**K**)	χ^2	**B – filter status**
$\epsilon\,Eri$	28.29	6.23	27.77	6.88	0.71	*on*
$70\,OphA_1$	28.35	6.15	27.87	6.79	0.66	*on*
$70\,OphA_2$	27.30	≤ 5.97	27.81	6.79	1.80	*on*
$61\,CygA$	27.29	≤ 5.97	26.89	6.77	0.85	*on*
$\chi^1\,Ori$	28.46	6.08	28.43	6.80	1.46	*on*
$OU\,Gem$	29.17	6.35	29.18	7.03	0.80	*on*
$\kappa\,Cet$	28.58	6.27	28.38	6.87	1.17	*on*
$Procyon$	27.47	6.08	26.14	6.63	0.39	*on*
$\xi\,Boo\,A$	28.65	6.16	28.44	6.87	1.34	*on*
$\xi\,Boo\,A$	28.35	6.16	28.38	6.77	0.85	*off*
$HD\,115404$	28.29	6.23	27.92	6.71	1.36	*on*
$HD\,115404$	28.24	6.23	28.03	6.72	0.51	*off*
$HD\,152391$	28.64	6.32	28.41	6.91	0.65	*on*
$HD\,152391$	28.27	6.05	28.42	6.66	0.42	*off*
$HD\,155886$	28.32	6.18	27.88	6.87	0.61	*on*
$HD\,155886$	28.08	6.16	27.92	6.80	0.86	*off*

Table 2.12: Two-Temperature Fits for the LMF code (1991), using XSPEC.

Star	log **Em1(LM)** (cm^{-5})	log **T1(LM)** (**K**)	log **Em2(LM)** (cm^{-5})	log **T2(LM)** (**K**)	χ^2	**B – filter status**
$\epsilon\,Eri$	28.55	6.12	28.23	6.73	1.14	*on*
$70\,OphA_1$	28.53	6.05	28.28	6.70	0.67	*on*
$70\,OphA_2$	27.93	6.72	27.93	6.74	4.07	*on*
$61\,CygA$	27.03	6.76	27.03	6.76	4.07	*on*
$\chi^1\,Ori$	28.45	5.88	28.83	6.72	2.24	*on*
$OU\,Gem$	29.26	6.26	29.54	6.86	0.78	*on*
$\kappa\,Cet$	28.67	6.08	28.85	6.74	1.27	*on*
$Procyon$	27.68	6.04	26.68	6.41	0.56	*on*
$\xi\,Boo\,A$	28.69	6.03	28.88	6.76	3.16	*on*
$\xi\,Boo\,A$	28.43	6.08	28.75	6.72	1.02	*off*
$HD\,115404$	28.55	6.11	28.28	6.66	1.30	*on*
$HD\,115404$	28.34	6.18	28.39	6.69	0.49	*off*
$HD\,152391$	28.80	6.14	28.90	6.75	0.67	*on*
$HD\,152391$	28.53	6.26	28.43	6.29	5.84	*off*
$HD\,155886$	28.47	6.06	28.32	6.74	0.82	*on*
$HD\,155886$	28.19	6.08	28.34	6.75	0.77	*off*

Table 2.13: The coronal emission measures and temperatures for the WFC observations of the five dwarfs as computed by the RS and LMF codes using XSPEC.

Star	log **Em(RS)** (cm^{-5})	log **T(RS)** (K)	log **Em(LM)** (cm^{-5})	log **T(LM)** (K)
χ^1 *Ori*	29.01	6.71	29.10	6.61
ϵ *Eri*	28.62	6.30	28.85	6.40
ξ *Boo A*	28.46	6.30	28.71	6.40
α *Cen A*	27.04	6.37	27.13	6.48
α *Cen B*	27.71	6.37	27.80	6.48

Results from the WFC:

The WFC results for the five dwarfs are listed in Table 2.13. These results are 1T fits (see Section 2.2.3) from filter ratios which correspond to relatively long wavelengths (see Table 2.3), and it is not surprising that they give intermediate temperatures. The WFC yields an average emission measure at an average coronal temperature, based on all the lines present in its wavelength range of detection *i.e.* it places all the material at one temperature. Since a distribution of emission measures with temperatures is in reality present, one would expect the emission measures to be too large, as is found by comparing the WFC results with those found from the corresponding PSPC observations; see also Section 3.5.5 of Chapter 3.

In view of the above discussion, I do not place particular weight on the WFC results, which have been presented for completeness.

2.6.1 Comparisons with Correlations

Power law correlations have been found to exist between X-ray fluxes and observable stellar parameters (see discussion and references in Section 1.5 of Chapter 1). Jordan & Montesinos (1991) used a sample of stars to derive correlations between the parameters $Em(T_c)$, T_c, g_*, the implied coronal magnetic field, B_c, and the Rossby number, R_o; (the Rossby number is an indicator of dynamo efficiency and is defined as $R_o = \Pi_{rot}/\tau_c$ (Noyes *et al.*, 1984), where

τ_c is the turnover time at the base of the convection zone). They used a sample of stars for which Schmitt *et al.* (1990) were able to obtain satisfactory 1T fits to their X-ray spectra, from observations made with the *Einstein Observatory*. Montesinos & Jordan (1993) revised the form of the correlations for this sample of late-type dwarf stars (henceforth referred to as *Sample A*), and extended the correlations to include the Ca II H & K emission and surface magnetic fields and filling factors.

In this section, I use the sample of ten dwarf stars (henceforth referred to as *Sample B*), observed with the PSPC, and analysed earlier in this chapter, to investigate to what extent the derived values of $Em(T_c)$ and T_c fit the correlations found by Montesinos & Jordan (1993). Since Schmitt *et al.* (1990) used the 1977 version of the RS code (see Raymond & Smith, 1977) some differences are to be expected. However, allowing for the difference of a factor of 2 in the definition of $Em(T_c)$ (Montesinos & Jordan (1993) used a plane parallel approximation; see Section 3.2 of Chapter 3), the coronal emission measures of Sample B are in good agreement with those derived by Schmitt *et al.* (1990), the differences between them being in the range of +0.01 to +0.25 dex. On the other hand, the temperatures derived show a greater difference, because the temperature is more sensitive to which code is used, as well as the instrument.

The correlations derived by Montesinos & Jordan (1993) have a small gravity dependence. Although some gravities could be updated, for the purposes of this comparison I have adopted the gravities used by Montesinos & Jordan (1993) for the common sample of stars.

For the purposes of comparing with the correlations derived by Montesinos & Jordan (1993), I have adopted the same form of the radiative power loss function as they did (*i.e.* $\mathbf{\Lambda}_{rad} = \alpha T_e^{-\delta}$, where $\alpha = 1.3 \times 10^{-19}$ erg cm^3 s^{-1} K$^{1/2}$, and $\delta = 0.5$).

Jordan & Montesinos (1991) showed that for F and G/K dwarves, correlations exist between the coronal temperatures (T_c), emission measures ($Em(T_c)$) and the R_o.

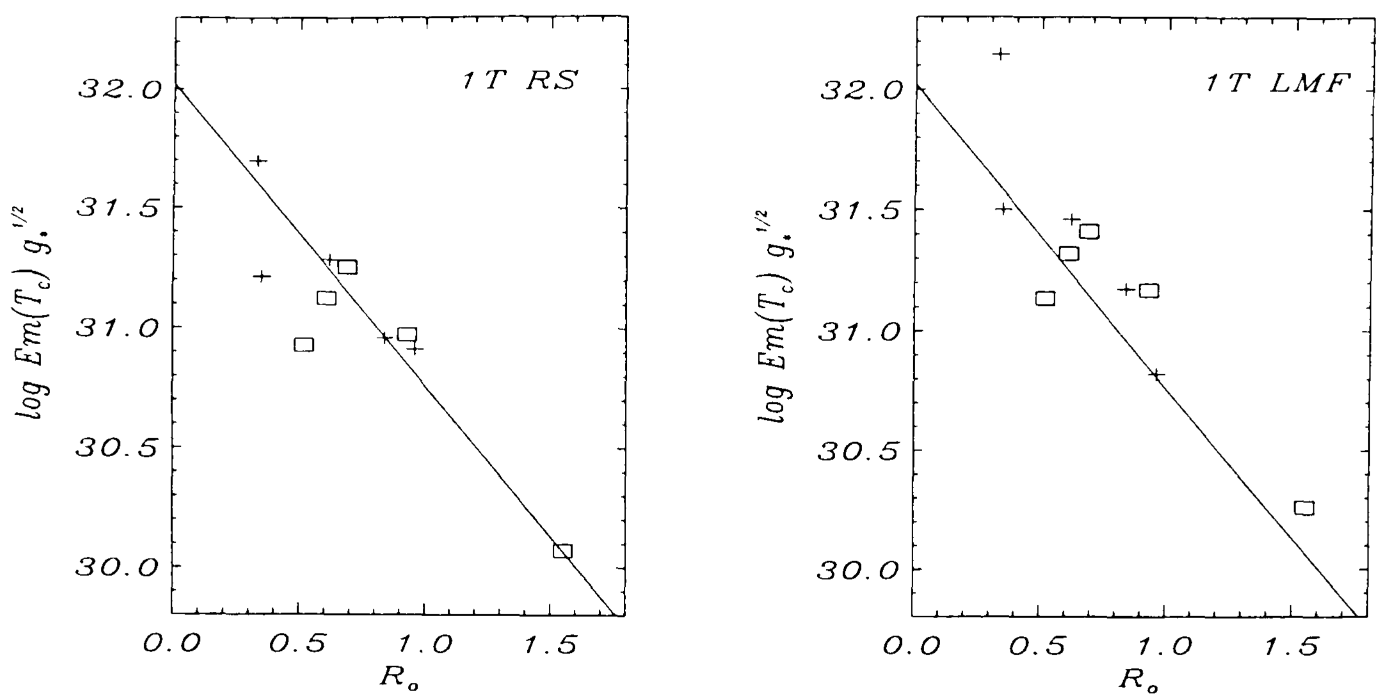

Figure 2.26: $\log (Em(T_c)\, g_*^{1/2})$ plotted against R_o for 1T RS (L.H.S. plot) and LMF (R.H.S. plot) fits for Sample B (see Tables 2.9 and 2.10). The squares represent the set of stars that are common to both Samples A & B (see text). The solid line represents the correlation given by equation (2.22).

Montesinos & Jordan (1993) found that the *observed* values of $Em(T_c)$ and T_c fitted the forms

$$\log (Em(T_c) g_*^{1/2}) = 32.03(\pm 0.10) - 1.26(\pm 0.07) R_o \tag{2.22}$$

and

$$\log (T_c g_*^{1/2}) = 9.09(\pm 0.07) - 0.38(\pm 0.07) R_o \tag{2.23}$$

Figure 2.26 shows $\log(Em(T_c) g_*^{1/2})$ plotted against R_o for the 1T RS and LMF fits to Sample B, and also equation (2.22). It can be seen that the stars in Sample B (which includes five stars in common with Sample A, and five more G/K dwarfs), fit well to the previous correlation. The fit using the RS code is marginally better than that using the LMF code. (The emission measures in Sample A were derived using the early version of the RS code).

Jordan *et al.* (1987) found that $Em(T_c)$ and T_c scaled according to $Em(T_c) \propto T_c^3 g_*$, the gravity dependence being important when evolved stars are included. For the dwarf stars,

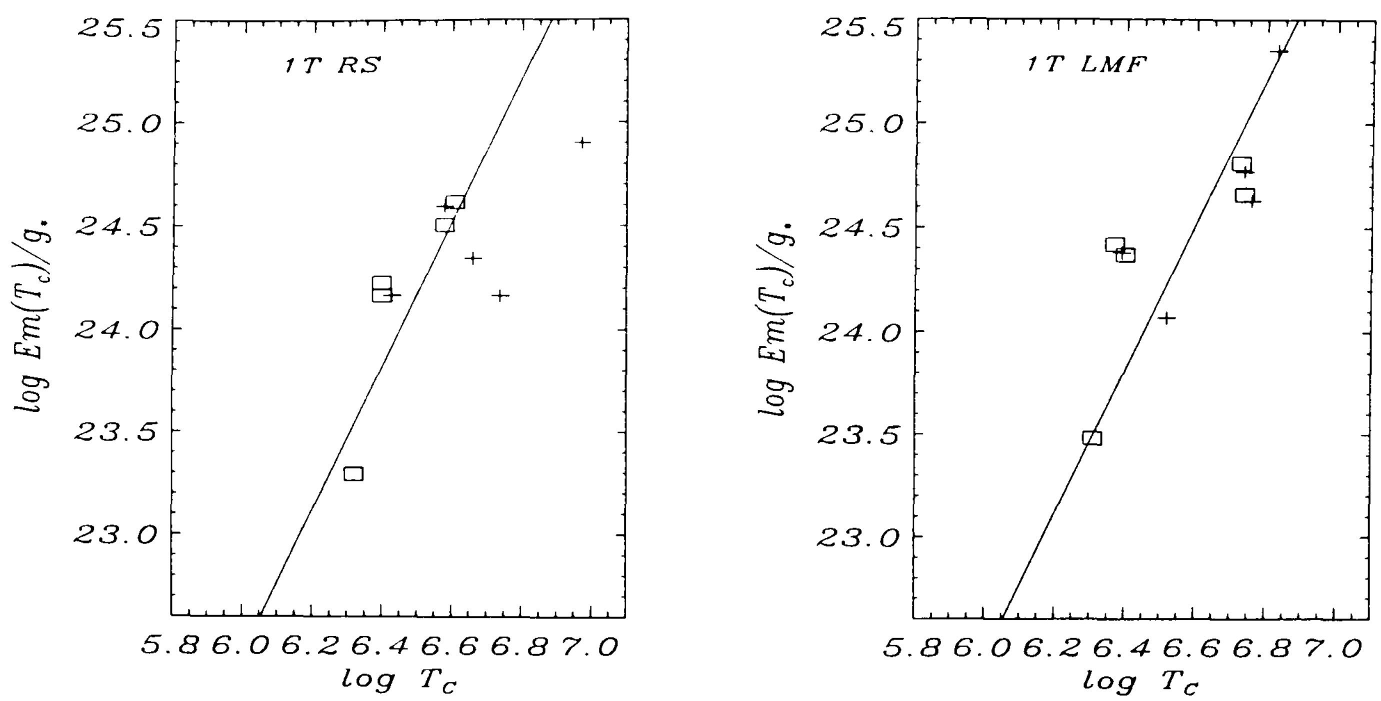

Figure 2.27: $\log(Em(T_c)/g_*)$ plotted against $\log T_c$ for 1T RS (L.H.S plot) and LMF (R.H.S. plot) fits for Sample B (see Tables 2.9 and 2.10). The squares represent the set of stars that are common to both Samples A & B (see text). The correlation given by equation(2.24) is shown as a solid line.

Montesinos & Jordan (1993) found a best fit with the form

$$\log(Em(T_c)/g_*) = 1.41(\pm 3.33) + 3.50(\pm 0.51)\log T_c \tag{2.24}$$

Figure 2.27 shows $\log(Em(T_c)/g_*)$ derived from Sample B and equation (2.24), for the results using the RS and LMF codes. Although the five stars in common to Samples A and B fit quite well to the previous results, HD 45088 and HD 155886 show some deviation using the RS code. However, the *form* of (2.22) is that expected if the ratio of the conductive flux ($F_c(T_c)$) to the radiative flux ($F_R(T_c)$) is *constant.* If $F_c(T_c)/F_R(T_c)$ is larger than average, then stars will lie to the right of the average trend, and vice-versa. The LMF fits give a marginally better fit to the previous trend.

The 2T fits (RS and LMF codes) do *not* fit the absolute values found for the 1T fits, although a similar trend with T_c can be seen (see Figure 2.28).

Montesinos & Jordan (1993) also found that the coronal energy losses $F_m(T_c) = F_R(T_c) +$

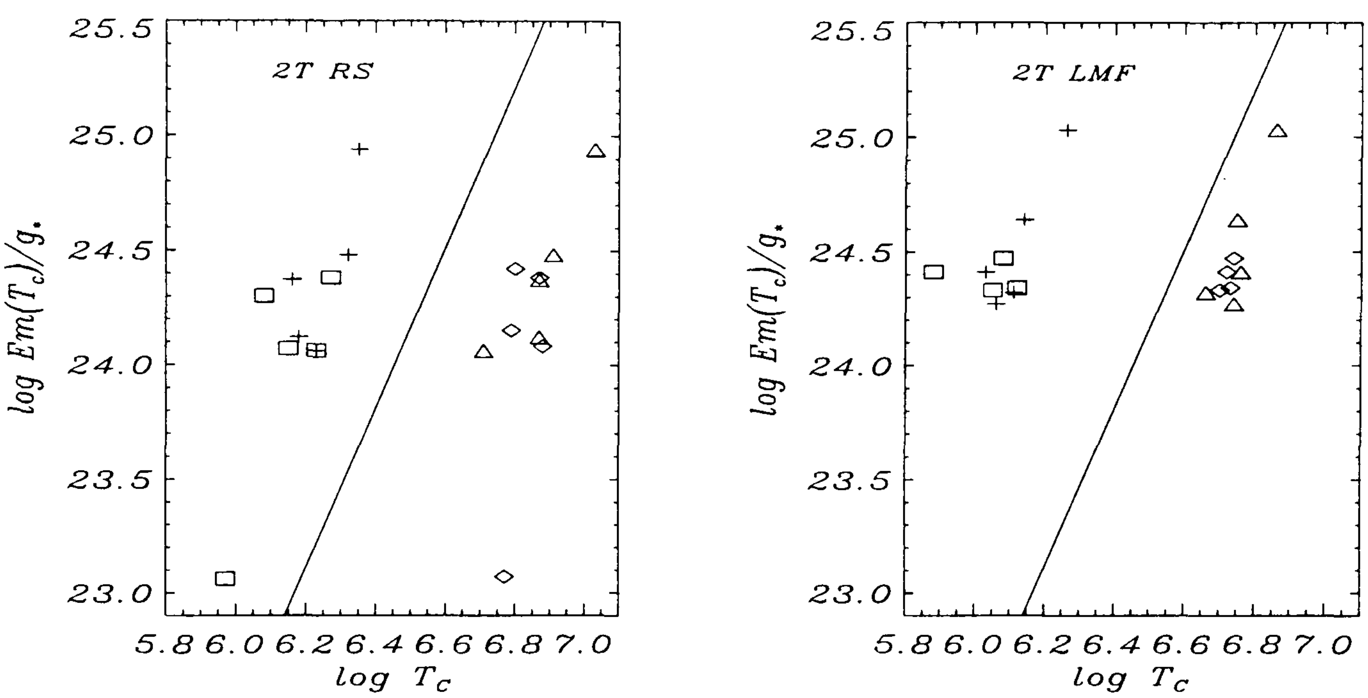

Figure 2.28: $\log(Em(T_c)/g_*)$ plotted against $\log T_c$ for the 2T RS (L.H.S. plot) and LMF (R.H.S. plot) fits for Sample B (see Tables 2.11 and 2.12). The lower temperature components are indicated by crosses and squares, while the higher temperatures components are shown as triangles and diamonds. The squares and diamonds represent the set of stars that are common to both Samples A & B (see text).The correlation given by equation (2.24) is shown as a solid line.

$F_c(T_c)$, scale simply with R_o^{-1}, using

$$F_R(T_c) = 1.04 \times 10^{-19} Em(T_c) T_c^{-1/2} \tag{2.25}$$

and estimating $F_c(T_c)$ through the energy required to balance the radiation losses below T_c, *i.e.*

$$F_c(T_c) = 5.68 \times 10^{-17} (Em(T_c) g_*)^{1/2} T_c. \tag{2.26}$$

Then the form found for $F_m(T_c)$ was

$$\log (F_m(T_c) g_*^{1/4}) = 8.99(\pm 0.09) - 0.99(\pm 0.10) R_o \tag{2.27}$$

(see Montesinos & Jordan (1993) for detailed derivation). Figure 2.29 shows the derived values of $\log (F_m(T_c) g_*^{1/4})$ plotted against R_o, and equation (2.27) (shown as a full line). The minimum energy loss (m.e.l.) solution of Hearn (1975, 1977), is virtually identical, and is shown as a dashed line

$$\log (F_m(T_c) g_*^{1/4}) = 8.97(\pm 0.17) - 0.98(\pm 0.10) R_o \tag{2.28}$$

As Montesinos & Jordan point out, the reason for the close agreement with the m.e.l. solution is that the *total* coronal energy losses $(F_R(T_c) + F_c(T_c))$ tend to be insensitive to the ratio of the fluxes $(F_c(T_c)/F_R(T_c))$.

In conclusion, the values of $Em(T_c)$ and T_c derived from the ROSAT observations, which give new results for five stars in Sample A, and results from five additional stars, support the previous relations found by Montesinos & Jordan (1993).

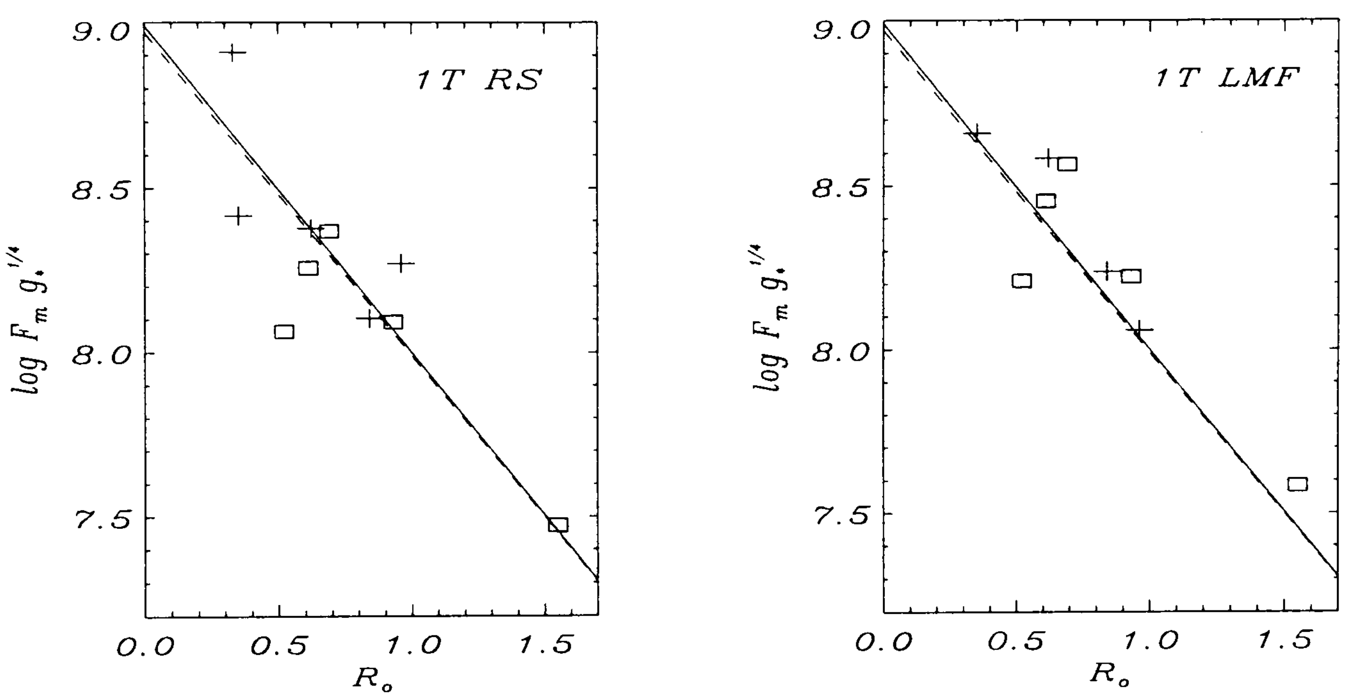

Figure 2.29: $\log(F_m(T_c)g_*^{1/4})$ plotted against R_o for 1T RS (L.H.S plot) and LMF (R.H.S. plot) fits for Sample B (see Tables 2.9 and 2.10). The squares represent the set of stars that are common to both Samples A & B (see text).The correlations given by equations (2.27) and (2.28), are shown as the solid and dashed lines, respectively.

Chapter 3

Emission Measure Modelling of the Five Dwarfs

§3.1 *Introduction*

This chapter presents models of the transition regions and coronae of χ^1 Ori (G0V), ϵ Eri (K2V), ξ Boo A (G8V), α Cen A (G2V) and α Cen B (K0V). The chromospheres and transition regions of these stars have been previously modelled by Jordan *et al.* (1987), using observations made with IUE, with the *Einstein Observatory* and other early instruments, but the new X-ray data discussed in Chapter 2 give improved information on the coronal regions.

The first step in modelling the structure of stellar transition regions and coronae is to determine the emission measure distribution (henceforth referred to as EMD). This quantity ($\int n_e^2\,dr$, more generally $\int n_e n_H\,dr$) is related to the amount of material in the atmosphere at a particular temperature. The parameters derived from the X-ray observations are coronal emission measures and temperatures. The types of fits, one temperature (1T), two temperature (2T) and continuous emission measure (CEM), have been discussed in Section 2.5 of Chapter 2. For each star, an emission measure and temperature has been chosen to best describe the coronal conditions. These are used as boundary conditions in computing the emission measure distribution in the upper transition region (*i.e.* above $\sim 2\times\ 10^5$ K), since apart from ξ Boo A, the EMD is not known from direct observations. In this region, which is below that where energy is deposited by non-thermal processes, the models are derived by assuming a balance between the energy deposited by thermal conduction and

Table 3.1: Observed stellar surface fluxes (in erg cm^{-2} s^{-1}) from Jordan *et al.* (1987).

Ion	**Star**				
	χ^1 *Ori*	ϵ *Eri*	ξ *Boo A*	α *Cen A*	α *Cen B*
Mg II	3.9×10^6	1.9×10^6	3.1×10^6	6.9×10^5	7.6×10^5
Si II	1.2×10^5	7.1×10^4	1.3×10^5	1.8×10^4	2.3×10^4
C II	3.9×10^4	1.4×10^4	4.7×10^4	4.8×10^3	6.6×10^3
Si III]	1.1×10^4	5.6×10^3	7.1×10^3	2.8×10^3	2.2×10^3
Si IV	5.7×10^4	7.2×10^3	3.2×10^4	2.5×10^3	2.1×10^3
C IV	6.6×10^4	2.8×10^4	5.1×10^4	5.4×10^3	5.5×10^3
N V	$\leq 1.4 \times 10^4$	$\leq 4.1 \times 10^3$	$\leq 9.7 \times 10^3$	$\leq 9.5 \times 10^2$	$\leq 7.5 \times 10^2$

lost by radiation. Plane parallel and spherically symmetric geometries are explored.

The EMDs of the transition regions were derived using line fluxes from IUE observations made by Ayres *et al.* (1983) and Jordan *et al.* (1987) (see Table 3.1). An iterative code (discussed in Section 3.3.2) has been written to produce a mean emission measure distribution that reproduces the line fluxes to within an accuracy of 0.1 dex which is better than the uncertainties associated with the atomic data and the extracted line fluxes which are typically 0.2 dex and 0.15 dex respectively).

In Section 3.6 the transition region and coronal emission measure distributions (for both plane parallel and spherically symmetric models) have been joined together to produce models of the outer atmosphere of these stars above the transition region ($\sim 10^4$ K).

Finally, a discussion and summary of the results follow in Sections 3.7 and 3.8.

§3.2 *The Geometry of Transition Regions and Coronae*

Although the volume emission measure ($\int n_e^2\, dV$) indicates the amount of material present in the line of sight over a limited temperature range, the spatial distribution of the material remains unknown. Since it is not possible to observe the supergranulation structure or effects of active regions, the volume emission measure is used to find the *apparent* emission measure over height by dividing by the stellar surface area. Two simple geometries are considered:

i. A *spherically symmetric* geometry allowing for the radial extent of the atmosphere. In this case, the fraction of the photons emitted that are not intercepted by the star is given by

$$G(r) = \frac{1}{2}\left(1 + \sqrt{1 - \frac{1}{f(r)}}\right) \tag{3.1}$$

where the radial term $f(r)$ is given by

$$f(r) = \left(\frac{r}{R_*}\right)^2 \tag{3.2}$$

ii. In high gravity stars such as the five dwarfs where the stellar radius exceeds the coronal isothermal scale-height, *plane parallel* geometry should be a good approximation, and in this case $f(r) = 1.0$ and $G(r) = 0.5$.

Thus, in general

$$Em(r)_{app} = \frac{Em(V)}{4\pi R_*^2} = \int n_e n_H f(r) G(r)\, dr \tag{3.3}$$

In view of the known structure of the solar atmosphere, both the above geometries are approximations and this will be discussed in Section 3.6.

§3.3 *The Transition Region Emission Measure Distribution*

The methods of analysing UV emission lines are well established and derive from the early work of Pottasch (1963). More recent accounts can be found in Jordan & Wilson (1971) and Jordan & Brown (1981).

The flux that is observed at the Earth ($F_\oplus$) is converted to its corresponding value at the stellar surface (F_*) by the following relation:

$$F_* = F_\oplus(\frac{d}{R_*})^2 \tag{3.4}$$

where d is the Earth-star distance and R_* is the stellar radius, both in units of centimetres. The stellar surface flux F_{*ij}, in an effectively optically thin, collisionally excited line for a two-level atom (transition $i \rightarrow j$), and adopting plane parallel geometry, is given by

$$F_{*ij} = \frac{1}{2}\frac{hc}{\lambda}\int n_j A_{ji}\, dr \tag{3.5}$$

where the factor $\frac{1}{2}$ allows for the downward emitted photons which are not observed, and A_{ji} is the spontaneous radiative decay coefficient. (In practice, more than two levels are treated, as appropriate to the ion). Statistical equilibrium is described by the following equation

$$n_j(C_{ji}n_e + A_{ji}) = n_i(C_{ij}n_e) \tag{3.6}$$

where n_j and n_i are the level populations of the upper and lower levels (j and i, respectively), C_{ji} and C_{ij} are the collisional excitation rate coefficients for the transitions $j \rightarrow i$ and $i \rightarrow j$ respectively, and n_e is the electron density. The *coronal approximation* $C_{ji}n_e \ll A_{ji}$ can be used for permitted electric dipole transitions in ions which have no low lying *metastable levels* and hence equation (3.6) is writen as

$$n_j A_{ji} = n_i C_{ij} n_e. \tag{3.7}$$

Using the *coronal approximation*, equation (3.5) can be rewritten as:

$$F_{*ij} = \frac{1}{2}\frac{hc}{\lambda}\int n_i C_{ij} n_e dr. \tag{3.8}$$

In order to compute the flux, equation (3.8) must be expressed in terms of other parameters which are known or can be calculated, *i.e.*:

$$F_{*ij} = \frac{1}{2}\frac{hc}{\lambda}\int \frac{n_i}{n_{ion}}\frac{n_{ion}}{n_E}\frac{n_E}{n_H} n_H C_{ij} n_e dr \tag{3.9}$$

where n_e/n_H is the elemental abundance relative to hydrogen assumed here to be constant. n_i/n_{ion} is the relative population of the lower level and n_{ion}/n_e is the relative ion abundance which was discussed in detail in Section 2.4.5 of Chapter 2. The elemental abundances have been taken from the solar photospheric values of Anders & Grevesse (1989) and Grevesse *et al.* (1992), which are the most up-to-date values available (see Section 2.4.3 of Chapter 2).

The collisional excitation rate coefficient C_{ij} can be written in terms of the mean collision strength Ω_{ij} (Seaton, 1964)

$$C_{ij} = 8.6 \times 10^{-6} \frac{\Omega_{ij}}{\omega_i} T_e^{-1/2} exp(-W_{ij}/kT_e) \quad cm^3 s^{-1} \tag{3.10}$$

where ω_i is the statistical weight of level i, and W_{ij} is the excitation energy of the transition. The main temperature dependent term can be written as

$$g(T_e) = \frac{n_{ion}}{n_E} T_e^{-1/2} exp(-W_{ij}/kT_e) \tag{3.11}$$

where W_{ij} is the line excitation energy.

From equations (3.9) to (3.11) one can write:

$$F_{*ij} = 8.6 \times 10^{-6} \frac{1}{2} \frac{hc}{\lambda} \frac{\Omega_{ij}}{\omega_i} \frac{n_E}{n_H} \int \frac{n_i}{n_{ion}} n_e n_H g(T_e)\, dr. \tag{3.12}$$

For the lines considered here, the collision strength does not vary significantly over the region of line formation. Table 3.2 gives the atomic data adopted from a variety of sources in the literature. In the transition region each line is formed over a restricted temperature range. In the simplest approximation, Pottasch (1963) assumed that $g(T_e)$ could be replaced by $0.70 g(T_e)_{max}$ and removed from the integral. The emission measure over height is then defined as

$$Em(0.3) = \int_{\Delta R} n_e n_H \, dr \tag{3.13}$$

but the temperature range corresponding to ΔR is not well defined. Since the contribution functions of the various emission lines have different shapes, it is better to replace $g(T_e)$ by a mean value $\overline{g}(T_e)$ over a fixed temperature range $\Delta \log T_e = 0.3$ dex centered at $T_{max} \pm 0.15$ dex, where T_{max} is the temperature of the peak of the contribution function. The mean value is found by replacing the actual function by a step function. The percentage of the emission found within $\Delta \log T_e = \pm 0.15$ dex, compared with the total, integrated over a wider range of temperature leads to a combined normalisation constant G (Jordan & Wilson, 1971). Then

$$\int_{\Delta R} g(T_e)\, d\log T = G.g(T_e)_{max}. \tag{3.14}$$

A mean value for the emission measure distribution can then be found by replacing $g(T_e)$ by $G.g(T_e)_{max}$ and removing it from the integral in equation (3.12). Other more formal inversion techniques were considered, as discussed in Section 3.3.1.

$n_e n_H$ can be expressed as

$$n_e n_H = x n_e^2 \tag{3.15}$$

where $x = n_H/n_e$. Above $\log T_e \sim 4.3$, x varies slowly, because hydrogen is predominantly ionised (the exact values adopted in this work will be discussed in Section 3.4). Although the emission measure is often defined in terms of n_e^2, since below $\sim 2 \times 10^4$ K x increases significantly, it is defined here in terms of $n_e n_H$. In ions without *low lying* metastable levels, $n_i/n_{ion} \simeq 1$, where n_i is now the population density of the ground term where the J states are assumed to have a Boltzmann distribution.

As seen from equation (3.12), the flux emitted in a particular line depends on both $g(T)$ and $n_e n_H$, and to find the emission measure involves an inversion.

3.3.1 Integral Inversion Techniques:

Integral inversion techniques have widely been used to compute differential emission measure (DEM) distributions. The flux emitted by a line as given by equation (3.12), can be re-expressed as

$$F = constant \int g(T_e)\phi(T_e)dT_e \tag{3.16}$$

Table 3.2: Atomic parameters for the observed lines.

Ion	$\lambda\,(\AA)$	$\Omega_{multiplet}$	$\frac{n_e}{n_H}$ †	log $T^{\spadesuit}_{gmax}$ (K)	$\frac{n_i}{n_{ion}}$ ◇
Mg II‡	2800	16.2^a	3.8×10^{-5}	3.8	1.0
Si II‡	1817	$15.4^{b,c}$	3.6×10^{-5}	4.3	1.0
C II‡	1335	6.3^b	3.6×10^{-4}	4.6	1.0
Si III]	1892	2.8^d	3.6×10^{-5}	4.7	*
Si IV‡	1400	$18.2^{e,f}$	3.6×10^{-5}	4.8	1.0
C IV‡	1500	9.8^g	3.6×10^{-4}	5.0	1.0
N V‡	1240	7.4^g	8.9×10^{-5}	5.3	1.0

† - Solar photospheric abundances from Anders & Grevesse (1989) and Grevesse *et al.* (1992).
‡ - Parameters refer to the whole multiplet.
* - The level populations of Dufton *et al.* (1983) have been adopted (see Section 3.3.3).
♠ - Temperature where the contribution function $g(T_e)$ has its maximum value.
◇ - n_i/n_{ion} applies to the ground term.
a - Mendoza (1981).
b - Lennon *et al.* (1985).
c - Dufton & Kingston (1991).
d - Dufton *et al.* (1983).
e - Keenan *et al.* (1988).
f - Dufton & Kingston (1987).
g - Cochrane & McWhirter (1983).

where $\phi(T_e) = n_e n_H \, dr/dT_e$ is the differential emission measure, and $g(T_e)$ is the contribution function as given by equation (3.11) and dT_e/dr is the temperature gradient (see equation (3.37)). Since $n_e = P_e/kT_e$ and $n_H = P_H/kT_e$ we can write

$$\phi'(T_e) = \frac{P_e P_H}{k^2 T_e^2} \frac{dr}{dT_e} \tag{3.17}$$

For each of s emission lines, we define kernels

$$K_{s,i} = constant \int_{T_e} g(T_e) dT_e \tag{3.18}$$

where i is the number of temperature intervals in the range of formation of the line; hence, the flux for line s is given by

$$I_s = \sum_i K_{s,i} f_i \tag{3.19}$$

where $f_i = \phi'(T_e)$.

The Maximum Entropy Method:

This method was initially developed for restoring noisy, degraded images of randomly pulsed objects (Frieden, 1972), and its use has since been extended to deal with a wide range of estimation problems. There are plans to use it for computing differential emission measure distributions from data to be obtained from the *Solar and Heliospheric Observatory* (SOHO). The basic assumption is that for any positive, discrete distribution f_i (such as the one defined above), consisting of M measurements (*i.e.* $i = 1, \ldots, M$), and which is normalised to unity, one can assign an entropy parameter E, defined as

$$E = -\sum_{j=1}^{M} f_i \ln f_i. \tag{3.20}$$

This is directly proportional to the amount of information present in the distribution. The aim of this technique is to find the most probable solution which according to Frieden (1972), is achieved by maximising the above equation so that $\mathrm{d}E/\mathrm{d}f_i = 0$.

Assuming that the data I_s have Gaussian errors with standard deviations σ_s, the χ^2 distribution is given by

$$\chi^2 = \frac{(I_s - I_{obs})}{\sigma_s^2} = M - N \tag{3.21}$$

where I_{obs} is the observed flux, and N is the number of degrees of freedom associated with the distribution. Lagrange's method of undetermined multipliers is used to constrain χ^2 to equal $M - N$. Thus,

$$S = \sum_{i=1}^{M} f_i \ln f_i + \frac{\lambda}{2} \sum_i \frac{(I_i - \sum_j w_j)^2}{\sigma_i^2} \tag{3.22}$$

where for measurement j ($j < i$), $w_j = ef_j$ and λ is the Lagrange multiplier whose value is always positive and is increased at each iteration so that χ^2 equals the number of observations. Maximising the above expression yields

$$\ln f_i = \ln w_i - 1 - 2\lambda \sum_s \frac{(I_s - I_{obs})K_{s,i}}{\sigma_s^2} \tag{3.23}$$

In order to test this method, I wrote an ME code and used a first hand-drawn approximation to the EMD)(see Section 3.3.2)in the temperature range $3.8 < \log T_e < 5.3$. The fluxes computed at each temperature interval over the range of formation of each line were summed to yield the *total* computed flux I_{obs}, which was then used in equation (3.12) in order to recompute the EMD.

There is a disadvantage associated with this approach, which is that in order to achieve ME the differences between the computed and observed fluxes $(I_s - I_{obs})$ for each line s, are summed to give a *total* flux difference. It is evident from equation (3.22) that in order to obtain a new EMD which approaches ME, this same flux difference is subtracted from every temperature interval of the distribution that was computed in the previous iteration. Hence, the distribution is treated as a whole and is shifted up or down by this factor until convergence is achieved. This usually occurs after ~ 110 iterations. As a result, the *shape* of the distribution remains identical to the initial *best fit*.

The summation of the flux differences has the effect of masking the real uncertainties associated with the emission line atomic data. Therefore, I have concluded that a ME solution is not a useful one as it solves the problem in a rigid mathematical way and adds little to the empirical initial *best fit*. The approach adopted in order to recompute the line fluxes is described in the section below.

3.3.2 Recomputing the Line Fluxes:

The contribution function $g(T_e)$ was computed for each line over its temperature of formation from equation (3.11), using the ion balance calculations of Arnaud and Rothenflug (1985). The ions formed at the lowest temperatures are Mg II and Si II. The calculations of Arnaud and Rothenflug (1985) do not give ion fractions for these ions below log T_e = 4.0. Detailed calculations by Judge (1986a,b) have shown that down to $T_e \sim 6300$ K these elements are predominantly in their first stage of ionisation because photoionisation plays an important role in determining n_i/n_e. Since I do not model the chromosphere below 10^4 K, I simply assume that below this temperature $n_i/n_e = 1$, for Mg II and Si II.

Assuming that *all* the flux is formed at each temperature *in turn*, an emission measure locus can be computed for each line so as to set upper limits to the emission measure distribution over the temperature range considered.

An initial *best fit* to the mean EMD was approximated by drawing a smooth curve (by hand) touching the locus of each spectral line once. The calculations were carried out for the temperature range log T_e = 3.8 - 5.3, in intervals of 0.1 dex. However, this curve does not necessarily reproduce the observed fluxes and an iterative recomputation of the EMD has to be done in order to reproduce all the fluxes to within reasonable accuracy. This recomputation is important especially at temperatures below 2×10^4 K because of the rapid increase of $\int n_e n_H \, dr$.

The flux from each temperature interval over the range of line formation was then computed from equation (3.12) and the individual contributions at each interval were summed to give the total flux emitted by the line, F_{comp}. Since from equation (3.12) it is evident that the observed flux F_{obs} is proportional to the emission measure, it follows that by calculating the difference between F_{obs} and F_{comp} at each temperature interval, a factor F_{obs} - F_{comp} can be added to its corresponding emission measure value at each temperature interval until the observed flux for each line is reproduced to within ± 0.1 dex. The process is started at 10^5 K, where C IV defines the emission measure. In the case where more than one line is formed in the same temperature interval (this usually occurs for a maximum of two lines), the values of the emission measures at the temperatures where the overlap occurs are varied such that the observed flux for each of the lines is reproduced to within the above accuracy. Although strictly speaking there is not a unique solution, the EMD is well defined above $\sim 2\times 10^4$ K.

The resulting EMDs for the five stars calculated using the assumption of plane parallel geometry are shown in relation to their emission line loci in Figures 3.1 - 3.5.

3.3.3 The Electron Pressure in the Transition Region

The electron pressure P_e can be determined by comparing the emission measure from the density sensitive Si III] intersystem line at 1892.0 Å, with that determined from the permitted C II and Si IV transitions. The emission measure loci shown in Figures 3.1 - 3.5, were calculated individually at pressures $\log P_e = 14.0$, 15.0, 16.00 and 16.5 (P_e in cm^{-3} K), using the following flux-emission measure relation,

$$F_{ij} = \frac{1}{2}\frac{hc}{\lambda}\frac{n_e}{n_H}\int \frac{n_i}{n_{ion}}\frac{A_{ji}}{n_e}\frac{n_{ion}}{n_e} n_e n_H \, dr \tag{3.24}$$

where the radiative decay rate $A_{ji} = 1.46 \times 10^4$ s^{-1}, as calculated by Dufton *et al.* (1983).

Having determined the emission measure distribution that reproduces the observed fluxes for all the other lines to ± 0.1 dex, equation (3.24) was iterated for Si III] using the level populations of Dufton *et al.* (1983) at constant pressure until the Si III] flux was reproduced to the same accuracy. The electron pressures in this way are given in Table 3.3. For χ^1 Ori, ϵ Eri and ξ Boo A, the uncertainties associated with the derived electron pressures are to within 0.3 dex, and these are directly related to the uncertainties of the Si III] fluxes given in Ayres *et al.* (1983). However, the uncertainties for α Cen A and α Cen B are to within

Table 3.3: Electron pressures derived from Si III].

Star	a	b
$\chi^1\,Ori$	15.7	15.7 – 16.3
$\epsilon\,Eri$	15.2	15.7 – 16.2
$\xi\,Boo\,A$	16.0	16.2 – 16.7
$\alpha\,Cen\,A$	14.1	$\leq$ 14.7 – 15.7
$\alpha\,Cen\,B$	14.9	14.7 – 15.7

a - $\log(P_e/k)$ (in units cm^{-3} K) computed as described in this section.
b - Range of $\log(P_e/k)$ (in units cm^{-3} K) from Si III] flux and local emission measure as found by Jordan *et al.* (1987).

0.9 dex which is due to the fact that they are in the low density limit.

Jordan *et al.* (1987) deduced a more approximate range of acceptable electron pressures from the flux and the local emission measure by determining the point where the C II and Si III loci match. Their results are also listed in Table 3.3. The iterative method with the updated abundances and atomic data should give improved results.

The compatibility of the electron pressures derived from the Si III] lines with those found from X-ray data, will be discussed in Section 3.7.

§3.4 *The Variation of the Pressure with Temperature*

The models of the upper transition region and corona, and modelling from the emission measure distribution in the lower transition region, require expressions for the total pressure (including waves), the gas pressure and the electron pressure. The formulation is given in spherical geometry, since the plane parallel version is easy to recover.

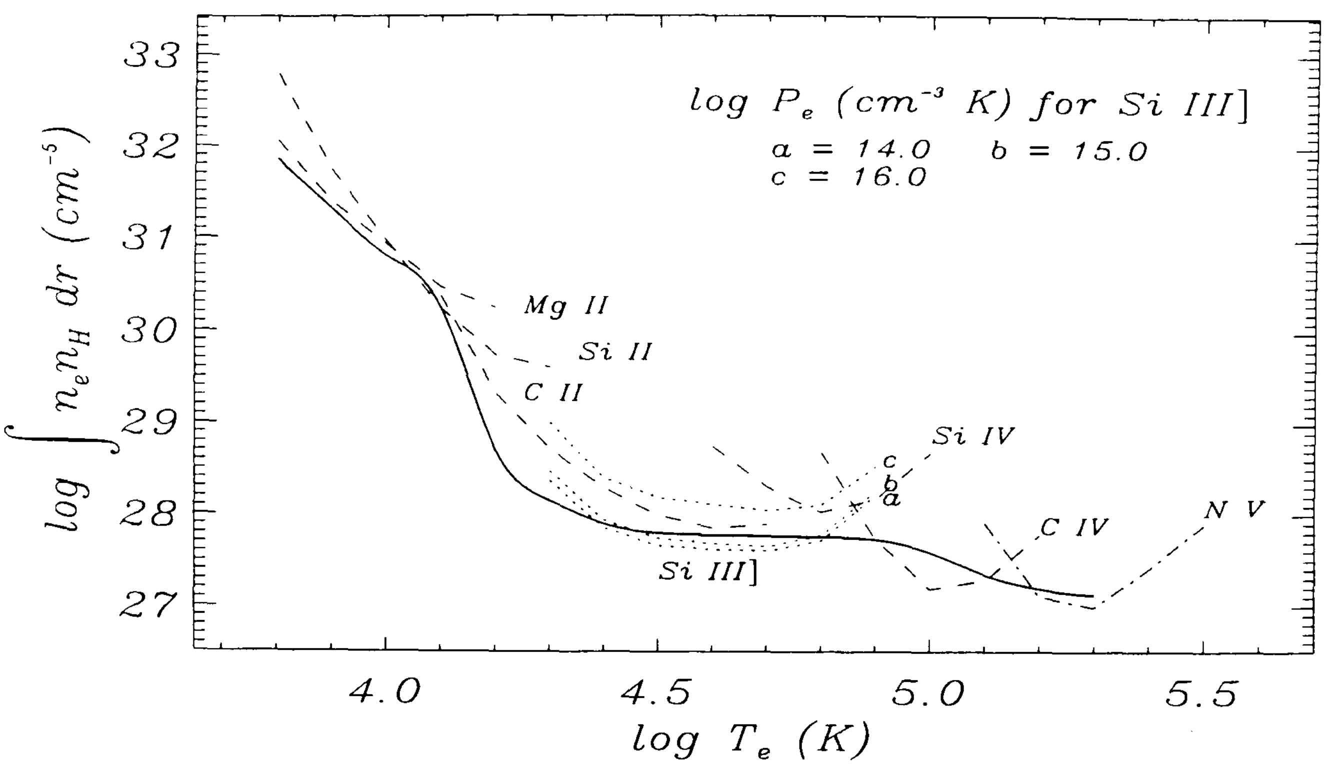

Figure 3.1: The recomputed EMD for χ^1 Ori in relation to the loci (dashed lines) of the observed line fluxes; the dotted lines represent the Si III] loci at the stated pressures, while the N V locus (dot-dash line) indicates an upper limit. Plane parallel geometry has been assumed.

3.4.1 The Gas Pressure and Electron Pressure

The gas pressure P_g is the sum of the following pressures

$$P_g = P_e + P_H + P_{He} + P_{metals} \tag{3.25}$$

Taking $x = P_H/P_e$, the above expression can be written as

$$P_g = P_e(1 + x(1 + y + z)) \tag{3.26}$$

where y and z are the abundances of He and the metals respectively; substituting the values given by Anders & Grevesse (1989) and Grevesse *et al.* (1993), where $n_{He}/n_H = 0.1$ and $n_{metals}/n_H \ll 0.1$, P_g can be expressed in terms of P_e, as follows (Harper, 1992)

$$P_g = P_e(1 + 1.1x). \tag{3.27}$$

A further useful expression is

$$P_e P_H = \frac{x}{(1 + 1.1x)^2} P_g^2 \tag{3.28}$$

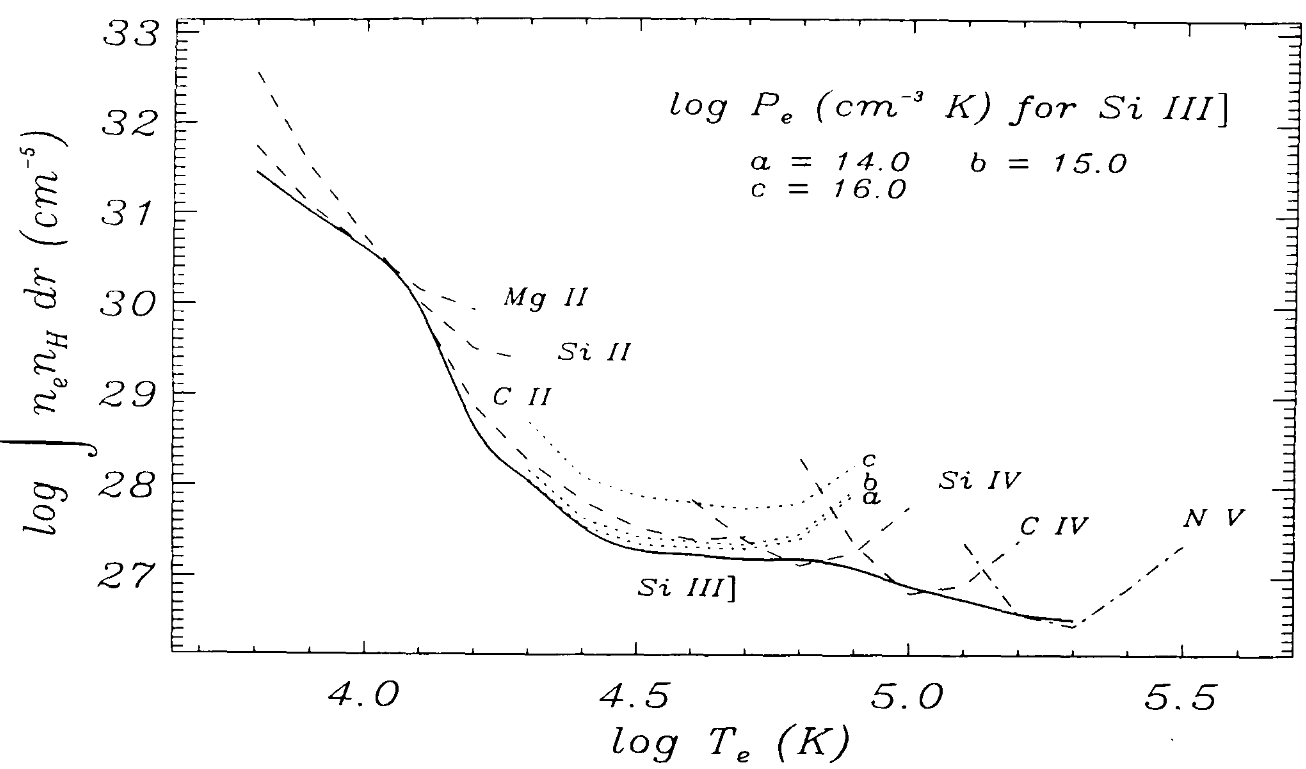

Figure 3.2: The recomputed EMD for ϵ Eri in relation to the loci (dashed lines) of the observed line fluxes; the dotted lines represent the Si III] loci at the stated pressures, while the N V locus (dot-dash line) indicates an upper limit. Plane parallel geometry has been assumed.

where the values for x are presented in Table 3.4, as computed by A. D. McMurry (private communication), using radiative transfer calculations from the MULTI code. The mean molecular weight μ is defined as

$$\mu = \frac{m_e n_e + m_H n_H + m_{He} n_{He} + \ldots}{n_e + n_H + n_{He} + \ldots} \tag{3.29}$$

and can then be expressed as

$$\mu = \frac{1.4x}{(1 + 1.1x)} \tag{3.30}$$

Assuming hydrostatic equilibrium, and allowing for the radial extent

$$\frac{dP_g}{dr} = -\rho g_* (\frac{R_*}{r})^2 \tag{3.31}$$

where g_* is the stellar surface gravity and $\rho = \mu m_H P_g / kT_e$. This can be expressed as

$$\frac{dP_g}{dT_e} = -\mu m_H g_* \frac{P_g}{kT_e} \frac{dr}{dT_e} \frac{1}{f(r)}. \tag{3.32}$$

The temperature gradient can be found from the emission measure, as follows:

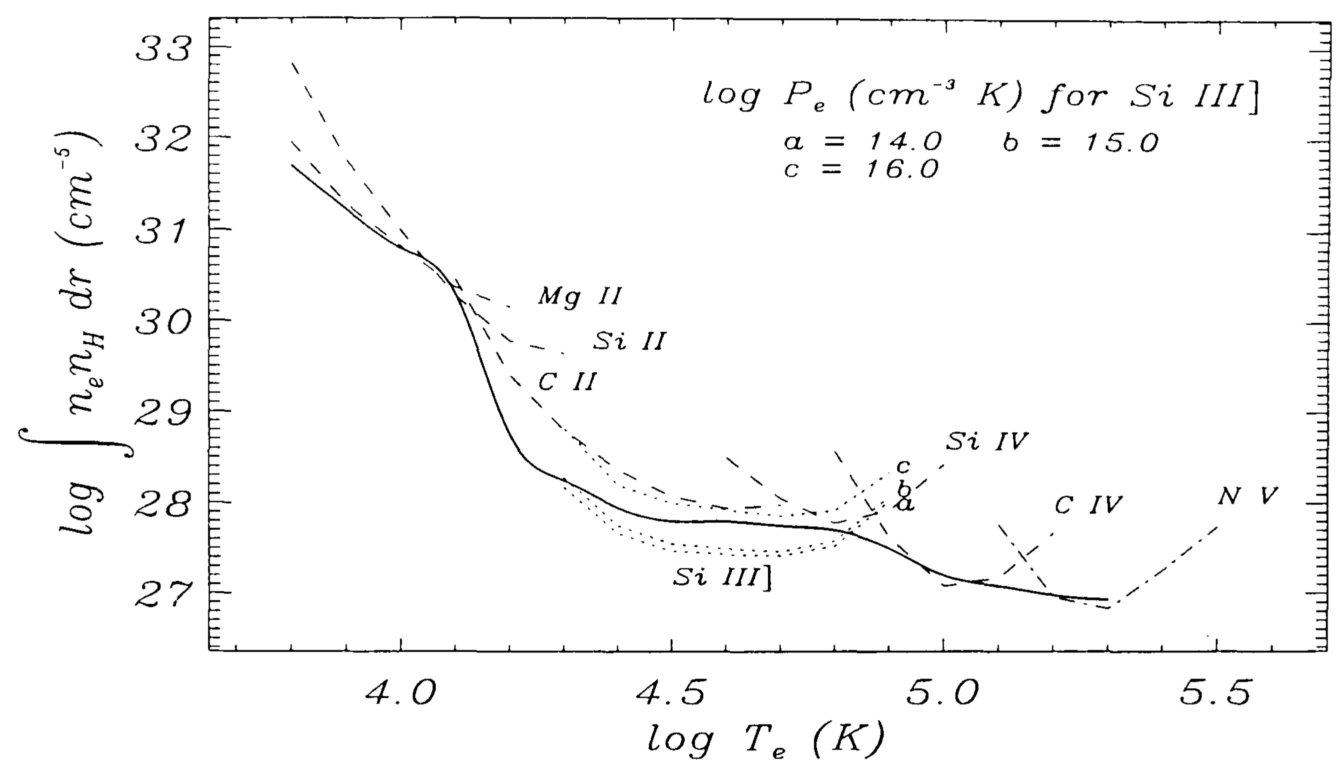

Figure 3.3: The recomputed EMD for ξ Boo A in relation to the loci (dashed lines) of the observed line fluxes; the dotted lines represent the Si III] loci at the stated pressures, while the N V locus (dot-dash line) indicates an upper limit. Plane parallel geometry has been assumed.

Table 3.4: Values for $x = n_H/n_e$ as computed by A. D. McMurry (private communication) for ξ Boo A using the radiative transfer code MULTI. These values were used for all the calculations presented in this chapter, since the stellar gravities are similar.

log $\mathbf{T_e}$ (K)	x	log T_e (K)	x
3.80	39.700	4.50	0.836
3.90	5.929	4.60	0.834
4.00	1.826	4.70	0.834
4.10	1.211	4.80	0.834
4.20	1.044	4.90	0.834
4.30	0.956	5.00	0.834
4.40	0.905	$\geq$ 5.10	0.833

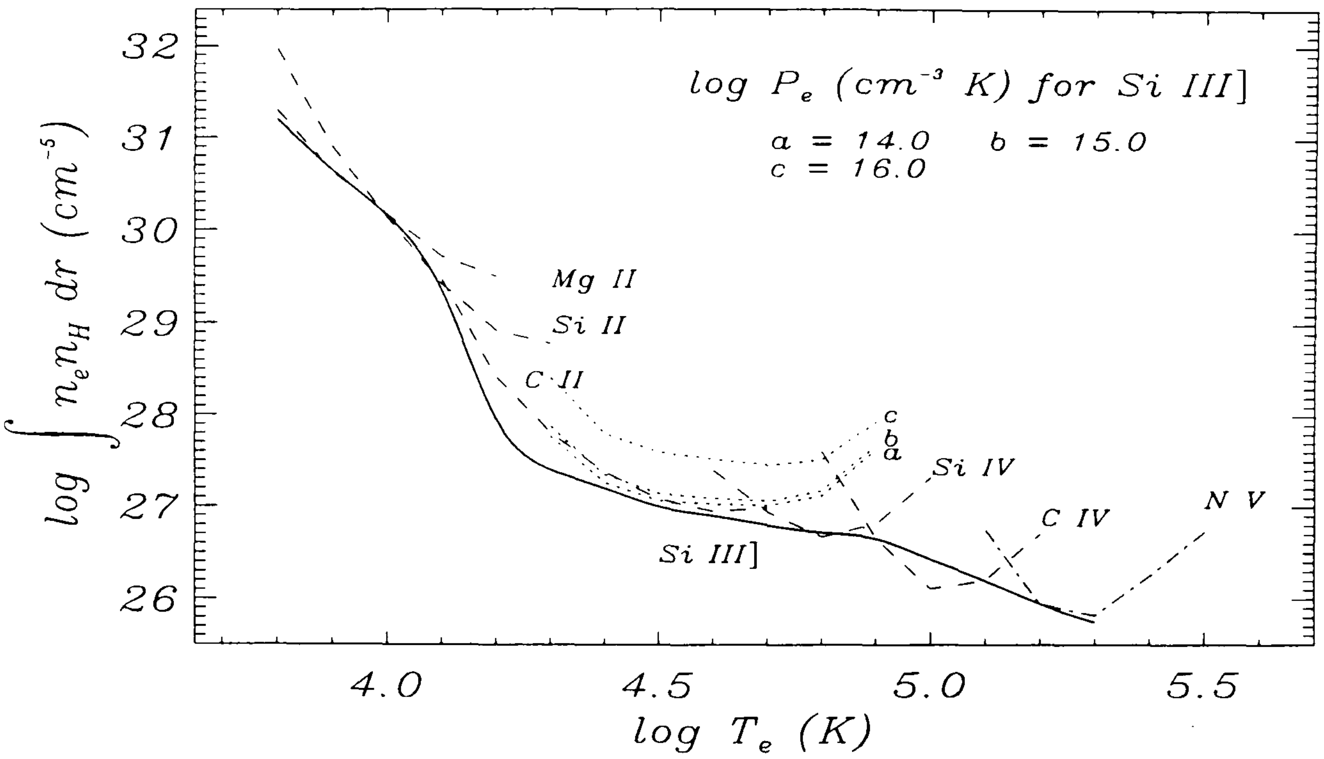

Figure 3.4: The recomputed EMD for α Cen A in relation to the loci (dashed lines) of the observed line fluxes; the dotted lines represent the Si III] loci at the stated pressures, while the N V locus (dot-dash line) indicates an upper limit. Plane parallel geometry has been assumed.

X-ray volume emission measures are usually defined through

$$F_{\oplus} = \frac{\int n_e n_H \mathbf{\Lambda}_{rad}(T_e)\, dV}{4\pi d^2} \tag{3.33}$$

where $F_{\oplus}$ is the flux at the Earth, corrected for any interstellar absorption.

The volume emission measure $\int n_e n_H \, dV$ is thus found assuming that *all* the photons escape from the emitting plasma. Following the method used by Pan & Jordan (1995) the *apparent* emission measure over the radial extent is defined by equation (3.3), since this is the quantity derived without knowing the geometry. The actual (*real*) emission measure is then

$$Em(r)_{real} = \frac{Em(r)_{app}}{f(r)G(r)} \tag{3.34}$$

The apparent emission measure over the region where $\Delta\, T_e$ is defined by $\Delta \log\, T_e = 0.3$ dex is

$$Em(0.3) = \int_{\Delta T_e} \frac{P_e P_H}{k^2 T_e^2} \frac{dr}{dT_e} f(r) G(r)\, dT_e. \tag{3.35}$$

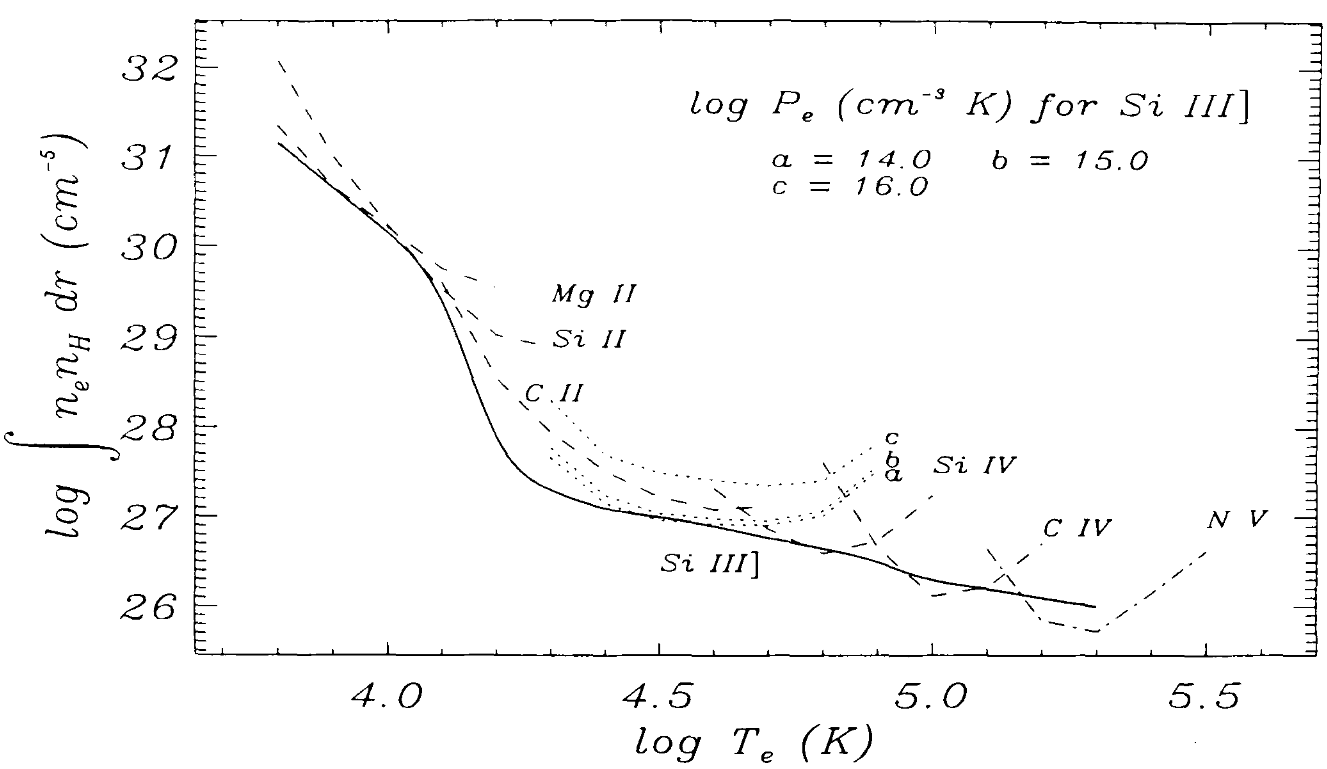

Figure 3.5: The recomputed EMD for α Cen B in relation to the loci (dashed lines) of the observed line fluxes; the dotted lines represent the Si III] loci at the stated pressures, while the N V locus (dot-dash line) indicates an upper limit. Plane parallel geometry has been assumed.

Assuming *initially* that dT_e/dr, P_eP_H, $f(r)$ and $G(r)$ are constant over the region of line formation, this can be written as

$$Em(0.3) = \frac{1}{k^2}\frac{P_eP_H}{\sqrt{2}\,T_e}\frac{dr}{dT_e}f(r)G(r). \tag{3.36}$$

The local temperature gradient above $T_e = 2.0 \times 10^4$ K is then given by:

$$\frac{dT_e}{dr} = \frac{1}{\sqrt{2}}\frac{P_eP_H}{k^2T_e}\frac{f(r)G(r)}{Em(0.3)}. \tag{3.37}$$

This can be substituted into equation (3.32) with P_e and P_H expressed in terms of P_g, and the latter can then be integrated to give

$$P_g^2 = P_{g\,top}^{\,2} + 2\sqrt{2}\,1.4\,m_H g_* k \int_{T_e}^{T_c} \frac{Em(0.3)(1+1.1x)}{f(r)^2\,G(r)}\,dT_e \tag{3.38}$$

where $P_{g_{top}}$ refers to the pressure which is at the base of the isothermal corona while T_c is the corresponding temperature. The electron pressure can then be found using equation

Table 3.5: The radial extent ($r - R_*$) of the atmosphere of χ^1 Ori with and without the inclusion of the turbulent pressure P_{turb} in the calculations. The results presented here, are from a model that assumes spherical symmetry and r is defined by equation (3.64).

log T_e (K)	$r_{*} - R_*$† (10^8 km)	$r_{*} - R_*$‡ (10^8 km)	log T_e (K)	$r - R_*$† (10^8 km)	$r - R_*$‡ (10^8 km)
3.80	1.69	1.18	5.40	1.96	1.33
4.00	1.92	1.31	5.60	1.98	1.33
4.20	1.94	1.32	5.80	2.04	1.35
4.40	1.94	1.32	6.00	2.23	1.44
4.60	1.94	1.32	6.20	2.96	1.91
4.80	1.95	1.32	6.40	6.02	4.36
5.00	1.95	1.32	6.60	21.10	18.10
5.20	1.95	1.32	6.74	66.80	63.20

† P_{turb} included in the calculation.
‡ P_{turb} excluded from the calculation.

(3.27). For much of the temperature range one could assume a constant pressure, but it is simple to use the more accurate approximation of *hydrostatic equilibrium* as above.

3.4.2 The Turbulent Pressure

In a similar manner that the motion of electrons exerts pressure in the atmosphere, so do large scale turbulent motions. Following early work on the solar chromopshere (McCrea, 1929), it has been recognised that turbulence provides an additional support term which subsequently reduces the effective gravity. Inclusion of a turbulent pressure in the equation of hydrostatic equilibrium has the effect of increasing the extent of the atmosphere, but reducing the total gas pressure. The effect on the former can be seen in Table 3.5.

Boland *et al.* (1975) and Jordan & Brown (1981) argue that turbulence is due to the passage of Alfvén or fast MHD waves. The wave pressure P_{turb} is defined as

$$P_{turb} = \frac{1}{2}\rho\,\xi^2 \tag{3.39}$$

where ξ^2 is the most probable turbulent velocity squared and is related to the observed

FWHM ($\Delta\lambda$) of the line as given in McWhirter *et al.* (1975), as follows

$$\frac{\Delta\lambda}{\lambda} = 7.1 \times 10^{-7}[\frac{T_e}{M_i} + (\xi^2 \frac{m_p}{2k})] \tag{3.40}$$

where $M_i = M_{ion}/m_H$. The mean-square turbulent velocity $< v_{turb}^2 >$ is defined as

$$< v_{turb}^2 > = \frac{3}{2}\xi^2 \tag{3.41}$$

Table 3.6 gives values for v_{turb} for the five dwarfs which were derived from equation (3.42) using the FWHM of Ayres *et al.* (1983). The turbulent velocities at a chosen temperature T_e, can computed from the relation:

$$< v_{turb}^2 >_e T_{obs}^{\beta} =< v_{turb}^2 >_{obs} T_e^{\beta} \tag{3.42}$$

where it is known from solar observations that on average $\beta = 0.5$ (Jordan *et al.*, 1987). This approximation is used up to log $T_e = 2 \times 10^5$ K. Above this temperature, v_{turb} is taken to be constant, again as indicated by solar observations. Table 3.6 lists the observed values of $< v_{turb}^2 >_{obs}^{1/2}$ as computed from the FWHM of the C IV lines given in Ayres *et al.*, (1983) at $T_e = 10^5$ K. The values adopted at $T_e \geq 2 \times 10^5$ K using equation (3.42), are also listed.

The turbulent velocities are not well determined ($\pm$ 7 km s^{-1}) for the five dwarfs because of the limited resolution of IUE even in the high dispersion mode and the noisy nature of the spectra. Observations with the GHRS on the HST should be able to significantly improve the measurement of the line widths. However in these stars the wave pressure is not a very important factor.

The total pressure P_T is taken as the sum of P_g and the turbulent pressure P_{turb} which is due to non-thermal wave motions of the plasma; thus, P_T is

$$P_T = P_g + P_{turb} \tag{3.43}$$

The equation of hydrostatic equilibrium then becomes

$$\frac{dP_T}{dr} = \frac{dP_g(1 + Y(T_e))}{dr} = -\frac{\mu m_H g_*}{kT_e}\frac{P_g}{f(r)} \tag{3.44}$$

Table 3.6: Observed turbulent velocities $< v^2_{turb} >^{1/2}_{obs}$ (units of km s^{-1}), computed from the FWHM of the C IV lines given in Ayres *et al.*, (1983) at $T_e = 10^5$ K; the turbulent velocities $< v^2_{turb} >^{1/2}_{e}$ at $T_e = 2 \times 10^5$ K are computed from equation (3.42).

	Star				
T$_e$ (K)	χ^1 *Ori*	ϵ *Eri*	ξ *Boo A*	α *Cen A*	α *Cen B*
1×10^5	62.8	37.3	49.8	38.9	32.5
2×10^5	74.6	44.3	59.2	46.2	38.6

where $Y(T_e) = \mu m_H < v^2_{turb} > /2kT_e$. Following the same procedure as before (see equation (3.38)), the expression for the total pressure is

$$P_T^2(T_e) = P_{T\,top}^2 + 2\sqrt{2}\,1.4 m_H g_* k \int_{T_e}^{T_c} \cdot \frac{Em(0.3)(1+Y(T_e))(1+1.1x)}{f(r)^2 G(r)} dT_e. \tag{3.45}$$

3.4.3 The Coronal Pressure

The initial coronal pressure can be found from the coronal emission measure and temperature. The true coronal emission measure can be expressed as

$$Em(T_c) = \int n_e n_H \, dr = \frac{P_e P_H}{k^2 T_c^2} \frac{H}{2} \tag{3.46}$$

where H is the isothermal scale height. Allowing for a *turbulent* pressure, using equation (3.31) applied to an isothermal region leads to

$$H = \frac{kT_c(1+Y(T_e))}{\mu m_H g_*} f(r_c) \tag{3.47}$$

where we assume that $f(r)$ at $r_c + H \gg f(r)$ ar r_c.

Then, from (3.46)

$$P_{T_c}^2 = 2.8\, m_H g_* \frac{(1+1.1x)(1+Y(T_c))}{f(r_c)} Em(T_c) k T_c. \tag{3.48}$$

§3.5 Empirical Models using Energy Balance

Although a non-thermal source of heating is required in the corona and below $T_e \sim 2\times 10^5$ K, in the upper transition region the heating required is small and could be provided either by a small amount of non-thermal energy or simply by thermal conduction from above. In this case, the variation of the conductive flux dF_c, over a height interval dr, is balanced by the change in the radiative flux dF_R in the same height interval, such that

$$\frac{dF_c}{dr} + \frac{dF_R}{dr} = 0. \tag{3.49}$$

3.5.1 The Conductive Flux

The conductive flux through a focal area is defined as

$$F_c = -\kappa T_e^{\frac{5}{2}} \frac{dT_e}{dr} \tag{3.50}$$

where for an ionised plasma, $\kappa \simeq 1.1 \times 10^{-6}$ erg cm^{-1} K$^{-7/2}$ s^{-1} (Spitzer, 1978). Thus, considering the variation of F_c over dr in spherically symmetric geometry,

$$\frac{1}{r^2}\frac{d(r^2 F_c)}{dr} = \frac{1}{r^2}\frac{d}{dr}\left[-\kappa r^2 T_e^{\frac{5}{2}} \frac{dT_e}{dr}\right]. \tag{3.51}$$

Multiplying the above expression by dr/dT_e and substituting for dT_e/dr in F_c, leads to

$$\frac{1}{r^2}\frac{d(r^2 F_c(T_e))}{dT_e} = -\gamma\left[\frac{3}{2} + \frac{2\,d\log\,P_g}{d\log\,T_e} - \frac{d\log\,Em(0.3)}{d\log\,T_e} + 4\frac{d\log\,r}{d\log\,T_e} + \frac{d\log\,G(r)}{d\log\,T_e}\right] \tag{3.52}$$

where

$$\gamma = \frac{\kappa}{\sqrt{2}}\frac{1}{k^2}\frac{x}{(1+1.1x)^2}\frac{P_g^2 T_e^{1/2}}{Em(0.3)} f(r)G(r) \tag{3.53}$$

and $Em(0.3)$ is again the *apparent* emission measure. Above $T_e = 2\times 10^5$ K, x is constant (see Table 3.4). If the second term on the R.H.S of equation (3.52) is negligible, and the radial terms are not important, then when $d\log\,Em(0.3)/d\log\,T_e < 3/2$, it is evident that conduction becomes an energy deposition mechanism.

3.5.2 The Radiative Flux

At a given temperature T_e, the radiation losses over the height interval dr can be computed from the expression

$$F_R(T_e) = \int_{\Delta R} n_e n_H \mathbf{\Lambda}_{rad}(T_e)\, dr \tag{3.54}$$

where $\mathbf{\Lambda}_{rad}$ is the radiative power loss in erg cm^3 s^{-1} (to be discussed below), or over the region $\Delta \log T_e = 0.30$ dex, corresponding to ΔR

$$\Delta F_R(T_e) \simeq Em(0.3)\mathbf{\Lambda}_{rad}(T_e)\frac{1}{f(r)G(r)} \tag{3.55}$$

where $Em(0.3)$ is the apparent emission measure. Hence, the total radiation flux is given by the sum of the contributions over the entire temperature range is given by

$$F_R = \sum_{\Delta R} \Delta F_R. \tag{3.56}$$

$\mathbf{\Lambda}_{rad}$ is only a function of temperature, (since the ion-balance calculations do not allow for the density dependence of di-electronic recombination), so F_R depends on the emission measure distribution and the geometric factors. Jordan (1986) and Jordan *et al.* (1987) found that the shape of the apparent emission measure distribution is very similar in the five main sequence stars they modelled, and that the product $Em(0.3)\mathbf{\Lambda}_{rad}$ is essentially constant over the range log T_e = 4.3 - 5.0. Thus, over this region it appears that the shape of the distribution is determined by the inverse of $\mathbf{\Lambda}_{rad}$, which then constrains the form of the energy deposition.

3.5.3 The Radiative Power Loss

The radiative power loss $\mathbf{\Lambda}_{rad}(T_e)$ is the sum of the power emitted in all lines and continua, and at high temperatures includes the contribution from free-free emission and two-photon decays.

Recent calculations by Cook *et al.* (1989) for $\mathbf{\Lambda}_{rad}(T_e)$ for the temperature range log T_e = 4.0 - 7.0 are given in Table 3.7 and plotted in Figure 3.6. They used the *coronal* abundances

Table 3.7: Comparison of the radiative power loss values Λ_{rad} (in $erg\,cm^3\,s^{-1}$) using (**a**) the coronal abundances of Meyer (1985) from Cook *et al.* (1989), and (**b**) the photospheric abundances of Anders & Grevesse (1989) or Grevesse *et al.* (1992), (new calculations). Column (*c*) gives the values of $\Lambda_{rad} = 1.25 \times 10^{-16}/T_e$ (see equation (3.57)), for temperatures greater than log $T_e \geq 5.3$. The values in brackets correspond to powers of 10.

log T_e (K)	a	b	c
4.0	1.60(−23)	1.48(−23)	−
4.3	1.62(−22)	1.62(−22)	−
4.7	2.43(−22)	3.53(−22)	−
5.0	3.88(−22)	7.08(−22)	−
5.3	3.26(−22)	8.53(−22)	6.26(−22)
5.7	2.90(−22)	3.20(−22)	2.49(−22)
6.0	2.77(−22)	2.41(−22)	1.25(−22)
6.3	6.73(−23)	6.43(−23)	6.26(−23)
6.7	1.58(−23)	1.73(−23)	2.49(−23)
7.0	1.94(−23)	1.84(−23)	1.25(−23)

of Meyer (1985). To be consistent, I have recalculated the values of $\Lambda_{rad}(T_e)$ by using the photospheric abundances of Anders & Grevesse (1989) and Grevesse *et al.* (1992). The abundances are given in Table 3.8. (Note that the values of Λ_{rad} given in Cook *et al.* (1989) are in intervals of 0.3 dex; in my calculations I used interpolated values between the given points).

In the temperature range log T_e = 3.8 - 4.0, the values of Λ_{rad} are rough approximations. On the basis of more detailed calculations (Hartmann & MacGregor, 1980), Λ_{rad} extends as a straight line below log T_e = 4.0. At log T_e = 3.8, $\Lambda_{rad}(T_e) = 10^{-25}$ erg cm^3 s^{-1}.

For temperatures greater than log T_e = 5.3, Λ_{rad} can be approximated by

$$\Lambda_{rad}(T_e) = \alpha T_e^{-\delta} \tag{3.57}$$

where for $\delta = 1.0$, $\alpha = 1.25\times10^{-16}$ erg cm^3 s^{-1} K. In the case where $\delta = 0.5$, $\alpha = 2.8\times10^{-19}$ erg cm^3 s^{-1} K$^{1/2}$. I have used $\delta = 1.0$ in all calculations.

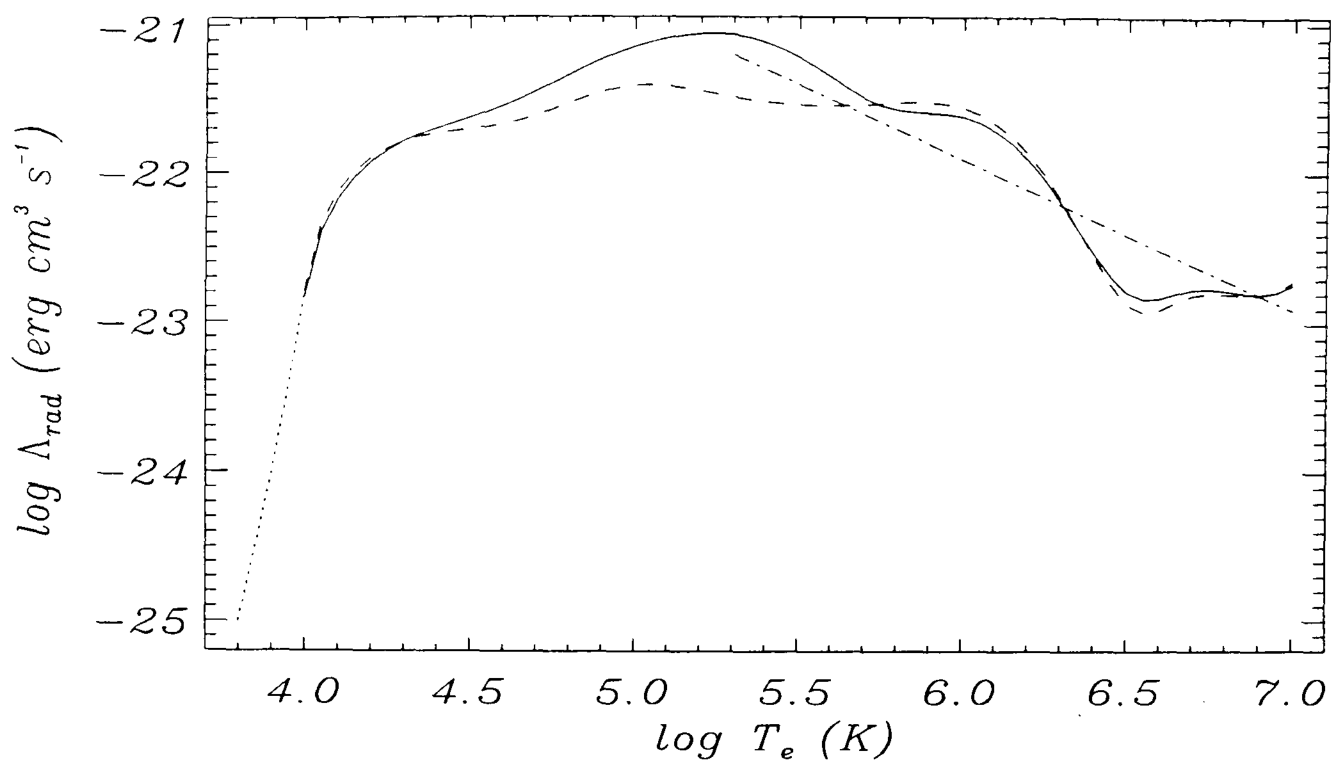

Figure 3.6: The dotted line represents the interpolated values of $\Lambda_{rad}(T_e)$ (see text), while the dashed curve is the radiative power loss from Cook *et al.* (1989). The solid curve represents the values of $\Lambda_{rad}(T_e)$ calculated by adopting the abundances from Anders & Grevesse (1989) or Grevesse *et al.* (1992). The dash-dot line indicates Λ_{rad} from equation (3.57).

Table 3.8: The coronal abundances n_e/n_H of (**a**) Meyer (1985) compared with the photospheric abundances of (**b**) Anders & Grevesse (1989) and Grevesse *et al.* (1992).

Element	**a**	**b**
H	1.00(+0)	1.00(+0)
He	9.80(−2)	9.77(−2)
C	2.35(−4)	**3.55(−4)**
N	3.92(−5)	**8.91(−5)**
O	2.47(−4)	**7.41(−4)**
Ne	3.53(−5)	1.23(−4)
Mg	3.73(−5)	3.80(−5)
Si	3.92(−5)	3.55(−5)
S	8.63(−6)	1.62(−5)
Ca	2.94(−6)	2.29(−6)
Fe	3.92(−5)	**3.23(−5)**
Ni	2.16(−6)	1.78(−6)

3.5.4 Energy Balance

Setting

$$\frac{dF_c}{dT_e} = -\frac{dF_R}{dT_e} \tag{3.58}$$

where

$$\frac{dF_R}{dT_e} = n_e n_H \Lambda_{rad}(T_e)\frac{dr}{dT_e} \tag{3.59}$$

and using equation (3.37) for dr/dT_e, $n_e n_H$ cancels. Using equation (3.52) and re-arranging, the following expression for $d\log\, Em/d\log\, T_e$ can be derived

$$\frac{d\log\, Em(0.3)}{d\log\, T_e} = \frac{2d\log\, P_e}{d\log\, T_e} + \frac{3}{2} + \frac{4d\log\, r}{d\log\, T_e} + \frac{d\log\, G(r)}{d\log\, T_e} - \beta \tag{3.60}$$

where

$$\beta = \frac{2}{\kappa}\frac{(1+1.1x)^2}{x}\frac{Em(0.3)^2 k^2}{P_g^2 T_e^{3/2}}\frac{\Lambda_{rad}}{G(r)^2 f(r)^2}. \tag{3.61}$$

By choosing a starting value of the coronal emission measure at T_c, the value of the coronal pressure can then be calculated from equation (3.48). The emission measure distribution can be iteratively computed from T_c down to $\log\, T_e = 5.3$, by subtracting the computed value of $d\log\, Em(0.3)$ at each temperature interval from the previous value of $Em(0.3)$, provided $d\log\, P_g$ is known. This can be found from equation (3.44) since

$$\frac{dP_g(1+Y(T_e))}{dT_e} = -\sqrt{2}\mu m_H g_* k\frac{Em(0.3)}{P_g G(r) f(r)^2}\frac{(1+1.1x)^2}{x} \tag{3.62}$$

and hence dP_g can be computed. Expressing the above equation in terms of logarithms and rearranging, we obtain the required expression for the logarithmic increment of the gas pressure:

$$\frac{d\log\, P_g}{d\log\, T_e} = -\frac{1.98\, m_H g_*}{k}\frac{Em(0.3)}{P_g^2 G(r) f(r)^2}\frac{T_e}{(1+Y(T_e))}(1+1.1x) - \frac{d\log\,(1+Y(T_e))}{\log\, T_e}. \tag{3.63}$$

In plane parallel geometry $G(r) = 1/2$ and $f(r) = 1$. In spherical geometry $G(r) = 1$ and $f(r) = 1$, and these values are used in the first run of the code. but are then replaced by the values corresponding to the calculated r. The energy balance models have to be run in conjunction with the models derived *from* the real (as opposed to the apparent) emission measure distribution below log $T_e = 2 \times 10^5$ K, in order to find a self-consistent value of r at the base of the energy balance region (2×10^5 K).

3.5.5 *The Models in Relation to the ROSAT Observations*

Figures 3.7 - 3.12, show the *apparent* coronal emission measures and temperatures that were derived from the analyses of the ROSAT observations (see Chapter 2). It is important to stress that these are the results of several alternative fits to the ROSAT spectra. Plotted on the same scale are the computed *apparent* EMDs derived from the plane parallel and spherically symmetric models by applying the relevant values of $G(r)$ and $f(r)$. Note that the starting values of the *apparent* coronal emission measures for the plane parallel and spherically symmetric models, are the *same*.

Taking the ROSAT observations into consideration, my choice of the starting values for the *apparent* coronal emission measure (Em_c) and temperature (T_c) used in the energy balance models of each of the five dwarfs, is justified as follows:

i. ξ **Boo A**: This star is discussed first since observations with EUVE allow conclusions to be drawn regarding which type of spectral fit to the ROSAT data has most physical significance. Figure 3.7 shows the results of spectral fitting to the ROSAT data; Figure 3.8 shows the emission measure loci of the lines Fe XV, Fe XVI and Fe XIX (and some upper limits for other lines) observed with EUVE on the same scale (Jordan, 1995a; Jordan *et al.*, 1996). It is clear that the results of 2T fits do not agree with those from the EUVE line spectra in spite of their giving a better formal fit than do 1T fits. The emission measure of the higher temperature material in the 2T fits tends to be too low, while the temperature tends to be too high. Conversely, the emission measure of the lower temperature material in the 2T fits is significantly larger than that allowed by the EUVE observations. Note that the WFC results lie at intermediate temperatures and high emission measures compared to the PSPC results, as was expected following the discussion in Section 2.6 of Chapter 2.

The 1T fits with the Boron filter *off* (allowing low energy counts to be included), also give an intermediate *average* temperature, and emission measures that tend to lie a little too high. The 1T fits with the Boron filter *on*, found using the RS and LMF codes agree quite well with the EUVE results, as do the CEM fits. The relatively good agreement between the 1T, Boron filter *on* and the CEM fit arises because the EMD decreases with temperature. My choice of a starting $Em(T_c)$ and T_c is therefore weighted towards the 1T fit (Boron filter *on*) and the CEM result.

ii. χ^1 **Ori**: The pattern of the different type of fits, using the three different codes is similar to that found for ξ Boo A. Haisch *et al.* (1994), have analysed spectra of χ^1 Ori that were obtained with EUVE and they used the Mewe, Gronenschild & van den Oord (1985) spectral emission code to derive a peak coronal emission measure of log $Em(T_c) = 28.68$ at log $T_c = 6.6$. This point is indicated in Figure 3.9. The choice of the initial $Em(T_c)$ is based on the 1T fits and the CEM fit which coincides exactly with the value found by Haisch *et al.* (1994), but the chosen value of log T_c is 0.14 dex higher than that proposed by Haisch *et al.* (1994). This difference is comparable with the inherent uncertainties.

Schrijver *et al.* (1995) have recently published best fit *differential* emission measure distributions (defined as $n_e n_H V \Delta \log T_e$, where V represents the emitting volume) from the EUVE spectra of several stars, including χ^1 Ori. The method used produces some negative emission measures, which reduces confidence in the results, and the paper does not give the observed line fluxes to allow emission measures to be derived with the methods used here.

iii. ϵ **Eri**: Although the 2T fits in Figure 3.10 cluster in the same manner as for ξ Boo A, the 1T fits give a significantly lower temperature than does the CEM fit. In view of the systematic behaviour of the CEM results for χ^1 Ori and ξ Boo A, I have weighted the starting values of $Em(T_c)$ and T_c towards this fit.

iv. α **Cen A & B**: These stars are part of a three component system. Their common proper motion companion α Cen C (dM5e) is the third component of the system. These stars are the nearest late-type main sequence stars to the Sun, thus forming the brightest targets of their respective spectral types.

Observations with ROSAT have been made only with the WFC. The spatial resolution of this instrument does not allow it to distinguish the fluxes that are emitted individually from the system and so the observed flux is merely the total. However, the HRI instrument on board the *Einstein Observatory* was able to resolve the stars and the stellar surface fluxes emitted individually by α Cen A & B are given in Golub *et al.* (1982), and are in the ratio of A : B $\simeq$ 0.22. So at the Earth α Cen A emits $\simeq$ 31% and α Cen B emits $\simeq$ 69% of the total emission (see Table 3.9). Hence, I have used this ratio to attribute individual fluxes to each of the two stars.

Jordan *et al.* (1987) used scaling law arguments to suggest that the coronal temperature of α Cen A is $\sim 10^6$ K. Golub's measurements show α Cen A to behave more like the quiet sun while α Cen B tends to be more active. The temperature derived by Golub *et al.* (1982) is for the combined system, and since α Cen B dominates the flux at the Earth, the value of log $T_c = 6.32$ is likely to reflect the coronal conditions of α Cen B; until higher resolution observations of α Cen are made, I have assumed the same coronal temperature for both stars, as discussed below.

The WFC observations were modelled with CEM and 1T fits (RS and LMF), only owing to the reasons discussed in Section 2.2.3 of Chapter 2. At $T_e \sim 2\times10^6$ K, the main emission occurs where the WFC is most sensitive, so the measured temperature should be quite reliable, although as discussed earlier the emission measure may be too large. From Figures 3.11 and 3.12, we can see that the CEM model gives higher $Em(T_c)$ at a distinctly lower temperature than the other models. In view of the

Table 3.9: Coronal parameters for α Cen A & B, from Golub *et al.* (1982), with their emission measures expressed as $\int n_e n_H \, dr$. T_c for α Cen A is not determined (see text).

Source	**Flux** $(erg\, cm^{-2}\, s^{-1})$	log $\mathbf{T_c}$ (K)	log $\mathbf{Em(T_c)}$ (cm^{-5})
$\alpha\, Cen\, A$	1.3×10^4	–	26.54
$\alpha\, Cen\, B$	6.1×10^4	6.32	27.14

observations of Golub *et al.* (1982), it would be unrealistic to consider such a low temperature for either α Cen A or B, thus I have chosen the starting values for the energy balance models of these stars as the average value between the RS and LMF fits.

More recent observations of this system have been made with EUVE by Mewe *et al.* (1995) and Schrijver *et al.* (1995) who have computed a differential EMD with a broad peak at log T_e = 6.47. This temperature is in excellent agreement with the value of 6.43 adopted in the energy balance models. Schmitt *et al.* (1990) failed to fit any model at all to the *Einstein* spectra for α Cen A & B.

Increasing the starting coronal emission measure ($Em(T_c)$) at a given T_c, increases the starting pressure P_c. However, there is a maximum $Em(T_c)$ that can be chosen, which will still give an energy balance solution all the way down to $T_e \sim 2\times 10^5$ K. For χ^1 Ori, the chosen values of $Em(T_c)$ and T_c do not give an energy balance solution in plane parallel geometry (see Figure 3.9). Also note that the plane parallel model for ξ Boo A shown in Figure 3.7 is very close to its limiting case.

§3.6 *Combining the Transition Region and Coronal Models*

The emission measure distributions for the low and high transition region must now be combined in order to derive models for the entire atmosphere above $\sim 10^4$ K. The combined

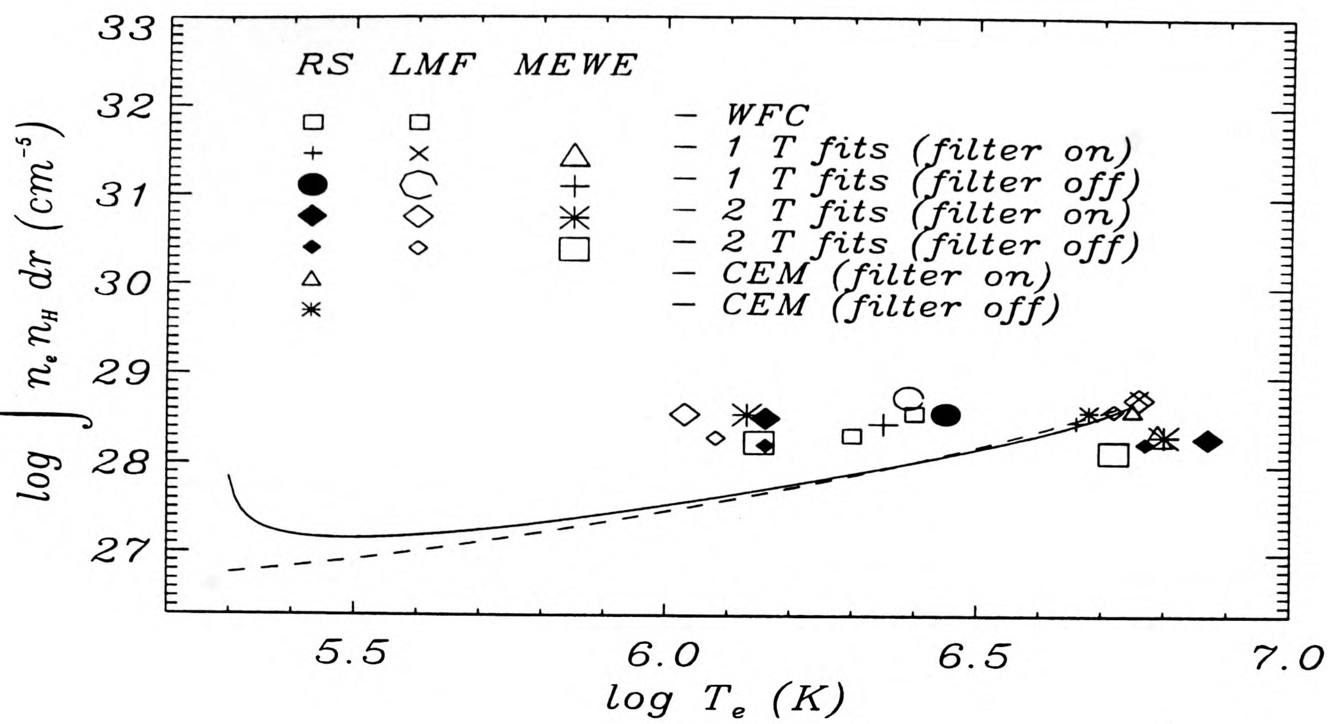

Figure 3.7: The *apparent* emission measures for ξ Boo A. The plane parallel model is indicated by the solid line, while the dashed line indicates the spherically symmetric case. The other symbols refer to the PSPC and WFC points discussed in Chapter 2.

models were calculated in:

i. plane parallel (pp), and

ii. spherically symmetric (ss) geometry,

as defined in Section 3.2. In these models, it is assumed that the emission is uniformly distributed across the whole surface area at a given height and temperature.

Deriving a combined model in pp geometry is a very straightforward task, since the EMD for the low transition region has been computed with this assumption. Thus, the two distributions were linked directly at the model base temperature (log T_o = 5.3), by simply interpolating between the value calculated for energy balance at T_o, and those derived from the IUE observations at log T_e = 5.0. The combined model is found by using the coronal starting pressure, and finding the pressure variation from equation (3.63), and the temperature gradient from equation (3.37). The heights above a chosen base height h_o at

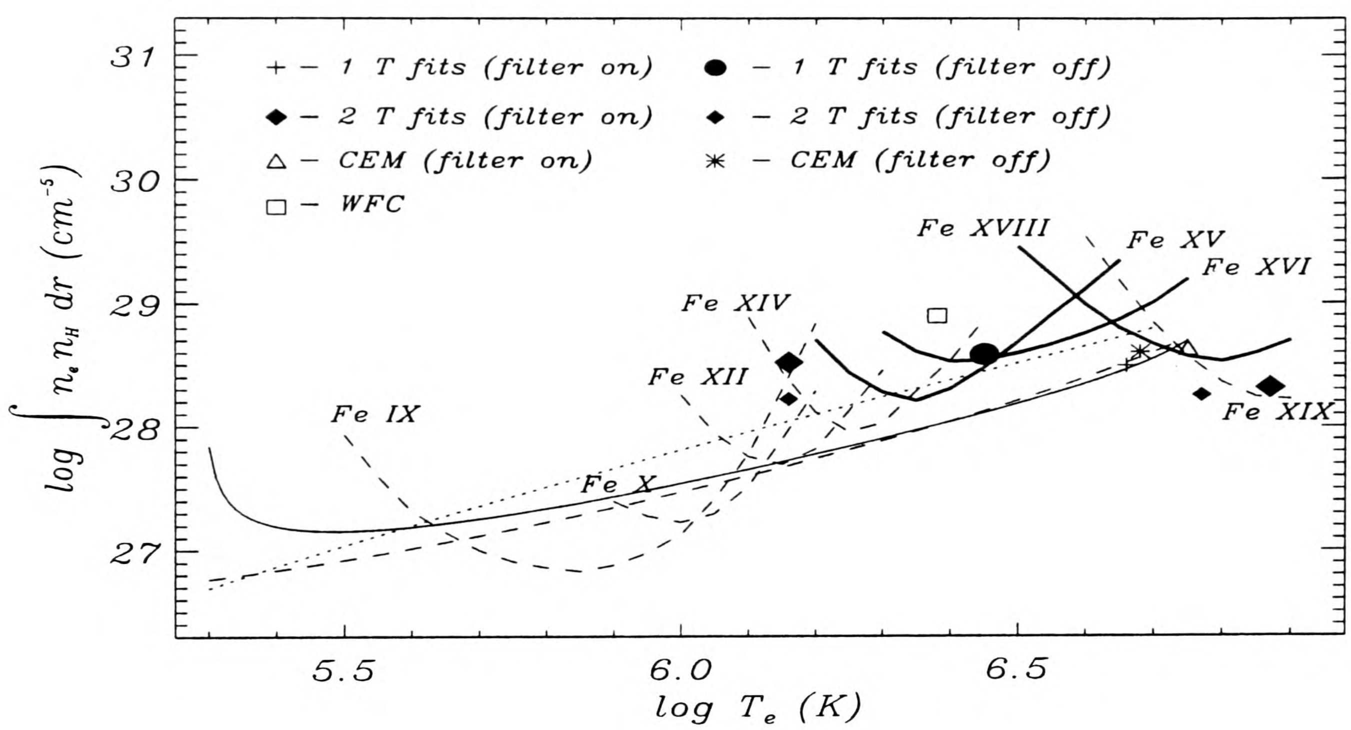

Figure 3.8: The *apparent* emission measures for ξ Boo A from EUVE line fluxes as given in Jordan (1995a). The short dashed lines indicate values derived from upper limits to the line fluxes. The dotted line is the spherically symmetric energy balance model of Jordan (1995a). The plane parallel (solid line) and spherically symmetric (dashed line) EMD's that were computed from energy balance have also been plotted for comparison. The alternative fits to the ROSAT observations shown here were deduced using the RS code. The WFC points differ from those shown in Figure 3.7 because Jordan (1995 a) used the reprocessed count rates of Pye *et al.* 1995, (see Table 2.4 of Chapter 2), while those shown in Figure 3.7 are from the WFC all-sky survey of Pounds *et al.*, 1993.

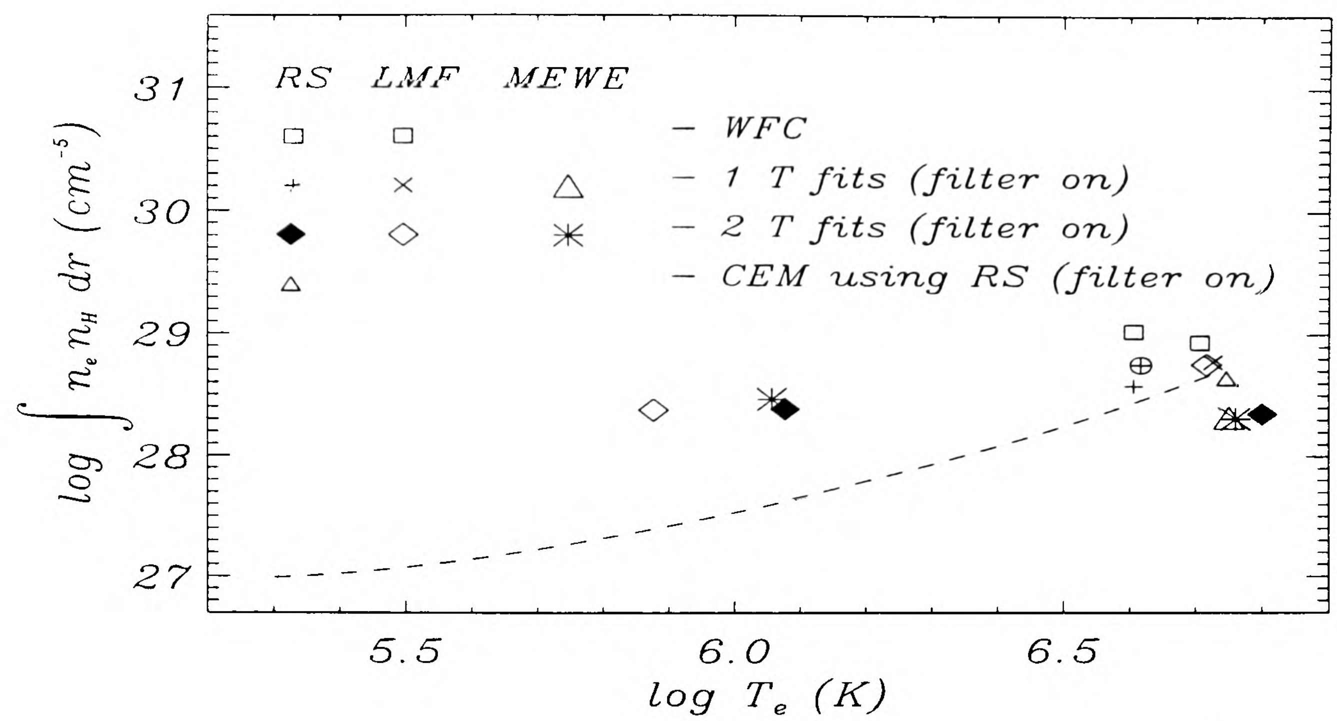

Figure 3.9: The *apparent* emission measures for χ^1 Ori. The spherically symmetric model is indicated by the dashed line, scaled up by a factor of two (a solution could not be obtained in plane parallel geometry). The other symbols refer to the PSPC and WFC points discussed in Chapter 2. The point $\oplus$ on the graph indicates emission measure found from EUVE observations by Haisch *et al.* (1994).

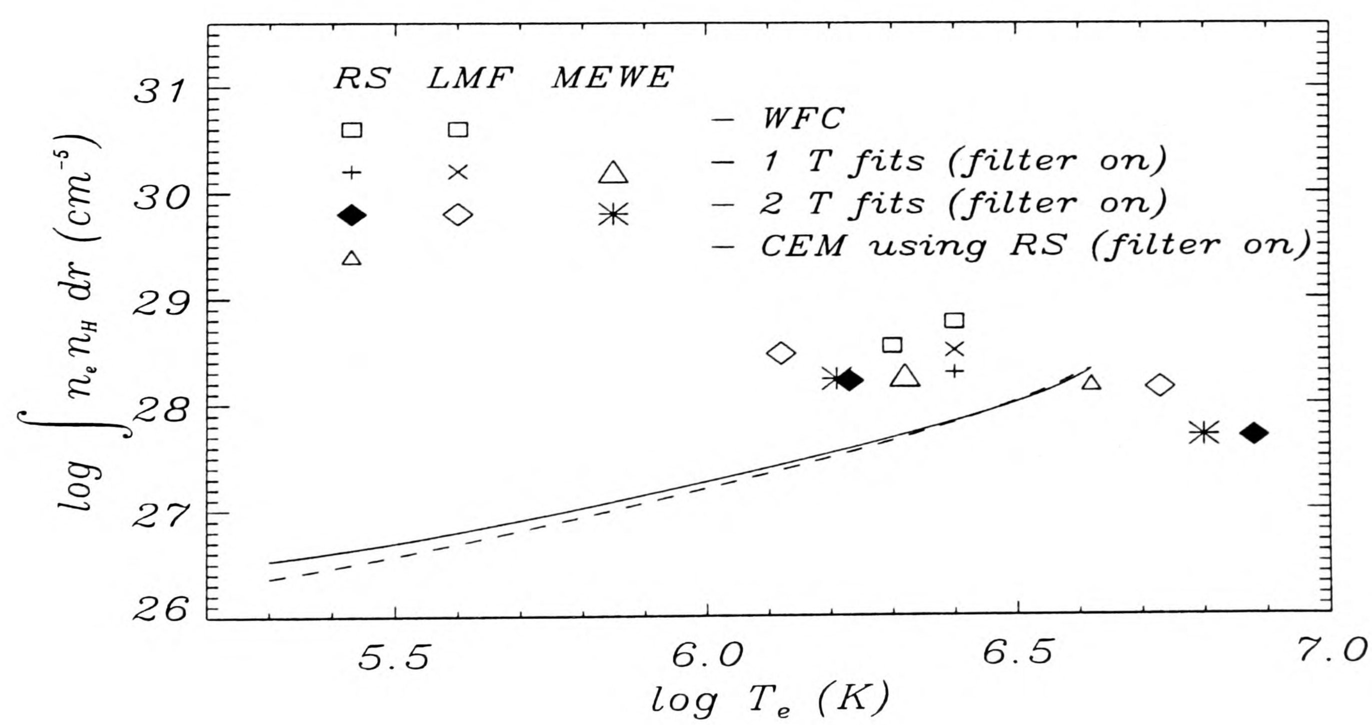

Figure 3.10: The *apparent* emission measures for ϵ Eri. The plane parallel model is indicated by the solid line, while the dashed line indicates the spherically symmetric case. The other symbols refer to the PSPC and WFC points discussed in Chapter 2.

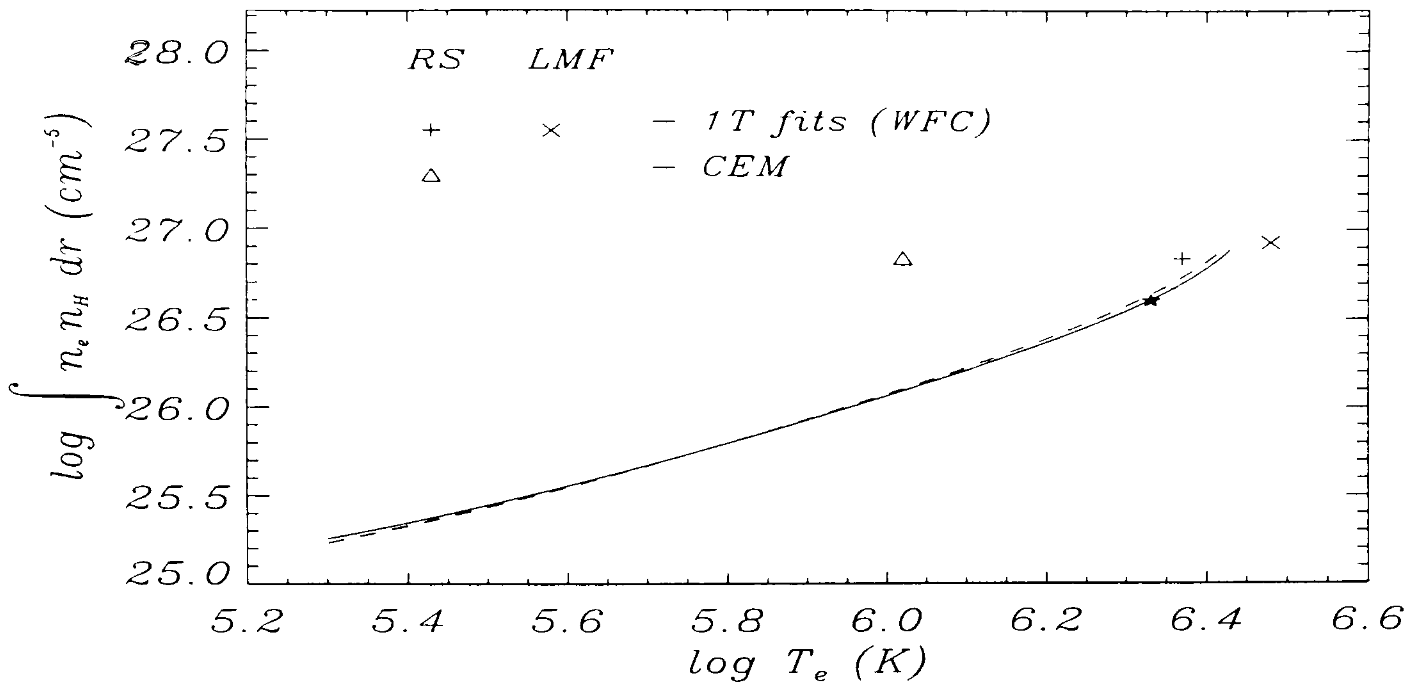

Figure 3.11: The *apparent* emission measures for α Cen A. The plane parallel model is indicated by the solid line, while the dashed line indicates the spherically symmetric case. The point $\star$ corresponds to the *Einstein* IPC and HRI observations analysed by Golub *et al.* (1982).

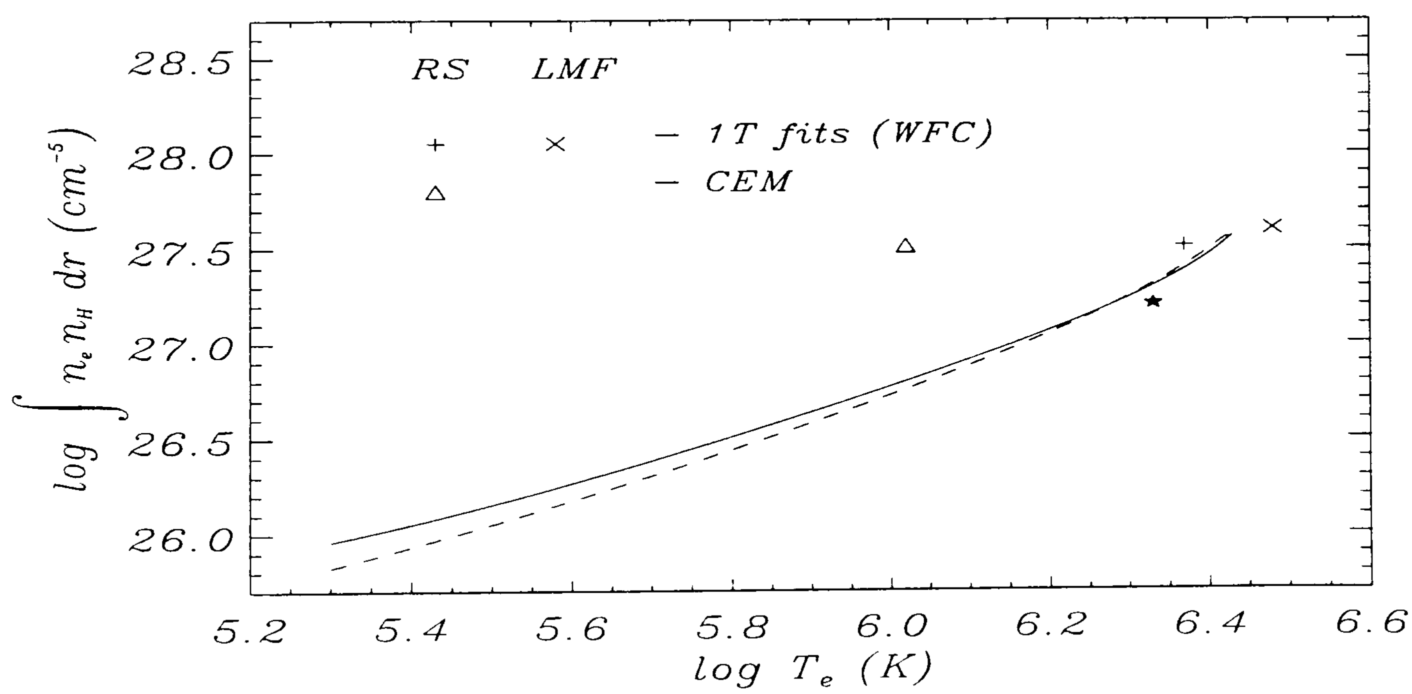

Figure 3.12: The *apparent* emission measures for α Cen B. The plane parallel model is indicated by the solid line, while the dashed line indicates the spherically symmetric case. The point $\star$ corresponds to the *Einstein* IPC and HRI observations analysed by Golub *et al.* (1982).

$\log T_e = 3.8$, are then determined.

Linking the EMDs in spherically symmetric models is not as simple:

i. Spherical symmetry must be incorporated in the transition region EMD starting from the apparent emission measures.

ii. Since the energy balance calculations depend on r at 2×10^5 K, the whole models must be iterated in spherical symmetry, updating $r(2 \times 10^5 K)$, until the solution converges. Then the absolute radius at each T_e is calculated by summing the values of dr found from dT_e/dr, so that

$$r(T_e) = r_o + \sum dr(T_e) \tag{3.64}$$

where r_o is the radial extent of the atmosphere at the base ($\log \mathrm{T}_e = 3.8$).

The extent of the atmosphere at $\log T_e = 3.8$ is scaled simply from that of the solar chromosphere, using the stellar *effective* gravity, which includes wave support (Jordan, private communication), which gives

$$r_o = R_* + (2.58 \times 10^{12} \frac{(1 + Y(T_e))}{g_*}). \tag{3.65}$$

where $Y(T_e)$ is defined in Section 3.4.2, and R_* and g_* are given in Table 2.1.

The resulting parameters (the *real* emission measure ($Em(r)$), total pressure (P_T), gas pressure (P_g) and electron pressure (P_e), as well as the radial extension ($r - R_*$) of the atmosphere at their respective temperature intervals) are listed in Appendix C. The calculations were performed at temperature intervals of 0.01 dex; however, the results in Appendix C (and for all subsequent models) are presented in temperature intervals of 0.1 dex.

Figures 3.13 - 3.17 show the *real* EMDs corresponding to these Tables. A common feature in all the graphs is a dip at the base temperature $\log T_o = 5.3$, where the energy balance models are linked to those of the lower transition region. In plane parallel geometry (with

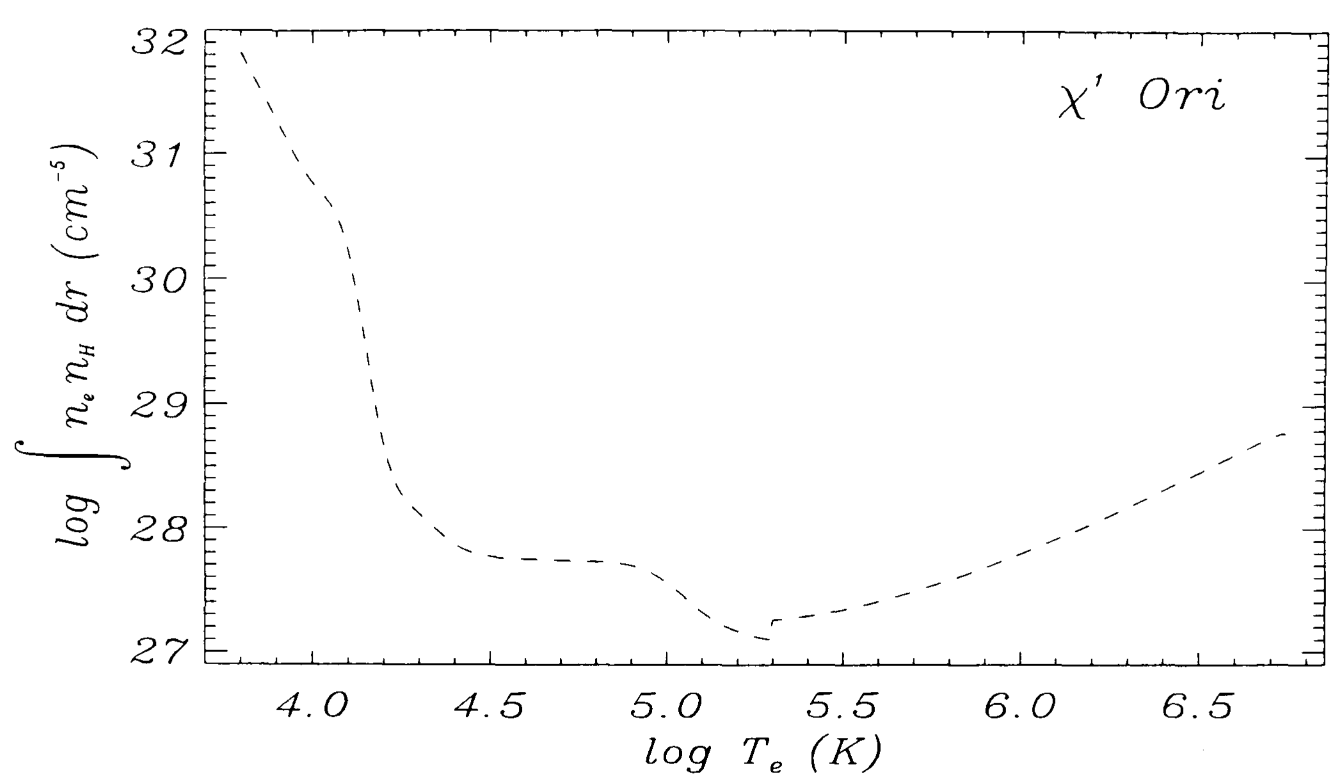

Figure 3.13: The *real* emission measure distributions for χ^1 Ori, computed assuming energy balance down to 2×10^5 K. The dashed line indicates the spherically symmetric case. No solution could be found using plane parallel geometry.

the exception of χ^1 Ori and ξ Boo A), the models can be matched to within $\sim$ 0.30 dex. On the other hand, the spherically symmetric models can be matched to within $\sim$ 0.15 dex, which is excellent agreement if the inherent errors are taken into consideration. (Note that a larger error is associated with α Cen A which is not resolved in X-rays, and this may account for the mis-match of $\sim$ 0.22 dex at log T_e = 5.3, in spherical symmetry).

In view of the above discussion, it is clear that spherical symmetry is a better description of the outer atmospheres of these stars above log T_e = 5.3 than plane parallel geometry, which should be regarded only as an approximation. Below 2×10^5 K, there is no significant difference between plane parallel and spherically symmetric models owing to the narrowness of the lower transition region.

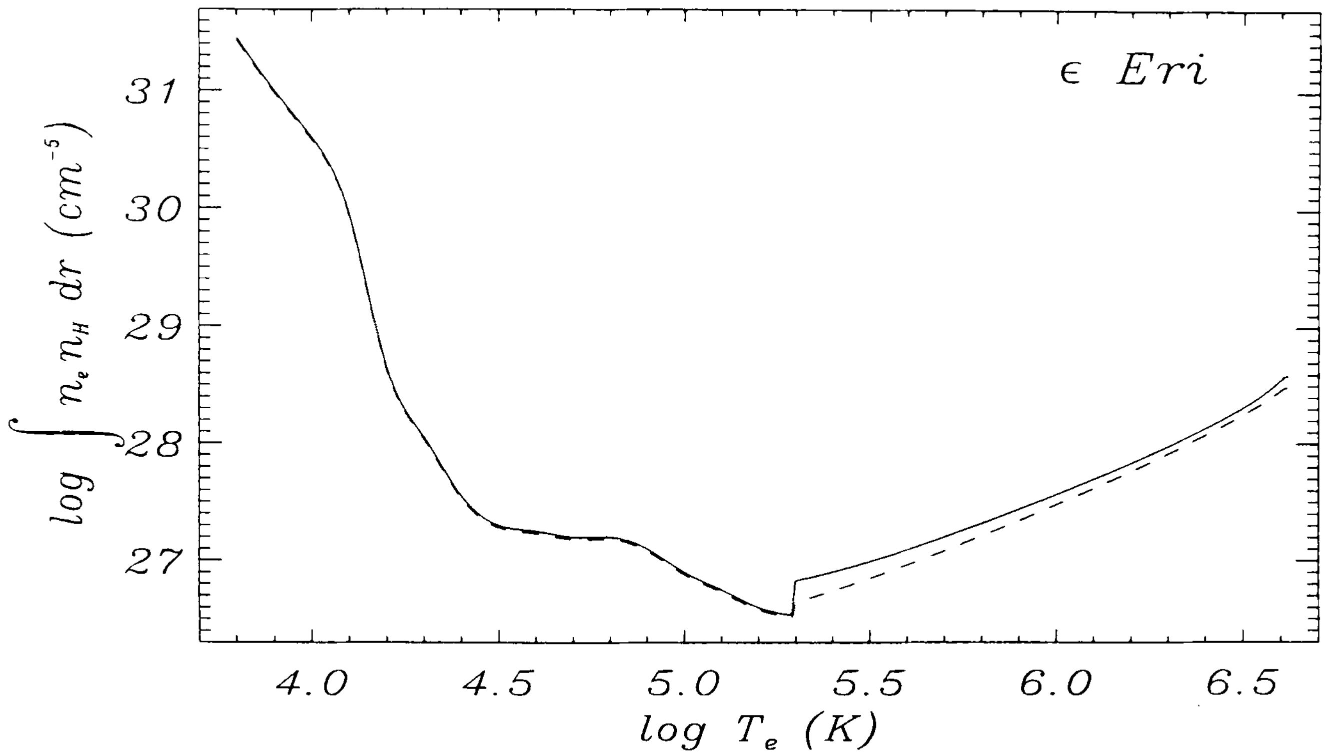

Figure 3.14: The *real* emission measure distributions for ϵ Eri, computed assuming energy balance down to 2×10^5 K. The plane parallel model is indicated by the solid line, while the dashed line indicates the spherically symmetric case.

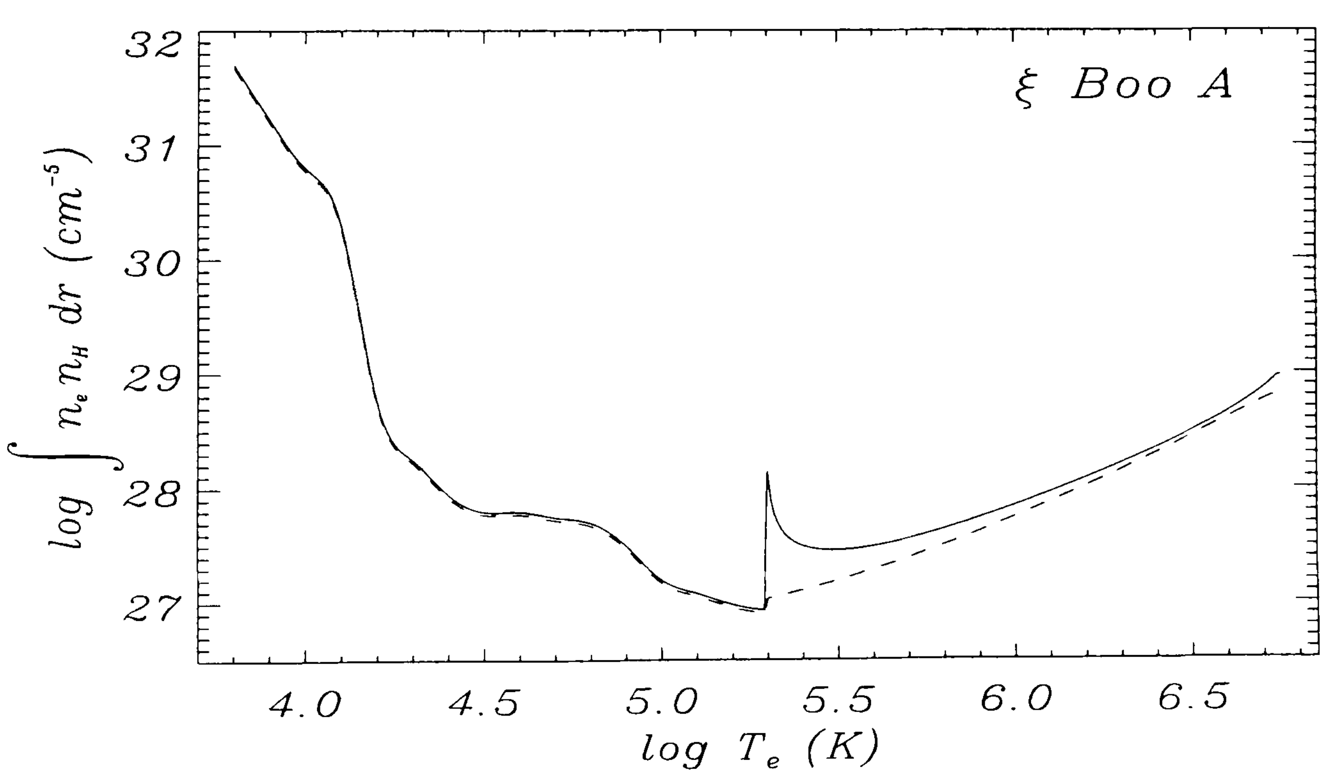

Figure 3.15: The *real* emission measure distributions for ξ Boo A, computed assuming energy balance down to 2×10^5 K. The plane parallel model is indicated by the solid line, while the dashed line indicates the spherically symmetric case.

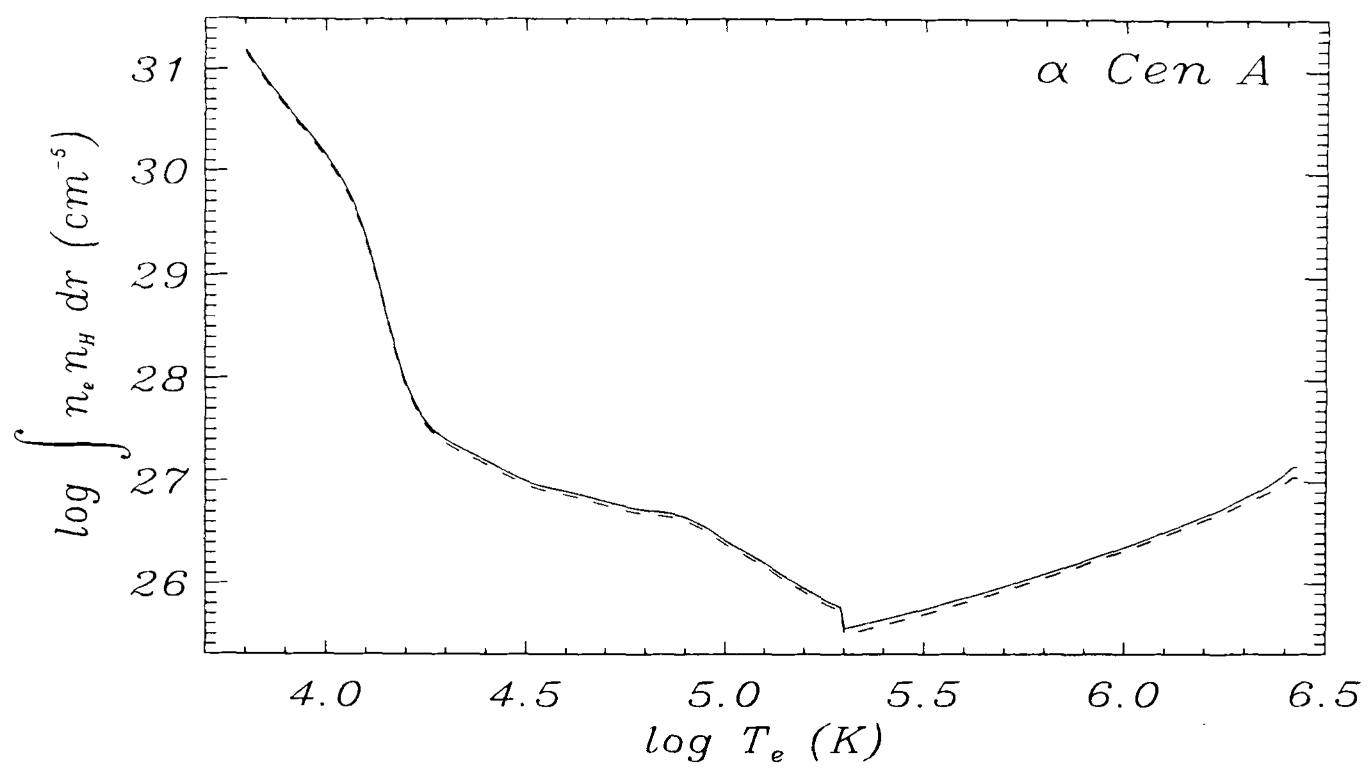

Figure 3.16: The *real* emission measure distributions for α Cen A, computed assuming energy balance down to 2×10^5. The plane parallel model is indicated by the solid line, while the dashed line indicates the spherically symmetric case.

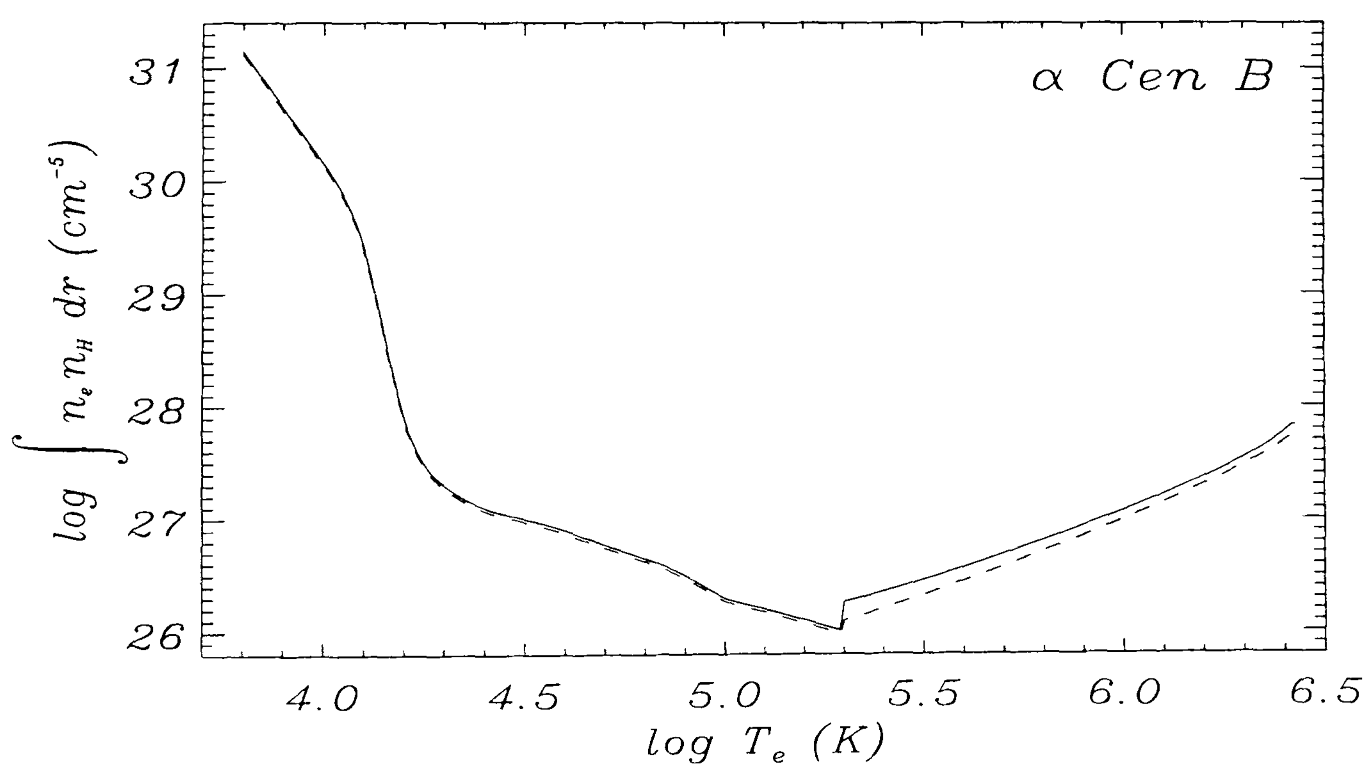

Figure 3.17: The *real* emission measure distributions for α Cen B, computed assuming energy balance down to 2×10^5 K. The plane parallel model is indicated by the solid line. while the dashed line indicates the spherically symmetric case.

§3.7 Discussion of the Results

3.7.1 The Atmospheric Structure

Figure 3.18 illustrates the models which are tabulated in the Appendix C. Like the Sun, all the stars have steep transition region temperature gradients.

In Section 3.3.3, values of P_e were computed from the density sensitive Si III] line fluxes. Looking at Table 3.10, these values tend to be lower than those computed from the energy balance model. The agreement between the values for χ^1 Ori and ξ Boo A is good and comparable to uncertainties. The observed values for α Cen A & B are the least reliable, as they are close to the low n_e limit. We know that in the Sun the emission from the transition region is enhanced by up to an order of magnitude on the supergranulation boundaries compared with cell interiors, and that the boundaries occupy $\sim$ 30% of the area (Reeves, 1976). However, the area filling factor of the the *quiet* corona may be closer to 1. The electron pressure for the Si III] lines is an average over the whole structure. Thus the *real* emission measure in the transition region cell boundaries would be about a factor of 2.7 larger than the spatially averaged value. In the boundaries it may be up to a factor of 2 larger than in the cell interiors (Dupree, Foukal & Jordan, 1976), and since the *relative* intensities of the Si III] line to permitted lines decreases with increasing n_e, the average may be weighted to the lower n_e regions. Thus, taking the *same* area factor all the way from the corona to the low transition region is clearly an approximation. With further observations of the upper transition region to *determine* the EMD, it would be possible to attempt modelling in a geometry where the magnetic field lines expand from the transition region to fill the corona. The *relative* values of the pressures found for the different stars. do follow the same trend, whether they are measured from the Si III] lines or determined from the models.

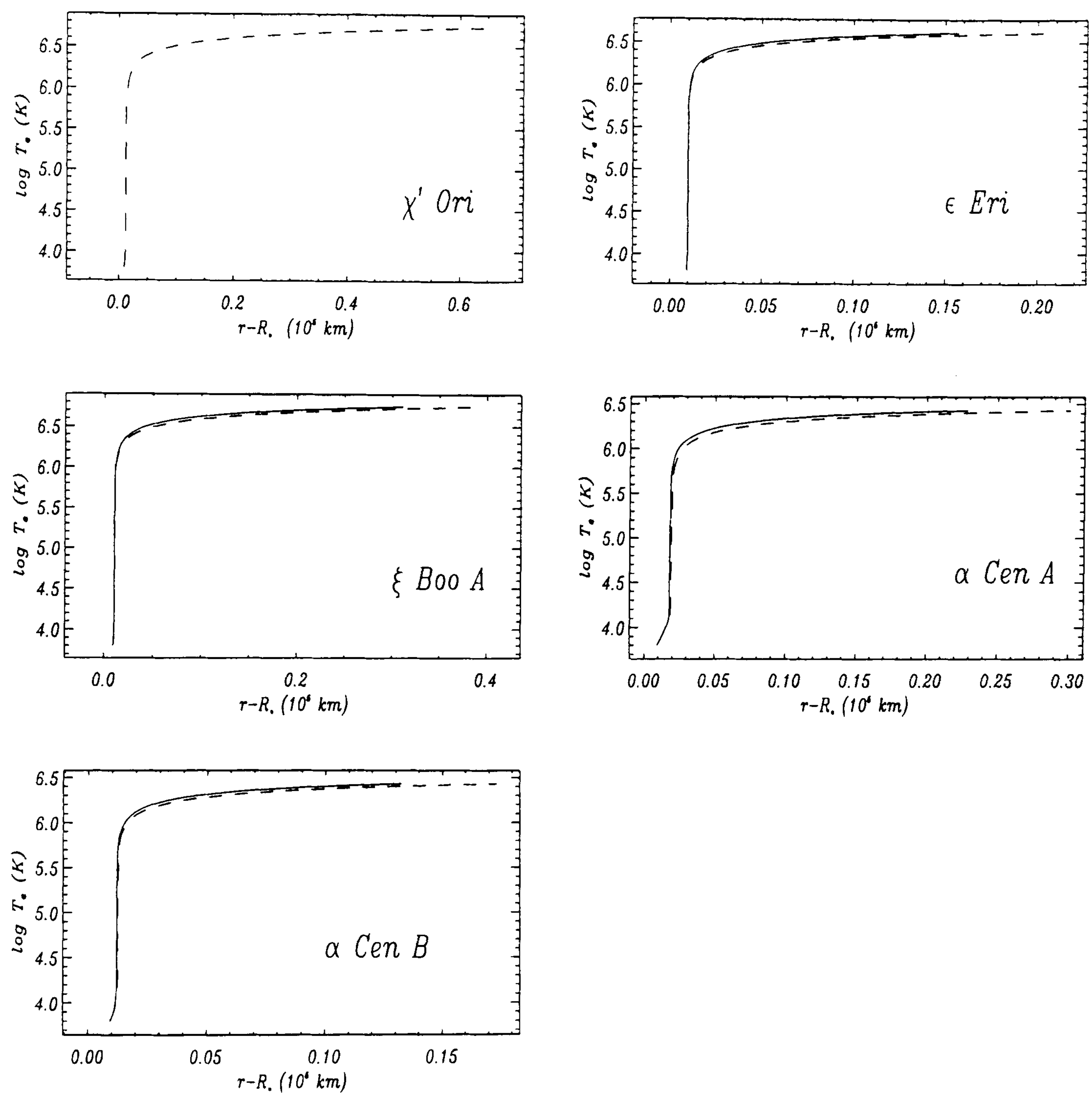

Figure 3.18: The radial extension $r - R_*$ of the transition regions and coronae of the five dwarfs, computed using plane parallel (solid line) and spherically symmetric (dashed line) geometries. The maximum heights shown correspond to the base of the corona; the isothermal region will extend beyond these points.

Table 3.10: Electron pressures computed from Si III] line flux (see Section 3.3.3) compared with those resulting from the plane parallel and spherically symmetric energy balance models, at log T_e = 4.6.

Star	a	pp†	ss†
χ^1 *Ori*	15.7	–	16.02
ϵ *Eri*	15.2	16.05	15.96
ξ *Boo A*	16.0	16.23	16.14
α *Cen A*	14.1	15.07	14.99
α *Cen B*	14.9	15.53	15.44

a - $\log(P_e/k)$ (in units cm^{-3} K) computed from Si III] flux (Section 3.3.3).
† - $\log(P_e/k)$ (in units cm^{-3} K) computed for plane parallel and spherically symmetric atmospheres (see Section 3.6).

3.7.2 Energy Propagation in Stellar Atmospheres:

Energy is transported down from the corona by thermal conduction. The net conductive flux (ΔF_c), can either transport energy out of a given region, or deposit energy in that same region. At temperatures greater than 2×10^5 K, in energy balance, the emission measure is related to the temperature via the expression

$$\frac{d\log Em(r)/G(r)}{d\log T_e} = 2\frac{d\log P_g}{d\log T_e} + \frac{3}{2} + 4\frac{d\log r}{d\log T_e} - \frac{2}{\kappa}\frac{(1+1.1x)^2}{x}\frac{Em(r)^2\, k^2}{P_g^2 T_e^{3/2}}\frac{\Lambda_{rad}}{G(r)^2 f(r)^2} \tag{3.66}$$

where the last term (defined as β in equation (3.63)), describes the ratio of radiative to the conductive flux, $\Delta F_R/F_c$, where ΔF_R is the radiation flux from a temperature range $\Delta \log T_e = 0.3$ and F_c is the downward conductive flux at the centre of this temperature range. This always has a value of < 1.0, implying that in the upper transition region and at the coronal temperature the downward conductive flux (not the *net* conductive flux) exceeds the local radiation losses.

The radiative fluxes (ΔF_R) of the lower transition region ($3.8 < \log T_e < 5.3$) for the spherically symmetric models are listed in Table 3.11, averaged over 0.3 dex in log T_e. The bulk of the radiation is emitted at around log $T_e = 4.1$, which corresponds to the Lyman α radiation. (Since the EMD below log $T_e < 4.0$ is not well defined (see discussion in Section 3.3.2), only the EMD where log $T_e \geq 4.0$ will be considered in the following calculations). Table 3.12 gives the *total* radiative flux, F_R, summed over the temperature interval log T_e = 4.0 - 5.3, the conductive fluxes at 10^5 K and the coronal temperatures ($F_c(T_o)$ and $F_c(T_c)$, respectively), the coronal radiative flux $F_R(T_c)$, and the sum of the coronal losses $F_m(T_c) = F_c(T_c) + F_R(T_c)$. Note that the coronal energy losses are dominated by conduction.

The following is a discussion of the typical uncertainties that are associated with the above-mentioned fluxes. From equation (3.55), the error associated with F_R (σ_{F_R}), are the same as the standard error in Em (σ_{Em}), which is of the order of 20%. On the other hand, the error on F_c (σ_{F_c}), is a combination of the errors on Em and P_e (σ_{P_e}) (see equations (3.37) & (3.51)). From equation (3.46), and taking into account the standard error on T_c (σ_{T_c}) which is $\sim$ 10%, the uncertainty of $P_e(T_c)$ is $\sim$ 20%. Hence, the error on $P_e(T_e)$ $\sim$ 30% (see equation (3.38)). Therefore σ_{F_c} $\sim$ 30% and σ_{F_m} $\sim$ 40%.

At the base temperature T_o, $F_c(T_o) \gg \Delta F_R(T_o)$ (*i.e.* the energy deposited by conduction greatly exceeds that which is radiated away in the layer immediately below T_o by up to two orders of magnitude). This results in an energy imbalance and clearly, there is a need for an additional energy loss mechanism, in order to dispose of this excess energy. This is a long-standing problem and was noted from very early work in the field (*e.g.* Giovanelli, 1949). Kopp & Kupperus (1968), suggested that this energy might drive spicular motions. Gabriel (1976a) pointed out allowing for the expansion of the magnetic field with height in energy balance models reduces the energy imbalance below 2×10^5 K. If the transition region material is restricted to an area A/A_*, then the *local* radiation losses will increase by A/A_*. The conductive flux would then need to be calculated with A/A_* varying between T_o and T_c. With this explanation, the areas required are smallest for the least active stars, and vice-versa. The same trend is found for the filling factor of surface magnetic fields (Montesinos & Jordan, 1993).

Table 3.11: The radiative losses (ΔF_R in erg cm^{-2} s^{-1}, averaged over 0.3 dex) in the lower transition regions (log T_e = 3.8 - 5.3) of the five dwarfs, as computed for the spherically symmetric models. (The numbers in brackets indicate powers of 10).

log $\mathbf{T_e}$	χ^1 *Ori*	ϵ *Eri*	ξ *Boo A*	α *Cen A*	α *Cen B*
3.80	6.6(6)	2.7(6)	4.7(6)	1.5(6)	1.3(6)
3.90	1.9(7)	9.5(6)	1.6(7)	4.2(6)	4.2(6)
4.00	8.7(7)	5.6(7)	8.8(7)	1.9(7)	2.0(7)
4.10	1.1(8)	5.6(7)	1.2(8)	1.4(7)	1.6(7)
4.20	5.5(6)	5.0(6)	6.2(6)	9.6(5)	8.7(5)
4.30	2.1(6)	1.7(6)	2.7(6)	3.7(5)	3.0(5)
4.40	1.5(6)	6.7(5)	1.7(6)	2.9(5)	2.3(5)
4.50	1.4(6)	4.4(5)	1.4(6)	2.1(5)	2.2(5)
4.60	1.6(6)	4.8(5)	1.7(6)	2.0(5)	2.1(5)
4.70	1.9(6)	5.3(5)	1.9(6)	2.0(5)	1.9(5)
4.80	2.5(6)	7.0(5)	2.2(6)	2.2(5)	1.9(5)
4.90	2.9(6)	7.0(5)	1.7(6)	2.4(5)	1.7(5)
5.00	2.6(6)	5.4(5)	1.1(6)	1.8(5)	1.3(5)
5.10	1.7(6)	4.3(5)	9.1(5)	1.2(5)	1.2(5)
5.20	1.3(6)	3.3(5)	7.8(5)	7.1(4)	1.0(5)
5.30	1.1(6)	2.7(5)	6.9(5)	2.0(4)	7.9(4)

Table 3.12: The radiative and conductive energy losses (F_R and F_c, respectively, and in units of erg cm^2 s^{-1}), in the upper transition regions and coronae of the five dwarfs, as computed for the spherically symmetric models. The acoustic flux (F_a) at 2×10^5 K is also listed. (The numbers in brackets indicate powers of 10).

Star	$F_R(T)^a$	$F_c(T_o)^b$	$F_c(T_c)^c$	$F_R(T_c)^d$	$F_m(T_c)^e$	$F_a(T_o)^f$
χ^1 *Ori*	7.4(7)	4.5(6)	1.5(7)	1.4(6)	1.6(7)	4.2(7)
ϵ *Eri*	4.1(7)	1.5(7)	1.6(7)	9.2(5)	1.7(7)	1.3(6)
ξ *Boo A*	7.7(7)	1.4(7)	2.6(7)	1.4(6)	2.7(7)	3.5(7)
α *Cen A*	1.2(7)	2.3(6)	2.4(6)	5.2(4)	2.5(6)	1.5(5)
α *Cen B*	1.3(7)	4.7(6)	5.6(6)	2.5(5)	5.9(6)	2.9(6)

a - The *total* radiative losses ($F_R = \Sigma \Delta F_R$), for the temperature interval log T_e = 4.0 - 5.3 K.
b - F_c conducted *down* at log T_e = 5.3.
c - F_c conducted *down* from the corona.
d - F_R from the corona.
e - $F_m(T_c) = F_c(T_c) + F_R(T_c)$
f - The acoustic flux passing through 2×10^5 K.

Jordan (1980) proposed that the excess energy in this scenario could account for the observed non-thermal line broadening. Raymond & Doyle (1981) suggested that in the quiet Sun, the excess thermal energy may be sufficient to drive gas upwards at 2×10^5 K at a velocity of 1 km s^{-1}. They achieved this by adding an extra term in the energy equation which described the enthalpy flux resulting from upflows.

More recently, Cally (1990) and Fiedler & Cally (1990) argue that a nonclassical turbulent conductive flux ($q_T = \kappa_T \nabla T_e$, where κ_T represents the turbulent conductivity), may lead to a solution to this problem. They suggest that the observed non-thermal broadening is associated with this process. They propose that turbulent conduction greatly exceeds classical conduction at temperatures below 1.6×10^5 K. Thus, instead of all the conductive flux having to be deposited locally, it can penetrate further into the low transition region where it could be lost by *e.g.* H Ly-α. In this picture, the radiation losses below $\sim 2\times10^5$ K would be balanced by the non-classical conductive flux, and no other non-thermal heating would be needed.

The existing line widths are not sufficiently accurate to determine the variation of any wave flux with temperature. However, the widths of the C IV lines can be used to examine the acoustic flux passing the region at 2×10^5 K, and to compare this with the total coronal energy losses. (Only modest values of B are required to give a sufficient Alfvén wave flux). Using

$$F_a = \rho < v_{turb}^2 > v_{prop} \tag{3.67}$$

where $\rho = \mu m_p P_g / k T_e$ is the gas density derived from the present models, $v_{prop} = 1.46 \times 10^4 \, T_e^{1/2}$ is the sound speed, and the values of $< v_{turb} >$ are given in Table 3.6. The resulting values of F_a are given in Table 3.12. For ϵ Eri, α Cen A and α Cen B, the values of F_a are lower than the total fluxes required. For ξ Boo A, F_a is marginally greater than that required, while for χ^1 Ori F_a exceeds the required value of F_m. However, the value of v_{turb} for χ^1 Ori is based only on the C IV (1548 Å) line, which is usually broader than the C IV (1500 Å) line, probably because of blending with lines of Fe II. Typical uncertainties for the FWHM given in Ayres *et al.* (1983) imply that the error in v_{turb}^2, $\sigma_{v_{turb}^2} \sim 15\%$. Taking the errors associated with the parameters in equation (3.67) into consideration, $\sigma_{F_a} \sim 30\%$.

The acoustic fluxes are therefore similar to the required non-thermal fluxes, but the combined uncertainties are around a factor of 2. Although in the Sun the acoustic flux predicted in this way is to within a factor of 2 of that required, detailed observations of line profiles fail to detect the signature of acoustic wave trains (*e.g.* Athay and White, 1978). The correlation discussed in Chapter 2 support the presence of a heating mechanism that is related to the magnetic field. Further observations of transition region line widths with the GHRS are needed to place clearer constraints on wave fluxes.

3.7.3 Coronal Scaling Laws:

Hearn (1975, 1977) predicted that for a corona with a base pressure P_o, there is an average coronal temperature T_c for which the total energy losses are a minimum. This is known as Hearn's minimum energy loss (m.e.l) hypothesis and it implies that there is a fixed ratio between the radiation losses and the conductive flux from the corona, which leads to simple scaling laws. The electron pressure P_c (in dyne cm^{-2}) and emission measure $Em(T_c)$ (in cm^{-5}) are given by (see Montesinos & Jordan, 1993)

$$P_c = 1.6 \times 10^{-27} \frac{g_* \, (1.5 - \delta)^{1/2} \, T_c^{1.75+\delta/2}}{\alpha^{1/2} \, (\delta + 1)} \tag{3.68}$$

$$Em(T_c) = 9.7 \times 10^{-15} \frac{g_* \, (1.5 - \delta) \, T_c^{2.5+\delta}}{\alpha \, (\delta + 1)^2} \tag{3.69}$$

where $Em(T_c)$ has the form $\int n_e^2 \, dr$. Here I have adopted $\delta = 1$ and $\alpha = 1.25 \times 10^{-16}$ erg cm^3 s^{-1} K, since these values were used in the modelling. In Table 3.13, the predicted values for $Em(T_c)^H$ (in terms of $\int n_e n_H \, dr$) and P_c^H are compared to the logarithmic difference of the coronal emission measures (log $Em(T_c)^H$ $-$ log $Em(T_c)$) and pressures (log P_c^H $-$ log P_c) deduced models in plane parallel geometry, because Hearn's treatment is for this case.

It can be seen that the emission measures and pressures for these stars agree with the m.e.l. hypothesis to within about a factor of four and two, respectively. The largest difference is for α Cen A, which has been assumed to have the same coronal temperature as α Cen B, since the system is not resolved. This difference suggests that T_c for α Cen A is in reality *lower* than that for α Cen B. The m.e.l. hypothesis predicts a ratio of conductive losses to radiative losses of 8. The small disagreements with the m.e.l. solutions arise because in the models this ratio is larger than 8.

Table 3.13: The coronal emission measures (Em_c^H, expressed in the form $\int n_e n_H \, dr$) and pressures (P_c^H) computed using Hearn's minimum energy loss hypothesis for δ = 1.0 and α = 1.25×10^{-16} erg cm^3 s^{-1} K. The adopted values of T_c are those used in the energy balance models. The values in brackets are the corresponding logarithmic differences between the emission measures and pressures from Hearn's m.e.l. hypothesis and those computed in plane parallel geometry.

Star	log $\mathbf{T_c}$ (K)	log $\mathbf{Em(T_c)^H}$ (cm^{-5})	log $\mathbf{P_c^H}$ ($cm^{-3}\,K$)
χ^1 *Ori*	6.74	28.84(–)	16.07(–)
ϵ *Eri*	6.62	28.83(+0.24)	16.20(+0.09)
ξ *Boo A*	6.75	29.11(+0.14)	16.33(+0.05)
α *Cen A*	6.43	27.81(+0.66)	15.43(+0.31)
α *Cen B*	6.43	28.06(+0.23)	15.68(+0.10)

§3.8 *Summary*

This chapter presents the results of modelling from the emission measure distribution of the lower transition region, by using line fluxes that were previously obtained using IUE, and updating the atomic parameters and abundances. For the upper transition region, the emission measure distributions were computed assuming energy balance. Plane parallel and spherically symmetric geometries were investigated.

The emission measure distributions of the lower and upper transition region were linked in order to produce full models above the chromosphere. The spherically symmetric models match on to their corresponding lower transition regions to within the uncertainties in the transition region fluxes and atomic data. An energy balance solution was not possible for χ^1 Ori in plane parallel geometry, and the solution for ξ Boo A is very close to its limiting value. Overall the spherically symmetric models are to be preferred. The electron pressures in the lower transition region calculated from the density sensitive Si III] line fluxes, tend to be lower than those computed using the energy balance models. In α Cen A & B, the density derived is close to the low density limit. The differences for the other stars are in the direction expected from averaging over supergranular structure.

The radiative and conductive fluxes from the spherically symmetric models were presented. At the base of the transition region in energy balance, the conductive fluxes exceed the radiative energy losses. This could imply that the emission is restricted in area, or that the energy conducted back is distributed over a range of temperatures, for example by non-classical conduction.

Finally, the coronal emission measure and pressures predicted using Hearn's minimum energy loss hypothesis, agree well (apart from those of α Cen A) with the observed values, assuming plane parallel geometry.

Chapter 4

The Transition Region and Corona of α CMi

§4.1 Introduction

Procyon A (α CMi) is a late-type subgiant of spectral type F5 IV-V that is evolving off the main-sequence. It is part of a binary system and its companion Procyon B, is a faint cool DF white dwarf with a forty year orbital period and does not have any influence on the spectrum of Procyon A; nor is it the source of any significant X-ray and EUV emission, as was confirmed by high resolution observations with the *Einstein Observatory* (Schmitt *et al.*, 1985). The mass of Procyon A can be found by observing the motion of Procyon B about the common center of gravity. Procyon A is thought to have been a late A-type dwarf without a sub-photospheric convection zone. On a colour-magnitude diagram, Woolley *et al.* (1970) have positioned α CMi about one magnitude above the main sequence, which implies that this star is slightly evolved.

α CMi is one of the most frequently studied late-type stars in the optical, X-ray and UV wavebands. Evans *et al.* (1975) made observations of Procyon with *Copernicus* in the UV waveband and made the first analysis of *stellar* chromospheric and transition region lines using the spectra obtained. Brown & Jordan (1981) made observations with the IUE satellite and determined the emission measure distribution in the transition region and hence made models of the structure and investigated the energy balance. Drake, Simon & Brown (1983) used radio data to detect the existence of magnetic regions in Procyon, suggesting the presence of a weak or intermittent solar-like dynamo. Observations in the

X-ray waveband have been made with the High Resolution Imager (HRI) and the Imaging Proportional Counter (IPC) on board the *Einstein Observatory* (Jordan *et al.*, 1986), with *EXOSAT* (Schrijver, 1984), and more recently with ROSAT.

Improved observations of UV line profiles have been made with the GHRS on the HST (Wood, Harper & Linsky, 1996). These reveal the presence of broad wings which these authors consider to be an indicator of microflaring. However, the spectra were obtained before the COSTAR correction. As Procyon is only slightly more active than the Sun (Ayres, Marstad & Linsky, 1981), the presence of such wings is surprising. Procyon's coronal emission measure distribution was also modelled by Drake *et al.* (1995), using in addition the line fluxes from recent high resolution observations with EUVE.

There are many arguments in favour of acoustic waves heating Procyon's atmosphere. Bohn (1984), used the Lighthill-Proudman theory (Lighthill, 1952; Proudman, 1952), to estimate the acoustic fluxes that are created in late-type stars, and found that such fluxes were enhanced by five orders of magnitude from those computed by previous authors. They also suggested that acoustic waves are able to balance coronal energy losses. Stepien and Ulmschneider (1989) postulate that in the highly active cool dwarfs (spectral type F-M), acoustic heating is not the dominant *coronal* heating mechanism, which may require magnetic processes. Musielak *et al.* (1994) appears rather sceptical of this and claims that the above formalism breaks down in F stars such as Procyon.

Mullan & Cheng (1994) computed a time-dependent hydrodynamical model for Procyon's chromosphere, transition region and corona, where acoustic mechanisms are entirely responsible for the energy deposition in these regions. Acoustic power was introduced in their calculations via long period velocity waves in the photosphere, which are most likely to arrive at the corona. Their results show quantitative evidence that the presence of a cool corona in Procyon is due to acoustic wave dissipation and their differential emission measure distribution agrees well with the empirical results of Jordan *et al.* (1986). However, Brown & Jordan (1981) concluded that provided the electron densities they adopted were correct, the acoustic flux is not sufficient to heat the atmosphere above $\sim 10^4$ K.

The reduction of our ROSAT observations is discussed in Section 4.2. The modelling of the upper transition region and corona is presented in Section 4.3. The resulting model is compared with various alternative fits to the ROSAT observations. In Section 4.4, the EMD for the lower transition region is derived from IUE fluxes (see Brown & Jordan, 1981). The full model of the outer atmosphere is presented in Section 4.5. Section 4.6 gives a discussion of electron densities, and implications of the atmospheric structure. A discussion of the heating requirements follows in Section 4.7.

§4.2 ROSAT Observations and Data Reduction

In Chapter 2, it was explained how the mean coronal emission measures and temperatures were derived from observations made in the X-ray wavelength with the PSPC instrument (B-filter in operation) on board ROSAT, using the most up to date versions of the Raymond & Smith (1990), the Landini & Monsignori Fossi (1992, private communication) and the Mewe *et al.* (1985) spectral emission codes, with the aid of the data analysis package XSPEC. The results that were obtained for Procyon from 1T and 2T fits are summarised in Tables 4.1 and 4.2.

4.2.1 Absorption by the Interstellar Medium

The attenuation by the interstellar medium is very small and value of log N_x^* (cm^{-2}) of 17.86 has been adopted (see discussion in Section 2.5 of Chapter 2). This value is slightly lower than that computed in the analysis of IUE spectra by Murthy *et al.* (1987) where log N_x^* was found to lie in the range of 17.98 - 18.34 for their analysis of IUE spectra. Drake *et al.* (1995) have adopted a value of 18.17 which agrees well with the value of

Table 4.1: Single Temperature Fits to the Raymond-Smith (1990), Landini-Monsignori Fossi (1992, private communication) and Mewe *et al.* (1985) spectral emission codes using XSPEC.

Code	log **Em** (cm^{-5})	log **T** (K)	χ^2
RS	27.50	6.12	3.93
LMF	27.70	6.10	5.38
$Mewe$	27.57	6.11	4.39
$CEM(RS)$	27.64	6.26	3.69

Table 4.2: Two-Temperature Fits Raymond-Smith (1991), Landini-Monsignori Fossi (1992, private communication) and Mewe *et al.* (1985) spectral emission codes using XSPEC.

Code	log **Em1** (cm^{-5})	**T1** (K)	log **Em2** (cm^{-5})	**T2** (K)	χ^2
RS	27.47	6.08	26.14	6.63	0.39
LMF	27.68	6.04	26.68	6.39	0.56
$Mewe$	27.56	6.07	26.02	6.55	0.35

log $N_x^* = 18.08$, derived by Linsky *et al.* (1995) from a preliminary analysis of HST GHRS observations of Procyon. The stellar parameters adopted are given in Table 4.3.

4.2.2 Abundances

Drake & Laming (1995) have recently reviewed the atmospheric parameters and elemental abundances of Procyon. They find that its photospheric and coronal abundances are similar to those of the solar photosphere. In their analysis they have used the photospheric abundance values of Anders & Grevesse (1989) for all elements, with the exception of Fe, for which they have adopted a value of [Fe/H] = 7.51, based on the re-examination of this abundance by Blackwell *et al.* (1994). This agrees with the value recommended by Grevesse *et al.* (1992), which is adopted here. Edvardsson *et al.* (1993) estimate the uncertainties

Table 4.3: The stellar parameters adopted for Procyon.

d (pc)	R_* ($R_\odot$)	B − V	Sp. Type	log g_* (CGS)
3.48[a]	2.05[b]	0.42[c]	$F5\,IV - V$	4.00[b]

a - Woolley *et al.* (1970).
b - Steffen (1985).
c - Hoffleit (1982).

in the abundances to be ± 0.10 dex, at the most.

Drake *et al.* (1995), suggest that the ionisation potential that separates low and high FIP (see Section 2.4.3 of Chapter 2) indicates the temperature ($\sim 10^4$ K) where fractionation occurs. Small spatial scales are required for element fractionation to work, as these prevent the elements from ionising during the separation process (von Steiger & Geiss, 1989). Drake *et al.* (1995) pointed out that such structures occur naturally in the presence of magnetic fields and concluded that the absence of a FIP effect (which is atypical of late-type stellar coronae) in Procyon's corona, strongly suggests that this star is heated by acoustic waves (see Section 4.7).

§4.3 *Models of the Upper Transition Region and Corona*

As discussed in Chapter 3, in the absence of any external heating mechanism below the corona, the net conductive flux dF_c over a height interval dr, is balanced by the radiative flux dF_R from the same height interval. Models of the upper transition region and corona of Procyon were investigated under this assumption, for plane parallel and spherically symmetric atmospheres.

4.3.1 The Models in Relation to the X-ray Observations

The relative positions of the *apparent* coronal emission measures and temperatures for 1T and 2T fits found from the three emissivity codes are shown in Figure 4.1. Plotted on the same scale, are the emission measures that were deduced from the *Einstein* observations (using the HRI and IPC instruments), as well as those made with *EXOSAT* (see Jordan *et al.*, 1986, and references therein). For both the HRI and IPC observations, Jordan *et al.* (1986) and Schmitt *et al.* (1985) used the Raymond & Smith (1977) emissivity code to obtain 1T fits. For the *EXOSAT* observations made in 1983, Schrijver (1984) found that a two component temperature model is required using the emissivities of Mewe & Gronenschild (1981), but Jordan *et al.* (1986) showed that the same data can be reproduced with an intermediate 1T fit. Although these results are included in Figure 4.1, the codes used are very early versions (see Chapter 2), and the results cannot be strictly compared to those from ROSAT.

The 1T fits from these codes give values of $Em(T_c)$ and T_c that are in good agreement. The values from the HRI and CEM give slightly higher tempertatures. The $Em(T_c)$'s and T_c's found from the lower temperature components of the 2T fits agree quite well with those from the 1T fits. The emission measures found from the ROSAT spectra at the higher component of the 2T fits are so much smaller that they may not be physically realistic, and may simply arise from the restricted method of fitting the spectra. As mentioned above, the EXOSAT 2T fits can be replaced by a fit at log $T_c = 6.2$ (Jordan *et al.*, 1986). Thus, the coronal temperature appears to lie between log $T_c \sim 6.1$ and 6.3, with log $Em(T_c) \simeq$ 27.6.

In order to compute energy balance solutions in plane parallel and spherically symmetric geometries, the base temperature was initially set at log $T_o = 5.3$. However, solutions could not be computed down to this temperature. Note that the models were very sensitive to the starting values of $Em(T_c)$ and T_c, and the $Em(T_e) - T_e$ space was carefully scanned

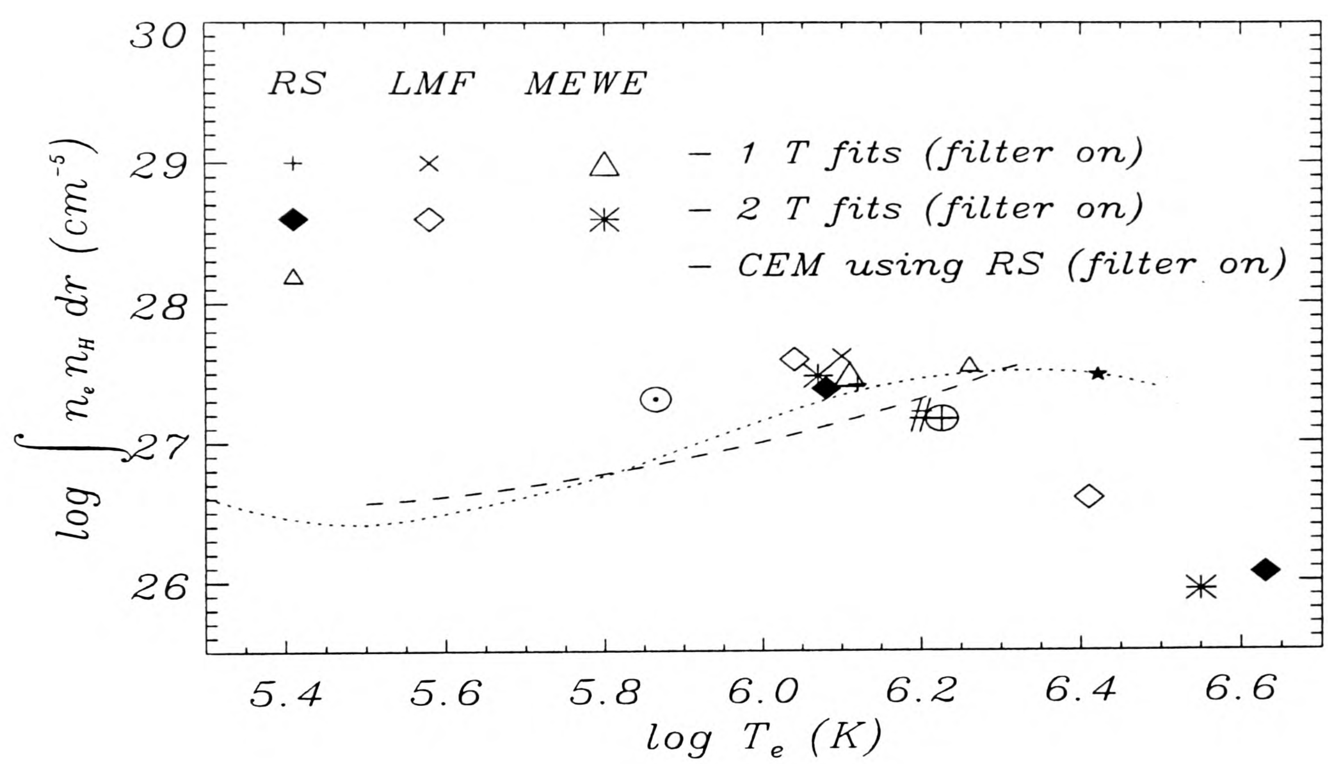

Figure 4.1: The *apparent* emission measure distribution for Procyon as computed from the spherically symmetric energy balance model (indicated by the dashed line). A solution could not be found in plane parallel geometry. The dotted line is the emission measure distribution as computed from the EUVE observations by Drake *et al.* (1995). The emission measures obtained with *Einstein* 1T fits using the HRI and IPC instruments, and *EXOSAT* (2T fit), are indicated as follows: # is the Em obtained from HRI (Jordan *et al.*, 1986), $\oplus$ is that from IPC (Schmitt *et al.*, 1985), $\odot$ is the low temperature component from the *EXOSAT* observations, and $\star$ is its corresponding high temperature component (Schrijver, 1984).

at intervals of 0.01 dex around the region of the observations that were earlier considered to be more realistic, in order to find solutions for both geometries. Although a solution could not be obtained in plane parallel geometry, a spherically symmetric solution could be computed down to log T_o = 5.5, using starting values for the *apparent* coronal emission measure of log $Em(T_c)$ = 27.55 and for the coronal temperature of log T_c = 6.32. The resulting *apparent* EMD in spherically symmetric geometry, is shown in Figure 4.1.

Drake *et al.* (1995) have derived an emission measure distribution in the temperature range log T_e = 5.2 - 6.5 by fitting a first order cubic spline to the emission measures of individual ions that were observed in EUVE spectra of Procyon (also shown in Figure 4.1). They have adopted the ionisation balance calculations of Arnaud & Rothenflug (1985) for all elements, rather than the more recent calculations by Arnaud & Raymond (1992). As discussed in Chapter 2, this means that for high stages of ionisation of Fe, the lines which tend to be formed at lower temperatures and the derived emission measures will tend to be larger by up to a factor of 2. They argue that the di-electronic recombination rate used for Fe IX is too low, as suggested to them privately by Jacobs & Feldman.

Jordan (1995c) analysed the EUVE emission line fluxes published by Drake *et al.* (1995) and found a logarithmic coronal emission measure of 27.43 cm^{-5} and log T_c = 6.20 using the emissivities of Brickhouse *et al.* (1995). These values are in reasonable agreement with results of the spherically symmetric energy balance model (log $Em(T_c)$ = 27.55 at log T_c = 6.32), and the differences can be traced to the different ion balance used.

§4.4 A Model of the Lower Transition Region

Models of Procyon's lower transition region have been computed using the methods set out in Chapter 3, unless otherwise stated. The emission measure distribution was derived by the iterative method of recomputing the line fluxes (see Section 3.3.2 of Chapter 3).

Table 4.4: Atomic parameters for the observed lines (where relevant they are for the whole multiplet).

Ion	λ ($\AA$)	$\mathbf{F}_*$ ($erg\,cm^{-2}\,s^{-1}$)	$\Omega^{\diamondsuit}_{\mathbf{multiplet}}$	$\frac{\mathbf{n_E}}{\mathbf{n_H}}^{\dagger}$	$\log \mathbf{T}^{\spadesuit}_{\mathbf{gmax}}$	$\frac{\mathbf{n_i}}{\mathbf{n_{ion}}}$
$Mg\,II$‡	2800	1.7×10^{6a}	16.2	3.8×10^{-5}	3.8	1.0
$C\,II$‡	1335	3.9×10^{4b}	6.3	3.6×10^{-4}	4.6	1.0
$Si\,III$	1206	3.5×10^{4a}	7.5	3.6×10^{-5}	4.8	1.0
$Si\,IV$‡	1400	9.1×10^{3a}	18.2	3.6×10^{-5}	4.8	1.0
$C\,IV$‡	1550	6.8×10^{4b}	9.8	3.6×10^{-4}	5.0	1.0
$N\,V$‡	1240	1.1×10^{4b}	7.4	8.9×10^{-5}	5.3	1.0
$O\,VI$	1032	1.4×10^{3c}	3.9^d	7.4×10^{-4}	5.5	1.0

† - Solar photospheric abundances from Anders & Grevesse (1989) and Grevesse *et al.* (1992).
‡ - Parameters refer to the whole multiplet.
♢ - For references see Table 1.2 of Chapter 2, unless otherwise stated.
♠ - Temperature where the contribution function $g(T_e)$ has its maximum value.
a - from high dispersion spectra.
b - from low dispersion spectra.
c - from *Copernicus* observations.
d - Brown & Jordan (1981).

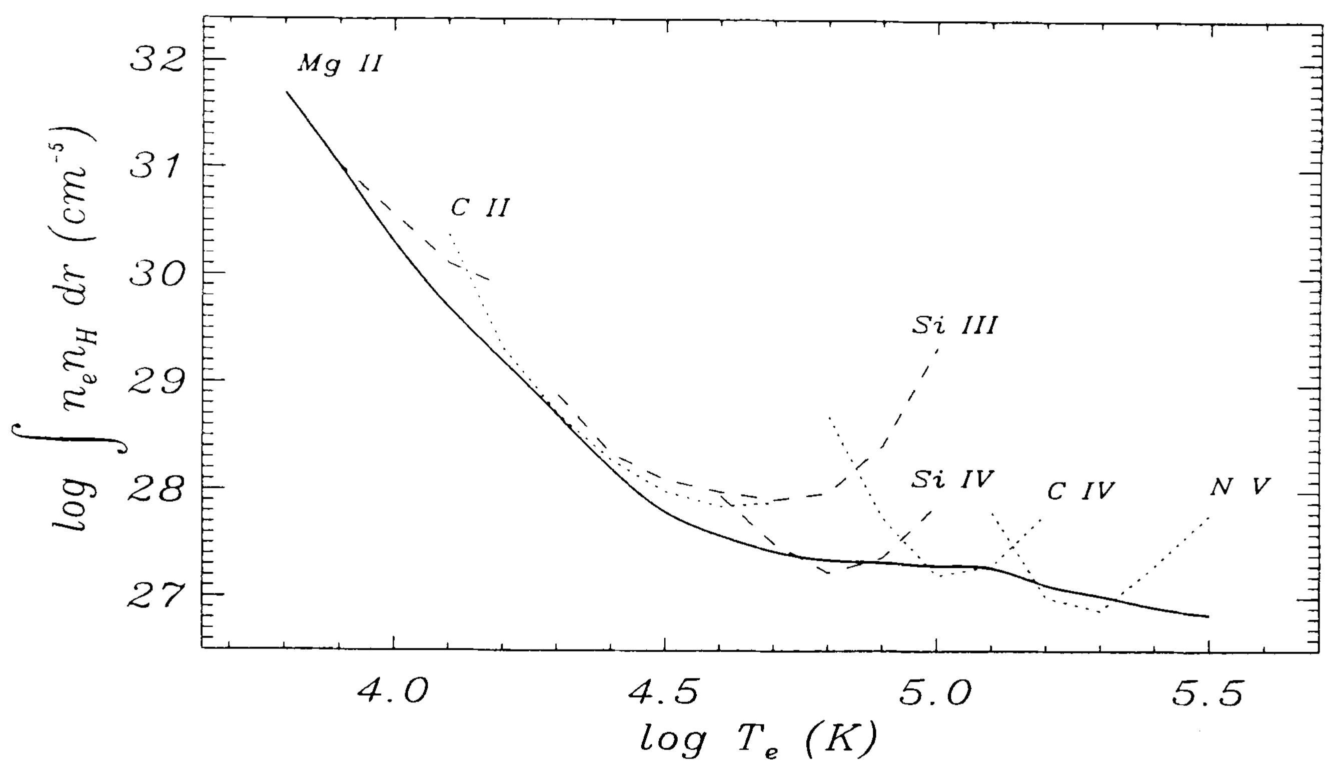

Figure 4.2: The recomputed EMD (full line) for Procyon in relation to the loci of the observed line fluxes from IUE. Plane parallel geometry has been assumed. The dashed loci indicate the lines for which fluxes were obtained from the high dispersion spectra while the dotted loci represent those lines for which the low dispersion spectra were used (see text for discussion).

Fluxes for the transition region emission lines are available from IUE observations (Brown & Jordan, 1981) and are listed in Table 4.4. The fluxes from the low dispersion spectra have been adopted except for the cases where there was blending or noise spots. In such cases, the high resolution spectra have been used, as indicated in Table 4.4.

Brown & Jordan (1981) adopted the O VI (1032 Å) flux from the *Copernicus* observations of Evans *et al.* (1975). However, calibration problems with the satellite are suspected which lead to uncertainties in the line fluxes of at least a factor of two (Brown & Jordan, 1981). I have chosen to exclude this line from this analysis.

The above authors adopted a height of 4500 km for the base of the transition region above its photosphere (*c.f.* 2000 km in the Sun) and I have adopted this height. The resulting optimum emission measure distribution fit to the IUE fluxes is shown in Figure 4.2.

Table 4.5: The observed and adopted turbulent velocities ($< v_{turb} >_{obs}$ and $< v_{turb} >_e$ respectively), for Procyon. The former was derived from the FWHM of the C IV (1548 Å) line observed by Wood, Harper & Linsky (1996) using equations (3.40) & (3.41), while the latter was calculated from (3.42).

Ion	log $\mathbf{T_e}$ (K)	$< v_{turb} >_{obs}$ $(km\, s^{-1})$	$< v_{turb} >_e$ $(km\, s^{-1})$
CIV	5.0	56.6	–
–	5.3	–	67.3

Brown & Jordan (1981) derived a turbulent velocity $< v_{turb} >_{obs} = 54$ km s^{-1} from the C IV lines. This is in good agreement with the adopted value of 56.6 km s^{-1} (see Table 4.5) derived from the GHRS observations of Procyon by Wood, Harper & Linsky (1996). Above $T_e = 2 \times 10^5$ K, a constant value of $< v_{turb} >_e = 67.3$ km s^{-1} was used, based on equation (3.42).

§4.5 The Full Transition Region and Coronal Model

The procedure for linking the EMD's of the lower and upper transition region at the base temperature T_o, is described in Section 3.6 of Chapter 3. Here, only the spherically symmetric case is considered. The resulting emission measure distribution is discussed below.

4.5.1 The Combined Models

The resulting *real* EMD in spherically symmetric geometry, is shown in Figure 4.3. Table 4.6 lists the corresponding values of temperature (T_e), *real* emission measures ($Em(0.3)$), total, gas and electron pressures (P_T, P_g and P_e, respectively), as well as the *absolute* radial extension ($r - R_*$) of the atmosphere, that were derived for the spherically symmetric model.

Looking at Figure 4.3, the following features show marked differences from the EMD's derived for the five dwarfs in Chapter 3:

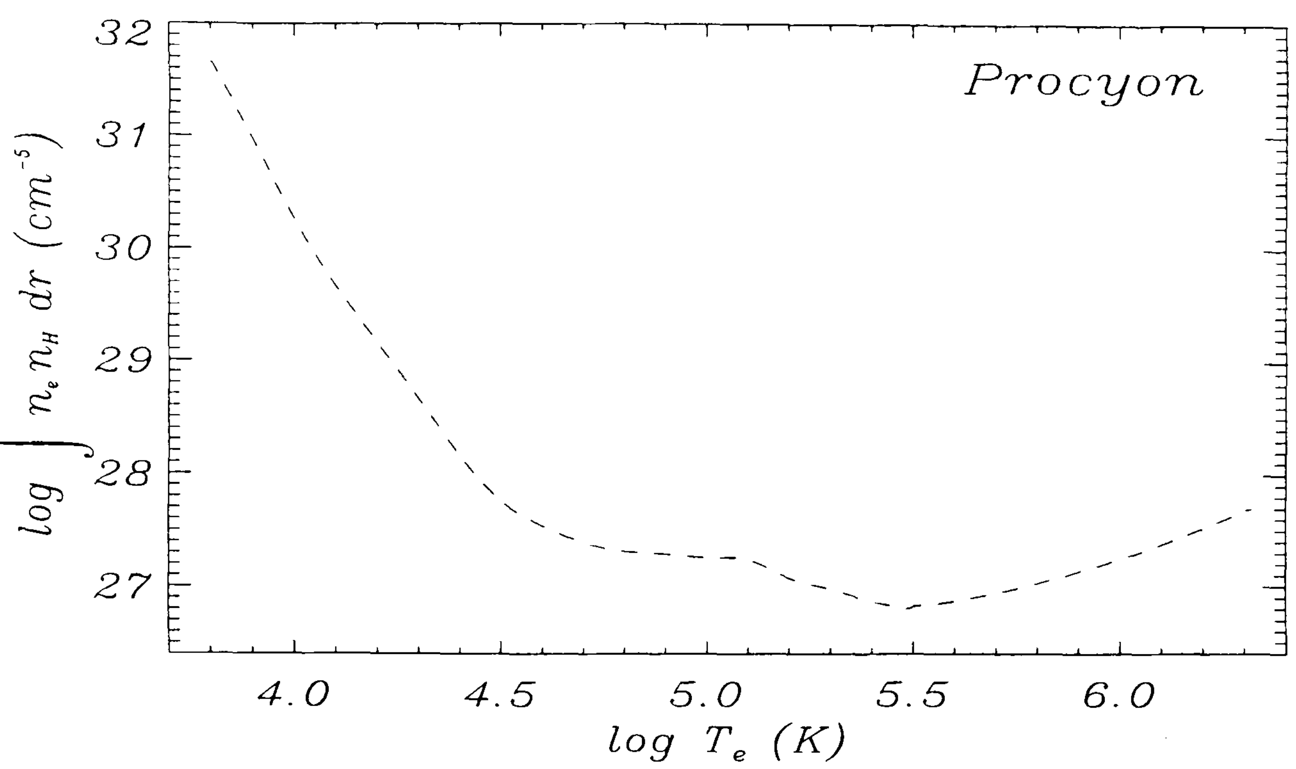

Figure 4.3: The *real* EMD for the lower and upper transition region of Procyon computed in spherical symmetry, using IUE line fluxes for temperatures below 2×10^5 K, while for higher temperatures energy balance was assumed.

i. The coronal value of $Em(T_c)$ relative to the emission measure at log T_e = 3.8 K is about an order of magnitude smaller in Procyon.

ii. The spherically symmetric model for the upper transition region links very smoothly onto its corresponding lower transition region model.

4.5.2 The Minimum in the EMD

Since the line fluxes in the temperature range log T_e = 5.3 - 5.5 are not well determined owing to the calibration uncertainties associated with the *Copernicus* spectra, there is no *accurate* way of determining where the minimum in the EMD occurs from line fluxes in this region. However, the O VI flux, even with an uncertainty of a factor of 2, suggests that the EMD continues to *decrease* above 2×10^5 K. As discussed above, energy balance models cannot be produced with a minimum in the EMD at log T_e = 5.3. The *minimum*

Table 4.6: Calculated parameters using the spherically symmetric model for Procyon, where the *real* emission measures ($Em(0.3)$), the *total*, *gas* and *electron* pressures (P_T, P_g and P_e, respectively), and the *absolute* radial extent of the atmosphere ($r - R_*$), are given as a function of the temperature (T_e).

log $\mathbf{T_e}$ (K)	log $Em(0.3)$ (cm^{-5})	log (P_T/k) ($cm^{-3}\,K$)	log (P_g/k) ($cm^{-3}\,K$)	log (P_e/k) ($cm^{-3}\,K$)	$r - R_*$ ($10^9\,cm$)
3.80	31.67	16.39	16.23	14.58	4.50
3.90	30.97	15.85	15.67	14.79	5.46
4.00	30.26	15.63	15.45	14.98	6.04
4.10	29.66	15.56	15.40	15.03	6.29
4.20	29.16	15.54	15.37	15.04	6.42
4.30	28.66	15.53	15.37	15.06	6.48
4.40	28.16	15.53	15.37	15.07	6.52
4.50	27.76	15.53	15.37	15.09	6.54
4.60	27.54	15.53	15.38	15.10	6.55
4.70	27.39	15.53	15.39	15.10	6.56
4.80	27.31	15.53	15.39	15.11	6.58
4.90	27.29	15.52	15.40	15.12	6.60
5.00	27.26	15.52	15.41	15.13	6.64
5.10	27.24	15.52	15.42	15.14	6.68
5.20	27.08	15.52	15.43	15.15	6.74
5.30	26.98	15.52	15.44	15.15	6.81
5.40	26.87	15.52	15.45	15.16	6.88
5.50	26.82	15.52	15.45	15.17	6.98
5.60	26.87	15.52	15.36	15.08	7.23
5.70	26.94	15.51	15.39	15.11	7.64
5.80	27.03	15.51	15.41	15.13	8.34
5.90	27.13	15.51	15.42	15.14	9.62
6.00	27.25	15.50	15.43	15.15	12.1
6.10	27.38	15.48	15.43	15.15	17.2
6.20	27.52	15.46	15.41	15.13	28.6
6.30	27.68	15.40	15.37	15.08	57.7
6.32	27.70	15.38	15.35	15.06	68.1

temperature at which the minimum in the EMD occurs is at log $T_e = 5.5$, and this model joins on smoothly on to the lower transition region. Thus, the EMD of Procyon differs from that of the five dwarfs in that the minimum in the EMD occurs at a higher temperature. This appears to be the natural consequence of an energy balance solution.

§4.6 Electron Densities - Comparison of Models and Observations

There are no density sensitive line ratios observable with IUE in the UV spectrum of Procyon. Brown & Jordan (1981) used the hottest lines observable (N V and O VI) to determine the *minimum* acceptable pressure, by attributing this emission to an isothermal corona, so that

$$P_{min}/k = 1.3 \times 10^4 (Em(T_{max})\, g_*\, T_{max})^{1/2} \tag{4.1}$$

For N V this gives $P_e/k = 2.5 \times 10^{14}$ cm^{-3} K. In 1981, no X-ray emission had been detected from Procyon. Brown & Jordan (1981) used the observed line widths and profiles of transition region lines to place further limits on the pressure. The expression for the opacity at the line centre in a Doppler broadened line is given by

$$\tau_o = 1.50 \times 10^{-15} \lambda(\mathring{A}) \frac{f_{ij}}{b} \frac{n_E}{n_H} \int \frac{n_i}{n_{ion}} \frac{n_{ion}}{n_E} n_H \, dh \tag{4.2}$$

where f_{ij} is the absorption oscillator strength, $b = FWHM/2\sqrt{\ln(2)}$ and is defined as the Doppler broadening parameter in the region of line formation. These parameters can be combined with the expression for the line flux, to replace $\int n_H \, dh$ by $\int n_e n_H \, dh \,/\, n_e$. Thus,

$$\tau_o P_e/k = 9.7 \times 10^{-8} \frac{g f \lambda(\mathring{A})^3 F_* T_e^{3/2}}{\Omega \Delta\lambda(\mathring{A})} exp(\frac{1.44 \times 10^8}{\lambda(\mathring{A}) T_e}) \tag{4.3}$$

where g is the statistical weight of the lower level, Ω represents the collision strength (see Table 4.4), F_* is the emission line flux at the star (given in Table 4.4), and $\Delta\lambda$ is the FWHM of the line (in Å). Brown & Jordan (1981) argued that the lines of Si III (1206 Å) and C II (1335 Å) were optically thick, from their line widths and profiles, compared with lines of

Table 4.7: Estimates of optical depths (τ_o) for some lines observed in the lower transition region of Procyon, using equation (4.1). The calculated mass column densities ($\int n_H\, dh$) were computed from the spherically symmetric model.

Ion	λ ($\AA$)	f_{ij}	$FWHM$ ($km\, s^{-1}$)	$\int n_H\, dh$ (cm^{-2})	τ_o
$C\,II$	1335	0.27^a	88^c	4.9×10^{17}	1.46
$Si\,IV$	1402	0.27^b	77^d	1.0×10^{17}	0.01
$C\,IV$	1548	0.19^a	79^d	1.3×10^{17}	0.13

a - from Wiese, Smith & Miles (1966).
b - from Wiese, Smith & Miles (1969).
c - from Brown & Jordan (1981).
d - from Wood, Harper & Linsky (1996).

lower opacity (*e.g.* C IV 1548, 1550 Å). Putting $\tau_o \geq 1$, or $\tau_o \leq 1$, into equation (4.3) then places limits on P_e. They found $P_e/k \geq 2.5 \times 10^{14}$ cm^{-3} K at 10^5 K, but $P_e/k \leq 3.8 \times 10^{14}$ cm^{-3} K at 4×10^4 K.

The line opacities from the present model have been derived to see whether or not they are consistent with the conclusions reached by Brown & Jordan (1981), and these are given in Table 4.7. The electron pressures computed in this model (see Table 4.6) are higher than those found by Brown & Jordan (1981). Using the *observed* line width, which will overestimate the Doppler width if the line is optically thick, the lines of Si IV and C IV are indeed optically thin, and the lines of C II do have a higher opacity ($\sim$ 1.5). At 4×10^4 K, the pressure in the present model is a factor of $\sim$ 3.3 larger than that proposed by Brown & Jordan (1981), which can be considered as reasonable agreement given the approximate nature of the opacity estimate.

The flux ratios of the density sensitive O IV] (1400 Å) multiplet lines are potentially the most accurate diagnostic for determining transition region densities. Wood, Harper & Linsky (1996) detected this multiplet using the GHRS spectra of Procyon and although the strongest line was prominent, the weaker lines were blended with the Si IV (1404 Å) line. From the observed ratios they calculated an upper limit for the electron density at $T_e \sim 1.5 \times 10^5$ K of log $n_e \leq 10.3$. This gives a pressure of log $P_e/k \leq 15.5$ consistent with the pressures found from the present model.

The low transition region pressure, $P_e/k = 3.2 \times 10^{14}$ cm^{-3} K at log $T_e = 5.00$, in model (c) of Brown & Jordan (1981), compared with the higher X-ray pressure $P_e/k \leq 6.4\times 10^{14}$ cm^{-3} K at log $T_e = 6.18$, led Jordan *et al.* (1986) to suggest the presence of supergranulation structures similar to those seen in the Sun with the UV emission originating from limited regions ($\sim$ 50%) of the stellar disk. A high coronal pressure was also derived by Drake *et al.* (1995), from the line ratios of the Fe XIV lines at 211.32 Å and 264.79 Å, for which log P_e was found to have an upper limit of 16.0 at log T_e = 6.3. However, the lines concerned are weak and blended, and this high pressure cannot be considered as reliable (see Jordan, 1995a,b,c). The coronal pressure of 1.59×10^{16} cm^{-3} K derived by Schmitt *et al.* (1994) at log T_c = 6.3, based on Fe XIV lines is also not reliable, owing to a blend with the S X line at 264.24 Å.

Wood, Harper & Linsky (1996) also concluded that higher coronal pressures compared with those of the transition region are due to inhomogeneities in the star's atmosphere (thus supporting the argument of Jordan *et al.*, 1986), on the grounds that such a pressure difference between the transition region and corona does not agree with spherically symmetric models in hydrostatic equilibrium, (but they did *not* compute such models).

In the present model, the *electron* pressure hardly varies between the low transition region and corona. This is due to the inclusion of a wave pressure term throughout the atmosphere, which has not been systematically included in previous models. Thus, the factor of 2 discrepancy between the transition region and coronal electron pressures found by Jordan *et al.* (1986) is largely removed. To within the present uncertainties in the emission measures and line widths, and in view of the good match between the EMD's of the lower and upper transition region, the new model is consistent with an atmosphere where both transition

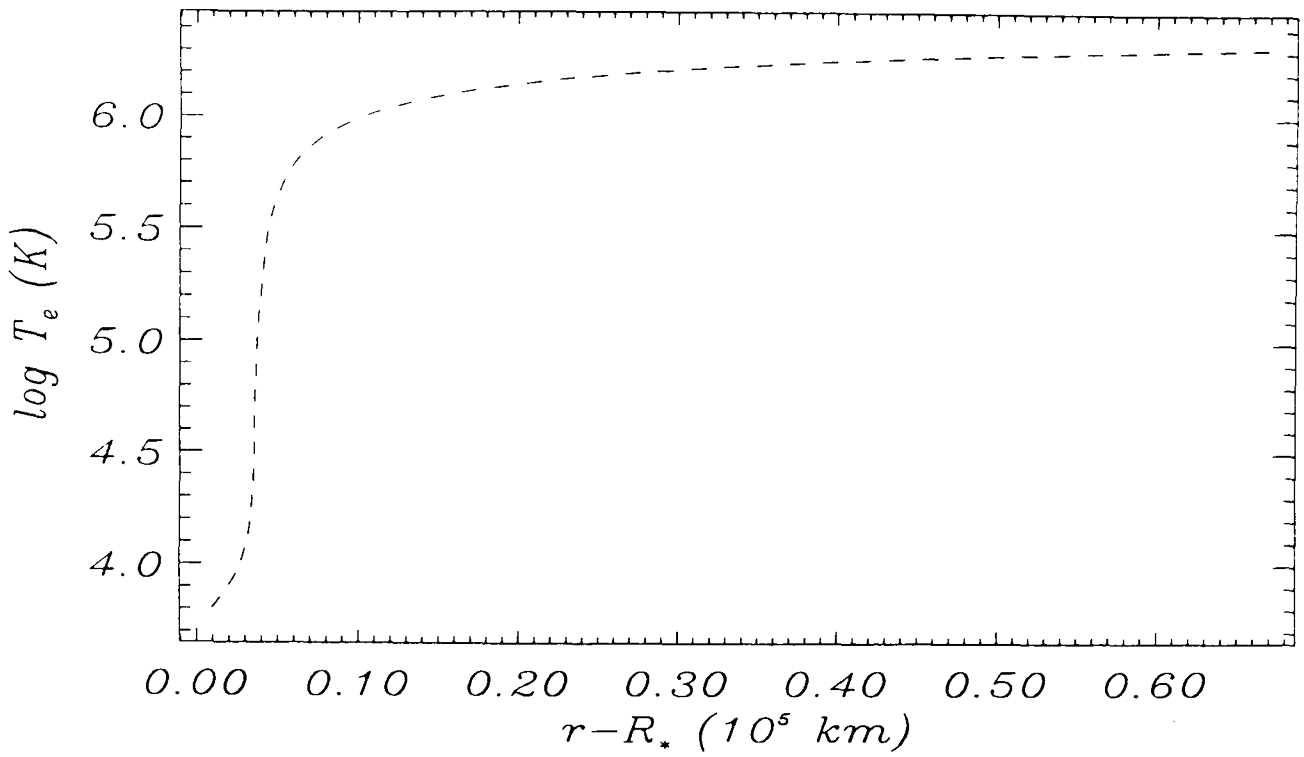

Figure 4.4: The variation of temperature with with the *absolute* radial extension ($r - R_*$) of Procyon, assuming a spherically symmetric geometry.

region and coronal material is approximately uniform in its spatial distribution. This is further supported from an analysis of EUVE observations by Schmitt *et al.* (1994), who proposed that Procyon's coronal structure consists of loops which are evenly distributed in order to account for the star's uniform coronal emission.

Figure 4.4 illustrates the variation of temperature with the *absolute* radial extension ($r - R_*$) of Procyon, in spherically symmetric geometry. The transition region temperature gradient is less steep than in the five dwarfs.

§4.7 Energy Requirements

The radiative fluxes (ΔF_R) of the lower transition region ($3.8 < \log T_e < 5.5$; note that the upper limit of this temperature range corresponds to the value of T_{min} for Procyon), are listed in Table 4.8, averaged over 0.3 dex. As for the five dwarfs, the bulk of the radiation

Table 4.8: The radiative losses (ΔF_R in erg cm^{-2} s^{-1}, averaged over 0.3 dex) in the lower transition region (log T_e = 3.8 - 5.5) of the Procyon, as computed for the spherically symmetric model. (The numbers in brackets indicate powers of 10).

log $\mathbf{T_e}$	ΔF_R	log $\mathbf{T_e}$	ΔF_R
3.80	4.6(6)	4.80	9.3(5)
3.90	9.4(6)	4.90	1.1(6)
4.00	2.7(7)	5.00	1.3(6)
4.10	3.0(7)	5.10	1.4(6)
4.20	1.7(7)	5.20	1.0(6)
4.30	7.4(6)	5.30	5.9(5)
4.40	2.8(6)	5.40	3.7(5)
4.50	1.3(6)	5.50	2.6(5)
4.60	9.7(5)		
4.70	8.6(5)		

is emitted at log T_e = 4.1, which corresponds to emission from Lyman α. (Since the EMD below log T_e < 4.0 is not well defined (see discussion in Section 3.3.2), only the EMD where log $T_e \geq 4.0$ will be considered in the following calculations). Table 4.9 gives the *total* radiative flux F_R, summed over the temperature interval log T_e = 4.0 - 5.5, the conductive fluxes at the base and coronal temperatures ($F_c(T_o)$ and $F_c(T_c)$, respectively), the coronal radiative flux $F_R(T_c)$, and the sum $F_c(T_c)$ + $F_R(T_c)$. The uncertainties associated with the above fluxes are as follows: σ_{F_R} ~ 20%, σ_{F_c} ~ 30% and σ_{F_m} ~ 40% (see discussion in Section 3.7.2 of Chapter 3).

The energy conducted down at 3×10^5 K ($F_c(T_o)$ = 3.8×10^5 erg cm^2 s^{-1}), *can* just be balanced by the radiation from the layer immediately below (F_R(log T_e = 5.3 - 5.5) = 3.7×10^5 erg cm^2 s^{-1}) to within uncertainties. Thus, unlike the situation in the five dwarfs, there is no need for significant area factors to raise radiation losses. The ratio of the conductive flux to the radiative flux from the corona is also *smaller* in Procyon.

Mullan & Cheng (1994) have proposed that acoustic waves may be responsible for heating Procyon's atmosphere. In contrast, Brown & Jordan (1981) found that acoustic waves

Table 4.9: The radiative and conductive energy losses (F_R and F_c, respectively, and in units of erg cm^2 s^{-1}), in the upper transition region and corona of Procyon, as computed for the spherically symmetric model. (The numbers in brackets indicate powers of 10).

$F_R(T)^a$	$F_c(T_o)^b$	$F_c(T_c)^c$	$F_R(T_c)^d$	$F_m(T_c)^e$
3.6(7)	3.8(5)	5.1(5)	3.0(5)	8.1(5)

a - The *total* radiative losses ($F_R = \Sigma \Delta F_R$), for the temperature interval log T_e = 4.0 - 5.5 K.
b - F_c conducted *down* at log $T_e = 5.5$.
c - F_c conducted *down* from the corona.
d - F_R from the corona.
e - $F_m(T_c) = F_c(T_c) + F_R(T_c)$

Table 4.10: The acoustic fluxes (F_a) for the transition region lines shown and their corresponding gas densities ρ, as computed from the present model. The FWHM used in this calculation are as shown in Table 4.7. C II is optically thick and gives only an upper limit.

Ion	λ ($\AA$)	**log** $\mathbf{T_e}$	ρ (cm^{-3})	$\mathbf{F_a}$ ($erg\,cm^{-2}\,s^{-1}$)
$C\,II$	1335	4.3	1.1(−13)	< 9.8(6)
$Si\,IV$	1402	4.8	4.0(−14)	4.7(6)
$C\,IV$	1548	5.0	2.7(−14)	3.9(6)

cannot heat the atmosphere beyond $\sim 10^4$ K, based on the electron densities available. Using the FWHM from the GHRS observations of Wood, Harper & Linsky (1996), I have re-computed the acoustic fluxes (F_a) implied by the present models using equation (3.67) of Chapter 3. (The value of $< v_{turb}^2 >$ adopted in this calculation is given in Table 4.5). Table 4.10 gives the resulting acoustic fluxes. The uncertainties of the FWHM quoted by Wood, Haprer & Linsky (1996) are $\sim$ 2% and these, in conjunction with the uncertainty associated with P_e yield $\sigma_{F_a} \sim 20\%$.

From Table 4.10, it appears that the acoustic flux at $T_e \sim 2 \times 10^4$ K is ample to account for the energy losses from the transition region and corona. The decrease in F_a between

2×10^5 K and 10^5 K is also sufficient to heat this part of the transition region. Similarly, F_a at 10^5 K exceeds the coronal energy losses ($F_c(T_c)$ and $F_R(T_c)$). These results, together with those of Mullan and Cheng (1994) and Drake *et al.* (1995), show that acoustic waves *can* heat the atmosphere of Procyon. The models discussed above are consistent with a uniform spatial distribution of material in the transition region and corona. This may imply that convection is not strong enough to confine the magnetic field to small areas in supergranulation boundaries, and magnetic modes of heating may be weaker. Although the evidence for abundance gradients in other stars is weak, the lack of small spatial scales in the magnetic field, proposed as source of a FIP effect, is consistent with the absence of a FIP effect in Procyon.

§4.8 *Summary*

Models of the transition region and corona of Procyon (α CMi) have been made, following a similar approach to that used for modelling the outer atmospheres of the five dwarfs (Chapter 3). The IUE fluxes from Brown & Jordan (1981) were used to compute EMD for the lower transition region, while the upper transition region was modelled by assuming energy balance between conduction and radiation. Both plane parallel and spherically symmetric geometries were investigated; however, an energy balance solution could only be obtained for the latter.

The energy balance model of the upper transition region joined smoothly to the lower transition region with a minimum in the EMD at log T_o = 5.5; although the fluxes of lines found between log T_e = 5.3 - 5.5, are uncertain, they do indicate a decreasing emission measure. Further observations of this region would be of great value. The higher value of T_c for the minimum emission measure is a practical consequence of the energy balance models. The EMD of Procyon was found to differ in other respects from those of the five dwarfs, *e.g.* the lower coronal emission measure relative to that of the low transition region.

These differences are probably due to the earlier spectral type and lower gravity of this star. Owing to the inclusion of wave pressure, the variation of the *electron* pressure derived from the present model is small throughout the transition region and corona. The transition region pressure derived from line fluxes is now consistent with the spherically symmetric uniform model and there is no need to invoke area factors to account for previous estimates of the electron pressure.

The energy requirements in the transition region and corona were examined. The radiation losses from the lower transition region must be balanced by non-thermal energy input other than conduction from the corona, since there is no significant energy imbalance between the conductive flux at the base of the upper transition region and the radiation losses immediately below. It was also shown that acoustic waves *can* provide the heating required in the transition region and corona of Procyon. This supports the findings of Mullan & Cheng (1994) and Drake *et al.* (1995), using other arguments.

From the EUVE spectra presented by Drake *et al.* (1995), it is clear that longer exposures of Procyon are required to enable a more definite identification of the weak lines used in their estimates of electron density.

Chapter 5

Conclusions

§5.1 *Summary and Conclusions*

In this thesis, I have modelled the structure of the transition regions and coronae of a set of late type stars for which it is possible to obtain high quality IUE and X-ray spectra, with the aim of investigating the heating requirements of their outer atmospheres.

The stars examined were the five dwarfs, χ^1 Ori (G0V), ϵ Eri (K2V), ξ Boo A (G8V), α Cen A (G2V) and α Cen B (K0V)), and the subgiant Procyon (α CMi F5 IV-V). Using new atomic data and the ROSAT observations, I have computed improved models of the lower transition regions and new models of the upper transition regions and coronae of these stars. These stars are important in understanding a range of correlations observed from a larger sample of stars for which only more limited observations are currently possible.

The analysis and reduction of the raw X-ray data from ROSAT was described in Chapter 2. Particular emphasis was placed in understanding the differences and limitations of the radiative power loss codes (Raymond-Smith, Landini-Monsignori Fossi, and Mewe, Gronenschild & van den Oord). The emission measures derived using the LMF code were systematically a factor of 2 higher than their corresponding values from the RS code. The former code was found to yield lower temperatures than the latter. From the discussions given in Chapter 2 it is evident that the choice of atomic physics, (in particular the choice of the ion balance calculations) in the different codes, are factors responsible for these disagreements. Work is in progress by the above three groups to reconcile the differences and improve the codes.

The lower transition regions were remodelled using previously obtained IUE line fluxes and up-to-date atomic parameters and abundances. Rather than use a maximum entropy approach I have obtained a best fit to the emission measure *loci* which reproduces the fluxes to within ± 0.1 dex.

The upper transition region was modelled assuming a balance between the energy deposited by thermal conduction and that lost by radiation, in both plane parallel and spherically symmetric geometries. The models were made in hydrostatic equilibrium, and unlike the earlier ones, they include a systematic treatment of wave pressure. Comparisons of the alternative fits to the ROSAT observations with results from EUVE, showed that the 1T (RS & LMF) and the CEM fits give the most consistent results.

The models of the transition regions and coronae were combined using an iterative procedure to give the full distribution between the corona and base of the transition region. The calculations were carried out assuming that the emission at each temperature occurs in a spatially uniform layer. The spherically symmetric energy balance models linked on to the lower transition region to within ± 0.15 dex, which in view of the inherent errors is excellent agreement. On the other hand, the match between the plane parallel models was not as good. It is therefore clear that above log T_e = 5.3, the outer atmospheres of these stars are better described by spherical symmetry, and that plane parallel geometry should be treated as an approximation. Thus, new models have been produced which now cover the whole region between the low transition region and corona.

Calculations of the conductive fluxes at the base of the transition region show that in the five dwarfs the energy cannot be radiated from the layers *immediately* below. This may either indicate that the emission is from restricted areas, so that the *local* radiation losses are larger, or that a process such as non-classical conduction allows the energy to be deposited over a larger temperature range. Magnetic heating is required since for the five dwarfs pure acoustic waves cannot carry sufficient flux.

Apart from α Cen A (for which the coronal temperature is not known), the coronal emission measures and pressures found from the plane parallel models, agree quite well with those predicted using Hearn's minimum energy loss hypothesis. The differences arise because the ratios $F_c(T_c)/F_R(T_c)$ are not precisely that determined by the m.e.l. assumption.

Models of transition region and corona of Procyon (α CMi) were investigated in plane parallel and spherically symmetric geometries. An energy balance solution could not be obtained for the former, but the spherically symmetric solution of the upper transition region matched smoothly on to the model of the lower transition region. The temperature of the minimum EMD was found at log T_e = 5.5, higher than the value of 5.3 found in main-sequence stars. This is a consequence of the energy balance. Further observations are required to improve the empirical EMD around this temperature range. The present model was found to differ in several respects from those of the five dwarfs, and this may be due to the earlier spectral type and lower gravity of this star. Thus, in contrast to earlier models, where the electron pressure appeared to be higher in the corona than in the transition region, there is no need to invoke supergranulation area factors.

The conductive fluxes at the base of the upper transition region can almost be matched by the radiation losses just below this point. This implies that there is a non-thermal heating of the low transition region. It appears that the dissipation of waves is able to heat the lower transition region, and that there is sufficient flux at 3×10^5 K to heat the overlying corona.

§5.2 *Suggestions for Future Work*

The gaps in the current state of affairs are evident, starting from the atomic physics, diagnostic techniques and instrumental resolution.

Two important X-ray missions are planned for 1998. The first is the European *X-ray Multiple Mirror* (XMM). This consists of three identical nests of grazing incidence telescopes whose spectral resolution is highly increased by reflection-grating spectrometers, such that $E/\Delta E = 300$ at 1.5 keV. The gratings will operate simultaneously with X-ray sensitive CCD detectors to provide resolved spectra in the 0.1 - 10 keV energy band. The second mission is NASA's *Advanced X-ray Astrophysical Facility* (AXAF) which is a direct successor to the *Einstein Observatory.* The teloscope mirror consists of four nested reflecting surfaces in a Wolter-I type arrangement, with a resolution of 0.3 arcseconds. A High Resolution Camera (HRC) with greatly improved specifications over ROSAT, will be used for high resolution imaging, fast timing measurements, as well as for observations requiring both. Further, the AXAF CCD Imaging Spectrometer (ACIS) will carry out simoultaneous imaging and spectroscopy. Its spatial and spectral resolution are an order of magnitude better than those of the *Einstein* IPC.

It will feature a newly developed X-ray bolometer for high-resolution spectroscopy (ΔE ~3eV). Further, two Transmission Grating Spectrometers (TGS) will yield high resolution spectra ($E/\Delta E$=800 at 1 keV) from which new improved values of the coronal parameters can be determined.

The recent launch of the *Solar and Heliospheric Observatory* (SOHO), in December 1995, will yield new observations of the Sun in the UV and EUV wavebands. Its position is at the L1 Lagrangian point, and thus its view of the Sun is unobstructed. Two major experiments on board, *The Coronal Diagnostic Spectrometer* (CDS) (Harrison & Sawyer, 1992), and the *Solar Ultraviolet Measurement of Emitted Radiation* (SUMER) (Lemaire *et al.*, 1992).

will carry out observations in the UV range (160 - 1600 Å) at high spatial and spectral resolution. This should improve our understanding of the structure and energy balance of the transition region and inner corona, for example by the measurement of line widths above 2×10^5 K.

The importance of an updated spectral analysis package and an updated spectral emission code was emphasised in Chapter 2. A major effort has been made to produce a spectral analysis package to analyse spectra from the Coronal Diagnostic Spectrometer (CDS) and the SUMER instruments on SOHO. The 1990 version of the LMF code is currently being updated (Monsignori Fossi & Landini, 1994); the addition of lines in the code and the higher spectral resolution of the solar observations will yield a more realistic model of the X-ray and EUV spectrum of optically thin plasmas which can be applied to improve the fitting of stellar parameters.

In stars, the form of the EMD from $\sim 2 \times 10^5$ K to $\sim 10^6$ K is still uncertain owing to a lack of observations of relevant lines. The *Orbiting Retrievable Far and Extreme Ultraviolet Spectrometers* (ORFEUS) which was launched in 1993, has made high resolution observations ($\lambda/5000$) of sources in the 390 and 1200 Å waveband (Hurwitz and Bowyer, 1996). Compared with other instruments, it has an advantage in the 800 Å - 1170 Å range. In particular, the O VI (1032 Å) lines formed at log T_e = 5.5 can be observed. With these data, more accurate constraints can be imposed on the EMD around the temperature minimum. Observations, as yet unpublished, have been made for Procyon, as well as for α Cen A & B. A second mission is scheduled for late 1996.

The models presented in this thesis have been made in plane parallel and spherically symmetric geometries, assuming a uniform spatial distribution of material. In practice, the distribution of material, as well as the area occupied may change between $\sim 10^5$ K and the corona as the magnetic field lines diverge. Thus, the deduced coronal emission measures and pressures should be treated as averages. Future models should treat the magnetic field and plasma simultaneously.

Line spectra from the upper transition region are available from EUVE observations. It is therefore possible to compute an optimum fit to this region as was done with the IUE line fluxes in the lower transition region, by using these fluxes as limits on the EMD. The lower transition region is a very narrow region, so that the geometry remains the same as a function of temperature. This is not the case for the upper transition region, where the magnetic fields expand and introduce a variable geometry as magnetic fields expand from the supergranulation boundaries to fill the corona. With improved EUVE or ORFEUS fluxes, the observed emission measures could be used to model the regions and the geometry deduced by comparison with energy balance models.

The element abundances have been assumed to be solar photospheric. Although there are claims that coronal and photospheric abundances differ in main-sequence stars, the conclusions are based on weak blended lines and cannot at present be considered to be definite. Even for the Sun, systematic new observations are needed to establish whether or not claimed abundance differences can be confirmed. These differences have not been found in Procyon. The radiative power loss also depends on the abundances.

Although some upper transition region and coronal line fluxes from EUVE observations have been published recently for the five dwarfs and Procyon (see Chapters 3 and 4), longer exposures of these targets are essential to identify and use the weak lines. The α Cen A & B system needs to be spatially resolved to determine the coronal flux and temperature of each star.

The line widths measured from IUE spectra should be replaced by more accurate values determined from GHRS spectra. Observations of ξ Boo A & B are planned in 1996, and other stars may be observed by others. GHRS spectra could also be used to improve the measurements of the transition region electron pressure.

The observations of the lower and upper transition region used have been made at different times. Since the line fluxes from the dwarf stars do show some (but not large) variations, probably associated with active regions, it would be valuable to obtain simultaneous observations in the UV and X-ray regions, and to monitor the X-ray emission to determine the contribution from active regions.

The present models refer to the region above $\sim 10^4$ K. Ultimately, these should be tied onto new models of the chromosphere, with the aim of obtaining full models of the atmospheres of late-type stars.

References

Alfvén, H.: 1947, *Mon. Not. R. astr. Soc.*, **107**, 211.

Allen, C., W.: 1973, *Astrophysical Quantities*, London, Athlone Press.

Anders, E., Grevesse, N.: 1989, *Geochimica et Cosmochimica Acta* **53**, 197.

Allen C.W.: 1973, *Astrophysical Quantities*, 3rd edn, Athlone Press, London.

Anderson, L. S., Athay, R. G.: 1989, *Astrophys. J.*, **336**, 1089.

Arnaud, M., Rothenflug, R.: 1985, *Astron. Astrophys. Suppl. Series*, **60**, 425.

Arnaud, M., Raymond, J.: 1992, *Astrophys. J.*, **398**, 394.

Athay, R.G.: 1966, *Astrophys. J.*, **145**, 784.

Athay, R.G.: 1976, *The Solar Chromosphere and Corona: Quiet Sun*, D. Reidel, Dordrecht, Holland, 504.

Athay, R.G., Holzer, T.E.: 1982, *Astrophys. J.*, **255**, 743.

Athay, R.G., White, O.R.: 1978, *Astrophys. J.*, **226**, 1135.

Athay, R.G., White, O.R.: 1979, *Astrophys. J. Suppl.*, **39**, 333.

Ayres, T.R., Marstad, N.C., Linsky, J.L.: 1981, *Astrophys. J.*, **247**, 545.

Ayres, T.R., Linsky, J.L., Simon, T., Jordan, C., Brown, A.: 1983, *Astrophys. J.*, **274**. 784.

Basri, G.: 1987, *Astrophys. J.*, **316**, 377.

Beckers, J.M.: 1972, *Ann. Rev. Astron. Astrophys.* **10**, 73.

Beckers, J.M.: 1976, *Physics of Solar Planetary Environments*, American Geophysical Union, D.J. Williams (Ed.), 89.

Bevington, P. R.: 1969, *Data Reduction and Error Analysis for the Physical Sciences.* New York: McGraw-Hill.

Biermann, L.: 1946, *Naturwissenschaften*, **33**, 118.

Biermann, L.: 1948, *Z. Astrophys.*, **25**, 161.

Blackwell, D.E., Lynas Gray, A.E., Smith, G.: 1995, *Astron. Astrophys.*, **296**, 217.

Böhm-Vitense, E., Canterna, R.: 1974, *Astrophys. J.*, **194**, 629.

Böhm-Vitense, E., Dettman, T.: 1980, *Astrophys. J.*, **236**, 560.

Bohn, H.U.: 1984, *Astron. Astrophys.*, **136**, 338.

Boland, B.C., Dyer, E.P., Firth, J.G., Gabriel, A.H., Jones, B.B., Jordan. C., McWhirter, R.W.P., Monk, P., Turner, R.F.: 1975, *Mon. Not. R. astr. Soc.*, **171**, 697.

Brandt, J.C.: 1970, *Introduction to the Solar Wind*, Freeman, San Francisco.

Brickhouse, N.S., Raymond, J.C., Smith, B.W.: 1995, *Astrophys. J. Suppl. Series* , **97**, 551.

Brown, A., Jordan, C.: 1981, *Mon. Not. R. astr. Soc.*, **196**, 757.

Burgess, A.: 1965, *Astrophys. J.* , **141**, 1588.

Burgess, A., Chidichimo, M.C.: 1983, *Mon. Not. R. astr. Soc.*, **203**, 1269.

Burgess, A., Tworkowski A.S.: 1976, *Astrophys. J. Letters*, **205**, L105.

Burgess, A., Summers, H.P., Cochrane, D.M., McWhirter, R.W.P.: 1977, *Mon. Not. R. astr. Soc.*, **179**, 275.

Burton, W.M., Jordan, C., Ridgeley, A., Wilson, R.: 1971, *Phil. Trans. R. Soc. Lond.*, **A270**, 81.

Cally, P.S.: 1990, *Astrophys. J.*, **355**, 693.

Catura, R.C., Acton, L.W., Johnson, H.M.: 1975, *Astrophys. J.*, **196**, L47.

Cochrane D.M., McWhirter, R.W.P.: 1983, *Physica Scripta*, **28**, 25.

Cook, J.W., Cheng, C.-C., Jacobs, V.L., Antiochos, S.K.: 1989, *Astrophys. J.*, **338**, 1176.

Cox, D. P.: 1970, *Ph.D. thesis*, University of Colorado, San Diego.

Dobson, A.K., Radick, R.R.: 1989, *Astrophys. J.*, **344**, 907.

Doschek, G.A., Cowan, R.D.: 1984, *Astrophys. J. Suppl. Series*, **56**, 67.

Drake, J.J., Laming, M.J.: 1995, *The Observatory*, **115**, No. 1126, 118.

Drake, J.J., Smith, G.: 1993, *Astrophys. J.*, **412**, 797.

Drake, J.J., Simon, T., Brown, A.: 1993, *Astrophys. J.*, **406**, 247.

Drake, J.J., Laming, M.J., Widing, K.G., Schmitt, J.H.M.M., Haisch, B., Bowyer, S.: 1995, *Science*, **267**, 1470.

Dufton, P.L., Kingston, A.E.: 1987, *J. Phys. B.*, **20**, 3899.

Dufton, P.L., Kingston, A.E.: 1991, *Mon. Not. R. astr. Soc.*, **248**, 827.

Dufton, P.L. Hibbert, A., Kingston, A.E., Doschek, G.A.: 1983, *Astrophys. J.*, **274**, 420.

Dupree, A.K., Foukal, P.V., Jordan, C.: 1976, *Astrophys. J.*, **209**, 621.

Edlén, B.: 1942, *Z. Astrophys.*, **22**, 30.

Edvardsson, B., Andersen, J., Gustafsson, B., Lambert, D.L., Nissen, P.E., Tomkin, J.: 1993, *Astron. Astrophys.*, **275**, 101.

Evans, R.G., Jordan, C., Wilson, R.: 1975, *Mon. Not. R. astr. Soc.*, **172**, 585.

Fawcett, B.C.: 1974, *Adv. Atomic Molec. Phys.*, **10**, 223.

Fawcett, B.C., Cowan, R.D., Kononov, E.Y., Hayes, R.W.: 1972, *J. Phys. B*, **5**, 1255.

Fiedler, R.A.S., Cally, P.S.: 1990, *Solar Physics*, **126**, 69.

Flannery, B.P., Ayres, T.R.: 1978, *Astrophys. J.*, **221**, 175.

Frieden, B.R.: 1972, *J. Opt. Soc. Am.*, **62**, 511.

Furenlid, I., Meylan, T.: 1990, *Astrophys. J.*, **350**, 827.

Gabriel, A.H.: 1976a, *Phil. Trans. R. Soc. Lond.*, **A281**, 339.

Gabriel, A.H.: 1976b, *The Energy Balance and Hydrodynamics of the Solar Chromosphere and Corona, IAU Coll. No. 36*, R.M. Bonnet, P. Delache, (Eds), 375.

Giacconi, R., Branduardi, G., Briel, U., *et al.*: 1979, *Astrophys. J.*, **230**, 540.

Gilman, P.A.: 1983, *Astrophys. J. Suppl. Series* , **53**, 243.

Giovanelli, R.G.: 1949, *Mon. Not. R. astr. Soc.*, **109**, 327.

Golub, L., Harnden, F.R. Jr., Pallavicini, R., Rosner, R., Vaiana, G.S.: 1982, *Astrophys. J.*, **253**, 242.

Gray, D.F.: 1976, *The Observation and Analysis of Stellar Photospheres*, J. Wiley &

Sons (New York), 426.

Grevesse, N., Noels, A., Sauval, A. J.: 1992, *Proceedings of the First SOHO Workshop, Anapolis, Maryland*, ESA SP-348, 305.

Grotrian, W.: 1939, *Naturwissenschaften*, **27**, 14.

Haisch, B., Drake, J.J., Schmitt, J.H.M.M.: 1994, *Astrophys. J.*, **421**, L39-L42.

Harper, G.M.: 1992, *Mon. Not. R. astr. Soc.*, **256**, 37.

Harrison, R.A., Sawyer, E.C.: 1992, *Proceedings of the First SOHO Workshop*, ESA SP-348, 17.

Hartmann, L., MacGregor, K.B.: 1980, *Astrophys. J.*, **242**, 260.

Hasinger, G., Prieto,A., Snowden, S.: 1994, *ROSAT Newsletter*, K. M. Smale (Ed.), NASA/GSFC, No.10, 4.

Hearn, A.G.: 1975, *Astron. Astrophys.*, **40**, 355.

Hearn, A.G.: 1977, *Solar Physics*, **51**, 159.

Hoffleit, D.: 1982, *The Bright Star Calaogue*, 4th Edition, Yale University, New Haven.

Hollweg, J.V.: 1982, *Astrophys. J.*, **254**, 806.

Hollweg, J.V., Jackson, S., Galloway, D.: 1982, *Solar Physics*, **75**, 35.

Howard, R.: 1977, *Ann. Rev. Astron. Astrophys.* **15**, 153.

Hundhausen, A.J.: 1972, *Coronal Expansion and Solar Wind*, Springer-Verlag, New York.

Hurwitz, M., Bowyer, S.,: 1996, *Astrophysics in the Extreme Ultraviolet*, IAU Colloquium 152, S. Bowyer and R.F. Malina (Eds), Kluwer Academic Publishers, 601.

Jacobs, V.L., Davis, J., Kepple, P.C., Blaha, M.: 1977, *Astrophys. J*, **211**, 605.

Jacobs, V.L., Davis, J., Rogerson, J.E., Blaha, M., Cain, J., Davis, M.: 1980, *Astrophys.J*, **239**, 1119.

Jamar, C., Macau-Hercot, P., Praderie, F.: 1976, *Astron. Astrophys.*, **52**, 373.

Jordan, C.: 1968, *J. Phys. B. Ser. 2*, , **1**, 1004.

Jordan, C.: 1969, *Mon. Not. R. astr. Soc.*, **142**, 501.

Jordan, C.: 1970, *Mon. Not. R. astr. Soc.*, **148**, 17.

Jordan, C.: 1980, *Astron. Astrophys.*, **86**, 355.

Jordan, C.: 1986, *Irish Astronomical Journal*, **17**, 227.

Jordan, C.: 1995a, *Astrophysics in the Extreme Ultraviolet*, IAU Colloquium 152, S. Bowyer and R.F. Malina (Eds), Kluwer Academic Publishers, 81.

Jordan, C.: 1995b, *Astrophysical Applications of Powerful New Databases*, S.J. Adelman and W.L. Wiese (Eds), ASP Conf. Series **78**, 371.

Jordan, C.: 1995c, *Laboratory, Solar and Stellar, Diffuse Astrophysical and Extragalactic Plasmas*, T.W. Hartquist, A.J. Willis (Eds), Kluwer, Dordrecht.

Jordan, C., Brown, A.: 1981, *Solar Phenomena in Stars and Stellar Systems*, Bonnet, R.M. and Dupree, A. (Eds), D. Reidel Publishing Company, 199.

Jordan, C., Linsky, J.L: 1987, *Exploring the Universe with the IUE Satellite*, Y. Kondo (Ed. in chief), Kluwer, Dordrecht, 259.

Jordan, C., Montesinos, B.: 1991, *Mon. Not. R. astr. Soc.*, **252**, 21.

Jordan, C., Wilson, R.: 1971, *Physics of the Solar Corona*, C.J., Macris (Ed.), D. Reidel, Dordrecht, Holland, 219.

Jordan, C., Ayres, T.R., Brown, A., Linsky, J.L., Simon, T.: 1987, *Mon. Not. R. astr. Soc.*, **225**, 903.

Jordan, C., Brown, A., Walter, F.M., Linsky, J.L.: 1986, *Mon. Not. R. astr. Soc.*, **218**, 465.

Jordan, C., Philippides, D., Pan, H.C., McMurry, A.: 1996, in preparation.

Judge, P.G.: 1986a, *Mon. Not. R. astr. Soc.*, **221**, 119.

Judge, P.G.: 1986b, *Mon. Not. R. astr. Soc.*, **223**, 239.

Kaastra, J.E.: 1992, *An X-ray Spectral Code for Optically Thin Plasmas*, Internal SRON-Leiden Report, V2.

Kamper, K.W., Wesselink, A.J.,: 1978, *Astron. J.*, **83**, 1633.

Karzas, W.J., Latter, R.: 1961, *Astrophys. J. Suppl. Series* , **6**, 167.

Kato, T.: 1976, *Astrophys. J. Suppl. Series*, **30**, 397.

Keenan, F.P., Dufton, P.L., Aggarwal, K.M., Kingston, A.E.: 1988, *Astrophys. J.*, **324**, 1068.

Kelch, W.L.: 1978, *Astrophys. J.*, **222**, 931.

Kelly, R.L.: 1987, *J. Phys. Chem. Ref. Data*, **16**, Suppl. 1.

Kelly, R.L., Palumbo, L.J.: 1973, *Atomic and Ionic Emission Lines Below 2000 Å*, NRL Rep. 7599 (Naval Res. Lab. Washington D.C.).

Kopp, R.A.: 1972, *Solar Physics*, **27**, 373.

Kopp, R.A., Kupperus, M.: 1968, *Solar Physics*, **4**, 212.

Kraft, R.P.: 1967, *Astrophys. J.*, **150**, 551.

Landini, M., Monsignori-Fossi, B.C.: 1970, *Astron. Astrophys.*, **6**, 408.

Landini, M., Monsignori-Fossi, B.C.: 1972, *Astron. Astrophys. Suppl. Series*, **7**, 291.

Landini, M., Monsignori-Fossi, B.C.: 1990, *Astron. Astrophys. Suppl. Series*, **82**, 229.

Landini, M., Monsignori-Fossi, B.C., Stern, R.: 1985, *Astrophys. J.*, **289**, 709.

Lemaire, P., *et al.*: 1992, *Proceedings of the First SOHO Workshop*, ESA SP-348, 13.

Lennon, D.J., Dufton, P.L., Hibbert, A., Kingston, A.E.: 1985, *Astrophys. J.*, **294**, 200.

Lighthill, M.J.: 1952, *Proc. Roy. Soc.*, A**211**, 564.

Linsky, J.L.: 1980, *Ann. Rev. Astron. Astrophys.*, **18**, 439.

Linsky, J.L., Diplas, A., Savage, B., Andrulis, C., Brown, A.: 1995, *Frontiers of Space and Ground-based Astronomy*, W. Wamsteker, M.S. Longair, Y. Kondo (Eds.), Kluwer, Dordrecht.

Lotz, W.: 1967, *Astron. Astrophys. Suppl. Series*, **14**, 207.

Lydon, T.S., Fox, P.A., Sofia, S.: 1993, *Astrophys. J.*, **413**, 390.

Maggio, A., Sciortino, S., Bookbinder, J., Harnden, F.R., Golub, L., Majer, P., Rosner, R., Vaiana, G.S.: 1987, *Astrophys. J.*, **315**, 687.

Mangeney, A., Praderie, F.: 1984, *Astron. Astrophys.*, **130**, 143.

Marcy, G.W., Basri, G.S.: 1989, *Astrophys. J.*, **345**, 480.

Mariska, J.: 1992, *The Solar Transition Region*, Cambridge University Press.

McCrea W.: 1929, *Mon. Not. R. astr. Soc.*, **89**, 718.

McWhirter, R.W.P., Thonemann, P.C., Wilson, R.: 1975, *Astron. Astrophys.*, **40**, 63.

Mendoza, C., 1981: *J. Phys. B.*, **14**, 2465.

Mewe, R.: 1972, *Solar Physics*, **22**, 45.

Mewe, R, Gronenschild, E.H.B.M.: 1981, *Astron. Astrophys. Suppl. Series*, **45**, 11.

Mewe, R., Gronenschild, E.H.B.M., van den Oord, G.H.J: 1985, *Astron. Astrophys. Suppl. Series*, **62**, 197.

Mewe, R., Schrijver, J., Sylwester, J.: 1980, *Astron. Astrophys. Suppl. Series*, **40**, 323.

Mewe, R., Kaastra, J.S., Schrijver, C.J., van den Oord., G.H.J., Alkemade, F.J.M.: 1995, *Astron. Astrophys.*, **296**, 477.

Mewe, R., Heise, J., Gronenschild, E.H.B.M., Brinkman, A.C., Schrijver, C.J., Den Boggende, A.J.F.: 1975, *Astrophys. J.*, **202**, L67.

Meyer, J.P.: 1985, *Astron. Astrophys. Suppl. Series*, **57**, 172.

Monsignori Fossi, B.C., Landini, M.: 1994, *Solar Physics*, **152**, 81.

Montesinos, B., Jordan, C.: 1993, *Mon. Not. R. astr. Soc.*, **264**, 900.

Morrison, R., MacCammon, D.: 1983, *Astrophys. J.*, **270**, 119.

Mullan, D.J., Cheng, Q.Q.: 1994, *Astrophys. J.*, **435**, 435.

Murthy, J., Henry, R.C., Moos, H.W., Landsman, W.B., Linsky, J.L., Vidal-Madjar, A., Gry, C.: 1987, *Astrophys. J.*, **315**, 675.

Musielak, Z. *et al.*: 1994, *Astrophys. J.*, **423**, 474.

Narain, U., Ulmschneider, P.: 1990 *Space Sci. Rev.*, **54**, No. 3/4, 377.

Noyes, R.W., Hartmann. L.W., Baliunas, S. L., Duncan, D. K., Vaughan, A.H.: 1984, *Astrophys. J.*, **279**, 763.

Nousek, J.A., Lesser, A.: 1993, *ROSAT Newsletter*, K. M. Smale (Ed.), NASA/GSFC, **8**, 13.

Nussbaumer, H., Storey, P.J.: 1983, *Astron. Astrophys.*, **126**, 75.

Nussbaumer, H., Storey, P.J.: 1986, *Astron. Astrophys. Suppl. Series*, **64**, 545.

Nussbaumer, H., Storey, P.J.: 1987, *Astron. Astrophys. Suppl. Series*, **69** , 123.

Oranje, B.J.: 1986, *Astron. Astrophys.*, **154**, 185.

Oranje, B.J., Zwaan, C., Middlekoop: 1982, *Astron. Astrophys.*, **110**, 30.

Pallavicini, R., Golub, L., Rosner, R., Vaiana, G.S., Ayres, T.R., Linsky, J.L.: 1981, *Astrophys. J.*, **248**, 279.

Pan, H.C., Jordan, C.: 1995, *Mon. Not. R. astr. Soc.*, **272**, 11.

Paresce, F.: 1984, *Astron. J.*, **89**, 1022.

Parker, E.N.: 1958, *Astrophys. J.*, **128**, 664.

Parker, E.N.: 1978 , *Astrophys. J.*, **201**, 494.

Parker, E.N.: 1983, *Astrophys. J.*, **264**, 635.

Pisarski, R., Seufert, E., Krishnaswamy, S.: 1994, *ROSAT Newsletter*, K. M. Smale (Ed.), NASA/GSFC, **10**, 10.

Pottasch, S.R.: 1963, *Astrophys. J.*, **137**, 945.

Pounds, K.A., *et al.*: 1993, *Mon. Not. R. astr. Soc.*, **260**, 77.

Priest, E.: 1982, *Solar Magnetohydrodynamics*, B.M. McCormack (Ed.), D. Reidel, Dordrecht, Holland.

Proudman, I.: 1952, *Proc. Roy. Soc.*, A**214**, 119.

Pye, J., McGale, P.A., Allan, D.J., Barber, C.R., Bertram, D., Denby, M., Page, C.G., Ricketts M.J., Stewart, B.C., West, R.G.: 1995, *Mon. Not. R. astr. Soc.*, **274**, 1165.

Raymond, J.C.: 1988, *Hot Thin Plasmas in Astrophysics*, R. Pallavicini (Ed.), 3.

Raymond, J.C.: 1990, *Astrophys. J.*, **365**, 387.

Raymond, J.C., Doyle, J.G.: 1981, *Astrophys, J.*, **247**, 686.

Raymond, J.C., Smith, B.W.: 1977, *Astrophys. J. Suppl. Series* , **35**, 419.

Reeves, E.M.: 1976, *Solar Physics*, **46**, 56.

Rumph, T., Bowyer, S., Vennes, S.: 1994, *Astron. J.*, **107**, 2108.

Rutten, R.G.M.: 1986, *Astron. Astrophys.*, **159**, 291.

Rutten, R.G.M.: 1987, *Astron. Astrophys.*, **177**, 131.

Saar, S.H.: 1987, *Observations and Analysis of Photospheric Magnetic Fields on G, K and M Dwarf Stars, Ph.D. thesis*, University of Colorado.

Saar, S.H., Linsky, J.L.: 1986, *Advances in Space Physics*, **6**, No. 8, 235.

Sampson, D.H., Zhang, H.L.: 1992, *Phys. Rev. A*, **45**, No. 3, 1556.

Schmitt, J.H.M.M., Haisch, B.M., Drake, J.J.: 1994, *Science*, **265**, 1420.

Schmitt, J.H.M.M., Harnden, F.R., Peres, G., Rosner, R, Serio, S.: 1985, *Astrophys. J.*, **288**, 751.

Schmitt, J.H.M.M., Collura, A., Sciortino, S. Vaiana, G.S., Harnden, F.R., Rosner, R.: 1990, *Astrophys. J.*, **365**, 704.

Schmitt, J.H.M.M., Golub, L., Harnden, F.R., Maxson, C.W., Rosner, R., Vaiana, G.S. : 1985, *Astrophys. J.*, **290**, 307.

Schrijver, C.J.: 1984, *18th ESLAB Symp.*, Schevgeningen.

Schrijver, C.J., Rutten, R.G.M.: 1987, *Astron. Astrophys.*, **177**, 155.

Schrijver, C.J., Mewe, R., van den Oord, G.H.J., Kaastra, J.S.: 1995, *Astron. Astrophys.*, **302**, 438.

Schwarzchild, M.: 1948, *Astrophys. J.* , **107**, 1.

Seaton, M.J.: 1964, *Planet Space Sci.*, **12**, 55.

Shafer, R.A., Haberl, F., Arnaud, K.A., Tennant, A.F.: 1990, *XSPEC - An X-Ray Spectral Fitting Package*, Version 2 of the User's Guide.

Shull, J.M., van Steenberg, M., 1982, *Astrophys. J. Suppl. Series*, **48**, 95.

Simon, T., Fekel, F.C.: 1987, *Astrophys. J.*, **316**, 434.

Simon, T., Herbig, G, Boesgaard, A.M.: 1985, *Astrophys. J.*, **293**, 553.

Smith, G., Edvardsson, B., Frisk, U.: 1986, *Astron. Astrophys.*, **165**, 126.

Spitzer, L.: 1978, *Physical processes in the Interstellar Medium*, J. Wiley & Sons.

Steffen, M.: 1985, *Astron. Astrophys. Suppl. Series*, **59**, 403.

Stenflo, J. O.: 1989, *Astron. Astrophys. Rev.*, **1**, 3.

Stepien, K, Ulmschneider, P.: 1989, *Astron. Astrophys.*, **216**, 139.

Summers, H.P.: 1974a, *Mon. Not. R. astr. Soc.*, **169**, 663.

Summers, H.P.: 1974b, *Appleton Laboratory Report*, AL-R-5, HMSO.

Tucker, W.H., Koren M.: 1971, *Astrophys. J.* , **168**, 283.

Ulmschneider, P.: 1971, *Astron. Astrophys.*, **14**, 275.

Vaiana, G.S., *et al.*: 1981, *Astrophys. J.* , **244**, 163.

van Regemorter, H.: 1962, *Astrophys. J.* , **136**, 906.

von Steiger, R., Geiss, J.: 1989, *Astron. Astrophys.*, **225**, 222.

Veck, N.J., Parkinson, J.H.: 1981, *Mon. Not. R. astr. Soc.*, **197**, 41.

Vernazza, J.E., Avrett, E.H., Loeser, R.: 1981, *Astrophys. J. Suppl.*, **45**, 635.

Vilhu, O.: 1984, *Astron. Astrophys.*, **133**, 117.

Wells, A.A., *et al.*: 1990, *Proc. SPIE*, **1344**, 230.

Wiese, W.L., Smith, M.W., Miles, B.M.: 1966, *At. Trans. Probabilities*, **1**, *Nat. Bur. Stand. Ref. Data Ser.*, N.B.S. No. **4**, (U.S. Gov. Printing Office, Washington D.C.).

Wiese, W.L., Smith, M.W., Miles, B.M.: 1969, *At. Trans. Probabilities*, **2**, *Nat. Bur. Stand. Ref. Data Ser.*, N.B.S. No. **22**, (U.S. Gov. Printing Office, Washington D.C.).

Withbroe, G.: 1976, *The Energy Balance and Hydrodynamics of the Solar Chromosphere and Corona, IAU Coll. No. 36*, R.M. Bonnet, P. Delache, (Eds), 263.

Withbroe, G.: 1983, *Astrophys. J.*, **267**, 825.

Withbroe, G.: 1988, *Astrophys. J.*, **325**, 442.

Wood, B.E., Harper, G.M., Linsky, J.L., Dempsey, R.C.: 1996, *Astrophys. J.*,**458**, 761.

Woolley, R. *et al.*: 1970, *R. Obs. Annals*, No. 5, 29.

Younger, S.E., 1981, *J. Quant. Spectros. Rad. Transf.*, **26**, 3229.

Younger, S.E., 1982, *J. Quant. Spectros. Rad. Transf.*, **27**, 541.

Younger, S.E., 1983, *J. Quant. Spectros. Rad. Transf.*, **29**, 61.

Appendix A

The Position Sensitive Proportional Counter (PSPC).

This instrument consists of two multiwire position sensitive counters in the local plane of ROSAT's X-ray mirror assembly. It has a 2° field of view. The counters contain a mixture of gas which is composed of argon, methane and xenon in the ratio 13:3:4, respectively. It operates at a pressure of 1.466 bars and a temperature of 22° C. X-ray photons from the emitting target enter through the entrance window which measures 8 cm in diameter and is made of a $1\,\mu m$ thin polypropylene tile which is coated with $50\,\mu g\,cm^{-2}$ of carbon and $40\,\mu g\,cm^{-2}$ of Lexan. This allows a $\sim$ 50% transition below the carbon edge at 0.28 keV, while just above the carbon-edge the window becomes opaque and this is evident from Figure A.1, which shows the quantum efficiency of the instrument. Note that the the X-ray absorption of the counter gas is $\sim$ 100% around 2keV, where the X-ray mirror cuts off.

Once an X-ray photon enters the window, it is fully absorbed by the gas mixture which is consequently ionised and hence a detection is recorded in the position sensitive cathode strip. The expression for the energy resolution of the counter over its entire sensitive area is given by

$$\frac{\Delta E}{E} = 0.43\,(\frac{E}{0.93})^{-0.5}\,(FWHM) \tag{A.1}$$

Its spatial resolution at 0.93 keV is 300 μm (corresponding to 25 arcseconds in the focal plane), with a 5% r.m.s deviation of the counters sensitive area. PSPC observations can be requested with and/or without the Boron filter, which enables the subdivision of the carbon band into two bands, since the filter has negligible transmission between 0.188 keV and 0.28 keV. The filter itself, is made up of a carbon film and a coating of boron carbide. The observations we obtained *without* the filter were ignored because they go to lower

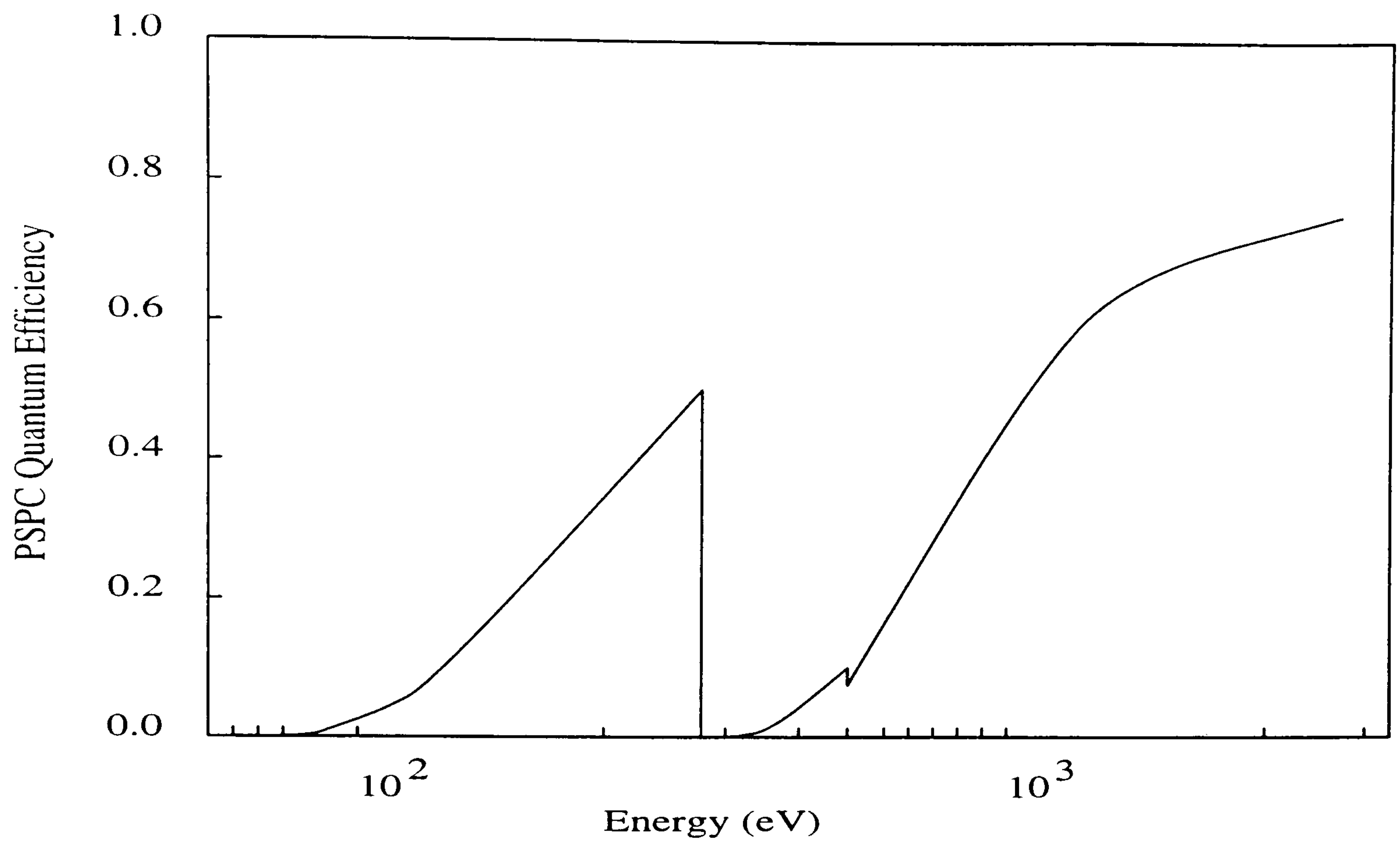

Figure A.1: PSPC Quantum Efficiency vs Energy. From *'ROSAT AO-2 Technical Description'*, (1991).

energies where problems are suspected with the calibration.

Appendix B

Flowdiagrams of RS and LMF Spectral Emission Codes

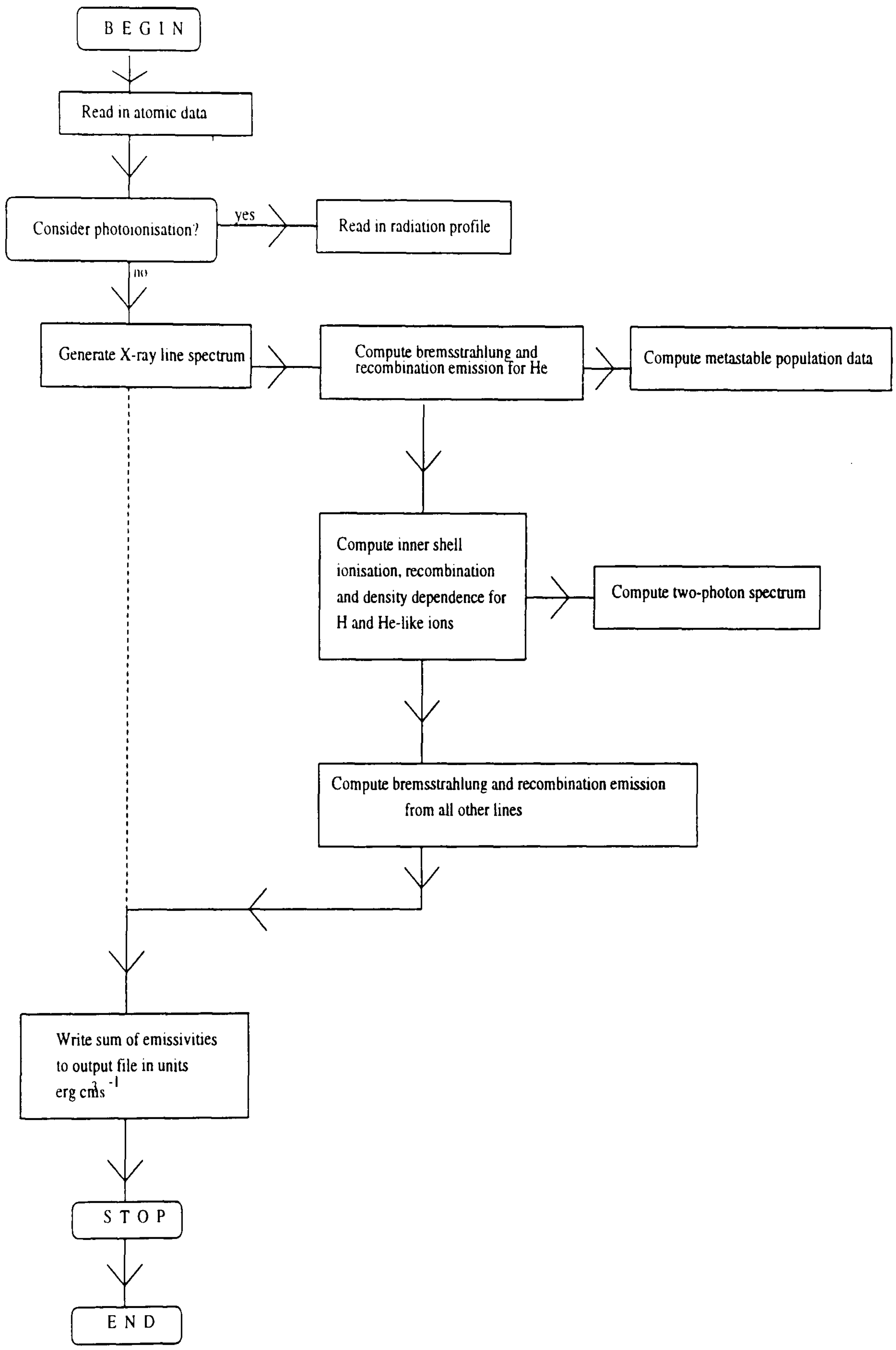

Figure B.1: Simplified flow-diagram for the RS code.

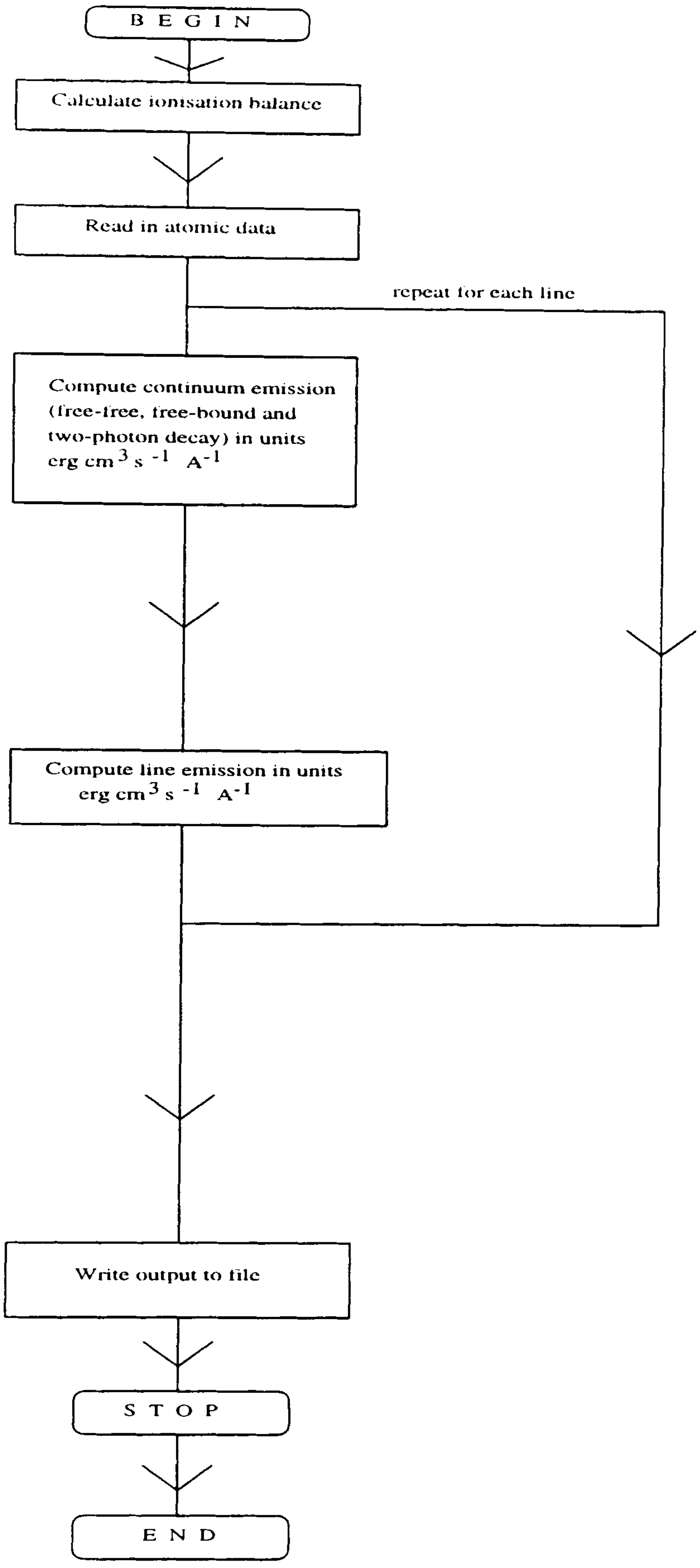

Figure B.2: Simplified flow-diagram for the LMF code.

Appendix C

The Plane Parallel and Spherically Symmetric Models

Table C.1: Calculated parameters using the spherically symmetric model for χ^1 Ori, where the *real* emission measures ($Em(0.3)$), the *total*, *gas* and *electron* pressures (P_T, P_g and P_e, respectively), and the *absolute* radial extent of the atmosphere ($r - R_*$), are given as a function of the temperature (T_e).

log $\mathbf{T_e}$ (K)	log $Em(0.3)$ (cm^{-5})	log (P_T/k) ($cm^{-3}\,K$)	log (P_g/k) ($cm^{-3}\,K$)	log (P_e/k) ($cm^{-3}\,K$)	$r - R_*$ ($10^8\,cm$)
3.80	31.82	16.73	16.57	14.92	1.69
3.90	31.27	16.50	16.31	15.44	1.88
4.00	30.77	16.46	16.29	15.81	1.92
4.10	30.22	16.45	16.28	15.91	1.94
4.20	28.67	16.45	16.28	15.95	1.94
4.30	28.12	16.45	16.28	15.97	1.94
4.40	27.87	16.45	16.28	15.98	1.94
4.50	27.77	16.45	16.29	16.01	1.94
4.60	27.75	16.45	16.30	16.02	1.94
4.70	27.74	16.45	16.31	16.02	1.94
4.80	27.73	16.45	16.31	16.03	1.95
4.90	27.70	16.45	16.32	16.04	1.95
5.00	27.56	16.45	16.33	16.05	1.95
5.10	27.32	16.45	16.34	16.06	1.95
5.20	27.17	16.45	16.35	16.07	1.95
5.30	27.26	16.45	16.36	16.08	1.95
5.40	27.29	16.45	16.18	15.90	1.96
5.50	27.34	16.45	16.23	15.94	1.97
5.60	27.41	16.45	16.26	15.98	1.98
5.70	27.49	16.45	16.29	16.01	2.00
5.80	27.59	16.44	16.32	16.04	2.04
5.90	27.69	16.44	16.34	16.06	2.11
6.00	27.80	16.44	16.36	16.08	2.23
6.10	27.92	16.44	16.38	16.09	2.48
6.20	28.04	16.44	16.39	16.10	2.96
6.30	28.18	16.44	16.39	16.11	3.94
6.40	28.32	16.43	16.40	16.11	6.02
6.50	28.46	16.42	16.39	16.11	10.6
6.60	28.61	16.40	16.37	16.09	21.1
6.70	28.75	16.35	16.33	16.05	46.8
6.74	28.78	16.31	16.30	16.01	66.8

Table C.2: Calculated parameters in plane parallel geometry for ϵ Eri, where the *real* emission measures ($Em(0.3)$), the *total*, *gas* and *electron* pressures (P_T, P_g and P_e, respectively), and the *absolute* radial extent of the atmosphere ($r - R_*$), are given as a function of the temperature (T_e).

log T_e (K)	log $Em(0.3)$ (cm^{-5})	log (P_T/k) ($cm^{-3}\,K$)	log (P_g/k) ($cm^{-3}\,K$)	log (P_e/k) ($cm^{-3}\,K$)	$r - R_*$ ($10^8\,cm$)
3.80	31.45	16.57	16.46	15.96	0.60
3.90	31.00	16.52	16.38	15.95	0.62
4.00	30.60	16.50	16.34	15.96	0.63
4.10	29.95	16.48	16.33	15.99	0.64
4.20	28.65	16.48	16.32	16.01	0.64
4.30	28.05	16.48	16.32	16.01	0.64
4.40	27.55	16.48	16.32	16.03	0.64
4.50	27.30	16.48	16.33	16.05	0.64
4.60	27.25	16.48	16.34	16.05	0.64
4.70	27.20	16.48	16.34	16.06	0.64
4.80	27.20	16.48	16.35	16.07	0.64
4.90	27.10	16.48	16.36	16.08	0.64
5.00	26.90	16.48	16.37	16.09	0.64
5.10	26.75	16.48	16.38	16.10	0.64
5.20	26.60	16.48	16.39	16.11	0.64
5.30	26.83	16.48	16.40	16.12	0.64
5.40	26.90	16.48	16.37	16.09	0.65
5.50	26.99	16.48	16.39	16.11	0.65
5.60	27.10	16.48	16.41	16.13	0.65
5.70	27.20	16.48	16.42	16.14	0.66
5.80	27.32	16.48	16.43	16.15	0.67
5.90	27.44	16.48	16.44	16.16	0.69
6.00	27.57	16.48	16.45	16.17	0.74
6.10	27.70	16.48	16.45	16.17	0.84
6.20	27.84	16.48	16.46	16.17	1.05
6.30	27.98	16.47	16.46	16.17	1.51
6.40	28.14	16.46	16.45	16.17	2.56
6.50	28.31	16.45	16.44	16.15	5.11
6.60	28.55	16.42	16.41	16.12	12.4
6.62	28.59	16.41	16.40	16.11	15.4

Table C.3: Calculated parameters using the spherically symmetric model for ϵ Eri, where the *real* emission measures ($Em(0.3)$), the *total*, *gas* and *electron* pressures (P_T, P_g and P_e, respectively), and the *absolute* radial extent of the atmosphere ($r - R_*$), are given as a function of the temperature (T_e).

log $\mathbf{T_e}$ (K)	log $Em(0.3)$ (cm^{-5})	log (P_T/k) ($cm^{-3}\,K$)	log (P_g/k) ($cm^{-3}\,K$)	log (P_e/k) ($cm^{-3}\,K$)	$r - R_*$ ($10^8\,cm$)
3.80	31.43	16.51	16.40	15.90	0.60
3.90	30.98	16.45	16.31	15.88	0.62
4.00	30.58	16.41	16.26	15.87	0.64
4.10	29.93	16.39	16.24	15.90	0.66
4.20	28.63	16.39	16.23	15.92	0.66
4.30	28.03	16.39	16.23	15.92	0.66
4.40	27.53	16.39	16.23	15.94	0.66
4.50	27.28	16.39	16.24	15.96	0.66
4.60	27.23	16.39	16.24	15.96	0.66
4.70	27.18	16.39	16.25	15.97	0.66
4.80	27.18	16.39	16.26	15.98	0.66
4.90	27.08	16.39	16.27	15.99	0.66
5.00	26.88	16.39	16.28	16.00	0.66
5.10	26.73	16.39	16.29	16.01	0.66
5.20	26.58	16.39	16.30	16.02	0.66
5.30	26.64	16.39	16.31	16.03	0.66
5.40	26.74	16.39	16.28	16.00	0.66
5.50	26.85	16.39	16.30	16.02	0.66
5.60	26.97	16.39	16.32	16.04	0.67
5.70	27.09	16.39	16.33	16.05	0.67
5.80	27.21	16.39	16.34	16.06	0.69
5.90	27.35	16.39	16.35	16.07	0.72
6.00	27.48	16.39	16.36	16.08	0.78
6.10	27.62	16.39	16.36	16.08	0.90
6.20	27.77	16.38	16.36	16.08	1.17
6.30	27.92	16.38	16.36	16.08	1.78
6.40	28.08	16.37	16.35	16.07	3.18
6.50	28.25	16.34	16.33	16.05	6.66
6.60	28.46	16.29	16.28	15.99	16.6
6.62	28.49	16.27	16.26	15.97	20.4

Table C.4: Calculated parameters in plane parallel geometry for ξ Boo A, where the *real* emission measures ($Em(0.3)$), the *total*, *gas* and *electron* pressures (P_T, P_g and P_e, respectively), and the *absolute* radial extent of the atmosphere ($r - R_*$), are given as a function of the temperature (T_e).

log $\mathbf{T_e}$ (K)	log $Em(0.3)$ (cm^{-5})	$\log(P_T/k)$ ($cm^{-3}\,K$)	$\log(P_g/k)$ ($cm^{-3}\,K$)	$\log(P_e/k)$ ($cm^{-3}\,K$)	$r - R_*$ ($10^8\,cm$)
3.80	31.70	16.85	16.69	15.04	0.94
3.90	31.22	16.69	16.51	15.63	1.01
4.00	30.80	16.67	16.49	16.02	1.03
4.10	30.30	16.66	16.49	16.12	1.03
4.20	28.75	16.66	16.49	16.16	1.04
4.30	28.25	16.66	16.49	16.18	1.04
4.40	27.95	16.66	16.50	16.20	1.04
4.50	27.80	16.66	16.50	16.22	1.04
4.60	27.80	16.66	16.51	16.23	1.04
4.70	27.75	16.66	16.52	16.24	1.04
4.80	27.70	16.66	16.53	16.24	1.04
4.90	27.50	16.66	16.54	16.25	1.04
5.00	27.20	16.66	16.55	16.26	1.04
5.10	27.08	16.66	16.56	16.27	1.04
5.20	26.98	16.66	16.56	16.28	1.04
5.30	28.14	16.66	16.57	16.29	1.04
5.40	27.50	16.66	16.48	16.19	1.04
5.50	27.46	16.66	16.51	16.22	1.05
5.60	27.49	16.66	16.53	16.25	1.05
5.70	27.56	16.66	16.56	16.27	1.06
5.80	27.64	16.66	16.57	16.29	1.07
5.90	27.74	16.66	16.59	16.31	1.10
6.00	27.85	16.66	16.60	16.32	1.14
6.10	27.96	16.66	16.61	16.33	1.23
6.20	28.08	16.65	16.62	16.34	1.41
6.30	28.21	16.65	16.62	16.34	1.78
6.40	28.34	16.65	16.63	16.34	2.56
6.50	28.49	16.64	16.62	16.34	4.29
6.60	28.65	16.63	16.61	16.33	8.29
6.70	28.86	16.60	16.59	16.30	18.8
6.75	28.97	16.58	16.57	16.28	31.1

Table C.5: Calculated parameters using the spherically symmetric model for ξ Boo A, where the *real* emission measures ($Em(0.3)$), the *total*, *gas* and *electron* pressures (P_T, P_g and P_e, respectively), and the *absolute* radial extent of the atmosphere ($r - R_*$), are given as a function of the temperature (T_e).

log $\mathbf{T_e}$ (K)	log $Em(0.3)$ (cm^{-5})	log (P_T/k) ($cm^{-3}\,K$)	log (P_g/k) ($cm^{-3}\,K$)	log (P_e/k) ($cm^{-3}\,K$)	$r - R_*$ ($10^8\,cm$)
3.80	31.67	16.81	16.65	15.00	0.94
3.90	31.19	16.62	16.44	15.56	1.02
4.00	30.77	16.58	16.41	15.93	1.05
4.10	30.27	16.57	16.41	16.04	1.06
4.20	28.72	16.57	16.40	16.07	1.06
4.30	28.22	16.57	16.41	16.09	1.06
4.40	27.92	16.57	16.41	16.11	1.06
4.50	27.77	16.57	16.42	16.14	1.06
4.60	27.77	16.57	16.42	16.14	1.06
4.70	27.72	16.57	16.43	16.15	1.06
4.80	27.67	16.57	16.44	16.16	1.06
4.90	27.47	16.57	16.45	16.17	1.06
5.00	27.17	16.57	16.46	16.18	1.06
5.10	27.05	16.57	16.47	16.19	1.06
5.20	26.95	16.57	16.48	16.20	1.06
5.30	27.04	16.57	16.49	16.21	1.06
5.40	27.11	16.57	16.39	16.11	1.06
5.50	27.19	16.57	16.42	16.14	1.07
5.60	27.29	16.57	16.45	16.17	1.07
5.70	27.39	16.57	16.47	16.19	1.08
5.80	27.50	16.57	16.49	16.21	1.09
5.90	27.62	16.57	16.50	16.22	1.12
6.00	27.75	16.57	16.52	16.23	1.17
6.10	27.88	16.57	16.53	16.24	1.28
6.20	28.01	16.57	16.53	16.25	1.51
6.30	28.15	16.56	16.54	16.25	1.98
6.40	28.30	16.56	16.54	16.25	3.02
6.50	28.45	16.55	16.53	16.25	5.34
6.60	28.60	16.53	16.51	16.23	10.8
6.70	28.76	16.49	16.48	16.19	24.5
6.75	28.81	16.44	16.43	16.14	38.7

Table C.6: Calculated parameters in plane parallel geometry for α Cen A, where the *real* emission measures ($Em(0.3)$), the *total*, *gas* and *electron* pressures (P_T, P_g and P_e, respectively), and the *absolute* radial extent of the atmosphere ($r - R_*$), are given as a function of the temperature (T_e).

log $\mathbf{T_e}$ (K)	log $Em(0.3)$ (cm^{-5})	log (P_T/k) ($cm^{-3}\,K$)	log (P_g/k) ($cm^{-3}\,K$)	log (P_e/k) ($cm^{-3}\,K$)	$r - R_*$ ($10^8\,cm$)
3.80	31.20	16.38	16.22	14.57	1.47
3.90	30.65	15.91	15.73	14.85	1.81
4.00	30.15	15.64	15.47	14.99	2.09
4.10	29.35	15.52	15.35	14.98	2.30
4.20	27.95	15.50	15.34	15.00	2.33
4.30	27.40	15.50	15.34	15.03	2.34
4.40	27.20	15.50	15.34	15.04	2.34
4.50	27.00	15.50	15.35	15.07	2.34
4.60	26.90	15.50	15.35	15.07	2.35
4.70	26.80	15.50	15.36	15.08	2.35
4.80	26.72	15.50	15.37	15.09	2.35
4.90	26.65	15.50	15.38	15.09	2.36
5.00	26.43	15.50	15.39	15.10	2.37
5.10	26.20	15.50	15.40	15.11	2.37
5.20	25.95	15.50	15.41	15.12	2.38
5.30	25.56	15.50	15.41	15.13	2.38
5.40	25.65	15.50	15.38	15.10	2.39
5.50	25.75	15.50	15.40	15.12	2.40
5.60	25.86	15.50	15.42	15.14	2.42
5.70	25.97	15.50	15.43	15.15	2.45
5.80	26.10	15.50	15.44	15.16	2.52
5.90	26.23	15.49	15.45	15.17	2.65
6.00	26.36	15.49	15.46	15.18	2.93
6.10	26.51	15.49	15.46	15.18	3.54
6.20	26.67	15.48	15.46	15.18	4.90
6.30	26.85	15.47	15.45	15.17	8.18
6.40	27.09	15.44	15.43	15.14	17.4
6.43	27.15	15.42	15.41	15.12	23.4

Table C.7: Calculated parameters using the spherically symmetric model for α Cen A, where the *real* emission measures ($Em(0.3)$), the *total*, *gas* and *electron* pressures (P_T, P_g and P_e, respectively), and the *absolute* radial extent of the atmosphere ($r - R_*$), are given as a function of the temperature (T_e).

log $\mathbf{T_e}$ (K)	log $Em(0.3)$ (cm^{-5})	log (P_T/k) ($cm^{-3}\,K$)	log (P_g/k) ($cm^{-3}\,K$)	log (P_e/k) ($cm^{-3}\,K$)	$r - R_*$ ($10^8\,cm$)
3.80	31.17	16.37	16.21	14.56	1.47
3.90	30.62	15.89	15.70	14.83	1.81
4.00	30.12	15.59	15.42	14.94	2.12
4.10	29.31	15.44	15.27	14.90	2.37
4.20	27.91	15.42	15.25	14.92	2.41
4.30	27.36	15.42	15.25	14.94	2.42
4.40	27.16	15.42	15.26	14.96	2.42
4.50	26.96	15.42	15.26	14.98	2.43
4.60	26.86	15.42	15.27	14.99	2.43
4.70	26.76	15.41	15.27	14.99	2.44
4.80	26.68	15.41	15.28	15.00	2.44
4.90	26.61	15.41	15.29	15.01	2.45
5.00	26.39	15.41	15.30	15.02	2.46
5.10	26.16	15.41	15.31	15.03	2.47
5.20	25.91	15.41	15.32	15.04	2.48
5.30	25.50	15.41	15.33	15.05	2.48
5.40	25.59	15.41	15.29	15.01	2.49
5.50	25.70	15.41	15.31	15.03	2.50
5.60	25.81	15.41	15.33	15.05	2.53
5.70	25.93	15.41	15.35	15.06	2.57
5.80	26.06	15.41	15.36	15.07	2.66
5.90	26.19	15.41	15.36	15.08	2.85
6.00	26.33	15.40	15.37	15.09	3.24
6.10	26.47	15.40	15.37	15.09	4.08
6.20	26.63	15.39	15.37	15.08	5.96
6.30	26.79	15.37	15.35	15.07	10.5
6.40	27.00	15.32	15.31	15.02	22.8
6.43	27.04	15.29	15.28	14.99	30.5

Table C.8: Calculated parameters in plane parallel geometry for α Cen B, where the *real* emission measures ($Em(0.3)$), the *total*, *gas* and *electron* pressures (P_T, P_g and P_e, respectively), and the *absolute* radial extent of the atmosphere ($r - R_*$), are given as a function of the temperature (T_e).

$\log \mathbf{T_e}$ (K)	$\log Em(0.3)$ (cm^{-5})	$\log(P_T/k)$ $(cm^{-3}\,K)$	$\log(P_g/k)$ $(cm^{-3}\,K)$	$\log(P_e/k)$ $(cm^{-3}\,K)$	$r - R_*$ $(10^8\,cm)$
3.80	31.15	16.51	16.35	14.70	0.83
3.90	30.65	16.13	15.95	15.07	0.98
4.00	30.15	16.00	15.83	15.35	1.06
4.10	29.40	15.96	15.80	15.43	1.09
4.20	27.90	15.96	15.79	15.46	1.09
4.30	27.30	15.96	15.79	15.48	1.09
4.40	27.10	15.96	15.80	15.50	1.09
4.50	27.00	15.96	15.81	15.52	1.10
4.60	26.90	15.96	15.81	15.53	1.10
4.70	26.77	15.96	15.82	15.54	1.10
4.80	26.65	15.96	15.83	15.55	1.10
4.90	26.50	15.96	15.84	15.55	1.10
5.00	26.30	15.96	15.85	15.56	1.10
5.10	26.20	15.96	15.86	15.57	1.10
5.20	26.10	15.96	15.87	15.58	1.10
5.30	26.26	15.96	15.88	15.59	1.10
5.40	26.35	15.96	15.87	15.59	1.10
5.50	26.46	15.96	15.89	15.61	1.11
5.60	26.57	15.96	15.90	15.62	1.12
5.70	26.68	15.96	15.91	15.63	1.14
5.80	26.81	15.96	15.92	15.64	1.17
5.90	26.94	15.96	15.93	15.64	1.25
6.00	27.07	15.95	15.93	15.65	1.42
6.10	27.21	15.95	15.93	15.65	1.77
6.20	27.36	15.94	15.93	15.64	2.56
6.30	27.54	15.93	15.91	15.63	4.47
6.40	27.76	15.90	15.89	15.60	9.75
6.43	27.83	15.88	15.87	15.58	13.1

Table C.9: Calculated parameters using the spherically symmetric model for α Cen B, where the *real* emission measures ($Em(0.3)$), the *total*, *gas* and *electron* pressures (P_T, P_g and P_e, respectively), and the *absolute* radial extent of the atmosphere ($r - R_*$), are given as a function of the temperature (T_e).

log $\mathbf{T}_e$ (K)	log $Em(0.3)$ (cm^{-5})	log (P_T/k) ($cm^{-3}\,K$)	log (P_g/k) ($cm^{-3}\,K$)	log (P_e/k) ($cm^{-3}\,K$)	$r - R_*$ ($10^8\,cm$)
3.80	31.13	16.49	16.33	14.68	0.83
3.90	30.62	16.08	15.90	15.03	0.99
4.00	30.12	15.92	15.75	15.27	1.08
4.10	29.37	15.87	15.71	15.34	1.13
4.20	27.87	15.87	15.70	15.37	1.14
4.30	27.27	15.87	15.70	15.39	1.14
4.40	27.07	15.87	15.71	15.41	1.14
4.50	26.97	15.87	15.72	15.43	1.14
4.60	26.87	15.87	15.72	15.44	1.14
4.70	26.74	15.87	15.73	15.45	1.14
4.80	26.62	15.87	15.74	15.45	1.14
4.90	26.47	15.87	15.75	15.46	1.14
5.00	26.27	15.87	15.76	15.47	1.14
5.10	26.17	15.87	15.77	15.48	1.14
5.20	26.07	15.87	15.77	15.49	1.14
5.30	26.10	15.87	15.78	15.50	1.14
5.40	26.21	15.87	15.78	15.50	1.15
5.50	26.32	15.87	15.80	15.51	1.15
5.60	26.45	15.87	15.81	15.53	1.16
5.70	26.57	15.87	15.82	15.54	1.19
5.80	26.71	15.87	15.83	15.55	1.23
5.90	26.85	15.86	15.83	15.55	1.33
6.00	26.99	15.86	15.84	15.55	1.53
6.10	27.14	15.85	15.84	15.55	1.99
6.20	27.30	15.84	15.83	15.55	3.03
6.30	27.47	15.82	15.81	15.53	5.60
6.40	27.68	15.78	15.77	15.48	12.8
6.43	27.74	15.75	15.74	15.45	17.3